Long Bolted HSS-to-HSS Connection for Modular Structures: A Solution for Indigenous Housing Challenges

A Thesis

submitted to the Faculty of Graduate Studies

in partial fulfilment of the requirements for the degree

DOCTOR OF PHILOSOPHY

in

Civil Engineering

Lakehead University

By

Mostafa Abdelhamed (Elhadary)

Supervisor:

Dr. Ahmed Elshaer
Associate Professor, Department of Civil Engineering at Lakehead University

Co-Supervisor:

Dr. Ahmed Bediwy
Assistant professor at United Arab Emirates University
Adjunct Professor at Lakehead University

ABSTRACT

Remote Indigenous communities across Canada are experiencing severe housing shortages and widespread repair needs, both stemming from engineering challenges encountered during construction. To address these issues, prefabricated steel moment-resisting frame modular houses are increasingly being adopted as alternatives to conventional housing. These structures offer several technical advantages, including enhanced quality control, lightweight components, and ease of transportation to remote and rural regions. This thesis explores the application of hollow structural sections (HSS) in panelized steel modular structures by introducing an innovative steel-bolted connection for joining HSS beams to HSS columns using high-strength long bolts as an efficient solution to the Indigenous housing challenge. The proposed connection is designed for easy installation without requiring skilled labour or heavy machinery. This thesis utilizes experimental testing, numerical analysis, and machine learning techniques to comprehensively address the overarching research problem through four integrated studies. In the first study, specimens were fabricated and tested under monotonic loading, with a Digital Image Correlation (DIC) camera used to capture full-field 3D displacement and deformation until failure. This research studies the structural performance of various geometric parameters, including bolt arrangement, extended plate thickness, number of bolts, and the presence of stiffeners in terms of joint stiffness, ductility, ultimate capacity, and failure modes. The second study focused on key connection parameters, including extended plate thickness, bolt arrangement, bolt diameter, and the number of bolts. Results highlighted the critical role of bolt configuration and quantity in maintaining the "strong column weak beam" principle, ensuring plastic hinging at the beam. The third study evaluated the effectiveness of three reinforcement techniques: (1) a stiffener below the extended plate, (2) concrete infill within the column, and (3) a combination of both. These

techniques significantly impacted the structural performance of different bolt configurations, preventing premature failures such as extended plate rupture and local column buckling and reducing the ultimate rotation of the connection. Failure mode charts were developed to predict failure modes for both unstiffened and stiffened configurations to streamline the design process. These charts eliminate the need for several iterations of full design analysis, reducing design processing time and trials. In the fourth study, machine learning techniques, including genetic regression, decision trees, and neural networks, were applied to predict the ultimate moment capacity and failure modes of the steel bolted connection under monotonic loading. A dataset of unstiffened configurations from the first study was used to train and test these models, demonstrating high predictive accuracy. Additionally, genetic regression was employed to develop mathematical formulas to predict the ultimate capacity of the connection. These models underscore their potential as reliable computational tools to complement both experimental and analytical approaches.

KEYWORDS

Prefabricated Steel Structure, Modular Structures, Bolted Connection, Hollow Structural Section, Indigenous Communities, Digital Image Correlation, Hollow Structural Section, Finite Element Model, Design guidelines, Machine learning, Regression, Artificial Neural Network, Failure mode.

CO-AUTHORSHIP STATEMENT

This thesis has been prepared in accordance with the regulations for an Integrated-Article format stipulated by the Faculty of Graduate Studies at Lakehead University. Information presented from outside sources, which has been used for analysis or discussion, has been cited where appropriate. This thesis has been co-authored as:

Chapter 2: Novel Steel Connection for Panelized Modular Houses in Indigenous Communities: An Experimental Study

Elhadary, M., Bediwy, A. and Elshaer, A. (2024). Novel steel connection for modular houses in indigenous communities: An experimental study. Journal of Construction Steel Research, 220: 108850. Elsevier. https://doi.org/10.1016/J.JCSR.2024.108850.

Chapter 3: Capacity and Failure Mode Prediction of Long-Bolted Connection in Panelized Modular Houses

Elhadary, M., Elshaer, A. and Bediwy, A. (2024). Capacity and failure mode prediction of long-bolted connection in panelized modular houses (submitted as a journal publication)

Chapter 4: Machine Learning-based Prediction of The Structural Performance of A Long-Bolted HSS-To-HSS Connection

Elhadary, M., Bediwy, A. and Elshaer, A. (2025). Machine Learning-based Prediction of The Structural Performance of A Long-Bolted HSS-To-HSS Connection. (submitted as a journal publication)

Chapter 5: Numerical Investigation of Reinforcement Techniques for HSS-to-HSS connection in modular houses

Elhadary, M., Bediwy, A. and Elshaer, A. (2025). Machine Learning-based Prediction of The Structural Performance of A Long-Bolted HSS-To-HSS Connection. (submitted as a journal publication)

DEDICATION

To my beloved mother, Emtyaz and my dear father, Refaat, whose unwavering love and support made this journey possible, may God grant you both the reward of this degree and may it weigh heavily in the balance of your good deeds.

ACKNOWLEDGEMENTS

In the name of Allah, the Most Gracious, the Most Merciful. I am deeply grateful to Allah Almighty for granting me the opportunity to embark on this Ph.D. journey, guiding me through unexpected paths, and blessing me with the strength and perseverance to see it through to completion. I am thankful to Allah for the hardship before ease.

I would like to express my deepest gratitude to my supervisors, Dr. “Ahmed Elshaer” and Dr. “Ahmed Bediwy”, for their unwavering support, guidance and advice. This endeavour would not have been possible without his mentorship, which has been vital in shaping my research and academic growth. From providing insightful feedback on my work to offering invaluable advice on navigating the challenges of academia and beyond, his dedication and commitment to my success have been truly remarkable.

I am also indebted to the members of my thesis committee, Prof. “Eltayeb Mohamedelhassan” Prof. “Kefu Liu”, and Prof. “Khaled Sennah” for their scholarly insights, constructive feedback, and invaluable contributions to shaping this research. Their expertise and guidance have been instrumental in refining the scope of the dissertation.

To my beloved mother, whose unwavering support and prayers carried me through every step of this journey. You believed in me when I doubted myself and pushed me to reach for the stars. Though you are no longer with me, your spirit and love will always be my guiding light. I wish you were here to see me achieve this milestone, but I know you are watching over me with pride. May Allah make this achievement a source of pride and honour for my Mama. One day, I will return to your grave in Egypt to tell you that I have fulfilled my dream of becoming a doctor. Thank you, Mama, for everything.

I am deeply grateful to my father, whose unwavering support and guidance have been instrumental in my journey. Without his encouragement and the education, he provided, I would not have reached this milestone of defending my Ph.D. He has been my role model, inspiring me to become an engineer and teaching me to approach problems easily and confidently. I pray that God grants him good health and a long life so that I may continue to learn from him.

I am deeply grateful to my sisters, Reham and Mai, and their husbands, for their unwavering support and encouragement throughout my journey. Your belief in me has been the driving force behind my pursuit of a Ph.D. and my dream of becoming a doctor. From the moments of doubt to the milestones of success, your presence has been a source of strength and inspiration.

Thanks should also go to the members of my research group, “SWERL” for their encouragement and support. I want to use this space to thank them, in no specific order: “Mutaz,” “Magdy”, “Raghdah,” “Tristen,” “Stephen,” “Amir,” and “Kendra.” Your collaboration and company have enriched my academic experience and made this journey more fulfilling. Whether it was research feedback or offering words of encouragement, I am grateful for the friendships and professional relationships built during this time. Also, thanks are extended to my office mates, “Mehran,” “Aysen,” “Zahra,” “Maral,” and “Ali.”

LIST OF JOURNAL PUBLICATIONS

Elhadary, M., Bediwy, A., and Elshaer, A. (2024). Novel steel connection for modular houses in indigenous communities: An experimental study." Journal of Construction Steel Research, 220: 108850. Elsevier. https://doi.org/10.1016/J.JCSR.2024.108850.

Elhadary, M., Elshaer, A., and Bediwy, A. (2024). Capacity and failure mode prediction of long-bolted connection in panelized modular houses. (submitted as a journal publication)

Elhadary, M., Bediwy, A. and Elshaer, A. (2025). Machine Learning-based Prediction of The Structural Performance of A Long-Bolted Steel Connection. (submitted as a journal publication)

Elhadary, M., Bediwy, A. and Elshaer, A. (2025). Numerical Investigation of Reinforcement Techniques for HSS-to-HSS connection in modular houses. (submitted as a journal publication)

Elhadary, M., Bediwy, A. and Elshaer, A. (2025). Numerical Investigation of a Novel Steel Connection for Panelized Modular Houses. (submitted as a journal publication)

LIST OF CONFERENCE PUBLICATIONS

Elhadary, M., and Elshaer, A. "Behaviour of Beam–Column Connection of Modular Steel Buildings," in Lecture Notes in Civil Engineering, vol. 348 LNCE, Springer, Cham, 2023, pp. 95–105. doi: 10.1007/978-3-031-34159-5_7.

Elhadary, M., Bediwy, A. and Elshaer, A. "Structural Performance of Novel Steel Connection for Indigenous Modular Houses," in Lecture Notes in Civil Engineering, Moncton, New Brunswick: Springer Singapore, 2025, pp. 253–266. doi: 10.1007/978-3-031-61535-1_21.

Elhadary, M., Bediwy, A. and Elshaer, A. 2024. "Experimental Investigation on a Novel Steel Connection for Modular Indigenous Houses." Can. Soc. Civ. Eng. 2024 Annu. Conf. Niagara Falls, Ontario.

Elhadary, M., Bediwy, A. and Elshaer, A. 2025. "Machine-learning-based models to predict ultimate moment capacity and failure modes of steel modular joint" Can. Soc. Civ. Eng. 2025 Annu. Conf. Winnepeg, Manitoba.

TABLE OF CONTENTS

LIST OF TABLES

LIST OF FIGURES

CHAPTER 1: INTRODUCTION TO INDIGENOUS HOUSING CHALLENGES AND PROPOSED SOLUTION

1.1 Background

Canada is currently grappling with a persistent housing shortage and increasing homelessness, particularly within Indigenous communities, a crisis deeply impacting Canadian society. This issue was highlighted in the United Nations Assembly General's 2019 report on Adequate Housing, which urged states to prioritize addressing the deplorable housing conditions faced by Indigenous peoples, whether on reserves, in rural, or urban areas (United Nations 2019). Media attention in the early 1990s brought these housing challenges to light, raising public awareness and prompting the Auditor General of Canada to investigate the matter in 2003. Statistics Canada reported that in 2016, approximately 63% of Indigenous people resided in remote and rural areas, while 27% lived in urban regions (“Statistics Canada” 2017). The 2021 census revealed Indigenous people as the fastest-growing demographic in Canada, nearly doubling the growth rate of the non-Indigenous population, now accounting for 1.8 million individuals. This rapid growth, coupled with high birth rates, has led to overcrowded housing conditions, exacerbating socio-economic issues. The COVID-19 pandemic further underscored these vulnerabilities, as pre-existing conditions and inadequate local healthcare infrastructure intensified the virus's impact within these communities. The housing challenges can be categorized into (i) Materials-related, (ii) Climate-related, and (iii) Construction-related difficulties, which will be further discussed in Chapter 2.

There is an urgent need for a structural solution that can address the unique climate and construction challenges while remaining affordable for remote and northern Indigenous communities. Steel modular structures are gaining popularity in the construction industry due to benefits like reduced waste, fewer on-site workers, improved quality control, and faster

construction times (Kamali and Hewage 2016; Lawson et al. 2012; Lopez and Froese 2016). Steel modular structures are believed to offer a viable solution to these complex issues, given their technical advantages, such as non-organic and non-combustible materials compared to traditional timber structures, and lightweight, space-saving properties compared to concrete structures during transportation. These structures have been utilized in various permanent facilities, such as hotels and apartments, to meet growing infrastructure demands in North America and parts of Europe. Following the catastrophic earthquakes in Turkey and Syria in 2023, 10,000 steel prefabricated houses (i.e., volumetric modules) were employed as temporary housing for over 1.5 million displaced individuals (Al Jazeera 2023). Steel modular construction can be categorized into three different categories based on the off-site construction methods, which are elemental, panelized, and volumetric, that can be used to form the structural system of a building (Corfar and Tsavdaridis 2022). The panelized technique involves fabricating structural components, such as roof, wall panels, and floor systems, in a factory and then transporting them to the construction site for assembly. This method differs from the volumetric approach, where entire pre-constructed modules are transported as units. The panelized technique is particularly suitable for northern and remote Indigenous communities, where transportation risks, such as the potential for damage or difficulty in moving large volumetric units, can be a significant concern. By relying on smaller, more easily manageable components, the panelized approach mitigates these risks and offers more flexibility in the construction process. Additionally, panelized construction requires less heavy machinery for on-site assembly, making it more adaptable to areas with limited access or infrastructure. This reduces not only the logistical challenges associated with transportation but also the costs of using large cranes and equipment for placement, which are necessary for volumetric units. Volumetric construction, with its fully pre-constructed modules, often faces

challenges during on-site assembly, as it requires precise coordination and heavy equipment to position the large units, which can be difficult in remote or confined spaces. In contrast, the panelized approach avoids these assembly complications by allowing for smaller components that are easier to handle and assemble on-site. Furthermore, the ability to customize and adjust individual panels on-site enhances the overall construction process, allowing for quicker adaptations to specific site conditions or design modifications. This flexibility is especially valuable when future expansions or alterations are required, as panelized components can be easily reconfigured or adjusted. In contrast, volumetric units are typically pre-designed and rigid, which limits customization once they are produced. As a result, the panelized approach provides improved efficiency, adaptability, and cost-effectiveness, while also offering enhanced seismic performance and greater flexibility in the design and future expansion of modular structures (EVstudio 2025; Kilander 2024; Quick Buildings Modular 2024). More detailed literature about the Volumetric modular structure will be discussed in Chapter 2.

Various studies have explored different types of column–column–beam joints in panelized steel modular structures, aiming to minimize transportation damage to structural components through on-site assembly using bolts (Liu et al. 2017; Zhan et al. 2021). Liu et al. (2017) proposed a fully bolted joint system connecting upper and lower box columns through bolted flanges, while securing H-shaped beams with extended cover plates and endplates. Their cyclic tests examined the effects of bolt slippage and the number of bolts on joint stiffness and energy dissipation during seismic events, demonstrating that increasing the number of bolts significantly improved energy dissipation capacity and seismic resilience (Liu et al. 2017, 2019). Further advancements were made by (Liu et al. 2020), who introduced a trapezoidal stiffener to the H-shaped beam connection, showing enhanced structural resilience under seismic loading—an important factor for modular

housing in seismic-prone regions. Wang et al. (2013) contributed to the understanding of bolted connections in moment-resisting frames by investigating blind bolted end plate joints connecting concrete-filled square hollow section columns to steel beams. Their experimental and numerical analyses explored alternative connection methods that improved joint performance, highlighting the advantages of bolted connections, such as ease of assembly, improved seismic behaviour, and cost-effective fabrication (Wang and Jr 2013). Meanwhile, welded connections have been widely studied in HSS-to-HSS and HSS-to-wide flange beam applications (Korol et al. 1993; Wang et al. 2022a; b). Fadden et al. (2012) examined welded unreinforced and reinforced HSS-to-HSS connections under seismic loading, demonstrating that reinforcement plates and plate thickness significantly affected connection stiffness and inelastic rotation factors critical for stability in modular systems (Fadden et al. 2012, 2015b; Fadden and McCormick 2013). More detailed literature about the panelized modular structure will be discussed in Chapter 2.

1.2 Research Gap

Bolted connections have been extensively explored for HSS-to-wide flange beam joints, but research on fully bolted moment-resisting HSS-to-HSS connections remains limited. In particular, the use of long bolts and extended plates to enhance structural performance has not been thoroughly investigated. Addressing this gap could lead to more efficient, transportable, and resilient modular steel structures, particularly in remote and seismic-prone regions where rapid assembly and structural reliability are critical. While a design for long steel bolted connections has been proposed, it has yet to be validated under real-world loading conditions. Therefore, there is a critical need to experimentally evaluate this connection using various geometric parameters. This will allow for an in-depth assessment of the connection's ultimate capacity, rotation, ductility, and joint stiffness, in accordance with (CSA 2019) for structural steel design. There is a need to extend

the investigation to cover a broader range of geometric parameters and reinforcement techniques, as these have not been thoroughly explored. Given the limitation with experimental testing to test a wide range of parameters, expanding this domain numerically is essential to conduct a parametric study that can later be used to develop design guidelines. Furthermore, the absence of practical design tools, such as failure mode charts, and the lack of advanced predictive methods to assess ultimate capacity and failure modes make it challenging to optimize geometry and reinforcement strategies effectively.

1.3 Thesis Objectives

Based on the identified research gaps, the primary objective of this thesis is to develop a steel-bolted connection for panelized modular houses and perform detailed structural analyses to evaluate their safety, performance, and potential failure modes. The research seeks to provide effective, practical solutions for housing in remote and northern communities, as well as in emergency and hazardous situations.

The specific objectives are as follows:

1. Conduct an experimental investigation of the proposed steel connection under monotonic loading to evaluate its behaviour with varying geometric parameters such as extended plate thickness, bolt arrangement, bolt number, and the presence of a stiffener beneath the extended plate to determine its ultimate capacity, ultimate rotation, stiffness, and failure modes.
2. Develop and validate a 3D finite element model (FEM) using experimental results to ensure reliable simulation of real-world performance, then utilize the validated model to explore the influence of untested geometric parameters including extended plate thickness, bolt

arrangement, number of bolts, and bolt diameter on the structural performance of unstiffened connections in terms of ultimate capacity, failure mode, and ultimate rotation. Additionally, develop failure mode design charts to assist in selecting the geometric parameters of the connection and predicting the expected failure mode and ultimate capacity.

3. Enhance the structural performance of modular houses for remote communities in Canada by applying machine learning techniques, specifically decision trees and artificial neural networks, to predict the ultimate moment capacity and failure modes of unstiffened connections. This approach eliminates the need for multiple finite element simulations and iterative design processes when evaluating different geometric parameters. Additionally, genetic regression is employed to develop mathematical formulas for predicting the ultimate capacity of the connection, validated through both experimental data and FEM-based simulations.

4. Utilize the validated finite element model to investigate the influence of reinforcement techniques specifically, the use of column infill, a stiffener beneath the extended plate, and their combination across various geometric parameters (i.e., extended plate thickness, bolt arrangement, number of bolts, and bolt diameter) to assess the connection's structural performance in terms of ultimate capacity, failure mode, and ultimate rotation. This investigation will focus on how these reinforcement strategies can mitigate or eliminate unfavourable and premature failure modes. Additionally, develop failure mode design charts to guide the selection of optimal geometric parameters and predict the expected failure mode and ultimate capacity.

1.4 Organization of Thesis

This thesis has been prepared in an "Integrated-Article" format, and it consists of six chapters:

1.4.1 Chapter 1: Introduction

This chapter (the current chapter) introduces the motivation, Research gap and objectives of the thesis, along with providing a brief background relevant to the research project.

1.4.2 Chapter 2: Novel Steel Connection for Modular Houses in Indigenous Communities: An Experimental Study

This chapter discussed the development of an innovative steel bolted connection tailored for ground-level modular houses. This endeavour also investigates housing-related challenges faced by Indigenous communities in Canada, aiming to address their unique needs through engineering solutions. The mechanical behavior of the proposed connection is experimentally studied to ensure its robustness and reliability. Additionally, a parametric study is conducted to examine different bolt and plate configurations, optimizing the design for practical application in diverse housing projects.

1.4.3 Chapter 3: Capacity and failure mode prediction of long-bolted connection in panelized modular houses

In this chapter, a 3D finite element model was developed and meticulously validated against experimental results using LS-DYNA software. The study involved a comprehensive examination of 240 finite element models for the unstiffened connection, assessing various parameters including the thickness of the extended plate, the number of bolts, bolt arrangement, and bolt diameter. These parameters were analyzed to understand their impact on the connection's moment capacity, failure mode, and inelastic rotation. From these analyses, design charts were developed

to predict failure modes based on selected parameters, significantly streamlining the design process and reducing the need for iterative trials.

1.4.4 Chapter 4: Machine Learning-based Prediction of The Structural Performance of A Long-Bolted Steel Connection

This chapter utilized machine learning techniques, including genetic regression, decision trees, and neural networks, to predict the ultimate moment capacity and identify proposed steel connection failure modes under monotonic loading, based on 240 finite element models from Chapter 3. Four machine learning algorithms were utilized for classification and regression, with hyperparameter optimization enhancing their accuracy. Genetic regression was used to develop mathematical formulas to predict the ultimate capacity of the connection. The results highlight the effectiveness of machine learning techniques in predicting failure modes and capacities of HSS connections, supporting their potential as robust design tools complementing experimental and analytical approaches.

1.4.5 Chapter 5: Numerical Investigation of Reinforcement Techniques for HSS-to-HSS connection in modular houses

In this chapter, 162 finite element models were developed using LS-DYNA software to investigate the effects of various Reinforcement techniques such as stiffeners, concrete within the column, and a combination of both on the ultimate moment capacity, ultimate rotation, and failure modes across different geometric parameters. The study reveals key findings, emphasizing the significant influence of plate thickness and bolt arrangements, along with the associated reinforcement techniques, on connection performance. Design charts are proposed to predict failure modes by altering design parameters, validated with tested specimens, thereby enhancing the reliability and efficiency of the design process. A case study on L-shaped connections was also conducted to evaluate specific aspects of the proposed steel-bolted connections. Two-dimensional prototype

connections were tested under different loading protocols to investigate the effect of bi-bending, providing valuable insights into their structural performance.

1.4.6 Chapter 6: Conclusions and Recommendations

This chapter summarizes the key findings, insights, and contributions made through the research. It has significant results and implications within the context of the structural design of steel modular connections. Moreover, it suggests avenues for future research to build upon the current findings.

1.5 References

Al Jazeera (2023) Qatar ships world cup portable homes to quake-affected Turkey | Turkey-Syria earthquake news |. https://www.aljazeera.com/news/2023/3/5/qatar-ships-world-cup-portable-homes-to-quake-affected-turkey. Accessed 14 Nov 2023

Corfar D-A, Tsavdaridis KD (2022) A comprehensive review and classification of inter-module connections for hot-rolled steel modular building systems. J Build Eng 50:104006

CSA (2019) CSA-S16-19: Design of steel structures. Toronto, ON

EVstudio (2025) Volumetric Modular vs Panelized Construction. https://evstudio.com/volumetric-modular-vs-panelized-construction/. Accessed 6 Mar 2025

Fadden M, Asce SM, Mccormick J, Asce AM (2012) Cyclic quasi-static testing of hollow structural section beam members. 138:561–570. https://doi.org/10.1061/(ASCE)ST.1943-541X.0000506

Fadden M, McCormick J (2013) Evaluation of HSS-to-HSS moment connections for seismic applications. Struct Congr 2013 Bridg Your Passion with Your Prof - Proc 2013 Struct Congr 2334–2345. https://doi.org/10.1061/9780784412848.204

Fadden M, Wei D, McCormick J (2015) Cyclic testing of welded HSS-to-HSS moment connections for seismic applications. J Struct Eng 141:1–14. https://doi.org/10.1061/(asce)st.1943-541x.0001049

Kamali M, Hewage K (2016) Life cycle performance of modular buildings: A critical review. Renew. Sustain. Energy Rev. 62:1171–1183

Kilander A (2024) Unraveling Modular Construction: Volumetric vs Panelized Approach

Korol RM, Ghobarah A, Mourad S (1993) Blind bolting W-shape beams to HSS columns. J Struct Eng 119:3463–3481. https://doi.org/10.1061/(asce)0733-9445(1993)119:12(3463)

Lawson RM, Ogden RG, Bergin R (2012) Application of Modular Construction in High-Rise Buildings. J Archit Eng 18:148–154

Liu XC, Cui FY, Zhan XX, et al (2019) Seismic performance of bolted connection of H-beam to HSS-column with web end-plate. J Constr Steel Res 156:167–181. https://doi.org/10.1016/j.jcsr.2019.01.024

Liu XC, Wang Y, Cui XX, et al (2020) Seismic performance of bolted beam-to-column connection with rib-stiffened splicing plate. J Constr Steel Res 174:106300. https://doi.org/10.1016/j.jcsr.2020.106300

Liu XC, Yang ZW, Wang HX, et al (2017) Seismic performance of H-section beam to HSS column connection in prefabricated structures. J Constr Steel Res 138:1–16. https://doi.org/10.1016/j.jcsr.2017.06.029

Lopez D, Froese TM (2016) Analysis of costs and benefits of panelized and modular prefabricated homes. Procedia Eng 145:1291–1297

Quick Buildings Modular (2024) Modular Construction Methods: Volumetric vs. Panelized. https://quickbuildings.net/2024/11/18/modular-construction-methods-volumetric-vs-panelized/. Accessed 6 Mar 2025

United Nations (2019) "Adequate housing as a component of the right to an adequate standard of living, and the right to non-discrimination in this context."

Wang H, Zhao X, Ma G (2022a) Experimental study on seismic performance of column-column-beam joint in panelised steel-modular structure. J Constr Steel Res 192:107240. https://doi.org/10.1016/j.jcsr.2022.107240

Wang H, Zhao X, Ma G (2022b) Novel coupled modular steel structure and seismic tests on high-performance interconnection. J Constr Steel Res 189:107058. https://doi.org/10.1016/j.jcsr.2021.107058

Wang J, Jr BFS (2013) Experimental and analytical behavior of blind bolted moment connections. JCSR 82:33–47. https://doi.org/10.1016/j.jcsr.2012.12.002

Zhan XX, Liu XC, Feng S, Yu C (2021) Seismic performance of a square HSS column to H-section beam bolted connection with double cover plate. Eng Struct 231:111729. https://doi.org/10.1016/j.engstruct.2020.111729

CHAPTER 2: NOVEL STEEL CONNECTION FOR MODULAR HOUSES IN INDIGENOUS COMMUNITIES: AN EXPERIMENTAL STUDY

2.1 Introduction

Indigenous communities are suffering from housing shortages and rising levels of homelessness in Canada, especially in remote and rural regions, which has been reported over the last decades by different governmental organizations and the United Nations in 2019 (United Nations 2019). Latter reports addressed the deteriorating housing conditions and warned about the shortage of housing supplements to replace deteriorated houses (Canada. Office of the Auditor General. 2003; Indigenous Services Canada 2018). These housing challenges can be categorized into (i) Materials-related, (ii) Climate-related, and (iii) Construction-related. Material-related challenges include mould and fire hazards (Garis 2021; von Stackelberg 2019). It was reported that construction materials such as wood were mouldy before the assembly stage because they could get wet during transportation over ice roads or were stored with minimal protection before use due to depending on traditional construction techniques (von Stackelberg 2019). Wildfires pose a serious risk in northern and remote Indigenous communities in Yukon, where fewer emergency services exist (Government of Yukon 2023). Wildfires could spread quickly because burning embers blown through the air could become dangerous to houses. This is attributed to the structural material of the home, which will significantly impact how resilient it is to wildfire embers. In another regard, Canada is affected by climate change at double the global rate due to its northerly location (Canada.ca 2023), which amplifies the climate-related challenges. Indigenous communities living in northern regions are highly susceptible to climate change, which results in wildfires and flood events, which cause substantial life risk and property damage ("Inadequate Housing and Crowded Living Conditions - #3 of 8 Key Issues" 2023). Also, Reserves are projected that wildland fires

will increase in number, size, and intensity due to climate warming. Also, reserves are often remote with limited access, which makes evacuation challenging and exacerbates firefighting efforts (Erni et al. 2021; "Inadequate Housing and Crowded Living Conditions - #3 of 8 Key Issues" 2023). Climate-related challenges could result in extreme weather events (i.e., storms, heavy snow, or rain damage), leading to an increase in the hazards of leaking or damaged roofs as strong winds could rip off the roofs and blocked drains could cause rainwater to leak through the walls (Environment and Climate Change Canada 2011; ISOPolar Airships 2020). Finally, remote Indigenous communities face unique construction-related challenges, such as (1) the construction season being shortened due to harsh weather conditions, leading to delayed shipment and increased cost of construction (Garneau 2022); (2) the impact of climate change, which led to warmer winters, has affected the winter road network and made those roads impassable, which promoted a state of emergency by First Nations in Manitoba and Ontario ("Impassable winter roads create 'dire' situation for Ontario First Nations" 2024), (3) limited access to services, lower labour market attachment (Bleakney et al. 2021), and high transportation costs (OECD 2016; Transport Canada 2016).

Based on the aforementioned challenges, there is an urgent need to find a structural solution to address all these non-typical climate and construction conditions while being affordable for these communities. It is believed that cold-formed steel modular structures can offer an adequate solution to these complex challenges to reduce the housing shortage because of their technical advantages, which include non-organic and non-combustible material compared to conventional timber structures and lightweight space-saving structures compared to concrete structures during transportation. These types of structures can make the construction materials easier to ship to remote and rural regions (Lawson et al. 1999) and can accelerate the on-site construction phase,

leading to decreases in cost compared to traditional on-site construction (Kamali and Hewage 2016; Lopez and Froese 2016). Steel modular structures are becoming more popular and have attracted significant attention in the construction industry because of less waste, fewer on-site workers, better quality control, and faster construction (Kamali and Hewage 2016; Lawson et al. 2012; Lopez and Froese 2016). Modularized steel structures were adopted in many permanent facilities such as hotels and apartments (e.g., Nova Residences of Quincy, USA) in North America and parts of Europe due to the growing demand for infrastructure. Also, after the catastrophic earthquakes in Turkey and Syria in 2023, 10,000 steel prefabricated houses (i.e., volumetric modules) were utilized as temporary buildings to accommodate more than 1.5 million people left homeless by the earthquakes (Al Jazeera 2023).

Steel modular construction can be categorized into three different categories based on the off-site construction methods, which are: elemental, panelized, and volumetric, that can be used to form the structural system of a building (Corfar and Tsavdaridis 2022). Volumetric modular construction permits the building units to be manufactured highly effectively as box-like structures at the factory, then transported to the construction site and assembled to form a complete structure. Transportation of volumetric modular units to remote and northern Indigenous regions is considered a challenge because the maximum segment length (i.e., 48 ft) and the capacity of the flatbed trailer (i.e., 35 tons) constrained the number of transported volumetric modular to a maximum of two units per travel depending on the used material, compared to four lightweight steel modular being transported in the form of panelized sections. The steel cross-section weighs 2.4 tons, and the concrete deck slab weighs 7.5 tons. In the panelized technique, the structural components, including the roof, wall panels, and floor system, are fabricated in a factory and delivered to the construction site for assembly. It has more advantages, including avoiding

transportation complexity and damage, compared to volumetric units, as panels can be stacked on top of each other, providing logistical advantages. Also, it allowed more flexibility, making it more adaptable to various project requirements (Kilander 2024).

In the frame-supported modular structure, where loads are transferred through edge beams to corner columns. The interconnections between different module units significantly impact the structural integrity and performance, which resist the lateral loads (e.g., wind and seismic). The bolt connection enhanced its plastic deformation capacity and ductility by dissipating energy and reducing lateral load damage by slipping on the bolt contact interface (Zhan et al. 2021). Bolted connections could be categorized into three types: column-to-column joint, beam-to-beam joint, and fitting-to-fitting joint. Column-to-column joints were the most common connection derived from the classic splice connection. Many studies have explored various geometric configurations to provide horizontal or vertical connectivity using end plates and bolts positioned externally to the column or within the cross-section of HSS (Hollow Structural Section) columns (Choi et al. 2016; Han et al. 2023; Sendanayake et al. 2019). However, introducing open access for connections results in weakened regions within the column. In contrast, other studies introduced different methods for providing both vertical and horizontal simultaneously by incorporating an intermediate plate between columns or, using long bolts within the build component inside the column cross-section or employing a combination of blind bolts and high-strength bolts within T-shape tenon (Ma et al. 2021; Rajanayagam et al. 2022; Yang et al. 2024). The beam-to-beam joint was achieved by shifting the joint from the column to the module's floor and ceiling beams. Many studies proposed different gusset plate configurations and bolts to connect floor and ceiling beams to utilize the space between these beams (Deng et al. 2017; Du et al. 2018; Lee et al. 2017; Wang and Su 2021; Zhai et al. 2022). However, this connection type may be restricted to open steel

cross-sections like channels. The third type of inter-module bolted connection was the fitting-to-fitting connection, where modules were connected through corner fittings adopted from shipped containers. Doh et al. (2017) developed a cubic steel box, which allowed all module units to be connected horizontally and vertically through bolts. Subsequent studies modified corner connections to include spigots on the intermediate plate and move the bolts toward the span of the floor beam (Shi et al. 2020). Lian et al. (2021) proposed a cruciform gusset plate between the corner fittings, with the vertical flange extended where horizontal bolts connected adjacent modules.

Many studies introduced a panelized steel modular structure joint called the column-column-beam joint (Liu et al. 2017; Zhan et al. 2021), where the joint will be assembled on-site using bolts to avoid transportation damage to structural components. Liu et al. (2017) introduced a fully bolted joint that vertically connects the lower and upper box columns through bolted flanges and horizontally connects the H-shaped beam using extended cover plates and an endplate They performed cycling tests to evaluate the impact of the number and slippage of bolts on the joint's stiffness and energy dissipation capacity (Liu et al. 2017, 2019). Liu et al. (2020) also improved the proposed connection for the H-shaped beam by adding a trapezoidal stiffener. They studied its seismic performance and concluded that relocating the web bolts on the beam flange could enhance seismic performance. Furthermore, the trapezoidal stiffener could improve both load-bearing capacity and energy dissipation (Liu et al. 2020) . Many studies focused on improving the joint for the HSS column with a wide flange beam (Wang et al. 2022a; b) without considering other effective frames, such as HSS-to-HSS moment resisting frames, which have more advantages in terms of bending, torsional and compression resistance, leading to a potential high-performance system.

Based on the aforementioned challenges, this study aims to address the shortcomings in the available connection options by developing a new bolted beam-to-column connection suitable for connecting HSS-to-HSS sections through high-strength long bolts without introducing weak regions in the column section. The proposed connection facilitated the HSS section connection without using welds or facing obstruction in installation on-site. Six full-scale steel connections were tested under monotonic loads to analyze the mechanical properties, including the initial stiffness, bending strength, rotational capacity, and ductility index. The digital image correlation (DIC) technique was used during testing to determine kinematic quantities of discrete points, such as rotation and multiple forms of strains. Different parametric analyses for bolt arrangement, number of bolts, the thickness of extended plates, and stiffener existence were conducted through an experimental program to obtain the main factors influencing the mechanical behaviours of the novel modular connection.

2.2 Details of the Proposed Novel Modular Connection

In this study, a novel modular steel connection was developed for prefabricated steel moment-resisting frames (Elhadary et al. 2025; Elhadary and Elshaer 2021). The modular units, both floor beams and columns, were made up of cold-formed HSS sections. HSS sections were adopted because of their advantages, such as a high strength-to-weight ratio, which provides superior compression performance, significant weight savings, reduced lateral bracing requirements (i.e., torsional resistance) and their smooth flat walls (Fadden and McCormick 2014). The connection between the HSS column and the HSS beams can be assembled through two extended plates welded to the column section. Bolt holes were pre-drilled on the extended plates and beam and connected on-site with long high-strength bolts. The two extended plates were groove welded across the whole column HSS sections to provide equal stress distribution to more column side

walls, preventing column face plastification and large stress through welds. Fig. 2-1.a describes the assembly stage for a single modular unit that is composed of corner HSS columns with HSS beams using high-strength long bolts with dimensions of 2.5 m×6 m×3 m. The figure shows three different shapes of the extended plates based on the column's location in the architecture layout, including (i) center column (i.e., a plus shape); (ii) side column (i.e., T-shape); and (iii) corner column (i.e., L-shape).

The on-site construction method involves the assembly of four panelized beams in conjunction with a plus-shaped column. This process incorporates two different configurations of panelized beams, which are assembled in accordance with the directions illustrated in Fig. 2-1.b. This modular connection is expected to be part of a panelized modular section, which can have multiple advantages including (1) it avoids potential damage to volumetric modular units during transportation as it will transport them as panelized sections, so many module units can be transported to the site on the standard truck, (2) it overcomes the connection problem of the volumetric four units (Lawson et al. 1999), as it provides more working space, (3) it offers more flexibility in design as it can be adapted for the three types of joints (corner, external, and internal) on the structural layout and ensures the integrity of the architectural appearance, addressing a challenge encountered with various connection location in modular steel connection, and (4) it is designed to be easily disassembled by changing the panelized floor, which is considered an adequate solution for Indigenous housing challenges as it can ease repair and reallocation of units.

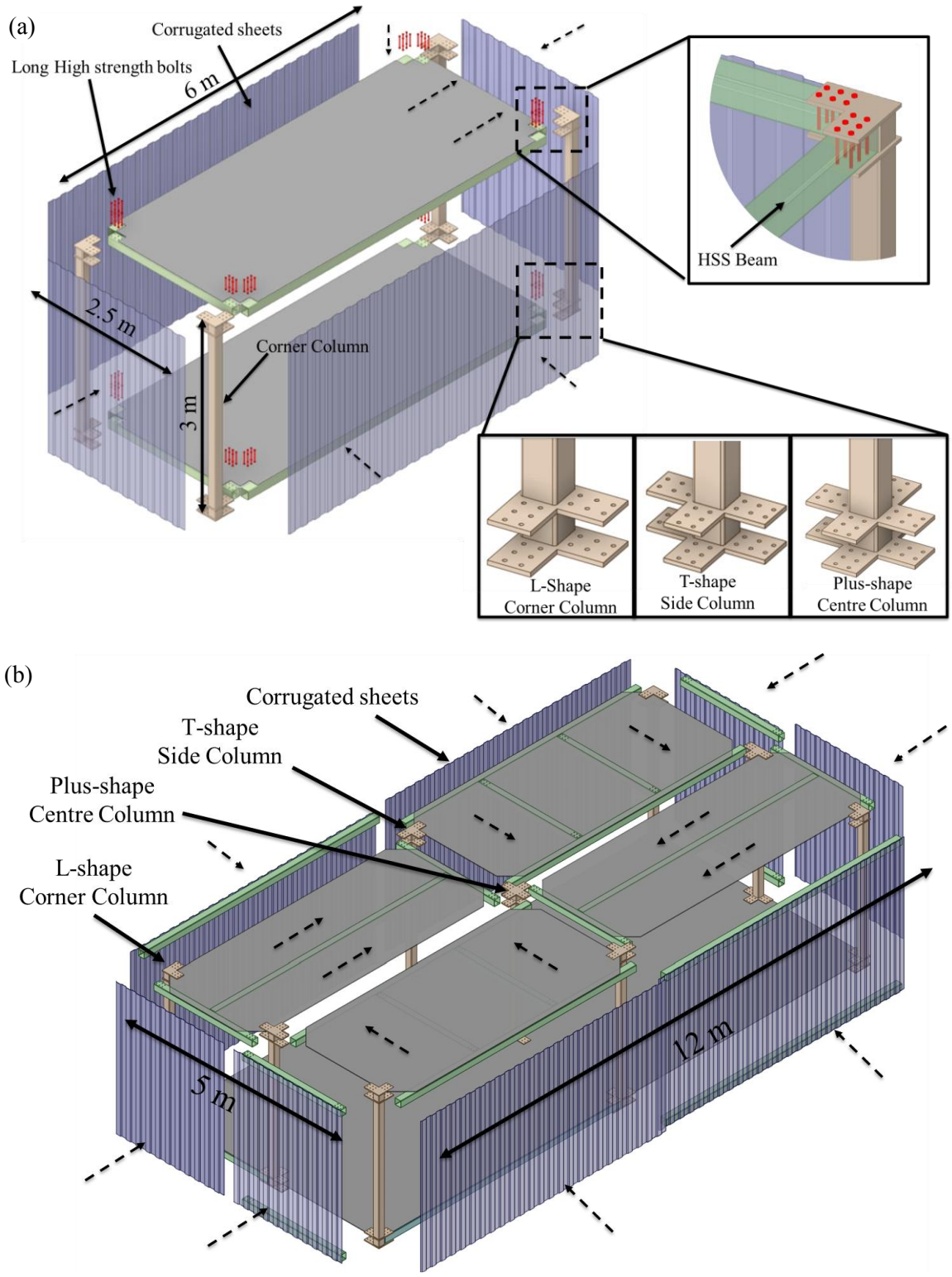

Fig. 2-1: Schematic diagram of (a) the proposed bolted connection for HSS-to-HSS moment resisting frame system and different configurations for the column joints, (b) the assembly technique of four box modules with different proposed column joints

2.3 Experimental study

2.3.1 Design details of the test specimen

The connection consists of four components: a beam, a column, two extended plates, and long tightening bolts. Cold-formed square tubular with different sectional dimensions were employed as modular column and beam sections, where a hollow square section (HSS) 152×152×9.53 mm of 678 mm in length was used as the modular column, while the beam section was HSS 152×152×6.4 mm of 1250 mm in length, which was a weaker section compared to the column in order to satisfy the principle of "a strong column weak beam''. This will ensure the formulation of the plastic hinge at the beam rather than the column. A ground-level residential modular steel building of a height of 3.0 m was adopted in this study. A numerical model was used to design the four stacked panel modules using ETABS software (Computers and Structures Inc. (CSI) 2019). This model demonstrated the most critical resiliency of the connection against a dynamic load (i.e., wind load and snow load) without the need for a lateral load-resisting system because adding more modules will increase the framing action resistance (Elhadary et al. 2025). So, four panels were considered the most critical case because this setup included the side, corner, and center columns. The dimensions of individual slab panels were 2.5 m× 6 m. The slab was designed to resist a superimposed dead load of 2.0 kN/m^2, a live roof load of 1.0 kN/m^2, wind load and snow load were applied on the slab according to the National Building Code of Canada 2015 (Canadian Commission on Building and Fire Codes - NRCC 2020). The wind and snow loads were evaluated for all Canadian cities from Appendix C-National Building Code of Canada 2015 (Canadian Commission on Building and Fire Codes - NRCC 2020). The section selection during the design procedure was based on the critical loads' combination (i.e., wind and snow loads) from the National Building Code of Canada (NBCC) 2015 (Canadian Commission on Building and Fire Codes - NRCC 2020) and followed Canadian steel code CSA S16-19 (CSA 2019). The beam,

column and extended plates were made of 350W steel. The beam and column were classified as having a compact cross-section. This classification was determined by the width-thickness ratio of the flange and the depth-thickness ratio of the web. These ratios fell within the limits for a compact section, as specified by CSA S16-19 (CSA 2019). High-strength long galvanized finished bolts grade A325 with a diameter of 5/8" (15.875 mm), length of 8" 1/2 (215.9 mm) and a standard thread length of 31.8 mm. Accompanying those bolts were ASTM F436 galvanized plain washers, according to the CSA S16-19 (CSA 2019), which were used to assemble the beam with the extended plates. The bolt holes were equivalent to 11/16" (17.2625 mm), according to CSA S16-19 (CSA 2019). The contact surfaces between the steel plates were sandblasted to remove any presence of rust or corrosion. All the welds were carried out using a complete penetration groove weld according to the CSA S16-19 (CSA 2019) to prevent any premature brittle failure from fillet welds during the test. A detailed drawing showing the dimensions of the specimen and groove weld details between the HSS column and the extended plate is illustrated in Fig. 2-2.

The uniaxial tensile tests were conducted to acquire the material properties of specimens. Flat coupons were extracted from the same material of tested specimens (i.e., beam, column, and extended plate) using a computer numerical control (CNC) machine, whose dimensions followed the ASTM A370 standard (ASTM 2014). Two coupons were tested from each beam, column, and extended plate of different thicknesses to guarantee the reliability of the material properties according to CSA S16-19 (CSA 2019). The high-strength bolts were uniaxial tested at the designated steel manufacturing facility, in accordance with the ASTM A370 standard (ASTM 2014). Table 2-1 lists the average values of the material properties obtained from the tensile tests.

Table 2-1: Material properties of the tested specimens

Component	Material Grade	Yielding Stress F_y (MPa)	Yielding Elongation ε_y (%)	Ultimate Stress F_u (MPa)	Ultimate Elongation ε_u (%)	Elasticity Modulus E (GPa)
Column	350W	366	0.18	465	15.3	204
Beam	350W	364	0.18	462	14.9	203
Extended plate	350W	367	0.18	470	15.5	204
High-strength bolts	A325	560	0.27	825	11.2	207

The beam and column cross-section remained unchanged for all tested specimens to study the effect of the extended plate thickness, the number of bolts in the extended plates, the bolt arrangement pattern, and the effect of the stiffener on the mechanical behaviour of the joint. The main design parameters of the six test specimens are illustrated in Fig. 2-3 and Table 2-2. The tested specimen was coded as follows: the thickness of the extended plate, the number of bolts, and the ratio between perpendicular and parallel pitch between bolts P_n/P_p was implemented using the AR abbreviation (i.e., arrangement ratio) where AR1.5= P_n/P_p =1.5, and AR1= P_n/P_p =1, and the existence of a stiffener was implemented using ST, as shown in Fig. 2-3. For example, in EP13-B6-AR1.5-ST, EP13 refers to an extended plate of 13 mm in thickness, B6 indicates the number of bolts to be 6, and the symbol AR1.5 represents the ratio P_n/P_p to have a value of 1.5, and ST indicates a stiffener below the lower extended plate. The perpendicular pitch distance between bolts (P_n) was considered as a factor of section depth (H) as follows: P_n=0.5H, to satisfy the allowable bolt pitch distance specified in the Canadian Steel Code CSA S16-19 (CSA 2019), as shown in Fig. 2-3. The parallel edge distance (e_p) was taken equal to the normal edge distance (e_n).

Table 2-2: Main design parameters of the test specimens

Specimen ID	Number of Bolts	Extended Plate Thickness (mm)	Bolt Arrangement (P_n/P_p)	Stiffener
EP13-B6-AR1.5	6	13	1.5	no
EP10-B6-AR1.5	6	10	1.5	no
EP10-B6-AR1.0	6	10	1	no
EP13-B8-AR1.5	8	13	1.5	no
EP13-B6-AR1.5-ST	6	13	1.5	yes
EP10-B8-AR1.5	8	10	1.5	no

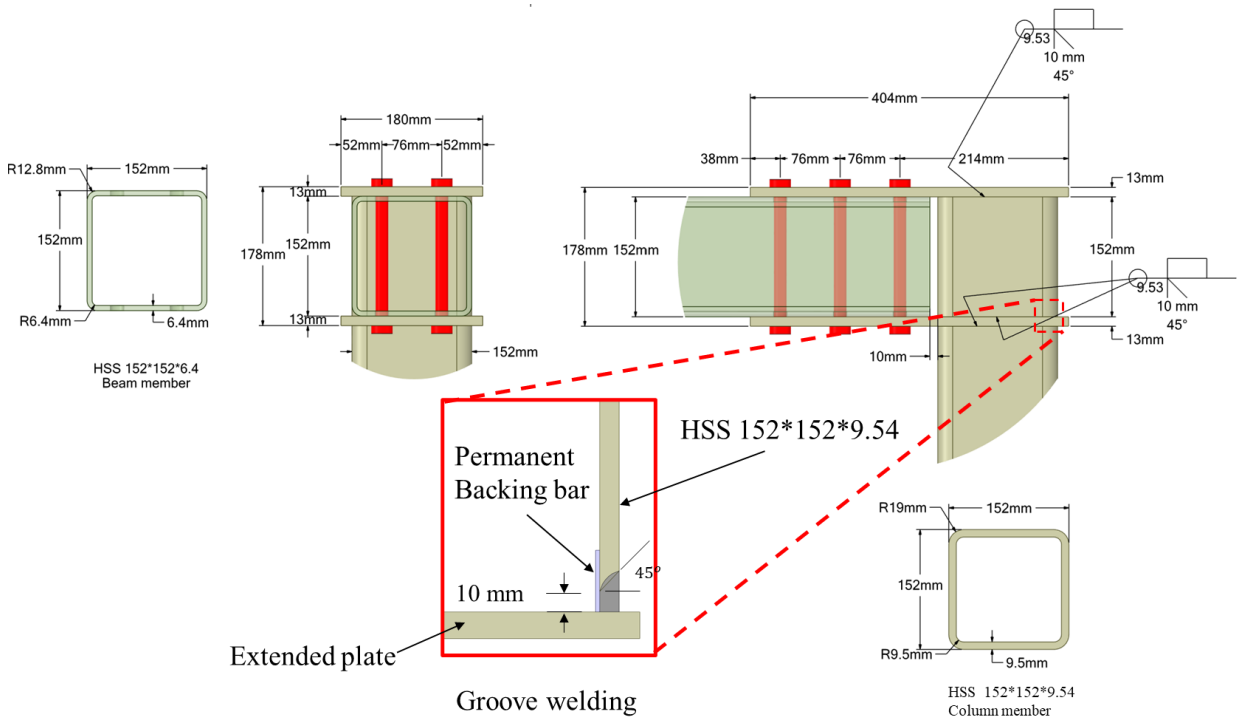

Fig. 2-2: Detailed drawings of the specimen and groove weld between the HSS and extended plate.

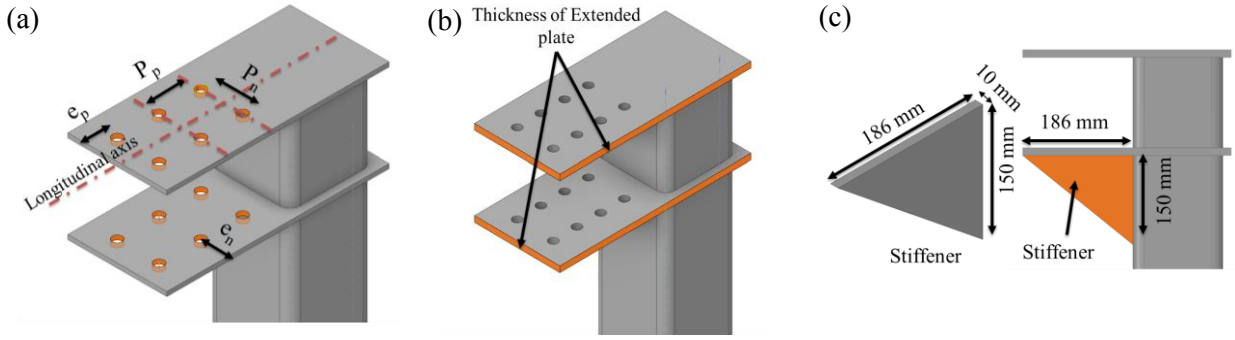

Fig. 2-3: Details of the main studied geometric parameters: (a) bolt arrangement pattern, (b) extended plate thickness, (c) stiffener at the lower extended plate

2.3.2 Test setup

Fig. 2-4 illustrates the schematic view for the monotonic test setup, where a W360×179 section with a length of 5 m was placed in the middle of the UTM floor. The column base plate was connected to the W-section via high-strength bolts with a diameter of 25.4 mm to simulate a fixed-end condition for the specimen during the test. The beam was connected by a steel roller bracket, which kept the loading point location unchangeable during the test and allowed the beam to rotate while applying the load. Lateral frame supports were used to ensure that the out-of-plane displacement of beams was restricted. The specimens were tested with a hydraulic universal testing machine (UTM) with a maximum capacity of 1300 kN through a loading rate of 2 mm/min (AISI 2015).

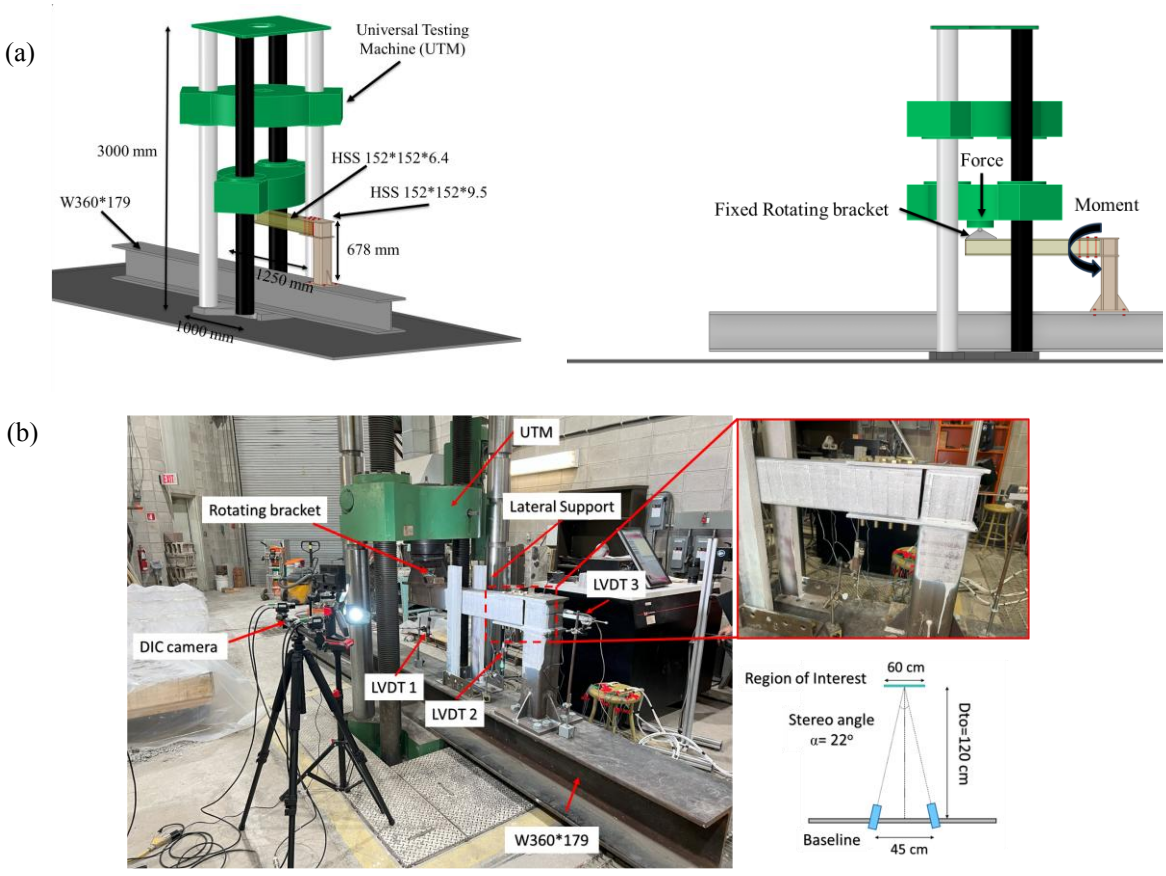

Fig. 2-4: Arrangement of the test device (a) 3D schematic view of the test setup; (b) photo of the loading machine, DIC camera stereoscopic setup and speckles pattern

2.3.3 Test Instrumentation

Three different measuring instruments were employed in the test to measure the displacement and strain distribution across the tested joint. The layout of the displacement sensors and strain gauges is shown in Fig. 2-5. The displacement sensors (i.e., Linear Variable Differential Transducers, LVDT) were marked as W, followed by a number, where displacement sensor W1 measured the beam end displacement at the loading point, and displacement sensor W2 measured the extended plate displacement, while the displacement sensor W3 measured the horizontal displacement at the column cap. The strain gauges on the column, the extended plates, and the beams were marked as C-n, E-n, and B-n, respectively, where n was the number of the strain gauge, as shown in Fig. 2-5. In the case of specimen EP13-B6-AR1.5-ST, the strain gauge has been affixed to the stiffener in the Y-direction and designated as S-n. The strain gauges and displacement sensors were calibrated before being utilized in the test.

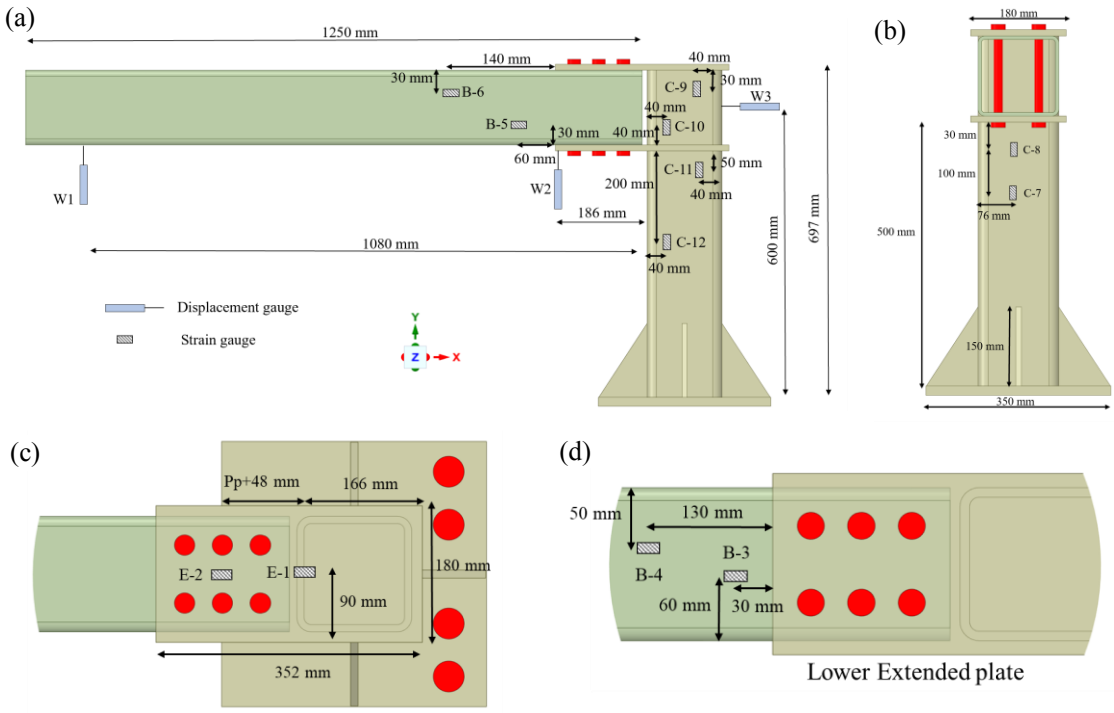

Fig. 2-5: Sketch of the measurement scheme in (a) elevation view, (b) side view, (c) top view, and (d) down view

A Digital Image correlation (DIC) camera was introduced into the test as a non-contacting measurement technique, which could determine an accurate displacement field and multiform strain distribution methods based on the correlation analysis for a series of digitally acquired images taken through the object surface's deformation process. A stereoscopic setup for the two USB vision cameras of resolution 2.3 Mpx was conducted, where the distance to the object Dto=1200 mm, baseline (i.e., the physical distance between the cameras) B=450 mm, and stereo angle α=22º (i.e., refers to the angle between the camera axis), as shown in Fig. 2-4. A speckles pattern of a size of 1.0 mm was drawn on the test joint to satisfy the camera resolution and field of view of 600 mm (i.e., the physical horizontal and vertical imaging area of an object) that provided an acceptable range between the standard minimum error of 0.05 pixels and the maximum standard error of 0.15 pixels during speckle pattern quality evaluation. A project calibration for the two cameras within the selected field of view was carried out using a 500 mm Calibration Target.

2.4 Results of the experimental work

2.4.1 Moment-rotation relationship and modes of failure

Fig. 2-6 shows the moment-rotation relationship for the tested specimens, where the moment was determined by multiplying the force extracted from the load cell by the distance measured from the load point to the column face (1080 mm). Whereas the connection rotation was calculated by subtracting the column’s rotation from the beam’s rotation. Fig. 2-7 illustrates the modes of failure for the tested specimens.

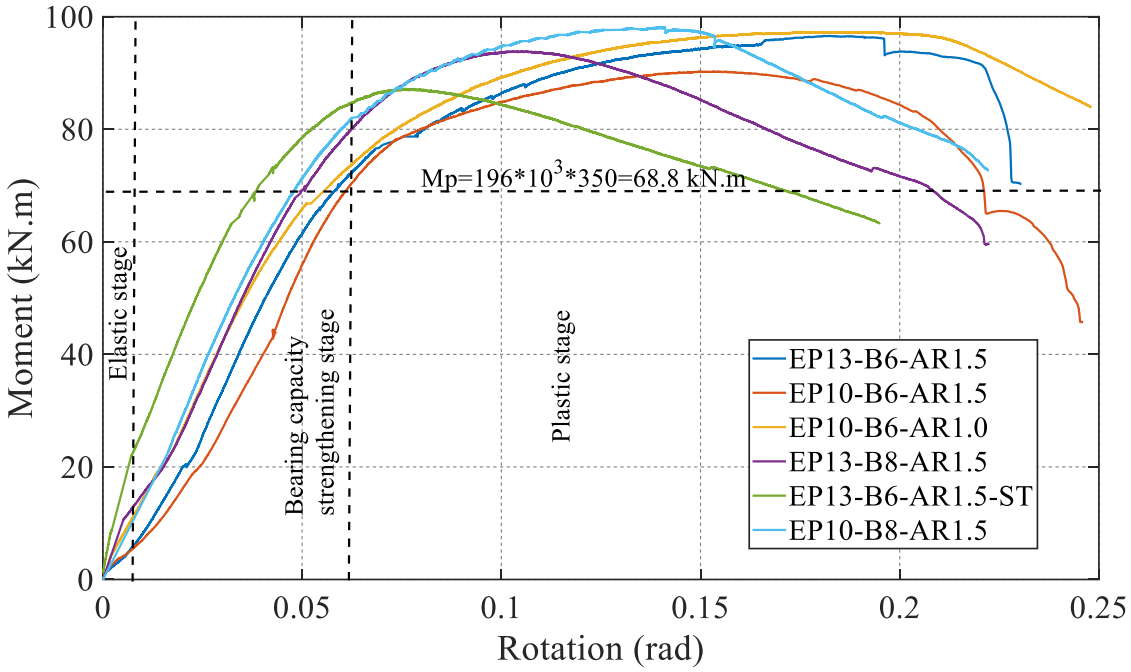

Fig. 2-6: Moment-rotation curve of test specimens

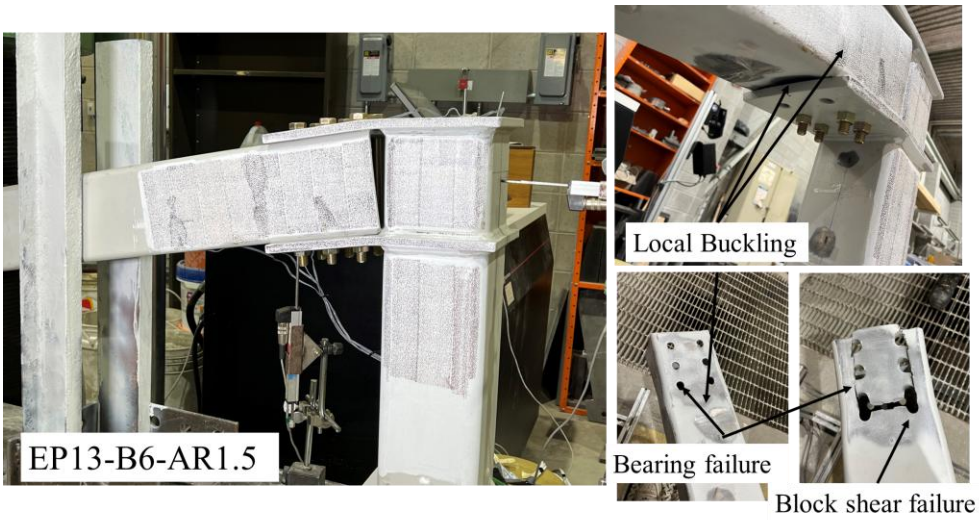

(a)


EP10-B6-AR1.5
Local Buckling
Bearing failure
Local Buckling
Block shear failure

(b)


Local Buckling
Local Buckling
EP10-B6-AR1
Local Buckling
Bearing failure

(c)


Local Buckling
EP13-B8-AR1.5
Local Buckling
Local Buckling
Bearing failure
Outer bolt row

(d)

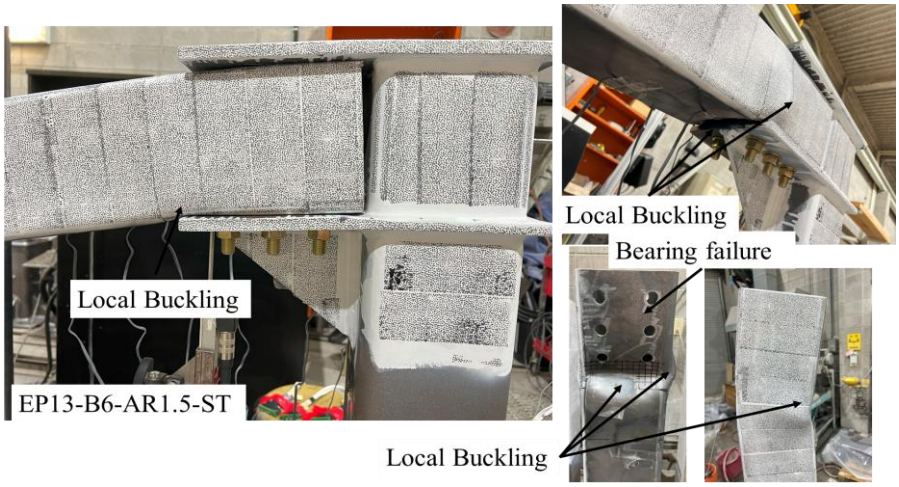

(e)

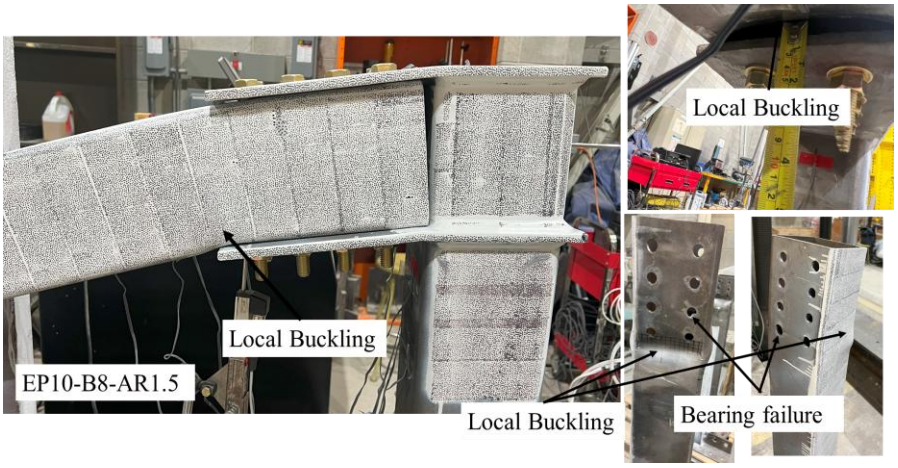

(f)

Fig. 2-7: Failure modes of different specimens: (a) EP13-B6-AR1.5, (b) EP10-B6-AR1.5, (c) EP10-B6-AR1.0, (d) EP13-B8-AR1.5, (e) EP13-B6-AR1.5-ST and (f) EP10-B8-AR1.5

The moment-rotation relationship for all specimens can be divided into four stages. The first stage was the 'elastic stage', which allocated between moment values from 0 to 20 kN.m with a corresponding joint rotation between 0.000 to 0.008 rad. A lower initial stiffness region appeared in the early loading stage due to the bolt clearance, as the joint gained its initial capacity through the rotation of the two extended plates, where the bearing between the beam and the two extended plates was activated until the outer bolts' row came into contact with the beam. Two specimens showed the highest initial stiffness because of the existence of a stiffener in specimens EP13-B6-AR1.5-ST, which prevented the rotation of the extended plates, and the existence of eight bolts in

specimen EP13-B8-AR1.5 because the two outer bolt rows got in contact with beam flanges, which triggered gaining more capacity by bolt bearing, compared to six bolts configurations, where the outer bolt row was in contact only during the elastic stage. While specimen EP10-B8-AR1.5 had an intermediate initial stiffness due to the decreasing thickness of the extended plate.

In the second stage, 'The bearing capacity strengthening stage', the moment capacity ranged from 7 to 68 kN.m, with a corresponding joint rotation ranging between 0.008 and 0.059 rad. The connection gained most of its capacity in this stage through the compression force between the bolt's shank and the beam holes, where the moment was transferred to the extended plates as tension and comparison forces. Specimen EP13-B6-AR1.5-ST gained the highest moment capacity because the stiffener prevented the rotation of the extended plate, which caused extensive yielding of the extended plates due to bending, which forced the beam to rotate only and gained capacity by bolt bearing through the whole bolt rows as illustrated in Fig. 2-7.f. On the other hand, specimens EP13-B8-AR1.5 and EP10-B8-AR1.5 had more bolts, increasing the connection gaining capacity through the participation of two bolt rows during the bearing capacity stage.

The third stage was the 'plastic stage', which started when the beam reached the plastic moment capacity equal to 69 kN.m within different corresponding rotations ranging between 0.044 to 0.059 rad due to the different capabilities of specimens to gain strength through the bearing capacity strengthening stage, resulting from the studied geometric parameters. Specimen EP13-B6-AR1.5-ST had the smallest plastic region domain. This was attributed to the high number of bolts, where the bearing stresses were distributed only to the outer bolt row, which led to a local buckling of the beam at the lowest value of the moment of 86 kN.m. It was noted that specimen EP10-B6-AR1.0 reached the highest plastic capacity of 97.3 kN.m without experiencing any sudden local buckling at the beam because of the use of proper bolt arrangement, which delayed the bolt bearing

failure and, therefore, increased the ultimate moment capacity and the ductility of the connection by 25% compared to the specimen EP10-B6-AR1.5.

In the last stage, 'the failure stage', the connection reached its maximum moment capacity due to the stress concentration of the bolt bearing forces on the compression flange of the beam, leading to local buckling of the beam, which was the most common failure experienced by all specimens. It is worth mentioning that all specimens experienced a drop in the load after reaching the peak load. However, specimen EP10-B6-AR1.0 with a square bolt arrangement has experienced a plateau region after reaching its maximum capacity, which can be attributed to its efficient distribution of the bolt bearing. The ultimate strength for specimen EP10-B6-AR1.0 was taken as the moment at a rotation of 0.2 rad according to AISC 360-16 Cl. B3.4 (AISC 2016).

Different modes of failure were exhibited in this study, such as local buckling of the beam, bearing failure and yielding of the extended plate, bearing failure, and block shear failure of the beam, as shown in Fig. 2-7. Bolt bearing failure at the beam compression flange was the dominant failure for all specimens, which led to local buckling of the beam. Specimens EP13-B6-AR1.5 and EP10-B6-AR1.5 exhibited block shear failure at the beam because the bolt arrangement AR1.5 triggered more bolt-bearing forces at the failure stage. Upon reaching the ultimate moment capacity, specimen EP10-B6-AR1.0 exhibited yielding in the compression extended plate, which was subsequently followed by local buckling of the beam due to the concentration of bearing stress. Specimen EP13-B6-AR1.5-ST experienced bolt bearing failure at the beam flanges, resulting in a local buckling of the beam compression flange without experiencing any significant deformation of the extended plates. Both specimens EP13-B8-AR1.5 and EP10-B8-AR1.5 reached their ultimate capacity without extensive bending of the extended plates, followed by local buckling of the beam due to bolt bearing failure at the flanges.

The joint ductility index (φ_j) is the key to preventing progressive collapse and brittle failure for steel moment-resisting frames (Kuhlmann et al. 2006). The ductility index is defined as the ratio between the rotation corresponding to the ultimate moment (φ_{max}) and the rotation corresponding to the yielding resistance (φ_y). The ductility coefficient of the six specimens ranged between 3.69 and 5.10, which exceeded the values specified in the Canadian code CSA S16-19 (CSA 2019), which are 3.0 and 5.0 for moderate ductility and ductile moment resisting frame, respectively. This confirmed that the ductility of this joint can reasonably resist lateral load, where the ductility is among the controlling parameters. The results of the moment-rotation curve, ductility index and failure modes for the specimens were summarized in Table 2-3. The yielding strain of steel sections value was derived from the uniaxial test. Subsequently, the graphical DIC visualization and strain gauges affixed to the beam were employed to ascertain the corresponding yielding rotation of the connection. Upon obtaining the yielding rotation of the connection, the first yielding moment for each specimen was determined using the moment-rotation curve. This first yielding moment was found to be approximately equivalent to the yielding moment computed from the section properties. The ultimate rotation capacity can be defined as the value of the connection rotation at the point where the resisting strength of the connection has dropped to 0.8 M_{max} according to AISC 360-16 Cl. B3.4 (AISC 2016).

Table 2-3: Experimental test results summarized from the moment-rotation curve.

Specimen ID	Initial Stiffness (kN.m/rad)	Yielding moment (kN.m)	Ultimate moment (kN.m)	Rotation (rad)		Ductility index (φ_j)	Failure mode
				At yielding moment	At ultimate moment		
EP13-B6-AR1.5	1169	58.1	96.5	0.047	0.227	4.82	1-Yielding of the extended plates 2- Local buckling at the beam and block shear failure
EP10-B6-AR1.5	720	61.6	90.2	0.054	0.220	4.07	1-Yielding of extended plates and local buckling at the lower plate 2- Local buckling and extensive bolt bearing failure at the beam.
EP10-B6-AR1.0	1560	64.3	97.3	0.049	0.250	5.10	1-Yielding of the extended plates 2- Local buckling and bolt bearing failure at the beam
EP13-B8-AR1.5	1996	65.3	93.6	0.046	0.186	4.04	1-Yielding of the extended plates. 2- Local buckling and bolt bearing failure at the beam
EP13-B6-AR1.5-ST	4327	58.1	86.7	0.024	0.170	7.08	1- Local buckling and bolt bearing failure at the beam
EP10-B8-AR1.5	1382	64.7	98.08	0.044	0.211	4.80	1-Yielding of the extended plates. 2- Local buckling and bolt bearing failure at the beam

2.4.2 Strain distribution in connection regions

Fig. 2-8 and Fig. 2-9 show the moment-strain relationship. The strains were measured and plotted in the X-direction for the beam and Y-direction for the column at different measuring points in connection regions with increasing the joint moment. The mechanical performance (i.e., rotation, deflection, and strain contour shapes of the tested specimens was captured using the DIC cameras. The DIC measurements series were analyzed using Istra-4D software (Dantec Dynamics 2016), where Table 2-4 illustrates the correlation parameters implemented during the evaluation process.

The measurement of the DIC camera was stopped at a rotation of 0.14 rad before reaching the failure to ensure the equipment's safety at the structural. Fig. 2-10 shows a graphic visualization of true effective strain for different specimens' connection regions through joint rotations.

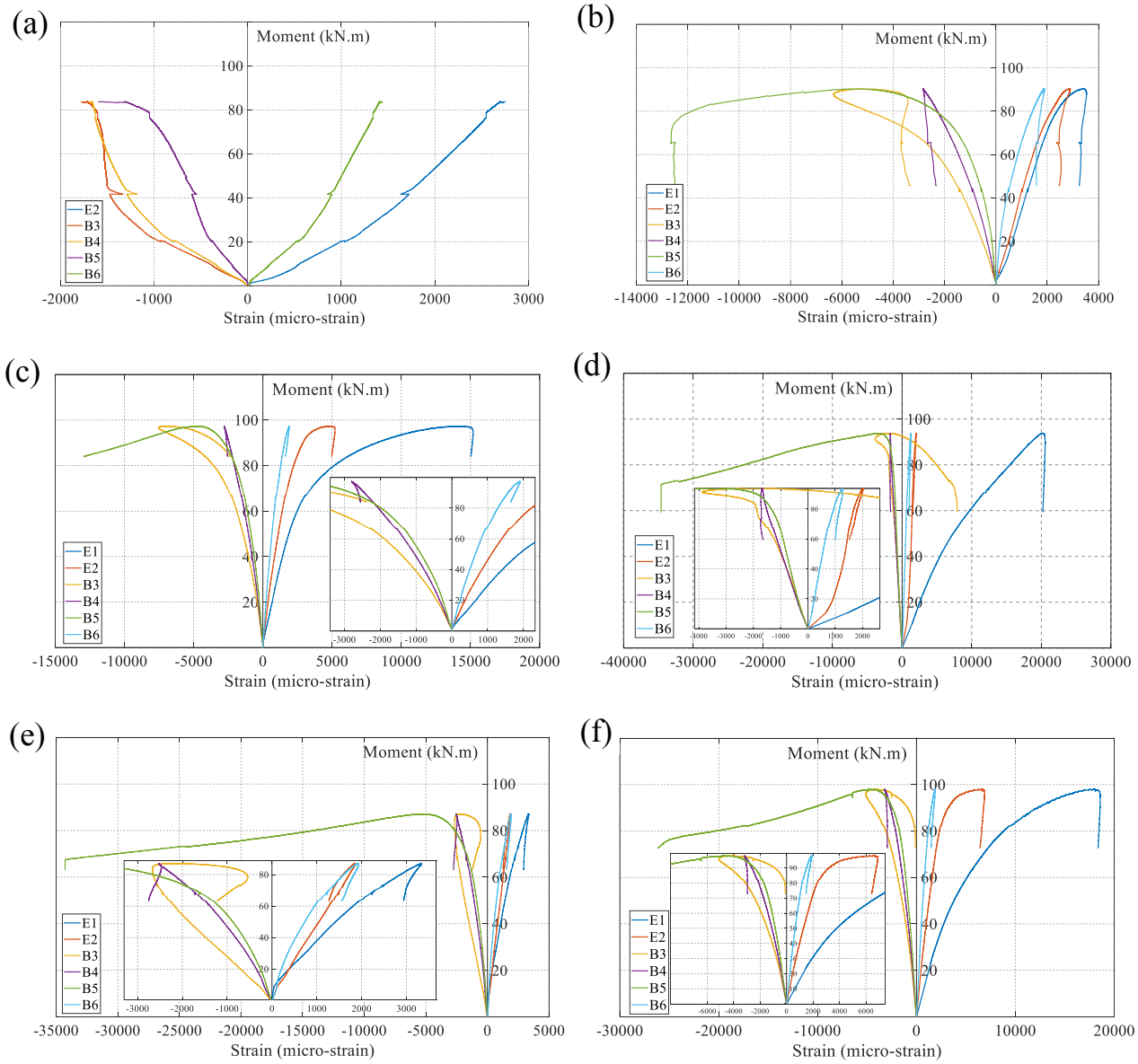

Fig. 2-8: Measured strain versus moment for X-direction strain gauges for different specimens; (a) EP13-B6-AR1.5; (b) EP10-B6-AR1.5; (c) EP10-B6-AR1.0; (d) EP13-B8-AR1.5; (e) EP13-B6-AR1.5-ST; and (f) EP10-B8-AR1.5 (i.e., magnification graph is provided for small strain within figures)

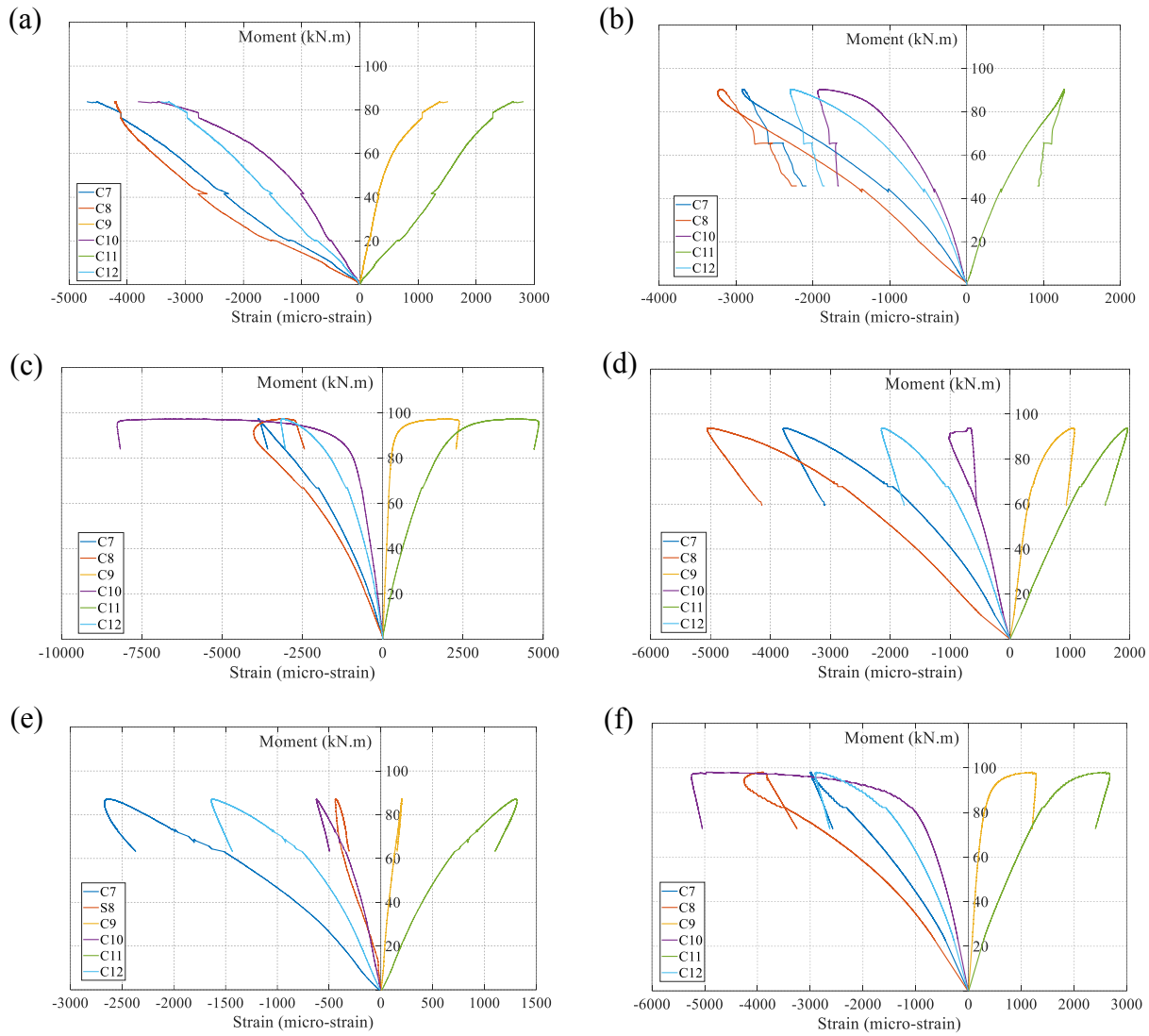

Fig. 2-9: Measured strain versus moment for Y-direction strain gauges for different specimens; (a) EP13-B6-AR1.5; (b) EP10-B6-AR1.5; (c) EP10-B6-AR1.0; (d) EP13-B8-AR1.5; (e) EP13-B6-AR1.5-ST; and (f) EP10-B8-AR1.5

Table 2-4: Key input parameters for the DIC measurements

Parameter	Definition	Value (pixel)
Facet size	A square grid of pixel dimensions	17
Accuracy	The permissible values define the criteria of the correlation algorithm	0.1
Residuum	Residuum of the correlation algorithm in gray value	20
3D residuum	Indicating the quality of the reconstructed point in 3D	0.1
Grid spacing	pixel distance from one subset/facet center to another	12

Strain gauges B3 and B4 were located to measure the strain concentration at the compression flange due to the bolt bearing. By comparing the reading of B3 in both specimens EP10-B6-AR1.5 and EP10-B6-AR1.0 at the same moment value (i.e., 80 kN.m), it was found that strain B3 in specimen EP10-B6-AR1.0 (i.e., 3500 micro-strain) was lower than specimen EP10-B6-AR1.5 (i.e., 5013 micro-strain) due to the bolts forces were distributed in a better way across the whole rows, which delayed the bolt bearing failure. For specimens with eight bolts (i.e., EP10-B8-AR1.5 and EP13-B8-AR1.5), strain gauge B3 reading was lower than specimens with six bolts (i.e., EP10-B8-AR1.5, and EP13-B8-AR1.5) because bolt bearing forces were distributed over more bolt row which led to decrease the strain concentration near strain gauge B3. Strain gauge B5 was located at the web near the compression in all specimens. Strain gauge B5 had lower values than strain gauge B3 across all specimens because forces were transferred across bolts; however, in the specimen with stiffener EP13-B6-AR1.5-ST, it was noticed that after moment 80 kN.m, strain gauge B3 stabilized and B5 increased more than B3 causing local buckling to happen first at the web then the compression flange. It is worth mentioning that strain gauges B5 and B3 had extreme strain values (e.g., 30000 micro-strain) during the occurrence of the local buckling, as it distorted the web and flange. The compression flange of the column in specimens with eight bolts (i.e., EP13-B8-AR1.5 and EP10-B8-AR1.5) showed higher strain values within strain gauges C7 and C8 (i.e., 5000 micro-strain) compared to specimens with six bolts because the capacity of the connection was transferred at an earlier stage through using more bolts. Strain gauges C10 and C11 showed opposite values, which illustrated that the welding forces were distributed all over the parameter of the column cross-section and prevented plastification of one side of the column only. In specimen EP10-B6-AR1.0, strain gauge C10 showed extreme values during stabilization of moment at 97.3 kN.m due to buckling of compression extended plate as shown in Fig. 2-7.d. It is

worth mentioning that strain gauge E1 for specimen EP13-B6-AR1.5 and strain gauge C9 for specimen EP10-B6-AR1.5 was malfunctioned during the test; however, a backup strain gauge E2 and DIC measurement series provided reliable data to compensate the damaged strain gauges E1 and C9.

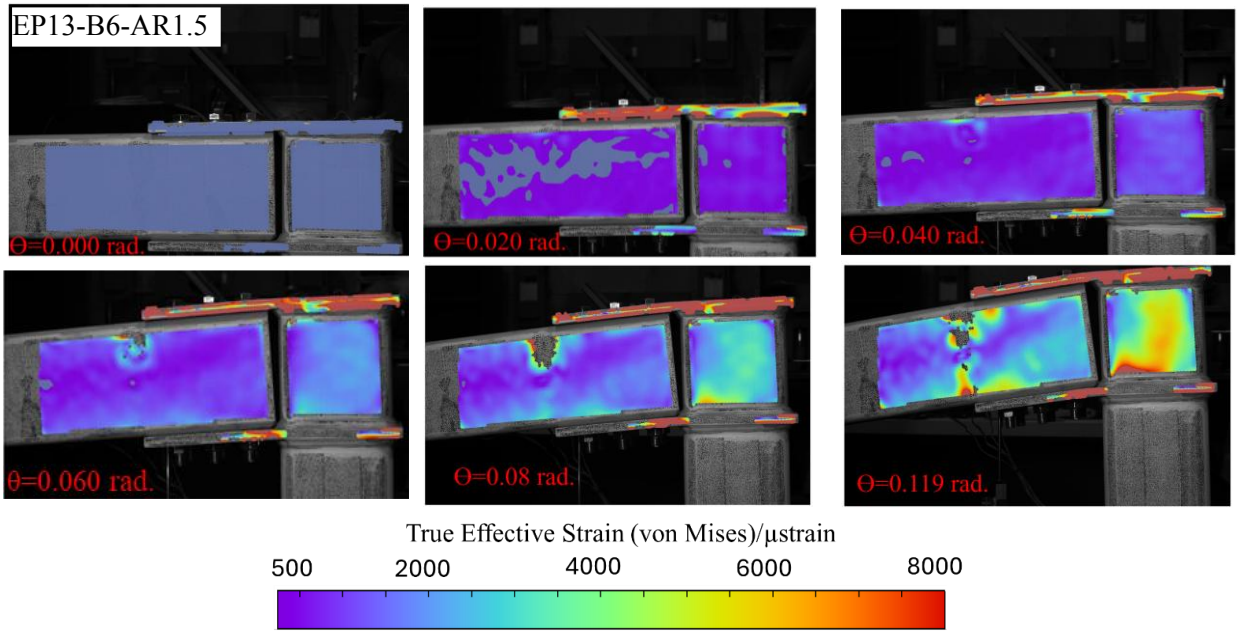

(a)

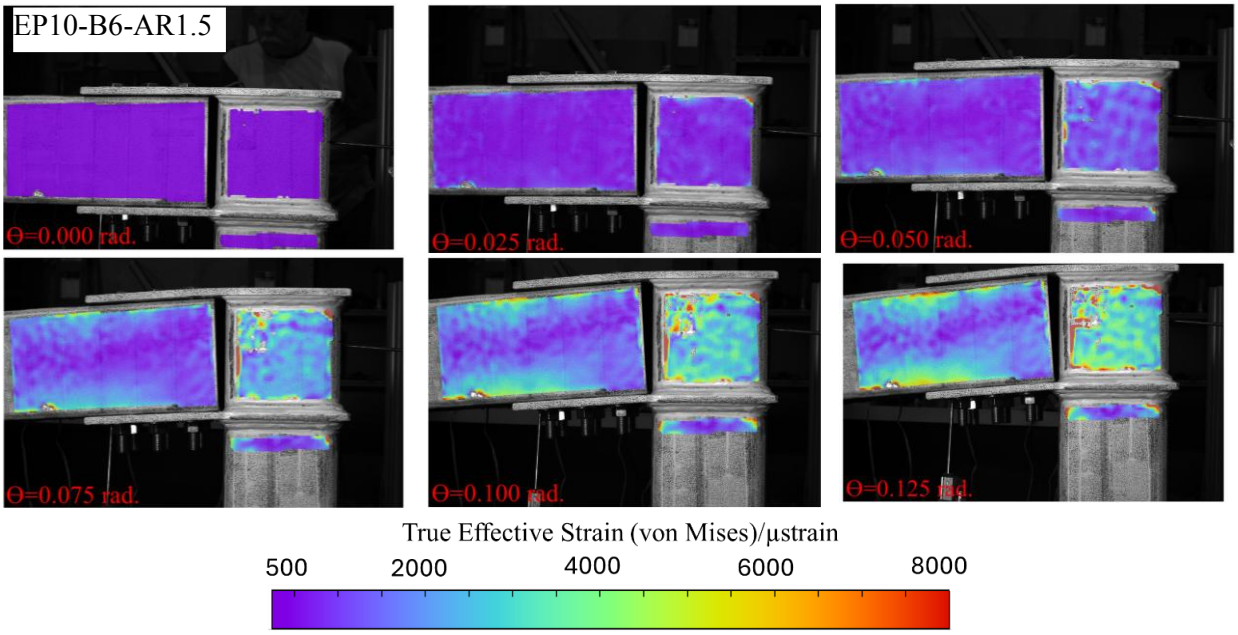

(b)

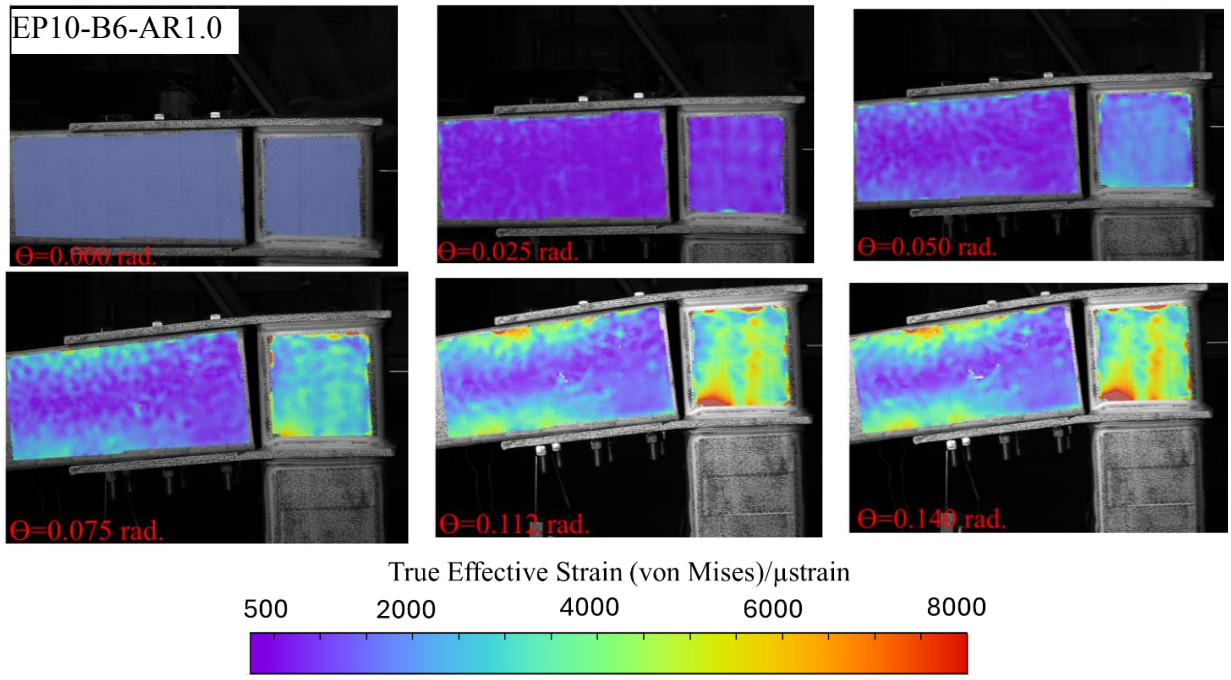
EP10-B6-AR1.0
Θ=0.000 rad.
Θ=0.025 rad.
Θ=0.050 rad.
Θ=0.075 rad.
Θ=0.113 rad.
Θ=0.140 rad.
True Effective Strain (von Mises)/μstrain
500
2000
4000
6000
8000

(c)

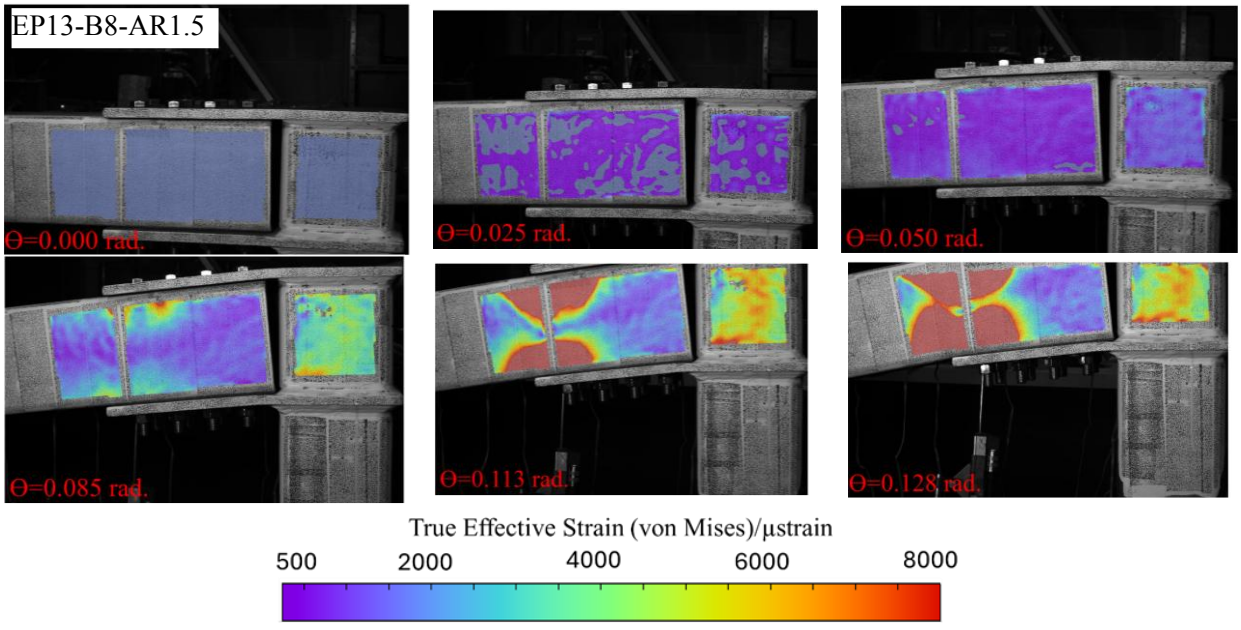
EP13-B8-AR1.5
Θ=0.000 rad.
Θ=0.025 rad.
Θ=0.050 rad.
Θ=0.085 rad.
Θ=0.113 rad.
Θ=0.128 rad.
True Effective Strain (von Mises)/μstrain
500
2000
4000
6000
8000

(d)

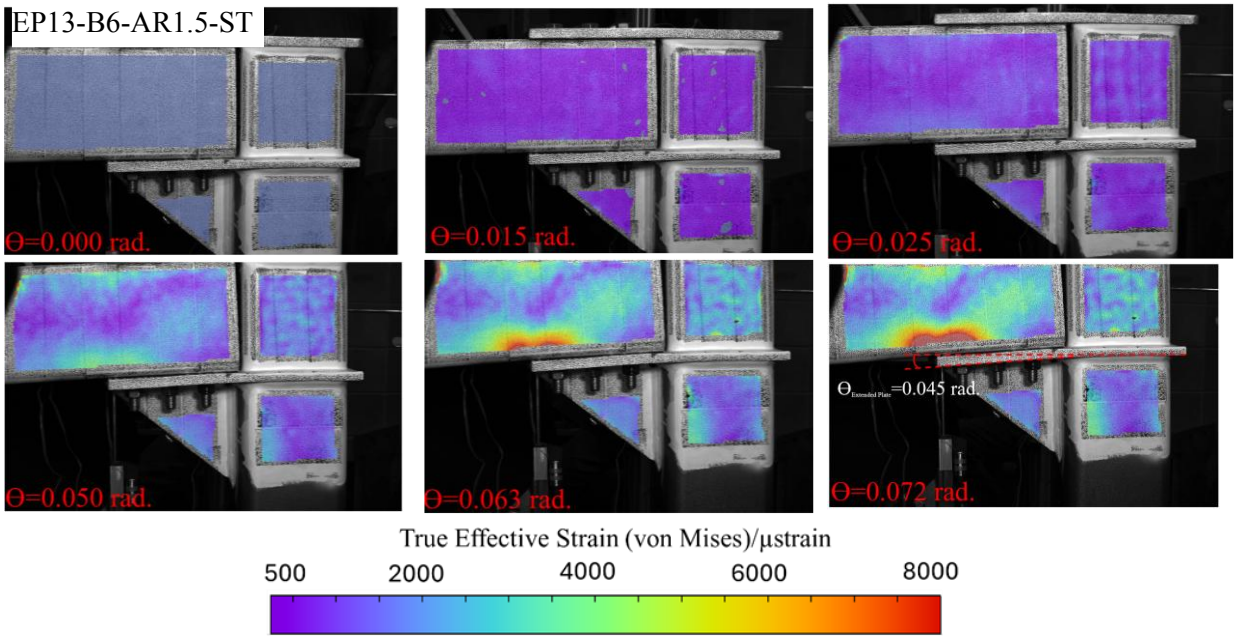

(e)

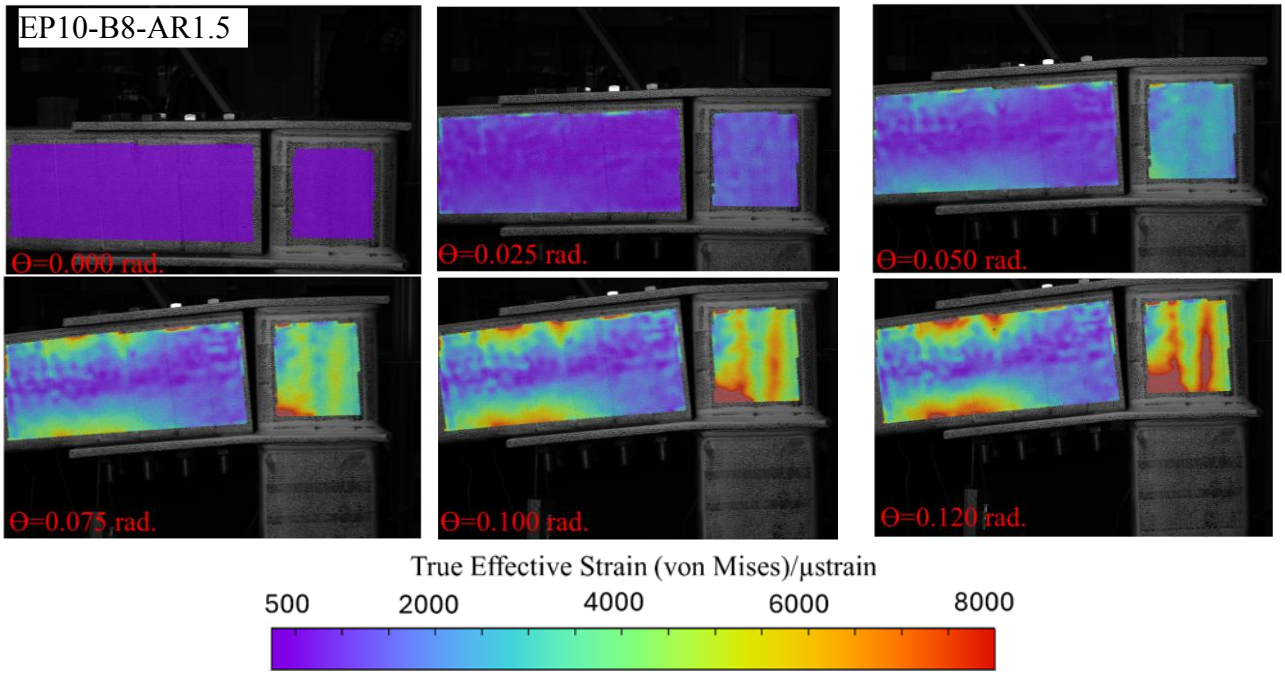

(f)

Fig. 2-10: DIC Graphic visualization of strain distribution (Von Mises) within different joint rotations for different specimens: (a) EP13-B6-AR1.5, (b) EP10-B6-AR1.5, (c) EP10-B6-AR1.0, (d) EP13-B8-AR1.5, (e) EP13-B6-AR1.5-ST and (f) EP10-B8-AR1.5

2.5 Analysis of the results

2.5.1 Effect of Increasing the Extended Plate Thickness

Two thickness values of extended plate dimensions (i.e., 13 mm and 10 mm) were compared within two different bolt configurations (i.e., six and eight bolts) to show their influence on the connection strength and rotation. For the six bolt configurations (i.e., EP13-B6-AR1.5 and EP10-B6-AR1.5), it was noted that increasing the thickness of extended plates from 10 mm to 13 mm led to an increase in the connection initial stiffness, ultimate capacity, and ductility by 60%, 7%, and 19%. This can be attributed to increasing the plate's cross-section, which prevented the bolt bearing failure on the extended plates and transferred more forces through them. So, it delayed the plates yielding during the loading stages and increased the connection stiffness as it depended on the stiffness of the two extended plates during initial rotation. Fig. 2-8.a. and Fig. 2-8.b show measured strain for the extended plates (i.e., E1 and E2), where specimen EP10-B6-AR1.5 reached yielding earlier at a rotation of 0.054 rad and could not gain more capacity after compared to the specimen EP13-B6-AR1.5 that reached the yielding at a rotation of 0.047 rad, as shown in Fig. 2-11.a. Also, in specimen EP10-B6-AR1.5, the two extended plates suffered from bolt bearing failure, which led to extensive rotation and local buckling at the compression extended plate (i.e., lower extended plate), as shown in Fig. 2-7.b.

As for the eight bolt configurations (i.e., EP13-B8-AR1.5 and EP10-B8-AR1.5), the extended plate thickness did not significantly influence the connection capacity during the loading stages except for the ultimate stage. The ultimate capacity and ductility of specimen EP10-B8-AR1.5 increased by 4% and 19 % with respect to specimen EP13-B8-AR1.5, as shown in Fig. 2-11.a, because the extensive rotation of the extended plate of 10 mm due to yielding led to better-bearing forces distribution over all bolt rows and prevented the local buckling at the compression plate and beam

from happening earlier. This phenomenon could be demonstrated well through the DIC measurement, as shown in Fig. 2-10.d and Fig. 2-10.f, where more strain concentrations were distributed near the outer bolts row at specimen EP13-B8-AR1.5, resulting from distributing more bearing forces only to the outer bolts row and led to local buckling of the beam at rotation 0.099 rad as shown in Fig. 2-7.d.

2.5.2 Effect of bolts arrangement

By comparing specimens EP10-B6-AR1.5 and EP10-B6-AR1.0, it was found that the bolt arrangement AR1.0 had a significant effect on increasing the connection strength, ductility and initial stiffness during the loading stages by 7%, 26%, and 216%, even with using an extended plate of 10 mm, as shown in Fig. 2-11.c. This can be explained as the bearing forces being better distributed through all bolt rows in equal value. This could be proven by comparing the DIC strains distributed over the beam in both specimens, as shown in Fig. 2-10.b and Fig. 2-10.c, where in specimen EP10-B6-AR1.5, strains were distributed over the outer bolts row compared to specimen EP10-B6-AR1.0, where strains were distributed along the bolts rows. In specimen EP10-B6-AR1.0, the beam web near the bolted region reached 4500 micro-strains, compared to EP10-B6-AR1.5 of 3000 micro-strains at a rotation of 0.15 rad. Increasing the distance in the longitudinal direction between bolts led to a delay in the stress concentration at the compression flange of the beam at outer rows as measured by the strain gauge B3 among two specimens, as shown in Fig. 2-8.b and Fig. 2-8.c. Also, Increasing the longitudinal pitch distance between bolts (AR1.0) prevented the block shear rupture at specimen EP10-B6-AR1.5 by increasing the area of the shear resistance within the beam, as shown in Fig. 2-7.b. It is worth mentioning that the extended plate failed by buckling after reaching a higher capacity of 69 kN.m, as shown in Fig. 2-7.c.

2.5.3 Effect of plate stiffener

By comparing specimen EP13-B6-AR1.5-ST with EP13-B6-AR1.5, it was found that the stiffener leads to a 9% reduction in connection capacity. This is due to the extensive rotation of the extended plate in the EP13-B6-AR1.5 specimen, which allows the bolts to transfer more of the bearing force to the inner rows of bolts. In contrast, the EP13-B6-AR1.5-ST specimen prevents the rotation of the extended plate, limiting the load transfer to the inner bolt rows and resulting in a lower moment capacity. However, it decreased the ultimate connection rotation by 70 % by eliminating extended plate yielding, as shown in Fig. 2-8.e (i.e., E1 and E2). The loading mechanics of the joint did not depend on the lower extended plate and stiffener to transfer load through the bearing, however the beam started to rotate within the two extended plates and transferred the loads through the bolt bearing, which can be explained precisely through the strain shape contour extracted from the DIC camera and strain gauge S8 attached to the stiffener, where both showed that the strain was below yielding as shown in Fig. 2-10.e and Fig. 2-9.e. However, the connection gained almost its capacity through the bolt bearing through the outer bolt's row, which triggered more stress concentration at the beam compression flange and led to local buckling at a capacity 12% less than EP13-B6-AR1.5, as illustrated in Fig. 2-11.b. No deformation was observed at the two extended plates and stiffener. It is worth mentioning that the maximum rotation the two extended plates in specimen EP13-B6-AR1.5-ST experienced was 0.045 rad, compared to 0.23 rad specimen EP13-B6-AR1.5 without stiffener, making specimen EP13-B6-AR1.5-ST more suitable for reuse by replacing the panelized beam without the need for column replacement because column module remained undamaged until the joint reached its ultimate capacity, and also the connection plates did not undergo significant rotation due to the presence of a stiffener.

2.5.4 Effect of increasing the number of bolts

Four specimens were implemented to investigate the influence of bolt numbers on the connection's initial stiffness, ductility, connection strength, and rotation within two different extended plate thicknesses. By comparing specimens of 13 mm extended plate thickness (i.e., EP13-B6-AR1.5 and EP13-B8-AR1.5). It was noticed that using more bolts triggered the strengthening stage early by transferring more bearing forces through bolts, causing the connection to gain capacity through bolts bearing, which could be explained by comparing DIC strain contours between the two specimens, illustrated in Fig. 2-10.a and Fig. 2-10.d. Specimen EP13-B8-AR1.5 had higher strain at the column cap because of transferring more forces by using more bolts through extended plates. Specimen EP13-B8-AR1.5 reached its maximum capacity without extensive rotation, resulting from bolt bearing failure on the beam flange, and the joint rotation and ductility decreased by 60% and 15%, without significantly increasing the ultimate capacity of the connection compared to specimen EP13-B6-AR1.5, as shown in Fig. 2-11.a. This can be attributed to the fact that more bearing forces were transferred through the outer bolt row only, triggering local buckling failure of the beam, as shown in Fig. 2-7.d. Also, increasing the number of bolts was found to increase the initial stiffness by 70% as more bolts were in contact with beam holes and decreased the effect of beam slippage. Meanwhile, the 10 mm extended plate thickness specimens EP10-B6-AR1.5 and EP10-B8-AR1.5 showed the same behaviour in increasing the initial stiffness by 52% as part of the stiffness included in decreasing the extended plate thickness. Also, the connection gained capacity at earlier stages, and the ultimate capacity increased by 8%. However, the connection rotation was slightly reduced by 7% due to bearing failure and the lower stiffness of the two extended plates.

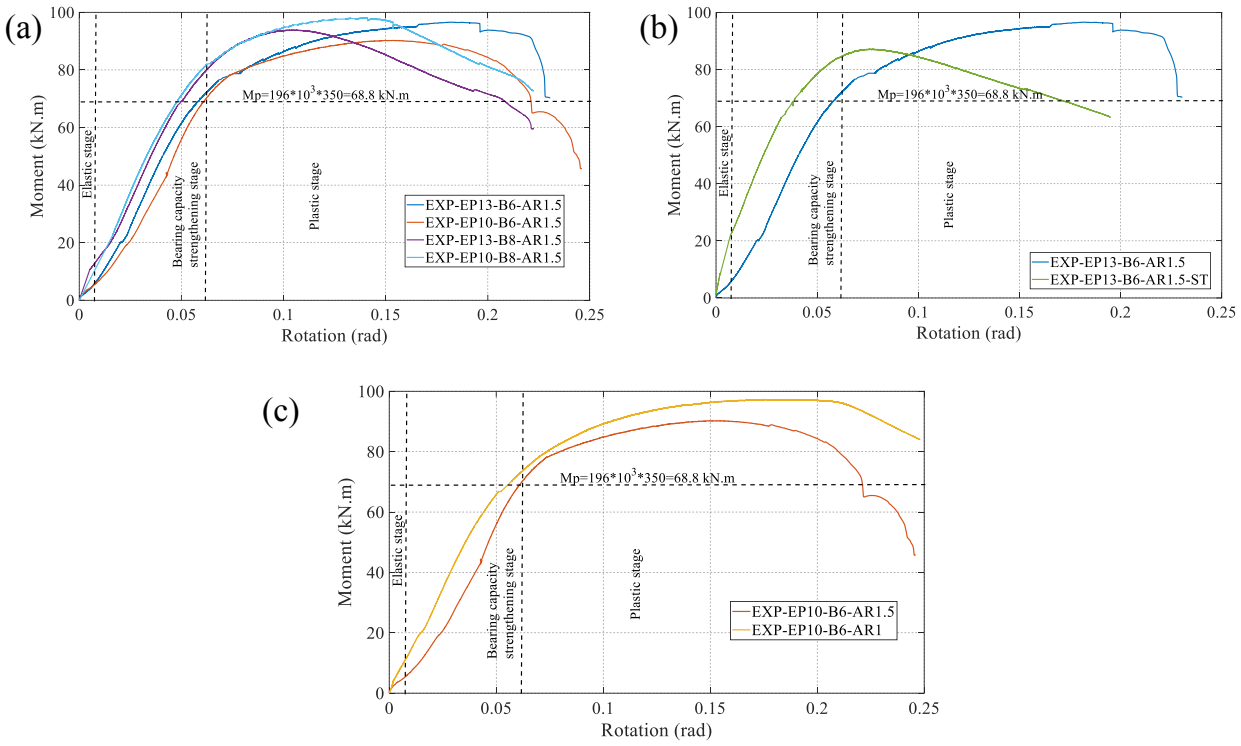

Fig. 2-11: Comparison of Moment-rotation curves for test specimens: (a) different extended plate thickness and number of bolts, (b) influence of existing stiffener, and (c) Bolt arrangement

2.5.5 Performance indicators

According to the classification of AISC 360-16 Cl. B3.4 (AISC 2016), all tested specimens were classified according to the joint stiffness, where the stiffness was calculated based on the secant stiffness $K_s = M_s/\theta_s$. The reason for using the secant stiffness method was due to the nonlinear behaviour at low moment-rotation levels. The moment at service loads was taken as M_s=0.67$M_{y,\,beam}$, while θ_s was the corresponding rotation at service loads. According to the stiffness classification, the boundary limits (k_sL/EI), where L and EI were the length and bending rigidity, respectively, of the HSS beam. The length of the beam was taken as 2500 mm (i.e., the smallest length of the module unit), and the bending rigidity of the beam was calculated as 2646 kN.m^2. The calculations for the tested specimens are illustrated in Table 2-5. It was found that specimens EP10-B6-AR1.0, EP13-B8-AR1.5, EP13-B6-AR1.5-ST, and EP10-B8-AR1.5 were

classified as partially restrained connections, while specimens EP10-B6-AR1.5 and EP13-B6-AR1.5 were classified as simply restrained connections. It is worth mentioning that the configuration and number of bolts exhibited significant influence in transitioning the unstiffened connection stiffness from a simple to a partially restrained connection. However, its boundary limit is still small compared to a stiffened connection. Further geometric investigation is required to enhance the stiffness limits of the unstiffened connection. Partially restrained connections are more important than simply restrained connections, especially in the application of modular houses composed of moment-resisting frames without the need for lateral resistance systems. In addition, the specimens were classified according to their strength following the AISC 360-16 Cl. B3.4 (AISC 2016). All specimens were at full strength because all the joint moment resistance was greater than the beam plastic moment, as illustrated in Fig. 2-12; this classification proved that the proposed connection could be an adequate candidate for a resistant frame in Indigenous houses.

Table 2-5: Connection classification

Specimen ID	Secant stiffness $K_s = M_s/\theta_s$ (N.mm/rad) *10^6	Boundary limit (k_sL/EI)	Classification (stiffness) AISC	Classification (strength) AISC
EP13-B6-AR1.5	1614.7	1.6	Simple restrained	Full Strength
EP10-B6-AR1.5	1336.3	1.3	Simple restrained	Full Strength
EP10-B6-AR1.0	2583.5	2.5	partially restrained	Full Strength
EP13-B8-AR1.5	2583.5	2.5	partially restrained	Full Strength
EP13-B6-AR1.5-ST	3875.3	3.7	partially restrained	Full Strength
EP10-B8-AR1.5	2768.1	2.7	partially restrained	Full Strength

Where K_s: Secant stiffness at service loads, M_s: Moment at service loads, (N-mm), θ_s: Rotation at service loads, rad, L_b: the length of the beam, and EI_b: The bending rigidity of the beam.

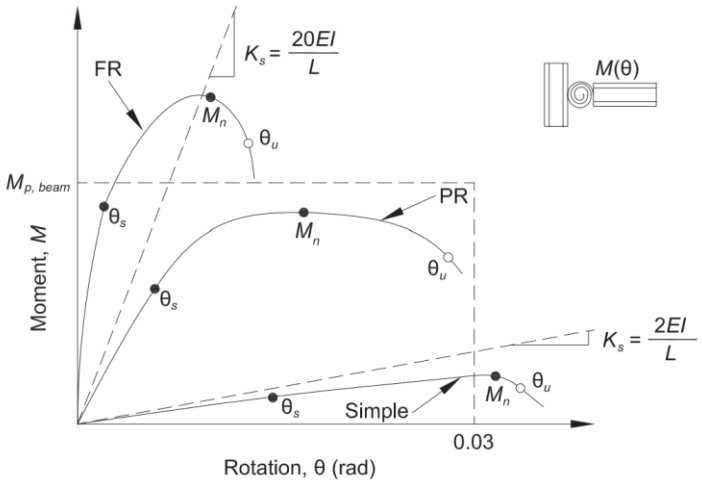

Fig. 2-12: AISC connection classification (AISC 2016)

2.6 Conclusion

This study introduced a beneficial new steel connection that can be used in modular houses for remote Indigenous communities. An experimental study of six bolted HSS-to-HSS moment connections was conducted to evaluate the mechanical behaviour to be employed in moment frame systems. The moment-rotation curve, stiffness, and ductility were carefully evaluated, and the source of inelastic rotation was considered to determine the potential limit state for the connection. The DIC technique was also adopted to better elevate the strain distribution in the connection regions to understand the load transfer mechanism and failure modes. The following conclusions were derived from the aforementioned study:

- The experimental test showed that the moment-rotation relationship can be divided into an elastic stage, a bearing capacity stage, a plastic stage, and a failure stage. Different modes of failure were noticed in this study: local buckling and bolt bearing failure at the beam, yielding, and bolt bearing failure of the extended plate. According to AISC (AISC 2016), this novel connection can be classified as a partially restrained full-strength joint. It was found that the stiffener's existence, configuration, and number of bolts played a crucial role

in increasing the stiffness of the proposed connection, which prompted it to be used in the moment-resisting frame.

- It was found that the thickness of the extended plate had a different influence on the initial stiffness and the ultimate capacity based on the configuration of the utilized bolt (i.e., six and eight bolts), as increasing the extended plate thickness from 10 to 13 within the six bolts configuration, increased the initial stiffness and moment capacity by 60% and 7%, respectively. For the eight-bolt configuration, a lower extended plate thickness (i.e., 10 mm) gained more capacity by 4% compared to the specimen (EP13-B8-AR1.5) because of the extensive rotation of extended plates that led to better force distribution among the inner bolt rows. An extended plate with a thickness of 13 mm is recommended to eliminate any premature failure, such as bearing failure and local buckling at the extended plates.
- In Specimen (EP13-B6-AR1.5-ST), using a stiffener significantly eliminated the yielding and decreased the rotation of the extended plates by 70% compared to the specimen (EP13-B6-AR1.5). However, it reduced the ultimate capacity by 12% because more forces were distributed through the outer bolt rows, leading to local beam buckling. A stiffener is recommended to facilitate the repair of the connection, enabling the assembly of new panelized beams without necessitating the replacement of the column.
- It was found that the bolt arrangement AR1.0 (i.e., specimen EP10-B6-AR1.0) had a significant impact on the connection capacity, initial stiffness, and ductility, as they were increased by 7%, 216 %, and 26%, respectively, compared to specimen EP10-B6-AR1.5. This was attributed to the fact that increasing the distance between bolts led to a delay in the stress concentration at the compression flange of the beam. It is recommended that the bolt arrangement be AR1.0 rather than AR1.5 to eliminate undesired block shear rupture.

- Using eight bolts (i.e., EP13-B8-AR1.5 and EP10-B8-AR1.5) at the extended plates increased the connection ability to gain more capacity at earlier stages within limit joint rotation (i.e., decreased by 60 %), compared to six bolts specimens (i.e., EP13-B6-AR1.5, and EP10-B6-AR1.5), as more bolts could transfer forces through bearing to the extended plate. It is recommended to use eight bolt configurations within an extended pate of thickness 13 mm to have a stiffer connection without extensive rotation of the extended plates (i.e., 10 mm)

For future work, it is essential to distinguish that the tested connection is a one-dimensional (1-D) prototype. However, the actual connection is a two-dimensional (2-D) prototype subject to biaxial bending with different layout configurations, as shown in Fig. 2-1. Comprehensive experimental and numerical analyses will be crucial to fully understand the behaviour of the actual connection when subjected to biaxial bending, particularly in the context of wind and seismic loading.

2.7 Appendix. Proposed connection design procedure

A summary of the design procedure used to determine the connection bolts, weld through the extended plates, and the extended plates' thickness is provided in Fig. 2-13. The procedure ensures that yielding of the extended plate or plastic hinging of the beam occurs before weld failure to meet the wind and seismic moment frame ductility requirement according to CSA S16-19 (CSA 2019).

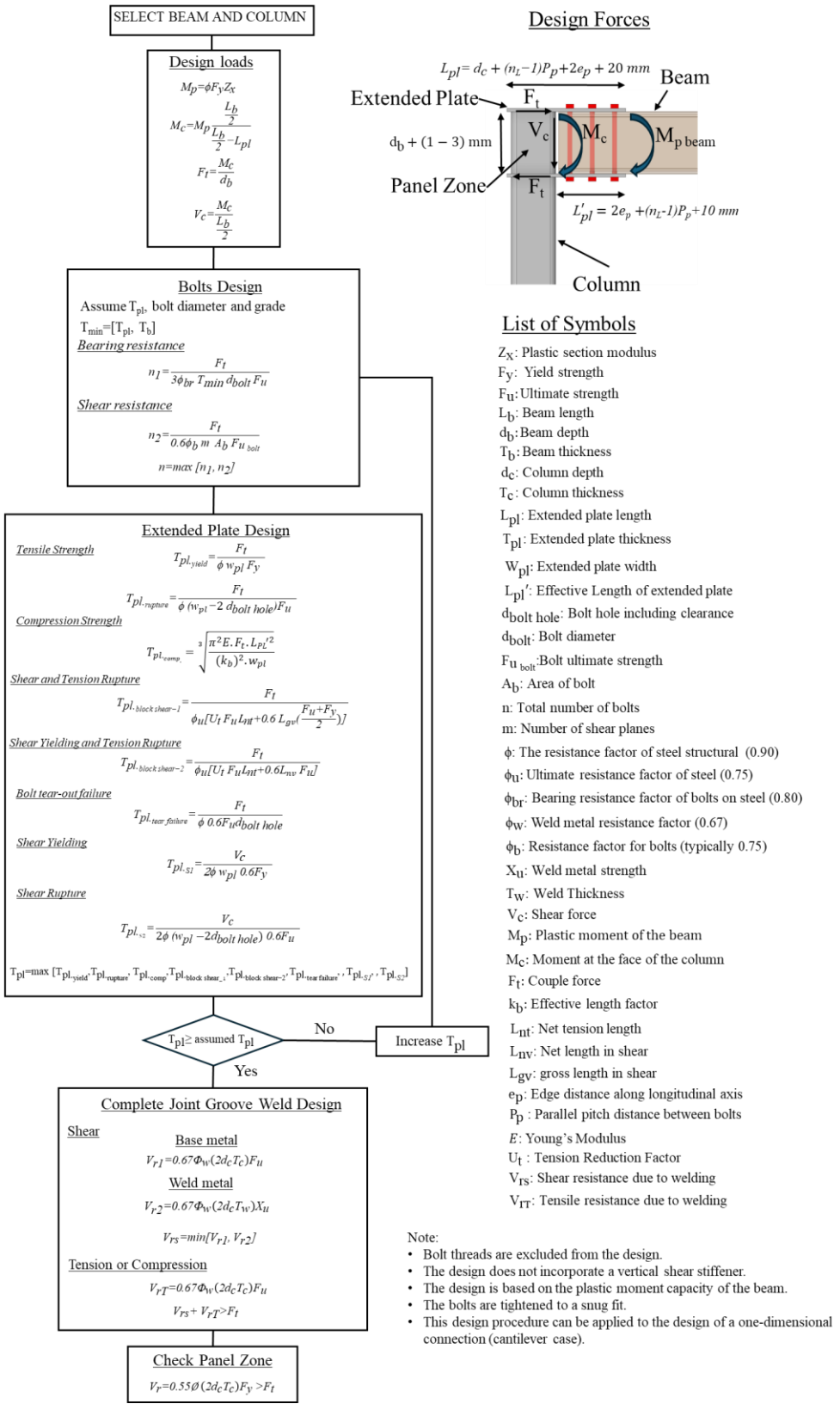

Fig. 2-13: Flow chart of the design procedure for sizing the bolts, extended plate, and weld of the HSS connection.

2.8 References

AISC. 2016. “Specification for structural steel buildings, an American National Standard.” Am. Inst. Steel Constr. Chicago, 612.

AISI. 2015. “S240-15, North American standard for Cold-Formed steel structural framing.” 204.

ASTM. 2014. “A370: Standard test methods and definitions for mechanical testing of steel products.” ASTM Int., 1–50.

Bleakney, A., H. Masoud, and H. Robertson. 2021. “Labour market impacts of COVID-19 on Indigenous people living off reserve in the provinces: March 2020 to August 2021.” Stat. Canada website, (45).

Canada. Office of the Auditor General. 2003. Report of the auditor general of Canada to the house of commons, April 2003. Office of the Auditor General of Canada.

Canada.ca. 2023. “Climate change adaptation in Canada.” Gov. Canada. Accessed October 14, 2022. https://natural-resources.canada.ca/climate-change/what-adaptation/10025.

Canadian Commission on Building and Fire Codes - NRCC. 2020. National Building Code of Canada. Gov. Canada.

Choi, K.-S., H.-C. Lee, and H.-J. Kim. 2016. “Influence of analytical models on the seismic response of modular structures.” J. Korea Inst. Struct. Maint. Insp., 20 (2): 74–85.

Computers and Structures Inc. (CSI). 2019. “ETABS - Building Analysis And Design.” Berkeley, California, U.S. Accessed February 6, 2023. https://www.csiamerica.com/products/etabs.

Corfar, D.-A., and K. D. Tsavdaridis. 2022. “A comprehensive review and classification of inter-module connections for hot-rolled steel modular building systems.” J. Build. Eng., 50 (January): 104006. Elsevier Ltd.

CSA. 2019. “CSA-S16-19: Design of steel structures.” Toronto, ON. Toronto, Ont.

Dantec Dynamics. 2016. “Laser optical measurement systems and sensors | Dantec Dynamics.” Accessed August 3, 2023. http://www.dantecdynamics.com.

Deng, E. F., J. B. Yan, Y. Ding, L. Zong, Z. X. Li, and X. M. Dai. 2017. “Analytical and numerical studies on steel columns with novel connections in modular construction.” Int. J. Steel Struct., 17 (4): 1613–1626.

Du, X., W. Wang, and T. M. Chan. 2018. “Seismic design of beam-through steel frames with self-centering modular panels.” J. Constr. Steel Res., 141: 179–188. Elsevier Ltd. https://doi.org/10.1016/j.jcsr.2017.11.016.

Elhadary, M., A. Bediwy, and A. Elshaer. 2023. “Structural Performance of Novel Steel Connection for Indigenous Modular Houses.” Can. Soc. Civ. Eng. 2023 Annu. Conf. Moncton, New Brunswick: Springer Singapore.

Elhadary, M., and A. Elshaer. 2021. “Behaviour of beam-column connection of modular steel buildings Keywords :” CSCE 2021 Annu. Conf. Whistler, British Columbia: Springer Singapore.

Environment and Climate Change Canada. 2011. “Warm season weather hazards - Canada.ca.” Goverment of Canada. Accessed September 9, 2023. https://www.canada.ca/en/environment-climate-change/services/seasonal-weather-hazards/warm-season-weather-hazards.html#toc7.

Erni, S., L. Johnston, Y. Boulanger, F. Manka, P. Bernier, B. Eddy, A. Christianson, T. Swystun, and S. Gauthier. 2021. “Exposure of the canadian wildland–human interface and population to wildland fire, under current and future climate conditions.” Can. J. For. Res., 51 (9): 1357–1367. Canadian Science Publishing. https://doi.org/10.1139/CJFR-2020-0422.

Fadden, M., and J. McCormick. 2014. “HSS-to-HSS seismic moment connection performance and design.” J. Constr. Steel Res., 101: 373–384. Elsevier Ltd. https://doi.org/10.1016/j.jcsr.2014.05.022.

Garis, L. 2021. “Fire risk for Indigenous people, firefighting in Canada.” On-line Annex Bus. media. Accessed November 2, 2022. https://www.firefightingincanada.com/fire-risk-for-indigenous-people/ accessed 01/10/2021.

Garneau, M. 2022. The effects of the housing shortage on Indigenous peoples in Canada: report of the standing committee on Indigenous and northern affairs.

Government of Yukon. 2023. “Additional funding bolsters Yukon First Nations-led wildfire risk reduction | Government of Yukon.” Accessed November 13, 2023. https://yukon.ca/en/news/additional-funding-bolsters-yukon-first-nations-led-wildfire-risk-reduction.

Han, X. Z., C. Wang, X. H. C. He, Y. F. Hu, T. M. Chan, and K. F. Chung. 2023. “Experimental investigation on bolted inter-module connections and subassemblies of steel modular frames.” J. Constr. Steel Res., 211 (June): 108118. Elsevier Ltd. https://doi.org/10.1016/j.jcsr.2023.108118.

Hwan Doh, J., N. M. Ho, D. Miller, T. Peters, D. Carlson, and P. Lai. 2017. “Steel bracket connection on modular buildings.” J. Steel Struct. Constr., 02 (02). OMICS Publishing Group.

"Impassable winter roads create 'dire' situation for Ontario First Nations." 2024. Accessed February 25, 2024. https://tworowtimes.com/news/impassable-winter-roads-create-dire-situation-for-ontario-first-nations/.

"Inadequate Housing and Crowded Living Conditions - #3 of 8 Key Issues." 2023. Accessed February 25, 2024. https://www.ictinc.ca/blog/inadequate-housing-3-of-8-key-issues.

Indigenous Services Canada. 2018. "Evaluation of the on-reserve income assistance pogram." Gov. Canada. Accessed July 26, 2022. https://www.sac-isc.gc.ca/eng/1557321693588/1557321741537.

ISOPolar Airships. 2020. "Addressing Canada's Indigenous housing shortage." Accessed July 26, 2022. https://isopolar.com/addressing-canadas-indigenous-housing-shortage/.

Al Jazeera. 2023. "Qatar ships world cup portable homes to quake-affected Turkey | Turkey-Syria earthquake news |." Accessed November 14, 2023. https://www.aljazeera.com/news/2023/3/5/qatar-ships-world-cup-portable-homes-to-quake-affected-turkey.

Kamali, M., and K. Hewage. 2016. "Life cycle performance of modular buildings: A critical review." Renew. Sustain. Energy Rev. Elsevier Ltd.

Kilander, A. 2024. Unraveling Modular Construction: Volumetric vs Panelized Approach.

Kuhlmann, U., J.-P. Jaspart, V. Olivier, K. Weynand, and R. Zandonini. 2006. "Robust structure by joint ductility."

Lawson, R. M., R. G. Ogden, and R. Bergin. 2012. "Application of Modular Construction in High-Rise Buildings." J. Archit. Eng., 18 (2): 148–154. American Society of Civil Engineers (ASCE).

Lawson, R. M., J. Prewer, and P. J. Trebilcock. 1999. Modular Construction using Light Steel Framing. Steel Construction Institute.

Lee, S., J. Park, E. Kwak, S. Shon, C. Kang, and H. Choi. 2017. "Verification of the seismic performance of a rigidly connected modular system depending on the shape and size of the ceiling bracket." Materials (Basel)., 10 (3).

Lian, J. Y., E. F. Deng, J. M. He, L. M. Cai, S. C. Gao, and J. J. Zhou. 2021. "Numerical analysis on seismic performance of corner fitting connection in modular steel building." Structures, 33 (May): 1659–1676. Elsevier Ltd. https://doi.org/10.1016/j.istruc.2021.05.044.

Liu, X. C., F. Y. Cui, X. X. Zhan, C. Yu, and Z. Q. Jiang. 2019. "Seismic performance of bolted connection of H-beam to HSS-column with web end-plate." J. Constr. Steel Res., 156: 167–181. Elsevier Ltd. https://doi.org/10.1016/j.jcsr.2019.01.024.

Liu, X. C., Y. Wang, X. X. Cui, C. Yu, and Z. X. Bai. 2020. “Seismic performance of bolted beam-to-column connection with rib-stiffened splicing plate.” J. Constr. Steel Res., 174: 106300. Elsevier Ltd. https://doi.org/10.1016/j.jcsr.2020.106300.

Liu, X. C., Z. W. Yang, H. X. Wang, A. L. Zhang, S. H. Pu, S. T. Chai, and L. Wu. 2017. “Seismic performance of H-section beam to HSS column connection in prefabricated structures.” J. Constr. Steel Res., 138 (June): 1–16. https://doi.org/10.1016/j.jcsr.2017.06.029.

Lopez, D., and T. M. Froese. 2016. “Analysis of costs and benefits of panelized and modular prefabricated homes.” Procedia Eng., 145: 1291–1297.

Ma, R., J. Xia, H. Chang, B. Xu, and L. Zhang. 2021. “Experimental and numerical investigation of mechanical properties on novel modular connections with superimposed beams.” Eng. Struct., 232. Elsevier Ltd.

OECD. 2016. OECD Regional Outlook 2016: Productive Regions for Inclusive Societies, OECD Publishing, Paris.

Rajanayagam, H., T. Gunawardena, P. Mendis, K. Poologanathan, P. Gatheeshgar, M. Dissanayake, and M. Corradi. 2022. “Evaluation of inter-modular connection behaviour under lateral loads: An experimental and numerical study.” J. Constr. Steel Res., 194 (May): 107335. Elsevier Ltd. https://doi.org/10.1016/j.jcsr.2022.107335.

Schneider, L. 1992. A time for action : aboriginal and northern housing : fourth report of the Standing Committee on Aboriginal Affairs.

Sendanayake, S. V., D. P. Thambiratnam, N. Perera, T. Chan, and S. Aghdamy. 2019. “Seismic mitigation of steel modular building structures through innovative inter-modular connections.” Heliyon, 5 (11): e02751. Elsevier Ltd.

Shi, F., H. Wang, L. Zong, Y. Ding, and J. Su. 2020. “Seismic behavior of high-rise modular steel constructions with various module layouts.” J. Build. Eng., 31 (November 2019): 101396. Elsevier Ltd. https://doi.org/10.1016/j.jobe.2020.101396.

von Stackelberg, M. 2019. “Homes on remote First Nations are mouldy before they’re even built, experts say.” CBC News. Accessed November 2, 2022. https://www.cbc.ca/news/canada/manitoba/first-nations-housing-mould-1.5074196.

Transport Canada. 2016. Minister-led Indigenous Roundtable on the Future of Transportation.

United Nations. 2019. “Adequate housing as a component of the right to an adequate standard of living, and the right to non-discrimination in this context.”

Wang, H., X. Zhao, and G. Ma. 2022a. “Experimental study on seismic performance of column-column-beam joint in panelised steel-modular structure.” J. Constr. Steel Res., 192 (October 2021): 107240. Elsevier Ltd. https://doi.org/10.1016/j.jcsr.2022.107240.

Wang, H., X. Zhao, and G. Ma. 2022b. “Novel coupled modular steel structure and seismic tests on high-performance interconnection.” J. Constr. Steel Res., 189 (November 2021): 107058. Elsevier Ltd. https://doi.org/10.1016/j.jcsr.2021.107058.

Wang, Q., and M. Su. 2021. “Stability study on sway modular steel structures with semi-rigid connections.” Thin-Walled Struct., 161 (June 2020): 107529. Elsevier Ltd. https://doi.org/10.1016/j.tws.2021.107529.

Yang, C., H. Chen, and J. Ou. 2024. “Seismic behavior of composite bolted T-shaped exterior joints in modular steel construction.” J. Constr. Steel Res., 212 (May 2023): 108249. Elsevier Ltd. https://doi.org/10.1016/j.jcsr.2023.108249.

Zhai, S. Y., Y. F. Lyu, K. Cao, G. Q. Li, W. Y. Wang, and C. Chen. 2022. “Experimental study on bolted-cover plate corner connections for column-supported modular steel buildings.” J. Constr. Steel Res., 189 (November 2021): 107060. Elsevier Ltd. https://doi.org/10.1016/j.jcsr.2021.107060.

Zhan, X. X., X. C. Liu, S. Feng, and C. Yu. 2021. “Seismic performance of a square HSS column to H-section beam bolted connection with double cover plate.” Eng. Struct., 231 (December 2020): 111729. Elsevier Ltd. https://doi.org/10.1016/j.engstruct.2020.111729.

CHAPTER 3: CAPACITY AND FAILURE MODE PREDICTION OF LONG-BOLTED CONNECTION IN PANELIZED MODULAR HOUSES

3.1 Introduction

3.1.1 Background

Canada is currently facing a critical housing shortage and rising rates of homelessness, especially in remote and northern communities. This housing crisis has been reported by several organizations, especially the United Nations General Assembly on Adequate Housing (United Nations 2019). These regions are subject to various engineering challenges, including materials, climate, and construction (Elhadary et al. 2024b). Modular housing is increasingly recognized as an adequate strategy to address the housing shortage, particularly in remote and northern communities, where transportation and lifting pose substantial challenges. This approach employs standardized building components or industrially fabricated modules, which are systematically assembled on-site through a mechanized installation process, enhancing efficiency and precision in construction. Modular construction is revolutionizing the industrialization of building processes as an emerging and innovative technology across different sectors, including residential, commercial, educational, and healthcare facilities. Modular construction techniques have been widely adopted in Nordic countries such as Finland, Norway, and Sweden, where 45% of residential properties are constructed using these methods (Modular construction reports & industry analysis 2023).

Modular construction can be classified into two primary categories based on module types: the 2D panelized system and the 3D volumetric system (i.e., box-like structure). The 2D panelized system involves the off-site production of individual structural components or panels, which are subsequently transported and assembled on-site. In contrast, the 3D volumetric system entails creating fully finished three-dimensional modules off-site, which are transported and assembled

into the final structure. The 2D panelized system has many advantages over the 3D volumetric system in terms of lower transportation costs, enhanced flexibility, and reduced resource wastage. The 2D system can be efficiently packaged for transport, resulting in substantial cost savings, especially in remote regions (Lawson et al. 1999). Furthermore, 2D is less constrained by transportation and lifting requirements, offering greater adaptability in various construction scenarios. In addition to its other advantages, the 2D panelized system significantly decreases the labour required for interconnection assembly. As a result, 2D panelized is generally favoured over the 3D volumetric system as the method of choice for modular construction. This preference is due to its efficiency and cost-effectiveness. The architectural framework of a standard 2D panelised system consisted of column modules and beam-floor modules. This system is commonly referred to as a "panelized steel-modular" structure. The joint of panelized steel modular structures adopts the beam-column connection to connect the columns with the beams of the beam floor module horizontally. These structures offer several technical advantages, making them an attractive alternative to traditional building materials. Unlike conventional timber structures, cold-formed steel is a non-organic material, which is not susceptible to issues such as rot, mould, or insect damage, which can compromise the integrity of organic materials over time (Rice 2017). Additionally, steel is a non-combustible material, enhancing the fire safety of the structures built with it (American Institute of Steel Construction 2021). Also, cold-formed steel modular structures are significantly lighter compared to concrete structures, which results in substantial savings in terms of transportation costs and other logistics (Steel Framing Industry Association (SFIA) 2024). The connection of the 3D volumetric modular can be categorized into post-tensioned joints, locking devices, and bolted connections (Corfar and Tsavdaridis 2022; Rajanayagam et al. 2021). Bolted connections could be classified into three categories: column-to-column, beam-to-beam, and fitting-to-fitting joints. Many techniques have been suggested in various studies to facilitate loading sharing and transmission between modular units, particularly for the column-to-column

joint, which is a derivative of the column splice joint. Numerous studies have proposed different methods for improving connection performance in modular structures. For example, Choi et al. (2016), Gunawardena et al. (2016), and Deng et al. (2018) suggested using plates and bolts around the perimeter of column sections to enhance the overall strength and stability. On the other hand, Zhang et al. (2024) introduced a novel column-to-column connection using high-strength bolts, improving tensile behavior. Other researchers, such as Zhong et al. (2024) and Ma et al. (2021) proposed incorporating steel boxes within column modules, with long bolts connecting the module columns. Lian et al. (2021) focused on the seismic performance of corner fitting connections in modular steel buildings, highlighting the critical role of robust column-to-column connections in resisting lateral forces during an earthquake. Additionally, Bazarchi et al. (2024) introduced an inbuilt component filled with grout, enhancing slip resistance between modules. Chen et al. (2017) proposed an innovative modular connection using plug-in devices and long bolts for vertical and horizontal connectivity through the module beams, offering improved ease of assembly and structural integrity. Finally, Deng et al. (2017) analyzed various steel column connections in modular construction, including novel gusset plate configurations and bolted connections for open beam cross-sections such as channels, concluding that these solutions optimize the modular structure's overall stiffness and performance. Xu et al. (2020) proposed a method for connecting ceiling and floor beams using bolts along their length, which maximizes the benefits of combined double-beam action in modular steel buildings. In a similar context, Lee et al. (2017) enhanced the rigidity of beam-to-beam connections by adding ceiling brackets and stiffener plates at the beam ends, significantly improving the seismic performance of the modular system. The third category is the fitting-to-fitting joint, where Doh et al. (2017) developed a cubic steel bracket, allowing all module units to be connected through bolts in various directions. They conducted an experimental study to evaluate the performance of steel brackets under bending and shear loading, finding that the connection provided substantial resistance to both. Yu et al. (2018) proposed a connection

detail for modular units resembling containers, which used an intermediate plate and a single bolt. Their study focused on the efficiency of the connection in terms of simplicity and cost-effectiveness, ensuring easy on-site assembly.

For 2D panelized steel modular structures, various studies have introduced different types of column-column-beam joints (Liu et al. 2017; Zhan et al. 2021), designed for on-site assembly using bolts to minimize transportation damage to structural components. Liu et al. (2017) proposed a fully bolted joint system connecting upper and lower box columns through bolted flanges while securing H-shaped beams using extended cover plates and an endplate. Their study, which included cyclic tests, assessed the influence of bolt slippage and the number of bolts on joint stiffness and energy dissipation during seismic events. They found that increasing the number of bolts significantly improved the connection's energy dissipation capacity, thereby enhancing its seismic resilience. Further improvements were made by Liu et al. (2020) by incorporating a trapezoidal stiffener to the H-shaped beam connection. Their research revealed that relocating the web bolts to the beam flange led to increased structural resilience under seismic loading, which has implications for modular housing in seismic-prone areas. While extensive research has focused on optimizing joints between Hollow Structural Section (HSS) columns and wide flange beams, limited attention has been given to HSS-to-HSS moment-resisting frames, which offer superior bending, torsional, and compression resistance, making them a promising high-performance structural system (Korol et al. 1993; Wang et al. 2022a; b). Fadden et al. (2012) introduced welded unreinforced and reinforced HSS-to-HSS connections, studying their performance under seismic load. Their findings indicated that reinforcement plates and the thickness of the plates significantly impacted the connection's stiffness and inelastic rotation, which are critical factors for ensuring stability in modular systems. Elhadary et al. (2024) proposed a bolted connection specifically for HSS sections in modular housing, exploring its potential use in moment-resisting frames. Their experimental investigation revealed that the extended plate thickness, bolt number, and

configuration significantly influenced the joint's stiffness and capacity, offering a cost-effective solution for high-performance modular housing, as shown in Fig. 3-1. This approach could be pivotal for addressing structural challenges in modular construction, especially for Indigenous communities requiring adaptable, resilient housing solutions (Elhadary et al. 2024a; b).

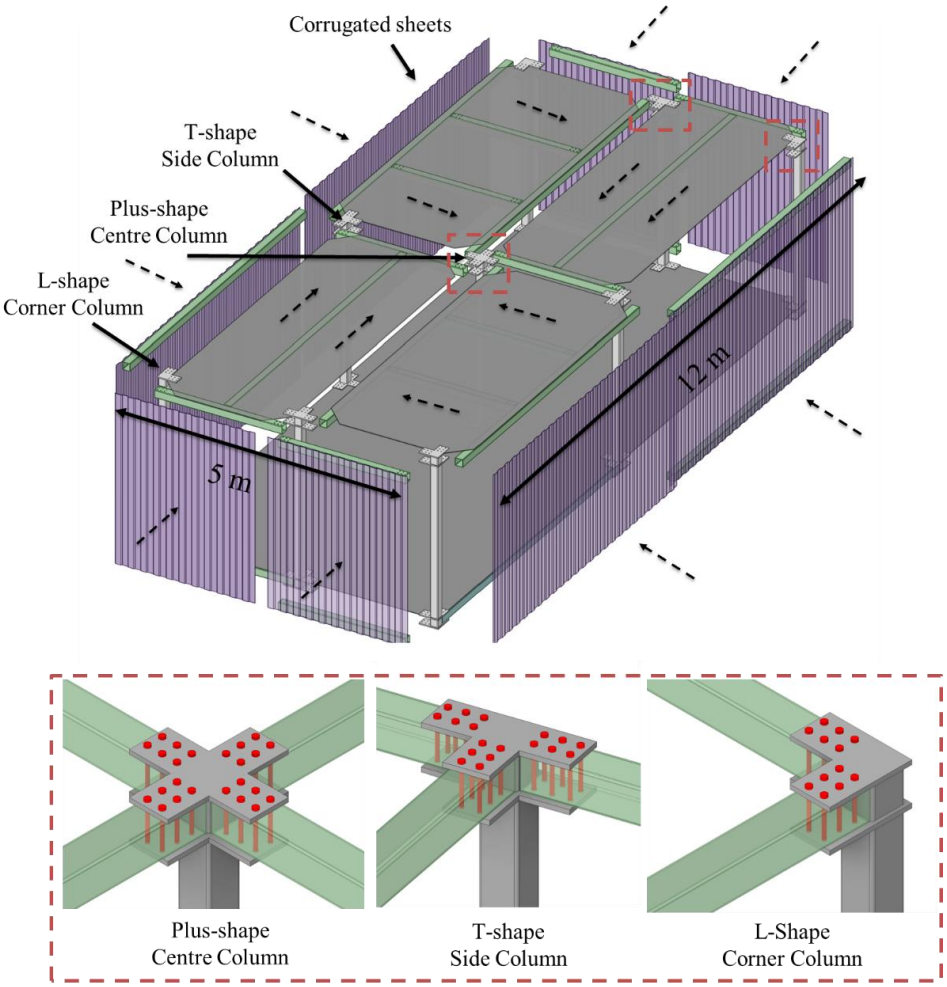

Fig. 3-1: Schematic diagram of the assembly technique of four box modules with different configurations of proposed column joints (Elhadary et al. 2024b)

3.2 Research Significance

The experimental study of the proposed bolt connection for HSS sections lacked a comprehensive analysis of the connection behaviour across various geometric parameters (Elhadary et al. 2024b). The upper and lower limits of each parameter were not tested in a randomized manner to determine the optimal parameters of bolt diameter, extended plate thickness, number of bolts, and bolt

arrangement. This gap necessitates a thorough investigation to provide design guidelines when selecting connection parameters. A detailed parametric study was conducted using 240 FEMs to examine the impact of different parameters, such as extended plate thickness, number of bolts, bolt arrangement pattern, and bolt diameter, on the mechanical behaviour of this innovative steel modular connection. The study offers design guidelines based on the analyzed parameters to prevent premature connection failure. Design charts were developed to aid in predicting the failure mode of the connection based on the selected parameters. These charts eliminate the need to design the connection by displaying the nominal moment of the connection as a ratio of the plastic moment of the beam, considering different bolt arrangements, extended plate thicknesses, and bolt diameters. This research holds significant implications for the future of housing in remote communities, potentially transforming the landscape of affordable and sustainable housing solutions.

3.3 Numerical study

3.3.1 Finite element model details

A 3D FEM of a modular beam-to-column connection was developed using LS-DYNA software (Livermore software technology corporation (LSTC) 2007) and validated with the experimental results conducted by (Elhadary et al. 2024b). Table 3-1 illustrates the main design parameters of the tested specimens (Elhadary et al. 2024b). The Finite Element (FE) simulations were executed on the Digital Research Alliance of Canada (Digital Research Alliance of Canada 2021) (i.e., SHARCNET). Each simulation required an average duration of 48 hours to achieve the designated termination point, encompassing 760 computational time steps. Fig. 3-2 describes the boundary conditions applied on the FEM aligned with the experimental test conditions, where the column was restrained by fixed support, the beam was laterally restrained in the X-direction, and the prescribed motion in the Y-direction was applied on the bracket plate of dimension 340×170 mm

with a moment lever arm of 1080 mm. All specimen components were defined as steel 350W and grade A325 high-strength long bolts of diameter 5/8" (15.875 mm) were used to assemble the joint. The material behaviour of the steel components was simulated using the "Mat_Piecewise_Linear_Plasticity" model available in LS-DYNA. The elastic properties were defined using Young's modulus and Poisson's ratio, while the plastic behaviour was characterized through a piecewise linear stress–plastic strain curve derived from the material's true stress–strain data. This approach allowed for an accurate representation of the steel's post-yield behaviour and strain hardening characteristics under monotonic loading conditions. The uniaxial test was performed using two Digital Image Correlation (DIC) cameras in accordance with ASTM A370 (ASTM 2014) to accurately determine the material properties and true stress-strain curves of 350W steel and A325-grade high-strength bolts, as shown in Fig. 3-3. The DIC cameras, employed as a non-contact optical measurement technique, captured precise strain distribution and variations within the cross-sectional area.

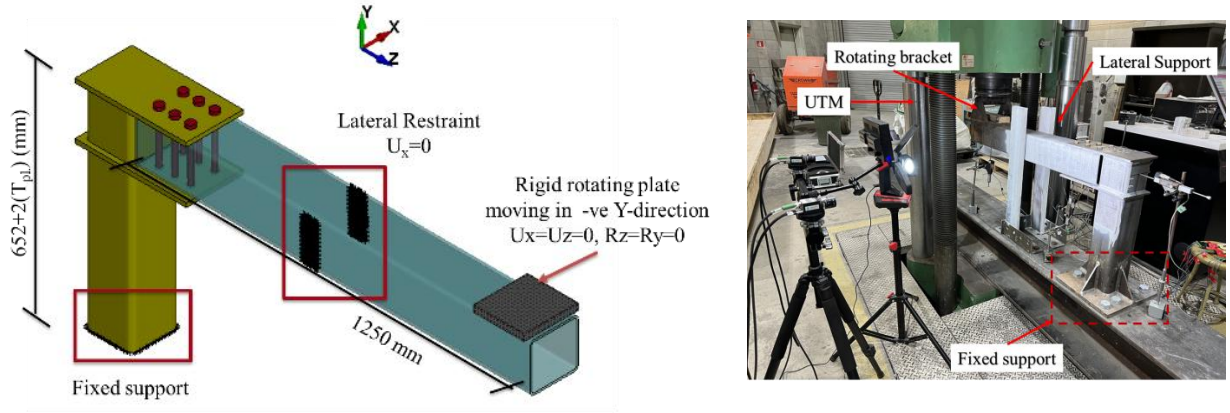

Fig. 3-2: Boundary conditions of the proposed FEM and tested specimens

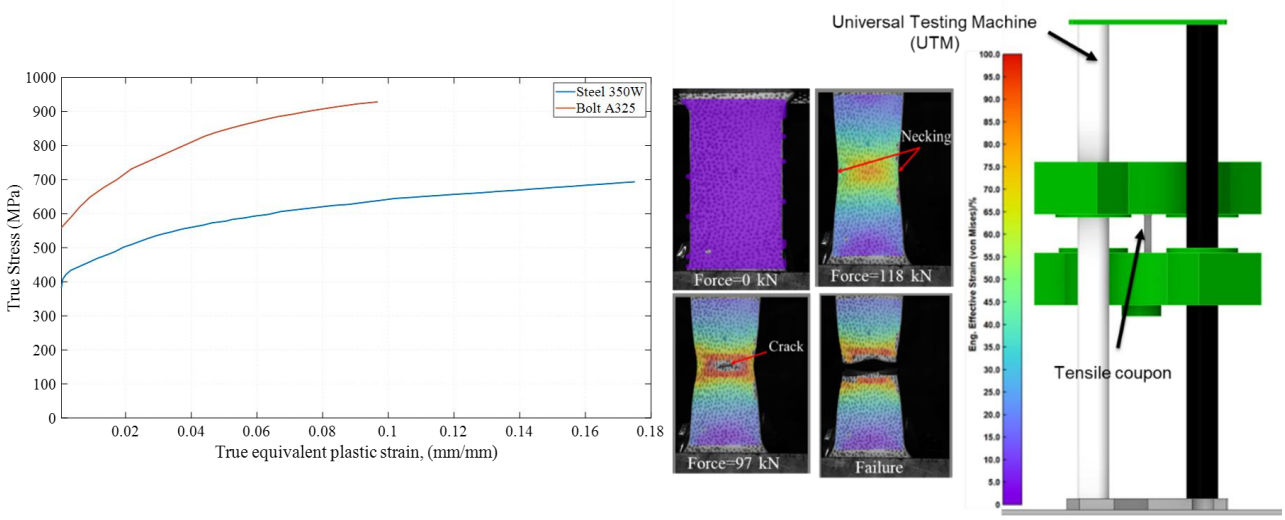

Fig. 3-3: The true stress-equivalent strain curves for tested specimens, the strain distribution utilizing the DIC camera, and a schematic diagram of the uniaxial test

Table 3-1: Main design parameters of the test specimens (Elhadary et al. 2024b).

Specimen ID	Extended Plate Thickness (mm)	Number of Bolts	Bolt Arrangement (P_n/P_p)	Stiffener
EP13-B6-AR1.5	13	6	1.5	no
EP10-B6-AR1.5	10	6	1.5	no
EP10-B6-AR1.0	10	6	1	no
EP13-B8-AR1.5	13	8	1.5	no
EP13-B6-AR1.5-ST	13	6	1.5	yes
EP10-B8-AR1.5	10	8	1.5	no

All model components were modelled using eight-node 3D solid elements with reduced integration, which contains hourglass model control to avoid shear self-locking. Several mesh densities were used in the FEM for different sections within the connection regions with a total number of 390,000 solid elements, as shown in Fig. 3-4. Inflation layers were used around the bolt holes to better capture the gradient of stresses. A cold-formed steel (CFS) beam was discretized using a fine mesh of 4 mm, and seven layers of smaller mesh were used to model profile thickness. This approach was adopted by a mesh sensitivity conducted by (Elhadary et al. 2025; Elhadary and Elshaer 2021). The contacts between connection components (i.e., Frictional components) were modelled using surface-to-surface-Mortar contact. The penalty formulation with a friction coefficient of 0.3 (i.e., represents the surface hardening by sandblasting) is defined by all the

tangential responses for all contact surfaces. The contacts between two extended plates with columns (i.e., welded components) were modelled using surface-to-surface-mortar-tied contact. The bolt clearance of 2 mm was modelled to capture the actual bolt behaviour mechanism. The von Mises yield surface was used in the classical metal plasticity model. All models were incorporated with non-linear material properties, non-linear time step analysis (i.e., implicit analysis), large deformation, and full Newton-Raphson with a modified arch length method.

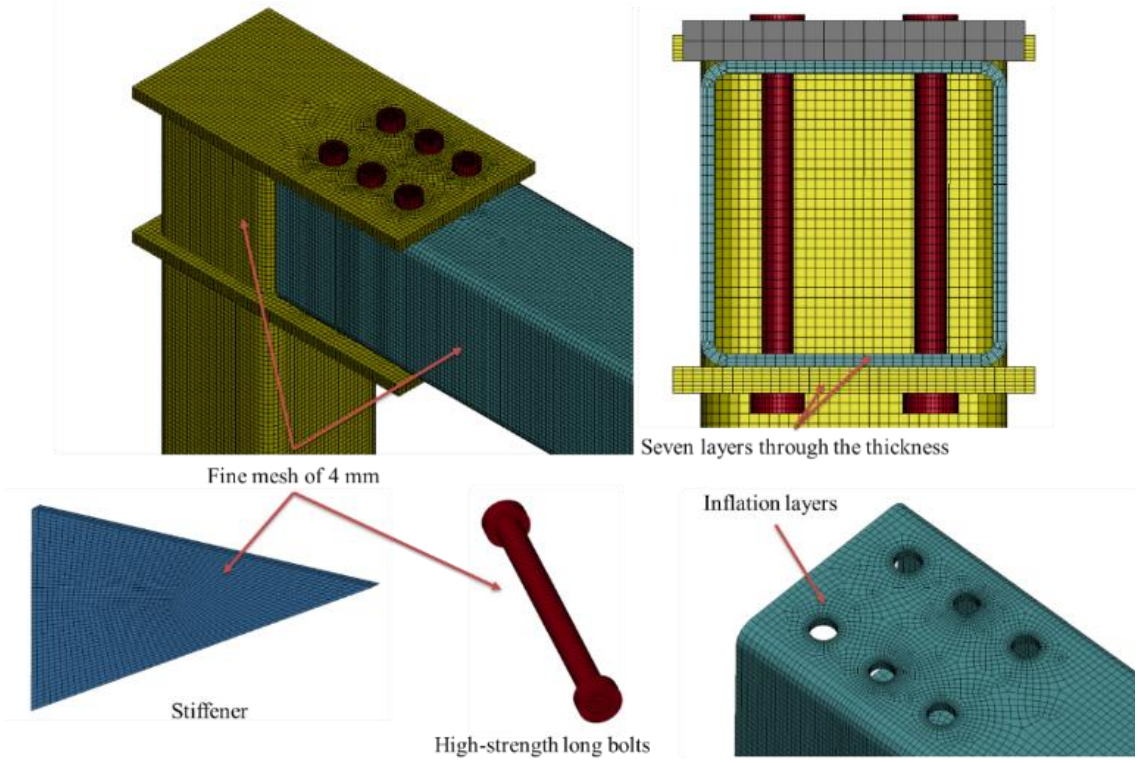

Fig. 3-4: Mesh Configuration of the FEM model

3.3.2 Model validation

Fig. 3-5 shows the comparison between the moment-rotation curves obtained from the experiment test and the proposed FEM for six specimens, where the moment was determined by multiplying the force extracted from the load cell by the distance of the load point to the column face (1080 mm), whereas the connection rotation was calculated by subtracting the column rotation from the beam rotation. The FEM agreed well with its corresponding specimens from the experimental

program, with an average error of 3%, as shown in Table 3-2. The FEM successfully captured the impact of bolt clearance during the loading process, which was identified as a rotational horizontal displacement without a substantial increase in connection capacity. Fig. 3-6 shows the failure mode derived from the proposed FEM and the corresponding specimens incorporated within the experimental program. The FEM effectively captured various failure modes that occurred during the loading of specimens. Some models, such as EP10-B6-AR1.0, EP13-B8-AR1.5, EP10-B8-AR1.5, and EP13-B6-AR1.5-ST, experienced bolt bearing failure, which subsequently triggered local buckling at the beam's compression flange. On the other hand, models like EP10-B6-AR1.5 and EP13-B6-AR1.5 underwent block shear failure following the immediate occurrence of the beam's local buckling.

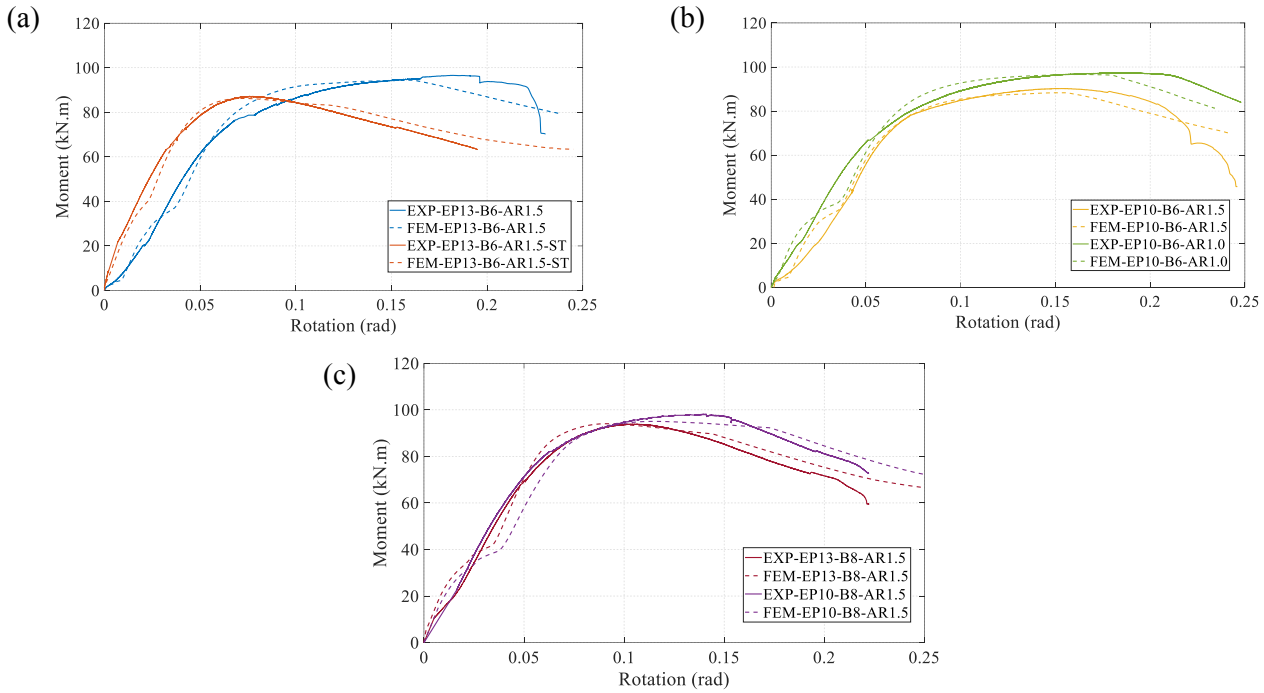

Fig. 3-5: Comparison between the moment-rotation curve of the test specimens and the FEM: (a) EP13-B6-AR1.5, EP13-B6-AR1.5-ST, (b) EP10-B6-AR1.5, EP10-B6-AR1.0, and (c) EP13-B8-AR1.5, and EP10-B8-AR1.5.

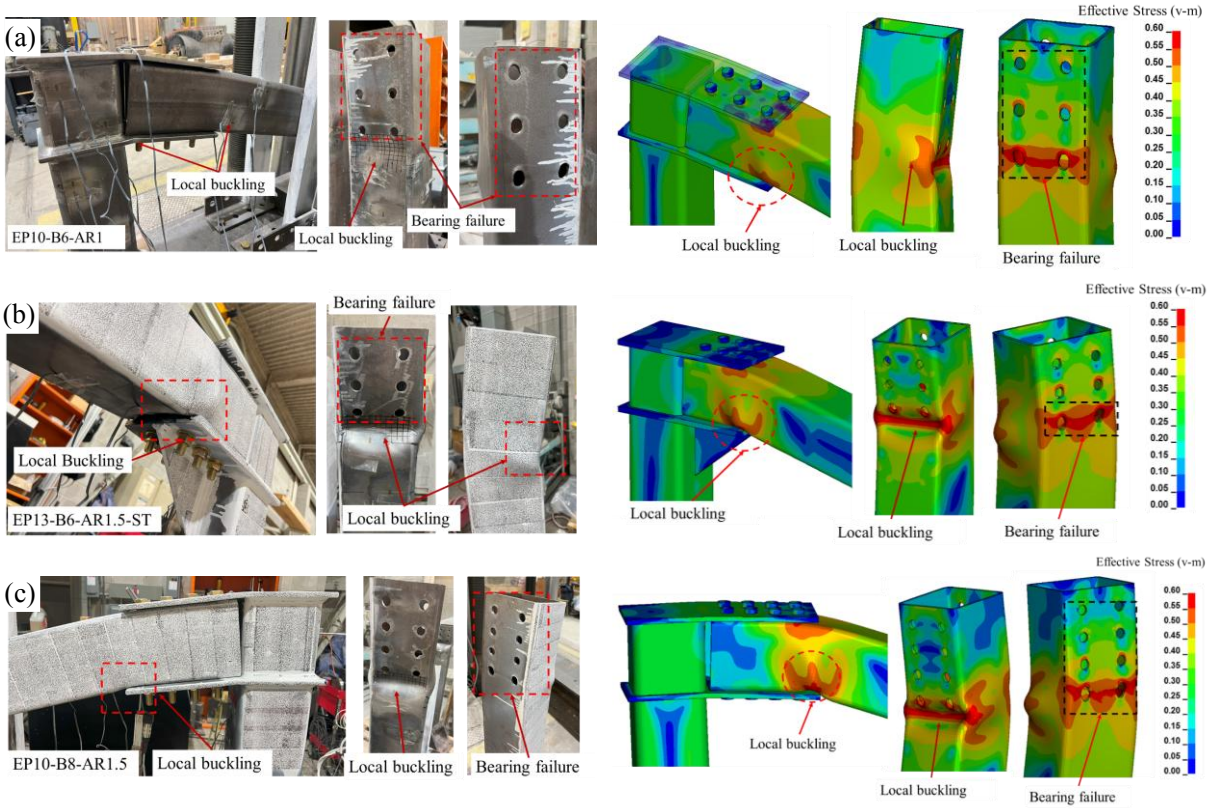

Fig. 3-6: Comparison between the proposed FEM and experimental results for three specimens: (a) EP10-B6-AR1.0, (b) EP13-B6-AR1.5-ST, and (c) EP10-B8-AR1.5.

Table 3-2: Comparison between experimental test and FEM results

Specimen ID	Mode of Failure	Experimental Ultimate moment (kN.m)	FEM Ultimate moment (kN.m)	FEM/EXP
EP13-B6-AR1.5	Local buckling and block shear failure at the beam.	96.3	94.4	0.98
EP10-B6-AR1.5	Local buckling and block shear failure at the beam.	90.2	88.3	0.98
EP10-B6-AR1.0	Local buckling and bolt bearing failure at the beam	97.1	96.6	0.99
EP13-B8-AR1.5	Local buckling and bolt bearing failure at the beam	93.8	94.03	1.01
EP13-B6-AR1.5-ST	Local buckling and bolt bearing failure at the beam	87.1	86.2	0.99
EP10-B8-AR1.5	Local buckling and bolt bearing failure at the beam	97.8	95.03	0.97

3.4 Study Parameters

A comprehensive parametric analysis involving 240 FEMs was conducted to investigate the impact of different geometric parameters on the mechanical performance of the proposed unstiffened edge modular connection (i.e., L-shape). These models are a blend of multiple parameters, which encompass the thickness of the extended plate (T_{pl}=8, 10, 13, 15 mm), the number of bolts (n=4, 6, 8, 10), the bolt diameter (D=12.7, 16, 19, 22, 25), and the bolt arrangement ratio (AR= 1.5, 1, 0.6), where the ratio between perpendicular and parallel pitch between bolts P_n/P_p was implemented using the AR abbreviation (i.e., AR1.5=P_n/P_p=1 .5, AR1= P_n/P_p=1, and AR0.6= P_n/P_p=0 .6). The interplay of these parameters is visually represented in Fig. 3-7 and Fig. 3-8. The extended plate dimensions depended on the bolt arrangement in HSS sections and the number of bolts. However, other parameters were kept constant throughout the parametric study, such as the length of the specimen, cross sections of the beam and column, and the pitch distance between bolts perpendicular to the member axis (P_n), which was considered as a factor of section depth (H) as follows: P_n=0.5H. The parallel edge distance was taken equal to the normal edge distance. The specimens were coded as follows: the thickness of the extended plate (EP), the number of bolts (B), the bolt arrangement (AR) and the bolt diameter (D). For example, in EP13-B6-AR1.5-D19, where EP13 refers to an extended plate of 13 mm in thickness, B6 indicates the number of bolts to be 6, the symbol AR1.5 represents the ratio P_n/P_p to have a value of 1.5, and D19 refers to the bolt diameter of 19 mm. Utilizing the results extracted from the 240 FEM, design charts have been developed to predict failure modes and guide the selection of various parameters, aiding decision-making during the design stage.

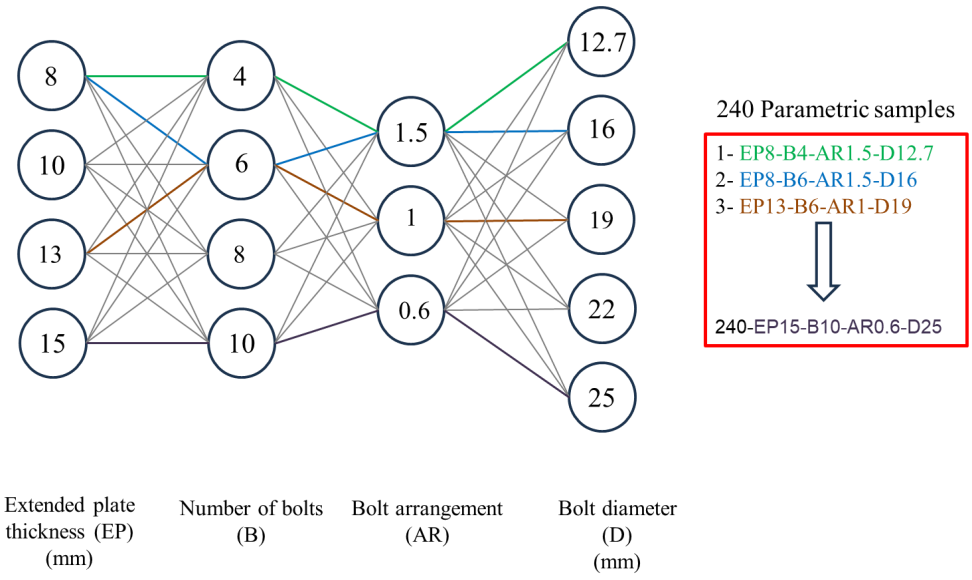

Fig. 3-7: A visual representation of the interplay between various parameters to generate 240 models

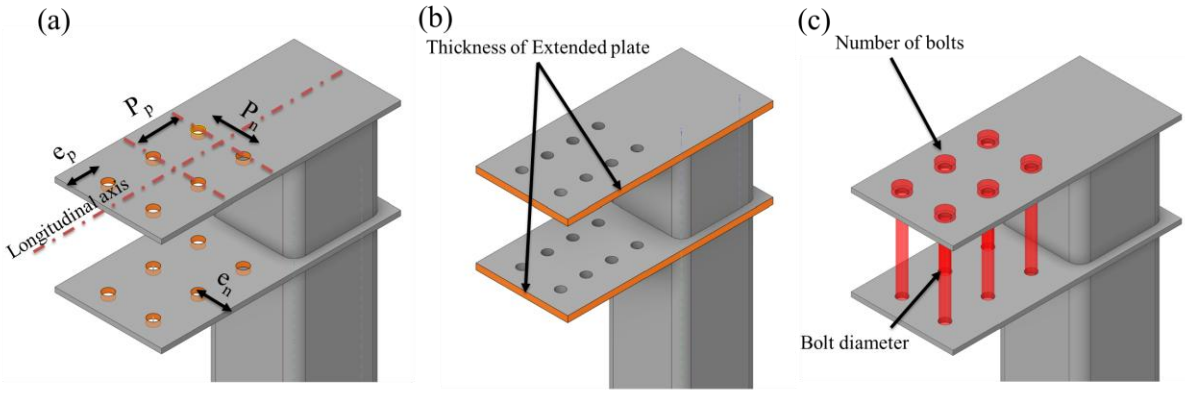

Fig. 3-8: Geometric parameters incorporated in the study: (a) bolt arrangement; (b) thickness of extended plate; and (c) number of bolts and bolt diameters (Elhadary et al. 2024b)

3.5 Results and discussion

The moment rotation curves, failure mode, and ductility of the 240 FEM models are summarized in Table 3-3 within the appendix. Different failure modes were found within the 240 models based on the different studied geometric parameters, such as block shear failure, bolt bearing failure and local buckling of the beam, bolt shear failure, tensile rupture failure of the upper extended plate and local buckling of the column, as shown in Fig. 3-9. The following sections will explain how

the studied parameters trigger the specific failure modes. Each parameter's influence on the failure modes will be thoroughly analyzed and discussed for a comprehensive understanding.

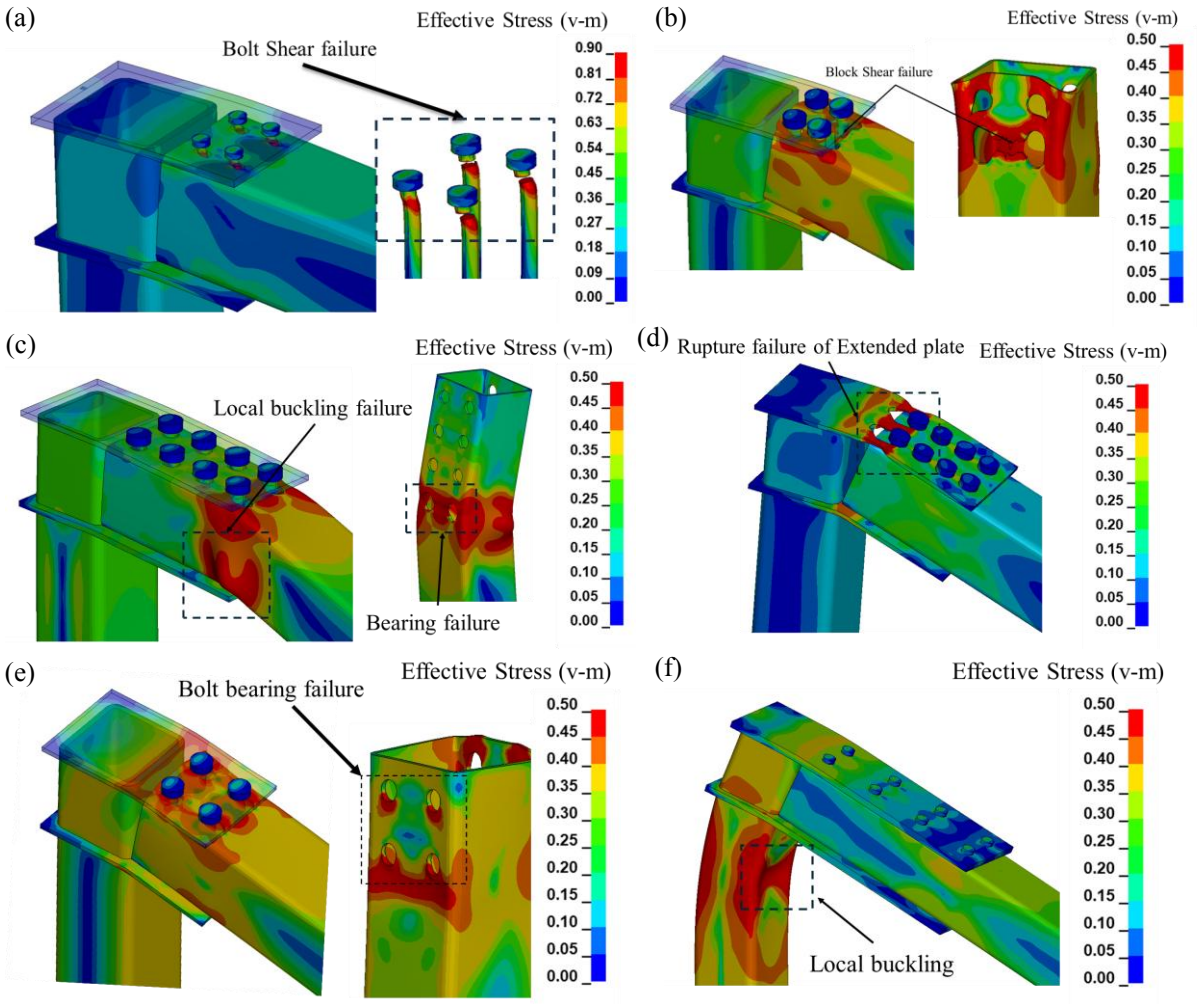

Fig. 3-9: The failure mode of different specimens (a) EP10-B4-AR1.5-D12.7; (b) EP8-B4-AR1.5-D25; (c) EP15-B8-AR1.5-D25; (d) EP8-B8-AR1.5-D22; (e) EP8-B4-AR1.0-D22; and (f) EP15-B8-AR0.6-D16

3.5.1 Effect of bolt arrangement

Three distinct bolt arrangements (i.e., AR1.5, AR1.0, and AR0.6) were examined in the study, each affecting the longitudinal length of the extended plate differently. The bolt arrangement was found to alter the connection failure mechanism (i.e., localizing the failure mode at the beam, column, or extended plate). The applied force on the beam is distributed via the bolt bearing and beam bearing on the extended plate. Fig. 3-10 illustrates the impact of the AR on the distribution

of forces through the bolts and lower extended plate for three specimens, namely EP15-B8-AR1.5-D22, EP15-B8-AR1.0-D22, and EP15-B8-AR0.6-D22. These specimens represent the dominant general behaviour of most of the studied parameters. This figure presents the resultant forces applied on the bolts and lower extended plate. The bolts are initially subjected to bearing forces in the X-direction, which result in a gradual increase in sliding. Meanwhile, beam-bearing forces are applied in the Y-direction to the lower extended plate. The forces acting on the bolts and extended plate are determined by the contact algorithm between the beam and bolts, as well as between the beam and the extended plate. Upon examining the force distribution across different bolt arrangements, it was noted that the force is not equally distributed among the bolts. The outer row of bolts, specifically bolt numbers seven and eight, transferred almost all the bearing forces compared to the other bolts. The AR1.5 bolt arrangement triggered the bolt bearing failure at an earlier loading stage, reducing the beam bearing forces applied on the extended plate. This resulted in a decrease in the ultimate rotation of the connection until the connection failed due to local buckling of the beam through bolt-bearing failure at the compression flange. For AR1.5 with an applied force of 40 kn, the outer bolts number 7 and 8 wasa able to reach the maximum bearing capacity of 100 kN and the lower extended plate was only affected by 65 kn which explain the lower rotation of the extended plate. The AR0.6 bolt arrangement influenced the bearing stage at the outer bolts. Initially, it caused column rotation without triggering the bolt bearing mechanism until the applied force reached 30 kN, as marked by the black circle on the curve. This led to a significant increase in the load on the lower extended plate, nearly doubling the force compared to AR1.5 (i.e., from 65 kN to 110 kN). The outer bolts only carried 60 kN, which delayed the activation of the bearing mechanism, and the connection relied more on the rotational capacity of both the column and extended plate. The altered force distribution caused extensive rotation of the lower extended plate, significantly affecting the upper extended plate. This resulted in rupture failure of the upper extended plate or, when the extended plate thickness exceeded 8 mm, caused

local column buckling, an undesirable failure mode for the connection. The AR1.0 bolt arrangement exhibited a combined behavior between the AR1.5 and AR0.6 configurations. It delayed the activation of the bolt bearing mechanism by inducing rotation in the column, while also increasing the force applied to the extended plate by 35%. However, the AR1.0 arrangement triggered bolt bearing mechanics at a later applied force of 55 kN, compared to 40 kN for AR1.5. This delay allowed for the postponement of local buckling of the beam due to bolt bearing failure at the lower flange. This behavior is clearly reflected in the moment-rotation curves, where the connection's maximum capacity increased by 16% compared to AR1.5, before stabilizing into a plateau between rotations of 0.16 and 0.21, as shown in Fig. 3-5 (i.e., EP10-B6-AR1.0-D16). Ultimately, the connection failed abruptly due to local buckling of the beam caused by stress concentration at the compression flange. To uphold the principle of "strong column weak beam" and prevent any undesirable column or extended plate failure, bolt arrangements AR1.5 and AR1.0 are recommended, as these configurations allow the connection to achieve its capacity through bolt-bearing failure, which leads to local buckling of the beam, unlike bolt arrangement AR0.6, which showed the undesirable mode of failures, which happened regardless of other parameters studied.

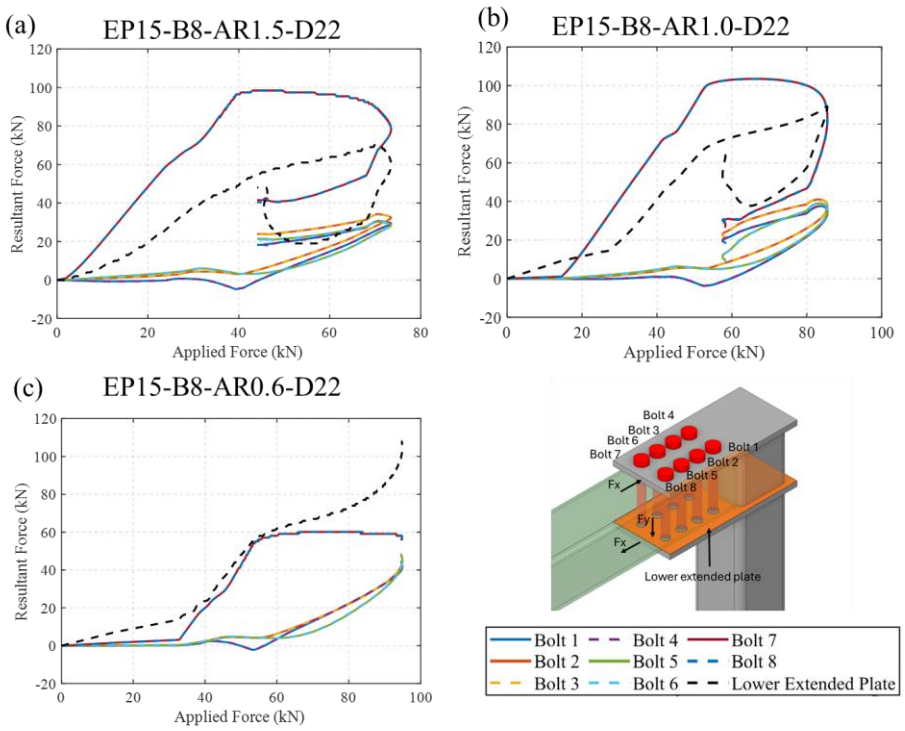

Fig. 3-10: Relationship between the force applied on the beam and the resultant forces distributed on the bolts and the lower extended plate for different bolt arrangements: (a) AR1.5; (b) AR1.0; (c) AR0.6, and (d) schematic diagram of the connection

3.5.2 Effect of increasing extended plate thickness

The thickness of the extended plate (i.e., 8 mm, 10 mm, 13mm, and 15 mm) was found to significantly influence the ductility and capacity of the proposed connection, as demonstrated in Table 3-3. When an extended plate with a thickness of 8 mm was used regardless of the number of bolts and bolt diameters, the connection experienced premature failure due to tensile rupture within the smaller/net cross-section of the plate at the level of the bolts, as depicted in Fig. 3-9.d. Such rupture failure of the extended plate was noted to be triggered by bolt arrangements AR1.0 and AR0.6 with bolts number equal to or greater than six, which relied heavily on the beam-bearing forces on the extended plates, which led to extensive rotation of both extended plates and ultimately resulted in the premature failure of the upper extended plate, as shown in Fig. 3-10. However, the bolt arrangement AR1.5, especially at the same extended plate thickness of 8 mm and bolt diameter of 16 mm, managed to prevent this failure, as shown in Fig. 3-11. This was due

to the unequal force distribution, where the outer bolt row reached its maximum bearing resistance first, allowing the other bolt rows to start resisting forces without distributing them to the tensile extended plate. This behaviour changes when larger bolt diameters (i.e., 19 mm, 22 mm, and 25 mm) are combined with bolt arrangement AR1.5 and an 8 mm-thick extended plate. In this case, the tensile extended plate reaches its maximum capacity before the inner bolt rows begin to share the load, due to the increased bolt bearing resistance provided by the larger bolt area. By increasing the thickness of the extended plates from 10 mm to 13 mm and from 10 mm to 15 mm, the ductility was enhanced with an average of 30% and 60%, respectively, based on different bolt configurations. Additionally, the ultimate capacity experienced an average increase of approximately 5 % and 10 %, respectively. This improvement was attributed to the larger thickness of the extended plate, which facilitated the transfer of more forces to the column cap and provided greater resistance to yielding, even after local buckling occurred at the peak moment, as shown in Fig. 3-9.c. It is recommended that the nominal tensile force capacity of the extended plate's net section be designed to resist at least 1.2 times the nominal force demand, where the force demand is calculated by dividing the ultimate nominal moment capacity of the connection by the beam depth. This ensures that the extended plate remains sufficiently strong to transfer the developed moment without premature failure. It is worth mentioning that the bolt arrangement is the primary factor in controlling failure mode, even when the thickness of the extended plate is increased to 15 mm. The following sections will discuss the combined impact of increased plate thickness, a bolt diameter of 12.7 mm, and the number of bolts.

3.5.3 Influence of the bolt numbers

The study examined the impact of the connection mechanism by utilizing four different numbers of bolts, four, six, eight, and ten bolts, with different bolt diameters. Fig. 3-11, Fig. 3-12, and Fig. 3-13 illustrate the failure mode that the specimen experienced according to the number of bolts and bolt arrangements (i.e., AR1.0, AR1.5, and AR0.6) utilized in the connection, which played a

crucial role in gaining moment capacity. It was found that using a bolt diameter of 12 mm with four and six bolts is not sufficient to achieve shear force resistance for all bolt arrangements because the forces are not distributed equally to the bolt rows, leading to premature failure of the connection by bolt shear failure as shown in Fig. 3-9.a. Increasing the number of bolts to 8 and 10 in conjunction with bolt arrangements AR0.6 and AR1.0 for a bolt diameter of 12.7 mm resulted in an undesirable failure mode. This caused the entire connection to rotate, preventing the bolt-bearing failure until the connection ultimately failed due to local buckling of the column. However, with bolt arrangement AR1.5 with eight and ten bolts, the connection failed by local buckling. This is because the increased number of bolts provided sufficient shear resistance to achieve the maximum connection capacity, and AR1.5 enhanced the bolt-bearing mechanism during the loading stage. The use of four bolts, particularly with a bolt diameter of 16 mm, with three studied bolt arrangements (i.e., AR1.5, AR1.0, AR0.6), resulted in an early connection failure due to bolt shear failure, predominantly in the outer bolt rows. For a bolt diameter of 19 mm, 22 mm and 25 mm, using four bolts with bolt arrangement AR1.5 resulted in premature block shear failure at the beam even with a thickness of 8 mm for the extended plate, as shown in Fig. 3-9.a. However, block shear failure was not observed with bolt arrangements AR1.0 with four bolts, as AR1.0 decreased the transferred forces to the bolts, leading to bolt bearing failure at the beam without causing local buckling. This was also observed for bolt arrangement AR0.6 with an extended plate thickness of 8 and 10 mm for a bolt diameter of 19 mm.

For AR1.5 with different bolt diameters (i.e., 16 mm, 19 mm, 22 mm, 25 mm), increasing the number of bolts from 6 to 8 and from 6 to 10 improved the connection capacity by an average of 11% and 18%, respectively. This increase in bolts distributed the bearing forces more effectively and delayed the local buckling of the beam. However, for the AR0.6 bolt arrangement, increasing the number of bolts from 6 to 8 and from 6 to 10 with different bolt diameters (i.e., 16 mm, 19 mm, 22 mm, 25 mm) only increased the capacity by an average of 10% in both cases. In the latter

case, AR0.6 depends on the ultimate strength of the column, which led to the undesirable local buckling failure mode of the column because it eliminated the bolt bearing force and caused the column to rotate by beam bearing on the extended plate until it reached its ultimate capacity and failed due to local buckling of the column's compression flange, as shown in Fig. 3-9.f. It is recommended to use only six bolts with bolt arrangement AR0.6 for different bolt diameters (16 mm, 19 mm, 22 mm, 25 mm) to achieve the desirable failure mode, which is the local buckling of the beam. This configuration achieves a higher capacity of 100 kN.m compared to the AR1.5 arrangement with ten bolts.

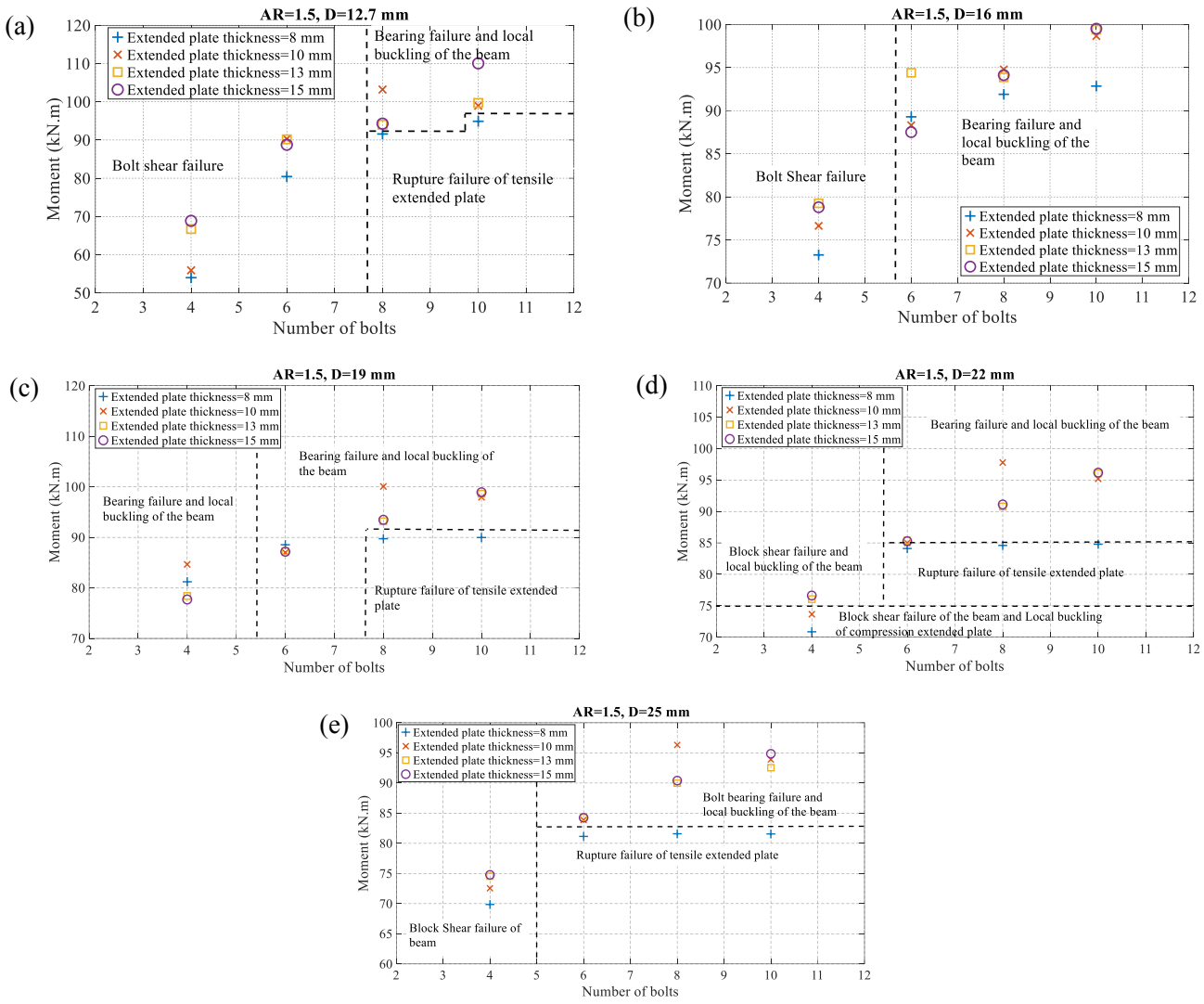

Fig. 3-11: Relation between the number of bolts vs extended plate thickness vs ultimate moment of bolt arrangement AR1.5 for different bolt diameters: (a) D12,7; (b) D16; (c) D19; (d) D22; and (e) D25

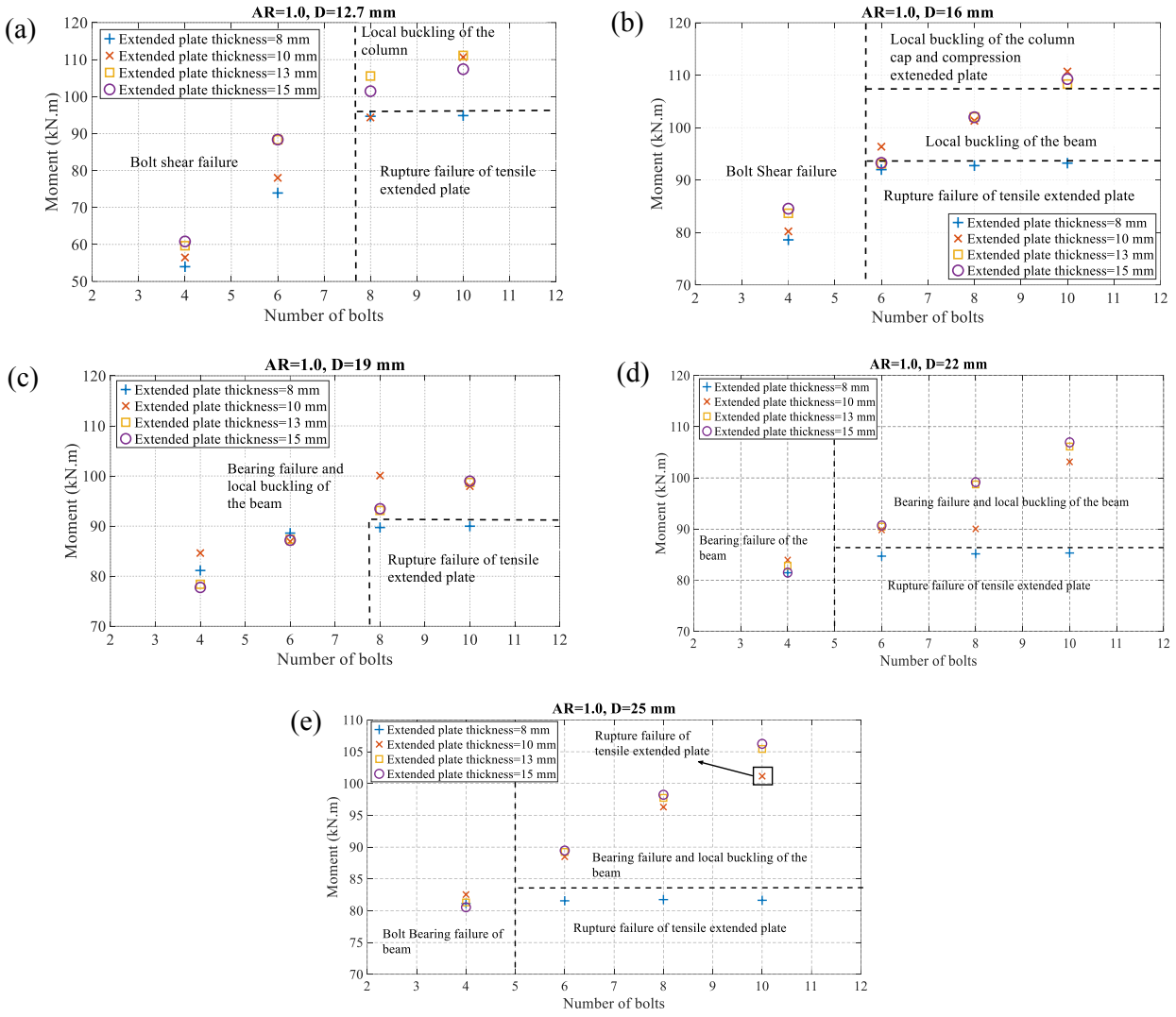

Fig. 3-12: Relation between the number of bolts vs extended plate thickness vs ultimate moment of bolt arrangement AR1.0 for different bolt diameters: (a) D12.7; (b) D16; (c) D19; (d) D22; and (e) D25

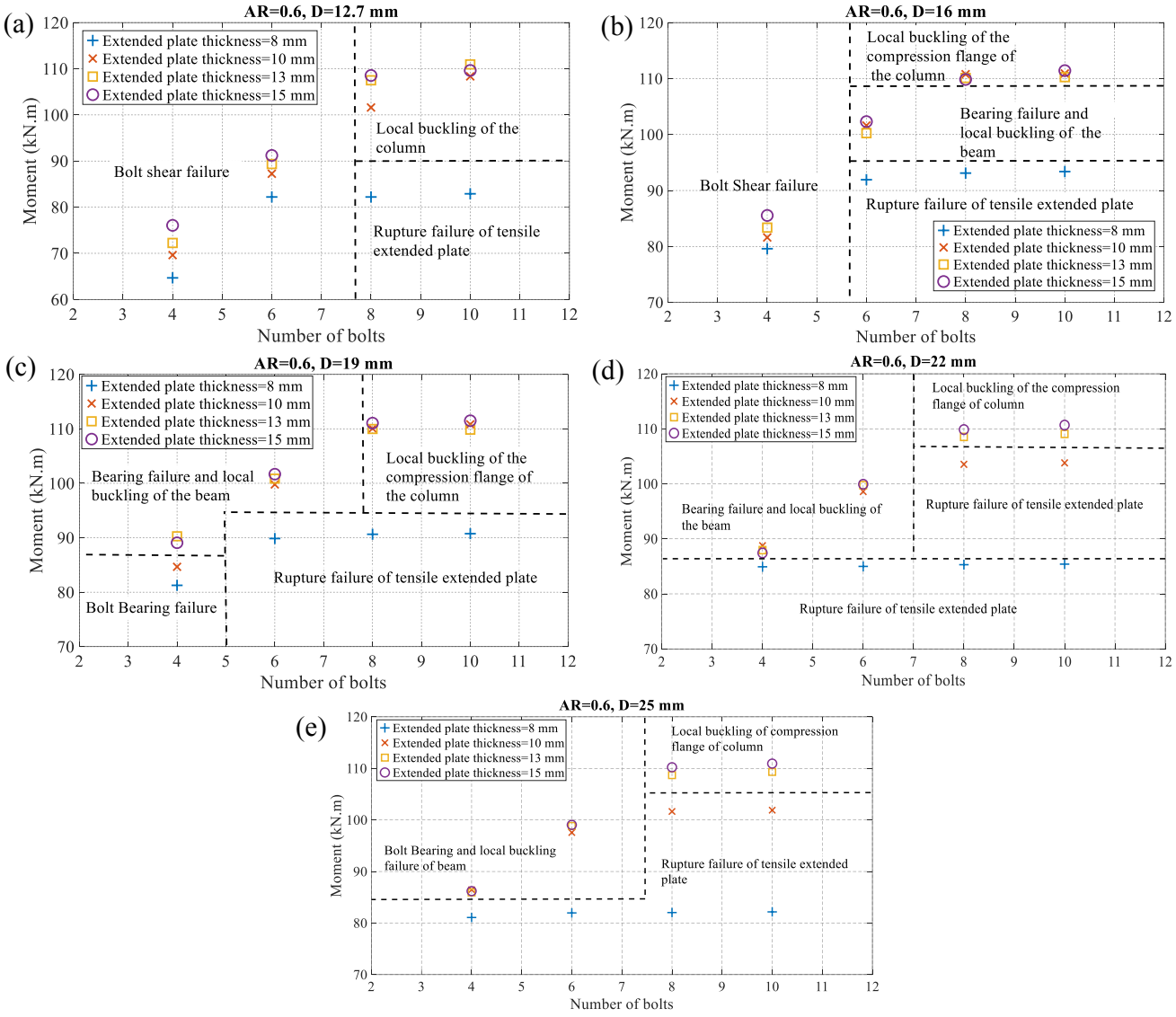

Fig. 3-13: Relation between the number of bolts vs extended plate thickness vs ultimate moment of bolt arrangement AR0.6 for different bolt diameters: (a) D12.7; (b) D16; (c) D19; (d) D22; and (e) D25

3.5.4 Influence of increasing the bolt diameter

The influence of different five-bolt diameters was investigated (i.e.,12.7 mm, 16 mm, 19 mm, 22 mm, and 25 mm). Utilizing a bolt diameter equal to 25 mm leads to an early capacity gain due to higher bearing resistance, and it reduces the ultimate rotation of the extended plate by an average of 60% compared to a bolt diameter of 16 mm. For bolt diameters of 19, 22, and 25 mm, the average ultimate moment capacity decreased by 10% for different bolt numbers and arrangements

(i.e., AR1.0 and AR1.5) compared to the 16 mm bolt diameter. This is attributed to the larger bolt-hole area at the beam flange, which triggered a higher stress concentration earlier at the beam's compression flange due to bolt-bearing force, leading to local buckling of the beam at a lower capacity value.

Fig. 3-14 shows the relationship between the nominal to plastic moment beam ratio, the bolt diameter to extended plate thickness ratio, and the number of bolts for bolt arrangements AR1.5 and AR1.0, only because those bolt arrangements triggered the gaining capacity through bolt bearing forces. Fig. 3-14.b illustrates how to determine a point on the 3D plot for a bolt diameter of 16 and a bolt number of 8 using arrows. The effect of different extended plate thicknesses on the different bolt diameters is shown for each group of bolt numbers. When the extended plate thickness is equal to or nearly equal to the bolt diameter, the nominal capacity increases by 20% (compared to the plastic moment of the beam) for bolt AR 1.5. This is because it reduces the bolt-bearing forces on the extended plate, allowing it to transfer more forces, as shown in the circle group of six bolts in Fig. 3-14.a. It can be observed that increasing the number of bolts from 6 to 8 and from 8 to 10 increases the capacity in AR 1.5 by an average of 10% and in AR 1.0 by an average of 20% due to the reduction in bearing forces on the extended plate. According to Fig. 3-14, it is recommended to maintain the ratio of bolt diameter to an extended plate thickness of less than 2. This strategy helps postpone the stress concentration occurring at the beam's compression flange and extended plate, which can otherwise lead to local buckling of the beam due to the bearing of the bolt.

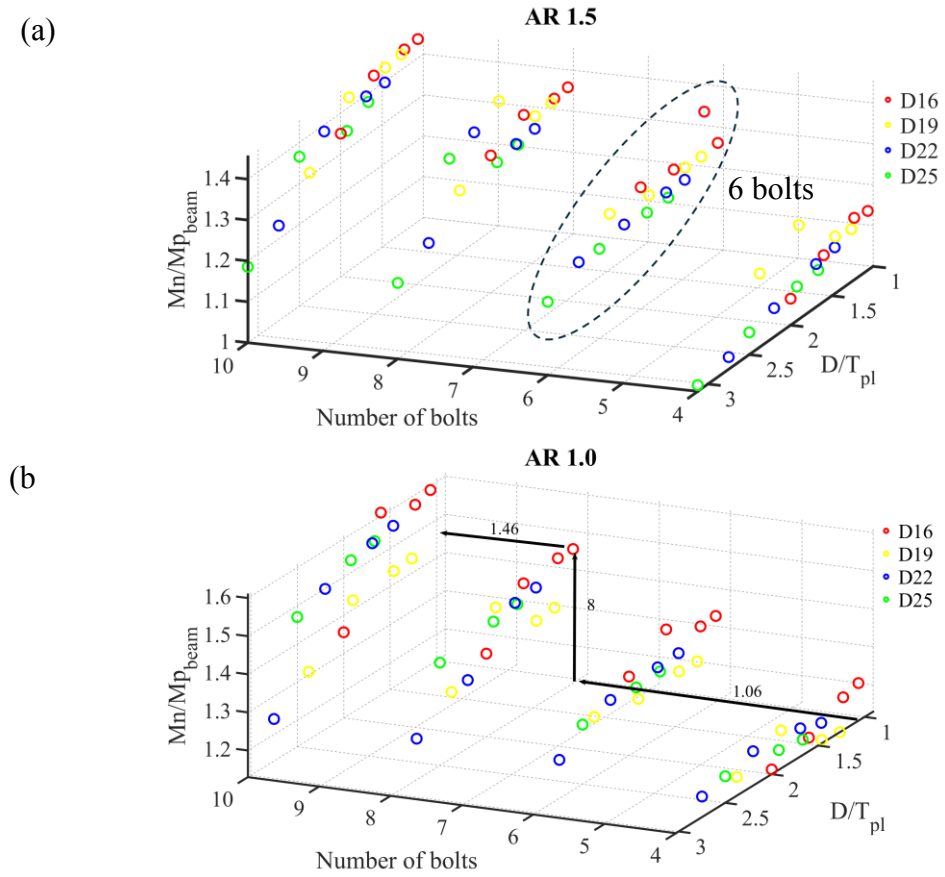

Fig. 3-14: Relation between the number of bolts and the ratios D/T_{pl}, and $M_n/M_{p\ beam}$ for two bolt arrangements: (a) AR1.5, and (b) AR1.0

3.6 Failure mode prediction charts

A total of 240 FEM and six test specimens (Elhadary et al. 2024b) were performed to cover the main design parameters, so it was crucial to summarize the failure modes to develop design charts. The failure mode charts are designed to help in predicting the failure mode of a connection by adjusting different design parameters. The connection's failure modes are categorized into five types: (1) bolt shear failure, (2) beam block shear failure, (3) rupture of the tensile extended plate, (4) local buckling of the beam and (5) local buckling of the column. The first three types are considered premature failures, occurring suddenly at lower values before reaching the maximum capacity of the connection at a value less than a plastic moment of the beam. On the other hand, the local buckling of the beam and column, helped the connection reach higher capacity; however,

it can affect the connection's integrity. To clarify, the failure mode should occur in the beam to adhere to the "strong column, weak beam" principle. These charts provide a streamlined way to achieve the desired connection strength and failure mode to achieve specified strength and failure modes by selecting the appropriate bolt diameter, number of bolts, and extended plate thickness without performing several iterations of full design analysis each time. Fig. 3-15 shows three failure mode charts for different bolt arrangements (AR1.5, AR1.0, AR0.6), where each chart contains subplots: the first subplot illustrates the relationship between the nominal moment of the connection and the plastic moment of the beam, with the number of bolts ranging from 4 to 10. The subsequent subplots, categorized by extended plate thickness (8 to 15 mm), show the relationship between the number of bolts and failure modes for different extended plate thicknesses. The design charts had certain constraints, such as maintaining constant column and beam cross-sections throughout the study. Specifically, the beam cross-section was HSS 152*152*6.4, and the column cross-section was HSS 152*152*9.54, based on the experimental specimens by Elhadary et al. (Elhadary et al. 2024b). The charts can be utilized for two main purposes: (i) to select the desired failure mode for the connection by determining the required combination of extended plate thickness, number of bolts, and bolt diameter, (ii) to select the required nominal connection moment and the available bolt diameter. Based on this selection, the required number of bolts can be determined. Then, by referring to the subplots, the failure mode can be determined based on the known number of bolts and the chosen extended plate thickness. Fig. 3-15.a. illustrates the first method on the failure mode charts, where the preferred failure mode of the joint can be chosen, such as the local buckling of the beam. This choice can be made from the lower subplots (i.e., highlighted in gray colour), considering the thickness of the extended plate equal to 10 mm. Subsequently, the number of bolts and their diameter (indicated by the dashed line) can be determined, which will be equal to 6 and 16 mm, respectively, necessary to achieve

the desired failure mode. Lastly, the upper graph can be used to accurately predict the ultimate moment of the joint based on that geometric combination.

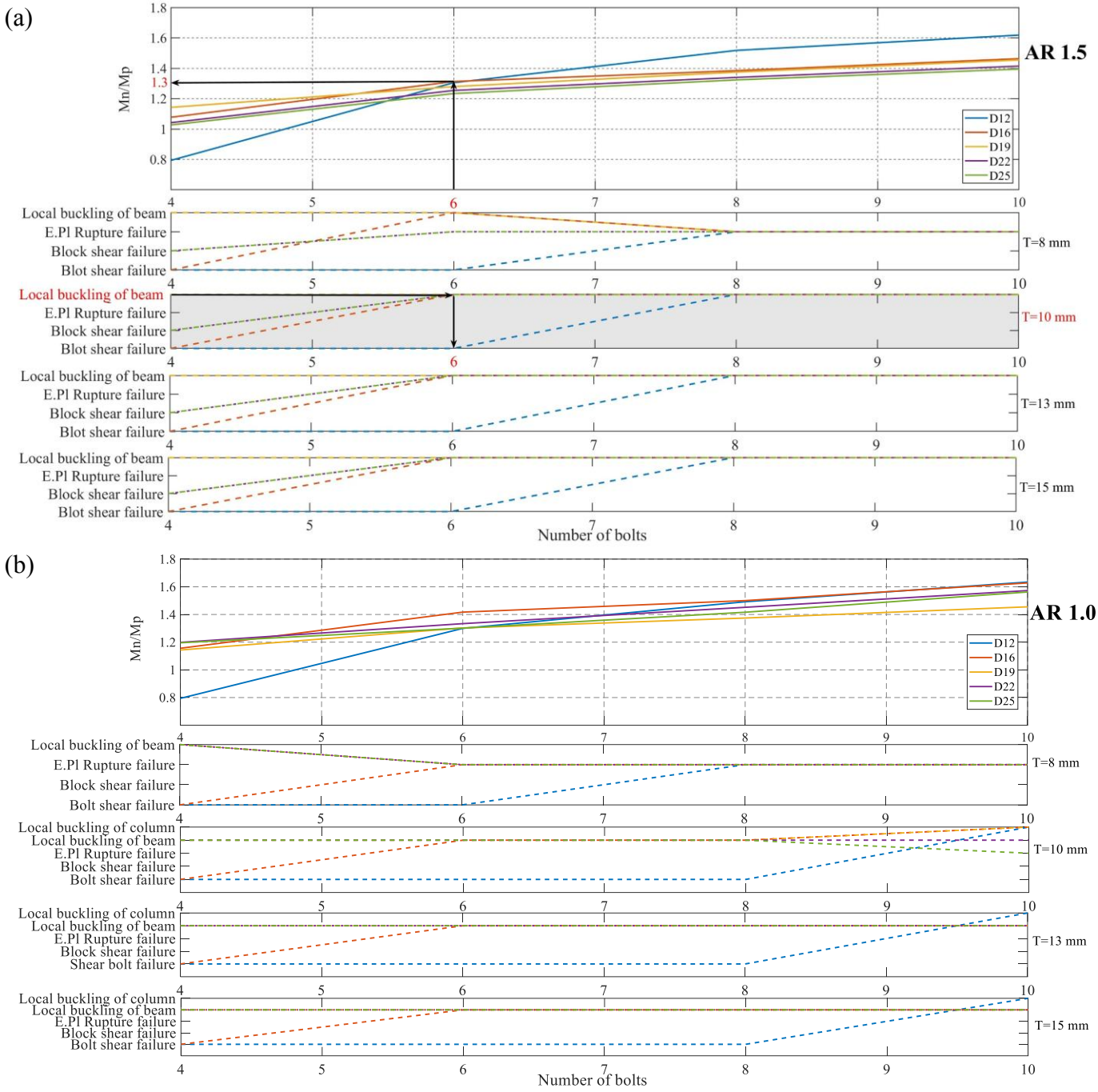

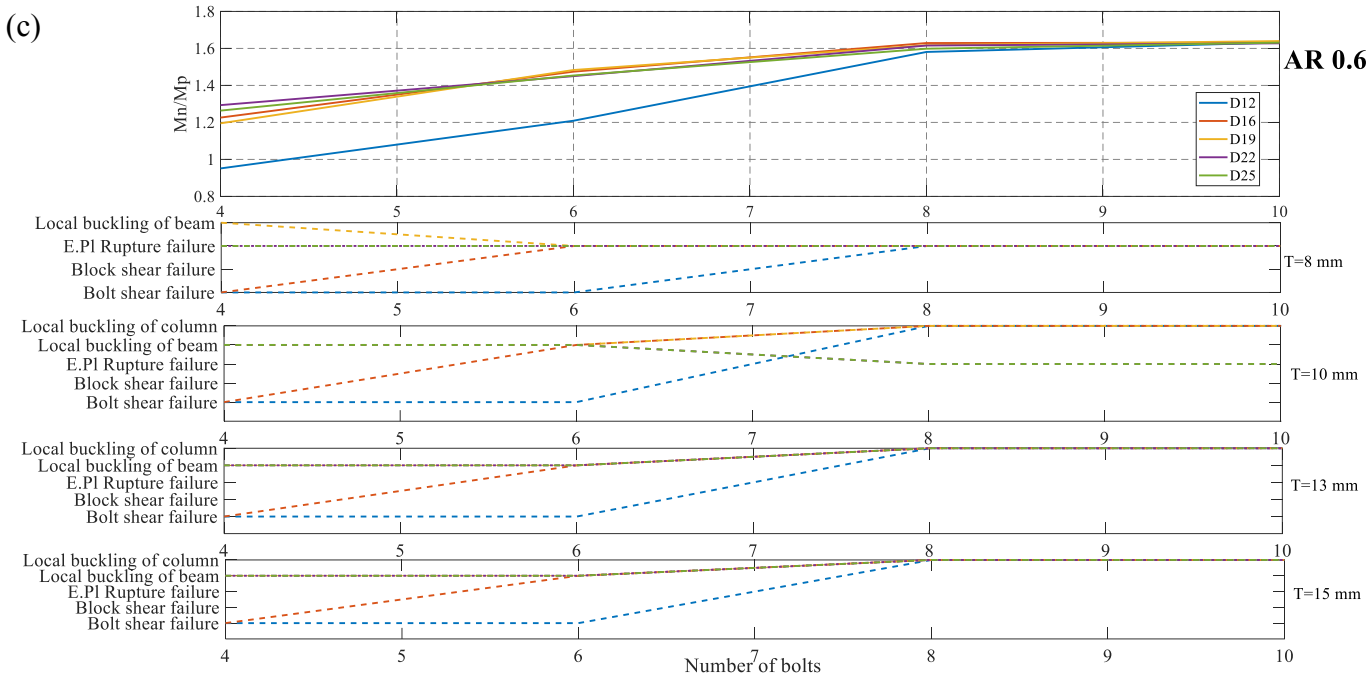

Fig. 3-15: Failure modes prediction charts for different bolt arrangement; (a) AR1.5; (b)AR1.0; and (c) AR0.6

3.7 Conclusions

This study studies the mechanical performance of the corner HSS-to-HSS connection for panelized modular houses in remote Indigenous regions. Two hundred and forty finite element models were developed for unstiffened extended plates to investigate the influence of different geometric parameters on ultimate moment capacity, rotation, failure modes, and ductility. The studied parameters showed that the bolt arrangement, number of bolts, extended plate thickness, and bolt diameter significantly influenced the connection capacity gain and failure mode. The following conclusion could be drawn from the above analysis:

- The FEM results were in good agreement with the experimental results, with an average error of less than 3%. It was found that the thickness of the extended plate had a different influence on the ductility and failure mode based on the configuration of the utilized bolt. It is recommended that the nominal force of the extended plate be equal to or greater than

1.2 times the plastic moment of the beam cross-section to eliminate the premature connection failure by rupture failure of the extended plate

- The utilization of AR1.5 and AR1.0 bolt arrangements is recommended, as these configurations enable the connection to reach its capacity through bolt bearing failure, thereby adhering to the "weak beam strong column" principle. The AR0.6 bolt configuration had an unfavourable effect on the loading mechanism of the connection, especially when 8 and 10 bolts were used, leading to column failure due to local buckling, which is indicative of a "weak column strong beam" scenario. This study emphasizes the critical role of bolt arrangement in maintaining the structural integrity and performance of connections.

- The number of bolts used significantly influences the distribution of bearing force and maximum capacity. It was noted that using four bolts with larger diameters (i.e., 22 mm and 25 mm) resulted in early failures, such as block shear failure in the beam during loading. Similarly, using four bolts with a diameter of 12 mm also led to premature bolt shear failure. When the number of bolts was increased to 8 or 10, particularly in AR0.6 and AR1.0 bolt arrangements, the failure was localized at the column, which is not a desirable failure. Six bolts are recommended for various bolt arrangements and bolt diameters of 16 mm or more. This strategy aligns with the "strong column weak beam" principle, which allows the plastic hinge to occur at the beam.

- It is recommended to maintain the ratio of bolt diameter to extended plate thickness below 2, which helps mitigate the onset of stress concentration and delay local buckling of the beam and bearing failure at the extended plate at an earlier stage.

- Design charts are proposed for different bolt arrangements that can predict failure modes by altering design parameters. The accuracy of the failure mode chart is validated with the tested specimens for the proposed connection.

3.8 Appendix

Table 3-3 summarizes the results of the 240 FEMs, detailing the ultimate and yielding moments along with their corresponding rotations, extracted from the moment-rotation curves. Additionally, the failure mode of each model is identified based on the geometric parameters used in the simulations.

Table 3-3: Summary of moment-rotation curve results for 240 FEMs

Specimen ID	Yielding moment (kN.m)	Ultimate moment (kN.m)	Rotation (rad)		Ductility index (φ_j)	Failure mode
			At yielding moment	At ultimate moment		
EP8-B4-AR1.5-D12.7	28.00	53.99	0.038	0.118	3.090	1- Bolt shear failure
EP10-B4-AR1.5-D12.7	24.72	55.92	0.028	0.118	4.293	1- Bolt shear failure
EP13-B4-AR1.5-D12.7	33.42	66.72	0.042	0.169	4.052	1- Bolt shear failure
EP15-B4-AR1.5-D12.7	31.76	68.85	0.038	0.200	5.328	1- Bolt shear failure
EP8-B6-AR1.5-D12.7	36.93	80.43	0.043	0.163	3.789	1- Bolt shear failure
EP10-B6-AR1.5-D12.7	35.49	90.29	0.042	0.207	4.963	1- Bolt shear failure and bolt bearing failure of the beam
EP13-B6-AR1.5-D12.7	37.37	90.17	0.041	0.183	4.451	1- Bolt shear failure and bolt bearing failure of the beam
EP15-B6-AR1.5-D12.7	40.84	88.76	0.042	0.166	3.995	1- Bolt shear failure and bolt bearing failure of the beam
EP8-B8-AR1.5-D12.7	35.39	91.57	0.041	0.147	3.624	1- Rupture failure of tensile extended plate
EP10-B8-AR1.5-D12.7	44.83	103.20	0.043	0.242	5.616	1- Local buckling and bearing failure of the beam
EP13-B8-AR1.5-D12.7	39.45	94.00	0.041	0.121	2.941	1- Local buckling and bearing failure of the beam
EP15-B8-AR1.5-D12.7	40.99	94.28	0.040	0.108	2.706	1- Local buckling and bearing failure of the beam
EP8-B10-AR1.5-D12.7	39.35	94.89	0.042	0.152	3.650	1- Rupture failure of tensile extended plate
EP10-B10-AR1.5-D12.7	43.07	98.96	0.043	0.143	3.291	1- Local buckling and bearing failure of the beam
EP13-B10-AR1.5-D12.7	45.41	99.70	0.041	0.111	2.681	1- Local buckling and bearing failure of the beam
EP15-B10-AR1.5-D12.7	50.32	110.05	0.042	0.262	6.303	1- Local buckling and bearing failure of the beam
EP8-B4-AR1.0-D12.7	26.01	53.99	0.035	0.124	3.492	1- Bolt shear failure
EP10-B4-AR1.0-D12.7	28.58	56.47	0.037	0.130	3.565	1- Bolt shear failure
EP13-B4-AR1.0-D12.7	31.36	59.66	0.038	0.113	2.971	1- Bolt shear failure
EP15-B4-AR1.0-D12.7	34.60	60.81	0.040	0.108	2.718	1- Bolt shear failure
EP8-B6-AR1.0-D12.7	41.28	73.92	0.045	0.095	2.096	1- Bolt shear failure and bolt bearing failure of the beam
EP10-B6-AR1.0-D12.7	42.25	78.02	0.044	0.169	3.804	1- Bolt shear failure and bolt bearing failure of the beam
EP13-B6-AR1.0-D12.7	45.07	88.33	0.044	0.145	3.304	1- Bolt shear failure and bolt bearing failure of the beam
EP15-B6-AR1.0-D12.7	43.85	88.37	0.042	0.133	3.149	1- Bolt shear failure and bolt bearing failure of the beam
EP8-B8-AR1.0-D12.7	39.82	94.67	0.044	0.180	4.089	1- Rupture failure of tensile extended plate
EP10-B8-AR1.0-D12.7	42.19	94.35	0.043	0.181	4.236	1- Bolt shear failure and bolt bearing failure of the beam
EP13-B8-AR1.0-D12.7	46.45	105.56	0.042	0.149	3.498	1- Bolt shear failure and bolt bearing failure of the beam

EP15-B8-AR1.0-D12.7	51.71	101.45	0.044	0.131	2.992	1- Bolt shear failure and bolt bearing failure of the beam
EP8-B10-AR1.0-D12.7	38.93	94.85	0.042	0.150	3.590	1- Rupture failure of tensile extended plate
EP10-B10-AR1.0-D12.7	44.47	110.65	0.041	0.272	6.567	1- Local buckling of compression flange of the column
EP13-B10-AR1.0-D12.7	50.65	111.12	0.043	0.272	6.391	1- Local buckling of compression flange of the column
EP15-B10-AR1.0-D12.7	49.46	107.40	0.042	0.237	5.691	1- Local buckling of compression flange of the column
EP8-B4-AR0.6-D12.7	30.28	64.68	0.052	0.154	2.953	1- Bolt shear failure
EP10-B4-AR0.6-D12.7	31.95	69.62	0.040	0.196	4.858	1- Bolt shear failure
EP13-B4-AR0.6-D12.7	31.35	72.25	0.038	0.192	5.101	1- Bolt shear failure
EP15-B4-AR0.6-D12.7	35.21	76.06	0.040	0.195	4.894	1- Bolt shear failure
EP8-B6-AR0.6-D12.7	35.25	82.21	0.040	0.146	3.684	1- Bolt shear failure
EP10-B6-AR0.6-D12.7	39.02	87.25	0.040	0.159	3.961	1- Bolt shear failure
EP13-B6-AR0.6-D12.7	43.25	89.35	0.042	0.145	3.430	1- Bolt shear failure
EP15-B6-AR0.6-D12.7	44.54	91.21	0.042	0.138	3.257	1- Bolt shear failure
EP8-B8-AR0.6-D12.7	35.94	82.21	0.040	0.146	3.684	1- Rupture failure of tensile extended plate
EP10-B8-AR0.6-D12.7	49.25	101.60	0.041	0.280	6.767	1- Local buckling of compression flange of column
EP13-B8-AR0.6-D12.7	50.93	107.50	0.045	0.243	5.409	1- Local buckling of compression flange of column
EP15-B8-AR0.6-D12.7	50.65	108.54	0.043	0.237	5.497	1- Local buckling of compression flange of column
EP8-B10-AR0.6-D12.7	38.24	82.90	0.040	0.146	3.684	1- Rupture failure of tensile extended plate
EP10-B10-AR0.6-D12.7	55.34	108.35	0.047	0.254	5.418	1- Local buckling of compression flange of column
EP13-B10-AR0.6-D12.7	61.38	110.94	0.047	0.264	5.618	1- Local buckling of compression flange of column
EP15-B10-AR0.6-D12.7	52.52	109.63	0.042	0.227	5.382	1- Local buckling of compression flange of column
EP8-B4-AR1.5-D16	45.93	73.27	0.048	0.200	4.150	1- Shear failure of bolts 2- Bolt bearing failure of the beam and extended plates
EP10-B4-AR1.5-D16	50.76	76.64	0.051	0.194	3.819	1- Shear failure of bolts 2- Bolt bearing failure of the beam
EP13-B4-AR1.5-D16	52.82	79.26	0.050	0.190	3.796	1- Shear failure of bolts 2- Bolt bearing failure of the beam
EP15-B4-AR1.5-D16	47.76	78.80	0.044	0.152	3.430	1- Shear failure of bolts 2- Bolt bearing failure of the beam
EP8-B6-AR1.5-D16	61.00	89.29	0.042	0.240	5.742	1- Local buckling and extensive bolt bearing failure of the beam.

						2- Bearing failure of the extended plates
EP10-B6-AR1.5-D16	64.69	88.31	0.055	0.239	4.322	1- Local buckling and extensive bolt bearing failure of the beam.
EP13-B6-AR1.5-D16	62.00	94.40	0.052	0.250	4.826	1- Local buckling and bearing failure of the beam
EP15-B6-AR1.5-D16	61.18	87.51	0.037	0.192	5.232	1- Local buckling and bearing failure of the beam
EP8-B8-AR1.5-D16	63.91	91.90	0.052	0.145	2.774	1- Rupture failure of tensile extended plate
EP10-B8-AR1.5-D16	68.50	94.78	0.057	0.232	4.077	1- Local buckling and bolt bearing failure of the beam
EP13-B8-AR1.5-D16	63.06	93.86	0.046	0.204	4.468	1- Local buckling and bolt bearing failure of the beam
EP15-B8-AR1.5-D16	65.59	94.13	0.048	0.201	4.203	1- Local buckling and bolt bearing failure of the beam
EP8-B10-AR1.5-D16	64.92	92.85	0.051	0.160	3.137	1- Rupture failure of tensile extended plate
EP10-B10-AR1.5-D16	62.66	98.66	0.047	0.221	4.702	1- Local buckling and bolt-bearing failure of the beam.
EP13-B10-AR1.5-D16	73.72	99.39	0.051	0.198	3.860	1- Local buckling and bolt-bearing failure of the beam.
EP15-B10-AR1.5-D16	76.98	99.51	0.052	0.192	3.730	1- Local buckling and bolt-bearing failure of the beam.
EP8-B4-AR1.0-D16	52.20	78.60	0.056	0.232	4.162	1- Shear failure of bolts 2- Bearing failure of the beam and extended plates
EP10-B4-AR1.0-D16	52.98	80.21	0.050	0.200	4.000	1- Shear failure of bolts 2- Bearing failure of the beam and extended plates
EP13-B4-AR1.0-D16	53.56	83.67	0.040	0.180	4.500	1- Shear failure of bolts 2- Bearing failure of the beam
EP15-B4-AR1.0-D16	49.48	84.54	0.044	0.161	3.643	1- Shear failure of bolts 2- Bearing failure of the beam and extended plates
EP8-B6-AR1.0-D16	60.61	91.99	0.053	0.172	3.219	1- Rupture failure of tensile extended plate
EP10-B6-AR1.0-D16	65.05	96.36	0.052	0.270	5.192	1- Local buckling and bolt-bearing failure of the beam.
EP13-B6-AR1.0-D16	66.76	93.09	0.052	0.227	4.340	1- Local buckling and bolt-bearing failure of the beam.
EP15-B6-AR1.0-D16	61.20	93.28	0.047	0.235	4.979	1- Local buckling and bolt-bearing failure of the beam.
EP8-B8-AR1.0-D16	67.46	92.75	0.053	0.120	2.276	1- Rupture failure of tensile extended plate
EP10-B8-AR1.0-D16	68.37	101.31	0.038	0.222	5.796	1- Local buckling and bolt-bearing failure of the beam.
EP13-B8-AR1.0-D16	69.69	102.02	0.037	0.211	5.657	1- Local buckling and bolt-bearing failure of the beam.
EP15-B8-AR1.0-D16	69.30	101.98	0.048	0.215	4.461	1- Local buckling and bolt-bearing failure of the beam.
EP8-B10-AR1.0-D16	63.18	93.23	0.048	0.153	3.168	1- Rupture failure of tensile extended plate

EP10-B10-AR1.0-D16	69.86	110.69	0.050	0.274	5.513	1- Local buckling of the column and the compression extended plate
EP13-B10-AR1.0-D16	73.21	108.30	0.039	0.300	7.772	1- Local buckling and bolt-bearing failure of the beam.
EP15-B10-AR1.0-D16	79.39	109.26	0.050	0.265	5.287	1- Local buckling and bolt-bearing failure of the beam.
EP8-B4-AR0.6-D16	49.20	79.60	0.060	0.230	3.833	1- Shear failure of bolts 2- Bearing failure of the beam
EP10-B4-AR0.6-D16	52.28	81.61	0.050	0.200	4.000	1- Shear failure of bolts 2- Bearing failure of the beam
EP13-B4-AR0.6-D16	54.76	83.37	0.040	0.180	4.500	1- Shear failure of bolts 2- Bearing failure of the beam
EP15-B4-AR0.6-D16	55.52	85.54	0.040	0.160	4.000	1- Shear failure of bolts 2- Bearing failure of the beam
EP8-B6-AR0.6-D16	59.78	91.93	0.052	0.200	3.817	1- Rupture failure of tensile extended plate
EP10-B6-AR0.6-D16	59.37	101.61	0.050	0.276	5.542	1- Local buckling and bolt bearing failure of the beam.
EP13-B6-AR0.6-D16	67.09	100.25	0.050	0.283	5.662	1- Local buckling and bolt bearing failure of the beam.
EP15-B6-AR0.6-D16	68.60	102.31	0.050	0.202	4.064	1- Local buckling and bolt bearing failure of the beam.
EP8-B8-AR0.6-D16	63.43	93.11	0.049	0.115	2.352	1- Rupture failure of tensile extended plate
EP10-B8-AR0.6-D16	68.04	110.78	0.036	0.268	7.363	1- Local buckling of compression flange of column and compression extended plate
EP13-B8-AR0.6-D16	76.24	110.11	0.038	0.263	6.939	1- Local buckling of compression flange of column
EP15-B8-AR0.6-D16	68.81	109.85	0.046	0.307	6.695	1- Local buckling of compression flange of column
EP8-B10-AR0.6-D16	68.41	93.38	0.049	0.145	2.941	1- Rupture failure of tensile extended plate
EP10-B10-AR0.6-D16	68.78	110.91	0.047	0.271	5.766	1- Local buckling of the column and compression extended plate
EP13-B10-AR0.6-D16	72.95	110.26	0.046	0.263	5.693	1- Local buckling of compression flange of column
EP15-B10-AR0.6-D16	76.94	111.42	0.046	0.295	6.399	1- Local buckling of compression flange of column
EP8-B4-AR1.5-D19	37.86	81.21	0.039	0.234	6.057	1- Bolt bearing failure of the beam
EP10-B4-AR1.5-D19	38.06	84.65	0.037	0.202	5.417	1- Local buckling and bolt bearing failure of the beam.
EP13-B4-AR1.5-D19	40.95	78.40	0.038	0.152	3.996	1- Local buckling and bolt bearing failure of the beam.
EP15-B4-AR1.5-D19	39.91	77.71	0.037	0.140	3.818	1- Local buckling and bolt bearing failure of the beam.
EP8-B6-AR1.5-D19	44.97	88.54	0.040	0.166	4.203	1- Local buckling and bolt bearing failure of the beam.
EP10-B6-AR1.5-D19	46.76	87.00	0.039	0.111	2.852	1- Local buckling and bolt bearing failure of the beam.

EP13-B6-AR1.5-D19	51.33	87.27	0.040	0.092	2.266	1- Local buckling and bolt bearing failure of the beam.
EP15-B6-AR1.5-D19	54.67	87.16	0.041	0.078	1.900	1- Local buckling and bolt bearing failure of the beam.
EP8-B8-AR1.5-D19	53.47	89.73	0.043	0.113	2.632	1- Rupture failure of tensile extended plate
EP10-B8-AR1.5-D19	56.89	100.07	0.042	0.115	2.759	1- Local buckling and bolt bearing failure of the beam.
EP13-B8-AR1.5-D19	57.25	93.18	0.041	0.081	1.964	1- Local buckling and bolt bearing failure of the beam.
EP15-B8-AR1.5-D19	58.96	93.48	0.041	0.080	1.951	1- Local buckling and bolt bearing failure of the beam.
EP8-B10-AR1.5-D19	57.91	89.97	0.046	0.103	2.259	1- Rupture failure of tensile extended plate
EP10-B10-AR1.5-D19	57.66	97.94	0.044	0.110	2.525	1- Local buckling and bolt bearing failure of the beam.
EP13-B10-AR1.5-D19	62.65	98.62	0.043	0.088	2.055	1- Local buckling and bolt bearing failure of the beam.
EP15-B10-AR1.5-D19	64.28	98.92	0.043	0.085	2.002	1- Local buckling and bolt bearing failure of the beam.
EP8-B4-AR1.0-D19	31.59	81.13	0.034	0.225	6.532	1- Bolt bearing failure of the beam
EP10-B4-AR1.0-D19	34.97	84.61	0.035	0.199	5.631	1- Bolt bearing failure and local buckling of the beam
EP13-B4-AR1.0-D19	34.53	78.37	0.034	0.155	4.602	1- Bolt bearing failure and local buckling of the beam
EP15-B4-AR1.0-D19	36.05	77.74	0.034	0.138	4.061	1- Bolt bearing failure and local buckling of the beam
EP8-B6-AR1.0-D19	46.66	88.59	0.041	0.165	4.068	1- Rupture failure of tensile extended plate
EP10-B6-AR1.0-D19	45.15	86.93	0.038	0.104	2.742	1- Bolt bearing failure and local buckling of the beam
EP13-B6-AR1.0-D19	47.90	87.34	0.038	0.089	2.329	1- Bolt bearing failure and local buckling of the beam
EP15-B6-AR1.0-D19	50.73	87.16	0.039	0.078	2.009	1- Bolt bearing failure and local buckling of the beam
EP8-B8-AR1.0-D19	48.18	89.71	0.040	0.110	2.758	1- Rupture failure of tensile extended plate
EP10-B8-AR1.0-D19	51.81	100.07	0.039	0.115	2.948	1- Bolt bearing failure and local buckling of the beam
EP13-B8-AR1.0-D19	52.83	93.11	0.039	0.080	2.061	1- Bolt bearing failure and local buckling of the beam
EP15-B8-AR1.0-D19	54.43	93.46	0.039	0.080	2.054	1- Bolt bearing failure and local buckling of the beam
EP8-B10-AR1.0-D19	48.83	89.97	0.040	0.102	2.545	1- Rupture failure of tensile extended plate
EP10-B10-AR1.0-D19	52.08	97.95	0.041	0.106	2.619	1- Local buckling of the compression flange of the column
EP13-B10-AR1.0-D19	55.33	98.71	0.039	0.093	2.394	1- Bolt bearing failure and local buckling of the beam
EP15-B10-AR1.0-D19	54.46	98.96	0.036	0.086	2.386	1- Bolt bearing failure and local buckling of the beam
EP8-B4-AR0.6-D19	30.72	81.26	0.034	0.241	7.126	1- Bolt bearing failure of the beam

EP10-B4-AR0.6-D19	33.99	84.66	0.035	0.206	5.977	1- Bolt bearing failure of the beam
EP13-B4-AR0.6-D19	38.89	90.27	0.035	0.173	4.865	1- Bearing failure and local buckling of the beam
EP15-B4-AR0.6-D19	40.33	89.08	0.035	0.161	4.544	1- Bearing failure and local buckling of the beam
EP8-B6-AR0.6-D19	33.84	89.86	0.034	0.114	3.375	1- Rupture failure of tensile extended plate
EP10-B6-AR0.6-D19	35.79	99.79	0.033	0.148	4.462	1- Bearing failure and local buckling of the beam
EP13-B6-AR0.6-D19	38.28	100.86	0.033	0.109	3.341	1- Bearing failure and local buckling of the beam
EP15-B6-AR0.6-D19	41.57	101.68	0.034	0.104	3.092	1- Bearing failure and local buckling of the beam
EP8-B8-AR0.6-D19	48.73	90.64	0.037	0.093	2.548	1- Rupture failure of tensile extended plate
EP10-B8-AR0.6-D19	45.33	110.06	0.028	0.257	9.172	1- Local buckling of compression flange of the column
EP13-B8-AR0.6-D19	49.19	109.98	0.027	0.258	9.550	1- Local buckling of compression flange of the column
EP15-B8-AR0.6-D19	55.99	111.06	0.036	0.180	5.036	1- Local buckling of compression flange of the column
EP8-B10-AR0.6-D19	48.99	90.75	0.035	0.090	2.585	1- Rupture failure of tensile extended plate
EP10-B10-AR0.6-D19	54.00	110.83	0.036	0.263	7.376	1- Local buckling of compression flange of the column
EP13-B10-AR0.6-D19	46.18	109.85	0.034	0.179	5.206	1- Local buckling of compression flange of the column
EP15-B10-AR0.6-D19	48.51	111.50	0.034	0.165	4.778	1- Local buckling of compression flange of the column
EP8-B4-AR1.5-D22	43.76	70.87	0.050	0.140	2.799	1- Block shear failure of the beam 2- Local buckling of compression extended plate
EP10-B4-AR1.5-D22	44.32	73.66	0.047	0.133	2.844	1- Block shear failure of the beam 2- Local buckling of compression extended plate
EP13-B4-AR1.5-D22	51.27	76.06	0.051	0.127	2.484	1- Block shear failure and local buckling of the beam
EP15-B4-AR1.5-D22	51.53	76.63	0.051	0.138	2.713	1- Block shear failure and local buckling of the beam
EP8-B6-AR1.5-D22	54.91	84.11	0.057	0.140	2.477	1- Rupture failure of tensile extended plate
EP10-B6-AR1.5-D22	55.08	85.00	0.054	0.135	2.501	1- Bearing failure and local buckling of the beam
EP13-B6-AR1.5-D22	56.41	85.37	0.052	0.107	2.074	1- Bearing failure and local buckling of the beam

EP15-B6-AR1.5-D22	55.69	85.27	0.050	0.098	1.975	1- Bearing failure and local buckling of the beam
EP8-B8-AR1.5-D22	55.47	84.60	0.056	0.111	1.973	1- Rupture failure of tensile extended plate
EP10-B8-AR1.5-D22	68.01	97.78	0.057	0.120	2.111	1- Bearing failure and local buckling of the beam
EP13-B8-AR1.5-D22	64.50	90.79	0.055	0.089	1.631	1- Bearing failure and local buckling of the beam
EP15-B8-AR1.5-D22	65.89	91.11	0.054	0.092	1.701	1- Bearing failure and local buckling of the beam
EP8-B10-AR1.5-D22	63.70	84.79	0.060	0.100	1.676	1- Rupture failure of tensile extended plate
EP10-B10-AR1.5-D22	66.31	95.19	0.057	0.106	1.870	1- Bearing failure and local buckling of the beam
EP13-B10-AR1.5-D22	68.52	96.06	0.055	0.095	1.731	1- Bearing failure and local buckling of the beam
EP15-B10-AR1.5-D22	69.77	96.17	0.054	0.088	1.623	1- Bearing failure and local buckling of the beam
EP8-B4-AR1.0-D22	46.99	81.47	0.052	0.206	3.991	1- Bearing failure of the beam
EP10-B4-AR1.0-D22	55.31	83.96	0.056	0.170	3.042	1- Bearing failure and local buckling of the beam
EP13-B4-AR1.0-D22	55.79	82.84	0.055	0.138	2.507	1- Bearing failure and local buckling of the beam
EP15-B4-AR1.0-D22	57.89	81.50	0.055	0.122	2.227	1- Bearing failure and local buckling of the beam
EP8-B6-AR1.0-D22	56.65	84.71	0.056	0.112	2.009	1- Rupture failure of tensile extended plate
EP10-B6-AR1.0-D22	65.42	89.84	0.059	0.105	1.777	1- Extensive Bearing failure of the outer row of bolts and local buckling of the beam
EP13-B6-AR1.0-D22	61.27	90.47	0.053	0.096	1.792	1- Extensive Bearing failure of the outer row of bolts and local buckling of the beam
EP15-B6-AR1.0-D22	64.24	90.70	0.054	0.090	1.676	1- Extensive Bearing failure of the outer row of bolts and local buckling of the beam
EP8-B8-AR1.0-D22	49.88	85.16	0.048	0.098	2.033	1- Rupture failure of tensile extended plate
EP10-B8-AR1.0-D22	60.50	90.04	0.056	0.106	1.878	1- Extensive Bearing failure of the outer row of bolts and local buckling of the beam
EP13-B8-AR1.0-D22	71.03	98.73	0.058	0.107	1.848	1- Extensive Bearing failure of the outer row of bolts and local buckling of the beam
EP15-B8-AR1.0-D22	72.34	99.16	0.057	0.103	1.806	1- Extensive Bearing failure of the outer row of bolts and local buckling of the beam
EP8-B10-AR1.0-D22	60.73	85.33	0.054	0.095	1.769	1- Rupture failure of tensile extended plate
EP10-B10-AR1.0-D22	59.19	103.13	0.051	0.192	3.765	1- Extensive Bearing failure of the outer row of bolts and local buckling of the beam

EP13-B10-AR1.0-D22	67.70	106.12	0.053	0.140	2.643	1- Extensive Bearing failure of the outer row of bolts and local buckling of the beam
EP15-B10-AR1.0-D22	71.78	106.94	0.054	0.136	2.524	1- Extensive Bearing failure of the outer row of bolts and local buckling of the beam
EP8-B4-AR0.6-D22	46.09	84.92	0.051	0.172	3.398	1- Rupture failure of tensile extended plate
EP10-B4-AR0.6-D22	52.88	88.75	0.054	0.166	3.068	1- Bearing failure and local buckling of the beam
EP13-B4-AR0.6-D22	54.48	87.95	0.056	0.153	2.747	1- Bearing failure and local buckling of the beam
EP15-B4-AR0.6-D22	59.02	87.43	0.054	0.146	2.684	1- Bearing failure and local buckling of the beam
EP8-B6-AR0.6-D22	59.33	84.99	0.057	0.104	1.819	1- Rupture failure of tensile extended plate
EP10-B6-AR0.6-D22	65.84	98.60	0.059	0.152	2.597	1- Bearing failure and local buckling of the beam
EP13-B6-AR0.6-D22	65.95	99.75	0.055	0.118	2.126	1- Bearing failure and local buckling of the beam
EP15-B6-AR0.6-D22	70.63	99.92	0.056	0.106	1.870	1- Bearing failure and local buckling of the beam
EP8-B8-AR0.6-D22	57.25	85.30	0.053	0.094	1.773	1- Rupture failure of tensile extended plate
EP10-B8-AR0.6-D22	66.08	103.54	0.055	0.181	3.281	1- Rupture failure of tensile extended plate
EP13-B8-AR0.6-D22	67.23	108.53	0.053	0.206	3.923	1-Local buckling of compression flange of column
EP15-B8-AR0.6-D22	68.94	109.86	0.052	0.208	4.007	1-Local buckling of compression flange of column
EP8-B10-AR0.6-D22	57.62	85.40	0.050	0.092	1.824	1- Rupture failure of tensile extended plate
EP10-B10-AR0.6-D22	68.21	103.81	0.054	0.173	3.205	1- Rupture failure of tensile extended plate
EP13-B10-AR0.6-D22	71.16	109.07	0.052	0.221	4.248	1- Local buckling of compression flange of column
EP15-B10-AR0.6-D22	74.85	110.67	0.052	0.185	3.547	1- Local buckling of compression flange of column
EP8-B4-AR1.5-D25	50.14	69.86	0.054	0.118	2.182	1- Block shear failure of the beam
EP10-B4-AR1.5-D25	65.04	72.55	0.056	0.105	1.869	1- Block shear failure of the beam
EP13-B4-AR1.5-D25	60.00	74.55	0.058	0.102	1.777	1- Block shear failure and local buckling of the beam
EP15-B4-AR1.5-D25	59.56	74.78	0.056	0.097	1.724	1- Block shear failure and local buckling of the beam
EP8-B6-AR1.5-D25	56.88	81.15	0.057	0.120	2.114	1- Rupture failure of tensile extended plate
EP10-B6-AR1.5-D25	60.51	83.88	0.056	0.102	1.813	1- Extensive Bearing failure of the outer row of bolts and local buckling of the beam
EP13-B6-AR1.5-D25	68.25	84.26	0.059	0.096	1.623	1- Extensive Bearing failure of the outer row of bolts and local buckling of the beam

EP15-B6-AR1.5-D25	68.13	84.25	0.057	0.088	1.529	1- Extensive Bearing failure of the outer row of bolts and local buckling of the beam
EP8-B8-AR1.5-D25	59.97	81.59	0.057	0.101	1.772	1- Rupture failure of tensile extended plate
EP10-B8-AR1.5-D25	69.65	96.32	0.057	0.110	1.932	1- Extensive Bearing failure of the outer row of bolts and local buckling of the beam
EP13-B8-AR1.5-D25	68.87	90.00	0.057	0.091	1.604	1- Extensive Bearing failure of the outer row of bolts and local buckling of the beam
EP15-B8-AR1.5-D25	71.64	90.41	0.057	0.088	1.546	1- Extensive Bearing failure of the outer row of bolts and local buckling of the beam
EP8-B10-AR1.5-D25	62.35	81.56	0.057	0.099	1.727	1- Rupture failure of tensile extended plate
EP10-B10-AR1.5-D25	69.74	93.91	0.059	0.107	1.829	1- Extensive Bearing failure of the outer row of bolts and local buckling of the beam
EP13-B10-AR1.5-D25	68.10	92.55	0.095	0.136	1.433	1- Extensive Bearing failure of the outer row of bolts and local buckling of the beam
EP15-B10-AR1.5-D25	61.09	94.86	0.038	0.086	2.232	1- Extensive Bearing failure of the outer row of bolts and local buckling of the beam
EP8-B4-AR1.0-D25	52.01	81.15	0.054	0.184	3.432	1- Bolt bearing failure of the beam
EP10-B4-AR1.0-D25	58.84	82.54	0.057	0.147	2.595	1- Bearing failure and local buckling of the beam
EP13-B4-AR1.0-D25	53.41	81.30	0.046	0.127	2.798	1- Bearing failure and local buckling of the beam
EP15-B4-AR1.0-D25	55.64	80.54	0.046	0.100	2.165	1- Bearing failure and local buckling of the beam
EP8-B6-AR1.0-D25	56.32	81.56	0.053	0.098	1.863	1- Rupture failure of tensile extended plate
EP10-B6-AR1.0-D25	62.56	88.49	0.054	0.091	1.677	1- Extensive Bearing failure of the outer row of bolts and local buckling of the beam
EP13-B6-AR1.0-D25	64.77	89.24	0.052	0.087	1.666	1- Extensive Bearing failure of the outer row of bolts and local buckling of the beam
EP15-B6-AR1.0-D25	67.99	89.46	0.053	0.083	1.567	1- Extensive Bearing failure of the outer row of bolts and local buckling of the beam
EP8-B8-AR1.0-D25	61.42	81.75	0.055	0.093	1.691	1- Rupture failure of tensile extended plate
EP10-B8-AR1.0-D25	64.16	96.30	0.054	0.111	2.065	1- Extensive Bearing failure of the outer row of bolts and local buckling of the beam
EP13-B8-AR1.0-D25	68.18	97.74	0.053	0.102	1.941	1- Extensive Bearing failure of the outer row of bolts and local buckling of the beam
EP15-B8-AR1.0-D25	71.41	98.23	0.055	0.099	1.812	1- Extensive Bearing failure of the outer row of bolts and local buckling of the beam

EP8-B10-AR1.0-D25	57.99	81.64	0.049	0.088	1.798	1- Rupture failure of tensile extended plate
EP10-B10-AR1.0-D25	68.24	101.15	0.053	0.153	2.861	1- Rupture failure of tensile extended plate
EP13-B10-AR1.0-D25	68.84	105.43	0.047	0.132	2.811	1- Bearing failure and local buckling of the beam
EP15-B10-AR1.0-D25	80.03	106.24	0.055	0.125	2.271	1- Bearing failure and local buckling of the beam
EP8-B4-AR0.6-D25	53.32	81.08	0.053	0.136	2.583	1- Rupture failure of tensile extended plate
EP10-B4-AR0.6-D25	59.73	86.47	0.055	0.150	2.713	1- Bearing failure and local buckling of beam
EP13-B4-AR0.6-D25	60.34	85.93	0.053	0.114	2.163	1- Bearing failure and local buckling of beam
EP15-B4-AR0.6-D25	57.67	86.20	0.047	0.100	2.141	1- Bearing failure and local buckling of beam
EP8-B6-AR0.6-D25	59.85	81.97	0.054	0.096	1.762	1- Rupture failure of tensile extended plate
EP10-B6-AR0.6-D25	68.31	97.56	0.057	0.131	2.313	1- Bearing failure and local buckling of the beam
EP13-B6-AR0.6-D25	66.77	98.84	0.052	0.106	2.029	1- Bearing failure and local buckling of the beam
EP15-B6-AR0.6-D25	66.71	99.04	0.050	0.099	1.974	1- Bearing failure and local buckling of the beam
EP8-B8-AR0.6-D25	59.61	82.04	0.050	0.087	1.727	1- Rupture failure of tensile extended plate
EP10-B8-AR0.6-D25	70.74	101.65	0.054	0.145	2.662	1- Rupture failure of tensile extended plate
EP13-B8-AR0.6-D25	70.96	108.69	0.051	0.183	3.606	1- Local buckling of compression flange of column
EP15-B8-AR0.6-D25	72.20	110.22	0.049	0.173	3.514	1- Local buckling of compression flange of column
EP8-B10-AR0.6-D25	63.32	82.17	0.050	0.086	1.704	1- Rupture failure of tensile extended plate
EP10-B10-AR0.6-D25	63.39	101.89	0.044	0.136	3.094	1- Rupture failure of tensile extended plate
EP13-B10-AR0.6-D25	71.37	109.31	0.046	0.186	4.088	1- Local buckling of compression flange of column
EP15-B10-AR0.6-D25	70.45	110.93	0.039	0.181	4.632	1- Local buckling of compression flange of column

3.9 References

American Institute of Steel Construction. 2021. “Fire protection.” Accessed October 1, 2024. https://www.aisc.org/why-steel/resources/fire-protection/.

ASTM. 2014. “A370: Standard test methods and definitions for mechanical testing of steel products.” ASTM Int., 1–50.

Bazarchi, E., A. Davaran, C. P. Lamarche, N. Roy, R. Gagné, and S. Parent. 2024. “Novel enhanced slip-resistant inter-modular connections with cementitious non-shrink grout: Experimental and numerical studies.” Structures, 66 (January): 106817. Elsevier Ltd. https://doi.org/10.1016/j.istruc.2024.106817.

Chen, Z., J. Liu, Y. Yu, C. Zhou, and R. Yan. 2017. “Experimental study of an innovative modular steel building connection.” J. Constr. Steel Res., 139: 69–82. Elsevier Ltd. https://doi.org/10.1016/j.jcsr.2017.09.008.

Choi, K.-S., H.-C. Lee, and H.-J. Kim. 2016. “Influence of analytical models on the seismic response of modular structures.” J. Korea Inst. Struct. Maint. Insp., 20 (2): 74–85.

Corfar, D.-A., and K. D. Tsavdaridis. 2022. “A comprehensive review and classification of inter-module connections for hot-rolled steel modular building systems.” J. Build. Eng., 50 (January): 104006. Elsevier Ltd.

Deng, E. F., J. B. Yan, Y. Ding, L. Zong, Z. X. Li, and X. M. Dai. 2017. “Analytical and numerical studies on steel columns with novel connections in modular construction.” Int. J. Steel Struct., 17 (4): 1613–1626.

Deng, E. F., L. Zong, Y. Ding, X. M. Dai, N. Lou, and Y. Chen. 2018. “Monotonic and cyclic response of bolted connections with welded cover plate for modular steel construction.” Eng. Struct., 167 (April): 407–419. Elsevier.

Digital Research Alliance of Canada. 2019.

Elhadary, M., A. Bediwy, and A. Elshaer. 2024a. “Experimental investigation on a novel steel connection for modular indigenous houses.” Can. Soc. Civ. Eng. 2024 Annu. Conf. Niagara Falls, Ontario.

Elhadary, M., A. Bediwy, and A. Elshaer. 2024b. “Novel steel connection for modular houses in indigenous communities: An experimental study.” J. Constr. Steel Res., 220: 108850. Elsevier. https://doi.org/10.1016/J.JCSR.2024.108850.

Elhadary, M., A. Bediwy, and A. Elshaer. 2025. “Structural performance of novel steel connection for indigenous modular houses.” Lect. Notes Civ. Eng., 253–266. Moncton, New Brunswick: Springer Singapore.

Elhadary, M., and A. Elshaer. 2021. “Behaviour of beam-column connection of modular steel buildings Keywords :” CSCE 2021 Annu. Conf. Whistler, British Columbia: Springer Singapore.

Fadden, M., S. M. Asce, J. Mccormick, and A. M. Asce. 2012. “Cyclic quasi-static testing of hollow structural section beam members.” 138 (May): 561–570. https://doi.org/10.1061/(ASCE)ST.1943-541X.0000506.

Fadden, M., and J. McCormick. 2013. “Evaluation of HSS-to-HSS moment connections for seismic applications.” Struct. Congr. 2013 Bridg. Your Passion with Your Prof. - Proc. 2013 Struct. Congr., 2334–2345. American Society of Civil Engineers. https://doi.org/10.1061/9780784412848.204.

Fadden, M., D. Wei, and J. McCormick. 2015. “Cyclic testing of welded HSS-to-HSS moment connections for seismic applications.” J. Struct. Eng., 141 (2): 1–14. https://doi.org/10.1061/(asce)st.1943-541x.0001049.

Gunawardena, T. 2016. “Behaviour of prefabricated modular buildings subjected to lateral loads.” The University of Melbourne Melbourne, Australia.

Hwan Doh, J., N. M. Ho, D. Miller, T. Peters, D. Carlson, and P. Lai. 2017. “Steel bracket connection on modular buildings.” J. Steel Struct. Constr., 02 (02). OMICS Publishing Group.

Korol, R. M., A. Ghobarah, and S. Mourad. 1993. “Blind bolting W-shape beams to HSS columns.” J. Struct. Eng., 119 (12): 3463–3481. https://doi.org/10.1061/(asce)0733-9445(1993)119:12(3463).

Lawson, R. M., J. Prewer, and P. J. Trebilcock. 1999. Modular construction using light steel framing. Steel Construction Institute.

Lee, S., J. Park, E. Kwak, S. Shon, C. Kang, and H. Choi. 2017. “Verification of the seismic performance of a rigidly connected modular system depending on the shape and size of the ceiling bracket.” Materials (Basel)., 10 (3).

Liu, X. C., F. Y. Cui, X. X. Zhan, C. Yu, and Z. Q. Jiang. 2019. “Seismic performance of bolted connection of H-beam to HSS-column with web end-plate.” J. Constr. Steel Res., 156: 167–181. Elsevier Ltd. https://doi.org/10.1016/j.jcsr.2019.01.024.

Liu, X. C., Y. Wang, X. X. Cui, C. Yu, and Z. X. Bai. 2020. “Seismic performance of bolted beam-to-column connection with rib-stiffened splicing plate.” J. Constr. Steel Res., 174: 106300. Elsevier Ltd. https://doi.org/10.1016/j.jcsr.2020.106300.

Liu, X. C., Z. W. Yang, H. X. Wang, A. L. Zhang, S. H. Pu, S. T. Chai, and L. Wu. 2017. "Seismic performance of H-section beam to HSS column connection in prefabricated structures." J. Constr. Steel Res., 138 (June): 1–16. https://doi.org/10.1016/j.jcsr.2017.06.029.

Livermore software technology corporation (LSTC). 2007. Livermore software technology corporation (LSTC). (2007). LS-DYNA keyword user's manual, Vol. 1, Livemore, California, USA, R13.0.

Ma, R., J. Xia, H. Chang, B. Xu, and L. Zhang. 2021. "Experimental and numerical investigation of mechanical properties on novel modular connections with superimposed beams." Eng. Struct., 232. Elsevier Ltd.

Modular construction reports & industry analysis. 2023.

Rajanayagam, H., K. Pologanathan, P. Gatheeshgar, G. E. Varelis, P. Sherlock, B. Nagaratnam, and P. Hackney. 2021. "A-state-of-the-art review on modular building connections." Structures, 34 (July): 1903–1922. Elsevier Ltd. https://doi.org/10.1016/j.istruc.2021.08.114.

Rice, J. 2017. "Making solid, sustainable choices with cold-formed steel framing." Accessed October 1, 2024. https://www.constructioncanada.net/making-solid-sustainable-choices-with-cold-formed-steel-framing/.

Steel Framing Industry Association (SFIA). 2024. "How does cold-formed steel compare to cast-in-place concrete?" Accessed October 1, 2024. https://buildsteel.org/why-steel/cold-formed-steel-101/cold-formed-steel-compares-cast-place-concrete-4-key-areas/.

United Nations. 2019. "Adequate housing as a component of the right to an adequate standard of living, and the right to non-discrimination in this context."

Wang, H., X. Zhao, and G. Ma. 2022a. "Experimental study on seismic performance of column-column-beam joint in panelised steel-modular structure." J. Constr. Steel Res., 192 (October 2021): 107240. Elsevier Ltd. https://doi.org/10.1016/j.jcsr.2022.107240.

Wang, H., X. Zhao, and G. Ma. 2022b. "Novel coupled modular steel structure and seismic tests on high-performance interconnection." J. Constr. Steel Res., 189 (November 2021): 107058. Elsevier Ltd. https://doi.org/10.1016/j.jcsr.2021.107058.

Xu, B., J. Xia, H. Chang, R. Ma, and L. Zhang. 2020. "Flexural behaviour of pairs of laminated unequal channel beams with different interfacial connections in corner-supported modular steel buildings." Thin-Walled Struct., 154 (April).

Yu, Y., and Z. Chen. 2018. "Rigidity of corrugated plate sidewalls and its effect on the modular structural design." Eng. Struct., 175 (April): 191–200. Elsevier. https://doi.org/10.1016/j.engstruct.2018.08.039.

Zhan, X. X., X. C. Liu, S. Feng, and C. Yu. 2021. “Seismic performance of a square HSS column to H-section beam bolted connection with double cover plate.” Eng. Struct., 231 (December 2020): 111729. Elsevier Ltd. https://doi.org/10.1016/j.engstruct.2020.111729.

Zhang, Y. J., L. Zhang, Y. F. Chen, G. S. Tong, and Y. C. Wang. 2024. “Tensile behavior of novel column-to-column connection for modular steel construction using high-strength bolts.” Structures, 65 (January): 106759. Elsevier Ltd. https://doi.org/10.1016/j.istruc.2024.106759.

Zhong, C. jun, Y. qi Huang, H. yang Li, Z. wei Yang, R. qiang Feng, and F. Aslani. 2024. “Experimental and numerical simulation study of mechanical properties of inner sleeve T-joint in modular gymnasia.” Thin-Walled Struct., 195 (June 2023): 111446. Elsevier Ltd. https://doi.org/10.1016/j.tws.2023.111446.

CHAPTER 4: MACHINE LEARNING-BASED PREDICTION OF THE STRUCTURAL PERFORMANCE OF A LONG-BOLTED STEEL CONNECTION

4.1 Introduction

The application of supervised Machine Learning techniques has enabled the detection of non-linear and multivariate complex behaviours over the last few years. Machine learning serves as a fundamental artificial intelligence tool that supports data-driven predictive methods. The method enables independent learning from the given databases to establish relationships between inputs and outputs that have multiple variables. The application of machine learning techniques has expanded its use into multiple areas of structural engineering to provide innovative solutions for modelling structural dynamics, designing optimizations and seismic demand evaluations. In the field of steel structures, various machine-learning models have been developed to accurately predict the ultimate loading capacity and buckling modes of steel tubular columns, I-section beam columns, and cold-formed steel built-up I-section columns (Hu et al., 2025; Lu et al., 2024; Rabi et al., 2023; Su et al., 2024; Xu et al., 2021a, 2021b). Machine learning was also applied to predict the shear strength of corrugated steel web girders, utilizing four algorithms, with the XGBoost model showing the best performance (Liu et al., 2025). Abarkan et al. (2024) used machine learning to optimize the design of circular hollow section stainless steel stub columns, comparing the results with Eurocode 3 predictions, thus enhancing design accuracy and efficiency. Chen et al. (2024) employed artificial neural networks to develop a model predicting the displacement of steel beams with hexagonal web openings under impact loading, contributing to a better understanding and safety assessments for impact-resistant designs. Asgarkhani et al. (2024) applied machine learning to predict the seismic response and performance of steel buckling-

restrained braced frames, providing valuable insights into their behaviour under seismic loading. Zhang et al. (2024) used soft computing methods to predict the axial strength of concrete-filled double-skin steel tube columns, contributing to the efficient design of these complex composite structures.

In optimization and structural design, a novel machine learning approach combines a new shape-finding concept with backpropagation and particle swarm optimization neural networks for optimizing the structural design of tree-like structures. This innovative method enhances the design process's efficiency and effectiveness by accurately locating the load-bearing center of each shape-finding unit (Du et al., 2022). Das et al. (2024) applied deep learning for multi-objective optimization of cross-laminated timber walls, aiming at improving the design of sustainable timber buildings. In seismic engineering, different improved machine learning algorithms have been employed to predict the seismic demands of steel moment-resisting frames (MRFs) by focusing on maximum inter-story and residual inter-story drift ratio; these methods have achieved high prediction accuracy exceeding 95% (Asgarkhani et al., 2023). Furthermore, when predicting the seismic limit-state capacities of steel MRFs, incorporating Soil-Structure Interaction effects has been a critical advancement. Machine learning algorithms have shown high prediction accuracy while reducing the complexity and computational cost of modelling these capacities (Kazemi and Jankowski, 2023). Nguyen et al. (2023) utilized machine learning models for seismic fragility analysis of steel moment frames, achieving high prediction accuracy for inter-story drift ratios. For predicting the structural dynamics of concrete beams, Li et al. (2025) developed a multi-fidelity neural network model for predicting load-moment interactions in concrete-filled steel tube columns, improving the accuracy of structural behaviour predictions. Lai et al. (2024) employed probabilistic machine learning models to predict the maximum displacements of concrete-filled

steel tubular columns under impact, advancing safety measures for structural systems under lateral impacts. Additionally, Chen et al. (2023) developed a predictive method for the ultimate bearing capacity of PBL systems, incorporating sensitivity analysis to improve design predictability and structural stability.

The effectiveness of machine learning in predicting structural performance is particularly relevant in the context of modular construction, which has emerged as a promising solution to address Canada's ongoing housing crisis, particularly in remote and northern communities. Canada is currently experiencing severe housing shortages, with rising homelessness rates, particularly in underserved regions where construction faces significant challenges such as material transportation, extreme climatic conditions, and logistical constraints (Elhadary et al., 2025, 2024b; United Nations, 2019). Modular construction offers an efficient and cost-effective alternative to traditional building methods, utilizing standardized prefabricated modules that are transported and assembled on-site. This approach has been widely adopted in Nordic countries such as Finland, Norway, and Sweden, where approximately 45% of residential properties are built using modular techniques (Modular construction reports & industry analysis, 2023). Modular construction can be classified into two primary categories: the 2D panelized system and the 3D volumetric system. The 2D panelized system involves the off-site fabrication of structural panels, which are then transported and assembled on-site. This system offers significant advantages over the 3D volumetric approach, including reduced transportation costs, increased flexibility, and minimized material waste (Lawson et al., 1999). Due to its superior adaptability and cost-effectiveness, the 2D panelized system has become the preferred choice for modular construction. The structural framework of 2D panelized steel modular systems typically consists of column modules and beam-floor modules, interconnected through beam-column joints. Cold-formed steel

is often utilized in these structures due to its non-combustibility, resistance to deterioration, and lightweight properties, resulting in significant transportation cost savings compared to traditional concrete structures. For 2D panelized steel modular structures, various studies have proposed bolted beam-column connections to facilitate on-site assembly and prevent transportation-induced damage. Liu et al. (2019) introduced a fully bolted joint that connects lower and upper box columns through bolted flanges and integrates H-shaped beams using extended cover plates and endplates. Further improvements were made by Liu et al. (2020), who incorporated trapezoidal stiffeners to enhance seismic performance. Studies by (Fadden et al., 2015, 2012; Fadden and McCormick, 2013) investigated welded and reinforced HSS-to-HSS connections under seismic loading, revealing that reinforcement plate thickness significantly influences connection stiffness and inelastic rotation. Other research has explored bolted configurations utilizing gusset plates, Tee plates, and extended endplates to enhance structural integrity (Akbari Hamed and Charkhtab Basim, 2020; N Kosteski and Packer, 2003; N. Kosteski and Packer, 2003; Park et al., 2021). Elhadary et al. (2024) recently proposed a bolted HSS-to-HSS connection for modular housing applications, conducting experimental studies to evaluate the effects of bolt configuration, plate thickness, and extended endplates on joint stiffness and moment capacity. However, predicting the performance of such connections remains challenging due to the interaction of multiple components, complex stress distributions, and nonlinear geometric and material behaviours. Traditional finite element analysis (FEA) methods provide detailed insights but are computationally intensive and require extensive experimental validation.

This study aims to address this gap by utilizing machine learning techniques to predict the ultimate capacity and failure modes of HSS modular connections. A validated FEM was used to generate an extensive dataset comprising 240 FEMs to train and validate machine learning models,

including regression and classification algorithms. Furthermore, genetic symbolic regression was employed to develop mathematical formulas for predicting the ultimate moment capacity, enhancing the interpretability and practicality of the proposed models. The performance of these predictive models was assessed by comparing their results against experimental and FEMs using statistical evaluation metrics. By integrating machine learning with FEA, this study seeks to provide a robust and efficient approach for optimizing modular steel connection design, contributing to the advancement of resilient and cost-effective housing solutions

4.2 Methodology

The current study employed a four-stage approach, as shown in Fig. 4-1. In Stage 1, a comprehensive dataset was generated with a wide range of design parameters such as extended plate thickness, number of bolts, bolt arrangement, and bolt diameter. This dataset was created using a FEM, which was validated against experimental results conducted by (Elhadary et al. 2024b). The database will be divided randomly into 70% for training, 15% for validation, and 15% for testing. In Stage 2, machine learning models were used to predict the failure mode and the corresponding ultimate capacity, including decision trees and bagged and boosted tree ensembles. The accuracy of these models was assessed using regression and classification metrics, such as the coefficient of determination and confusion matrix evaluation. Stage 3 involved using artificial neural networks to explore various capacities for predicting the ultimate capacity of the connections. Finally, stage 4 focused on developing mathematical formulas using genetic symbolic regression to predict the capacity of long bolt HSS-to-HSS connections. The accuracy of this equation was evaluated using the Pearson correlation coefficient (R) for both trained and tested models.

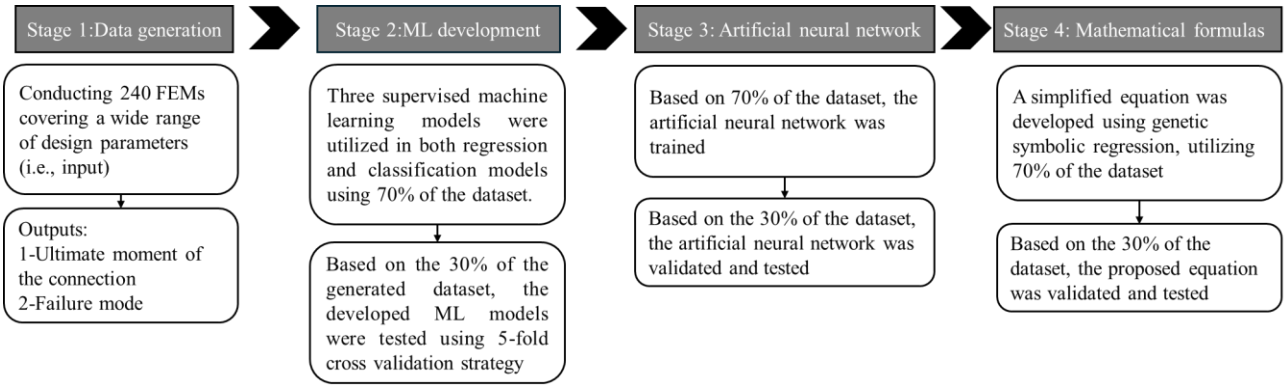

Fig. 4-1: HSS bolted connection performance prediction methodology

4.2.1 Validation of FEM

A 3D FEM of a modular beam-to-column connection was developed using LS-DYNA software (Livermore software technology corporation (LSTC) 2007) and validated with the experimental results conducted by (Elhadary et al. 2024b) to enable reliable numerical predictions. The Finite Element (FE) simulations were executed on the Digital Research Alliance of Canada (Digital Research Alliance of Canada 2021) (i.e., SHARCNET). Each simulation required an average duration of 48 hours to achieve the designated termination point, encompassing 760 computational time steps. The tested specimens' main design parameters and material properties are shown in Table 4-1 and Table 4-2. The steel's elastic-plastic and hardening behaviours were modelled using a material model named mat-piecewise-linear-plasticity. Fig. 4-2 describes the boundary conditions applied on the FEM aligned with the experimental test conditions, where the column was restrained by fixed support, the beam was laterally restrained in the X-direction, and the prescribed motion in the Y-direction was applied on the bracket plate of dimension 340×170 mm, with a moment lever arm of 1080 mm. The contacts between connection components (i.e., Frictional components) were modelled using surface-to-surface-Mortar contact. The penalty formulation with a friction coefficient of 0.3 (i.e., represents the surface hardening by sandblasting) is defined by all the tangential responses for all contact surfaces. The contacts between two

extended plates with columns (i.e., welded components) were modelled using surface-to-surface-mortar-tied contact. An eight-node 3D solid element with reduced integration was selected for meshing. A mesh sensitivity study was conducted, and the result was 390000 solid elements, as shown in Fig. 3-4. Inflation layers were used around the bolt holes to capture the distribution of stresses better. A cold-formed steel (CFS) beam was discretized using a fine mesh of 4 mm, and seven layers of smaller mesh were used to model profile thickness. The bolt clearance of 2 mm was modelled to capture the actual bolt behaviour mechanism, releasing the bolt pretension load resulting from snug tightening. All models were incorporated with non-linear material properties, non-linear time step analysis (i.e., implicit analysis), large deformation, and full Newton-Raphson with a modified arch length method. The explanation of the specimen IDs is comprehensively detailed in section 2.2. (development of training database).

Table 4-1: Main design parameters of the test specimens (Elhadary et al. 2024b).

Specimen ID	Extended Plate Thickness (mm)	Number of Bolts	Bolt Arrangement (Pn/Pp)	Stiffener
EP13-B6-AR1.5	13	6	1.5	no
EP10-B6-AR1.5	10	6	1.5	no
EP10-B6-AR1.0	10	6	1	no
EP13-B8-AR1.5	13	8	1.5	no
EP13-B6-AR1.5-ST	13	6	1.5	yes
EP10-B8-AR1.5	10	8	1.5	no

Table 4-2: Material properties of the tested specimens

Profile	Material Grade	Yielding Stress F_y (MPa)	Yielding Elongation ε_y (%)	Ultimate Stress F_u (MPa)	Ultimate Elongation ε_u (%)	Elasticity Modulus E (GPa)
Column	350W	366	0.18	465	15.3	204
Beam	350W	364	0.18	462	14.9	203
Extended plate	350W	367	0.18	470	15.5	204
High-strength bolts	A325	560	0.27	825	11.2	207

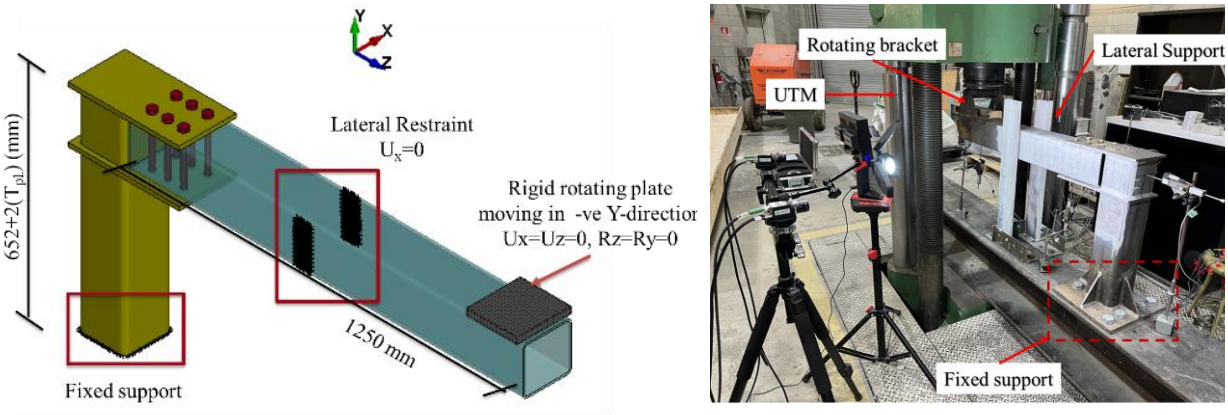

Fig. 4-2: Boundary conditions of the proposed FEM and tested specimens

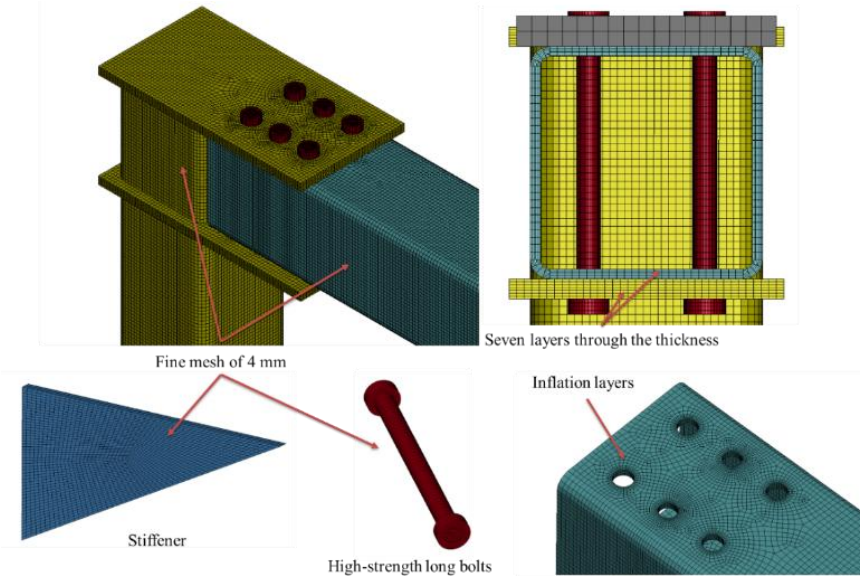

Fig. 4-3: Mesh Configuration of the proposed FEM

To validate the FEM, the numerical predicated moment-rotation curve was validated against test results conducted by (Elhadary et al. 2024a; b). Fig. 4-4 presents the comparison between the moment-rotation curves obtained from the experiment test and the proposed FEM for six specimens, where the moment was determined by multiplying the force extracted from the load cell by the distance of the load point to the column face (1080 mm), whereas the connection rotation was calculated by subtracting the column rotation from the beam rotation. The FEM predictions are in excellent agreement with corresponding specimens from the experimental

program, with an average error of 3%, as shown in Table 4-3. The FEM successfully captured the impact of bolt clearance during the loading process, which was identified as a rotational horizontal displacement without a substantial increase in connection capacity. Fig. 4-5 presents a sample of the failure model derived from the proposed FEM and the corresponding specimens incorporated within the experimental program.

Table 4-3: Comparison between experimental and FEM results

Specimen ID	Mode of Failure	Experimental Ultimate moment (kN.m)	FEM Ultimate moment (kN.m)	FEM/EXP
EP13-B6-AR1.5	Local buckling and block shear failure at the beam.	96.3	94.4	0.98
EP10-B6-AR1.5	Local buckling and block shear failure at the beam.	90.2	88.3	0.98
EP10-B6-AR1.0	Local buckling and bolt bearing failure at the beam	97.1	96.6	0.99
EP13-B8-AR1.5	Local buckling and bolt bearing failure at the beam	93.8	94.03	1.01
EP13-B6-AR1.5-ST	Local buckling and bolt bearing failure at the beam	87.1	86.2	0.99
EP10-B8-AR1.5	Local buckling and bolt bearing failure at the beam	97.8	95.03	0.97

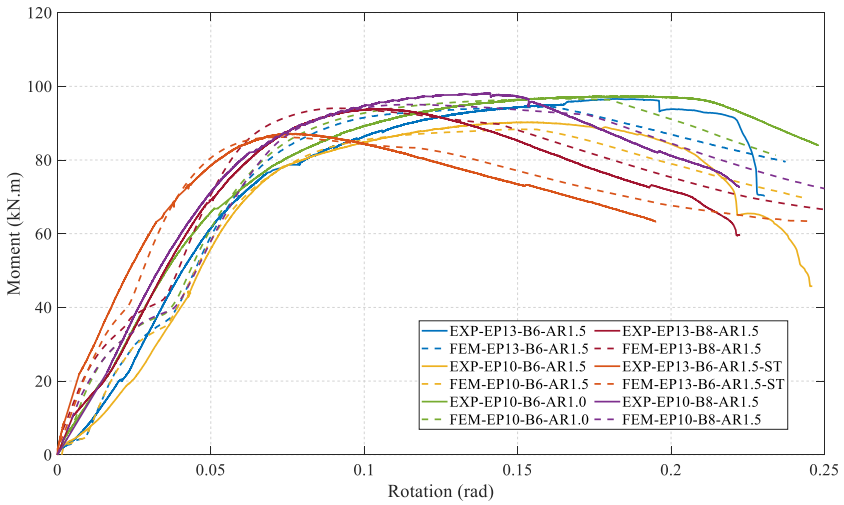

Fig. 4-4: Comparison between the moment-rotation curve of the test specimens and the proposed FEM

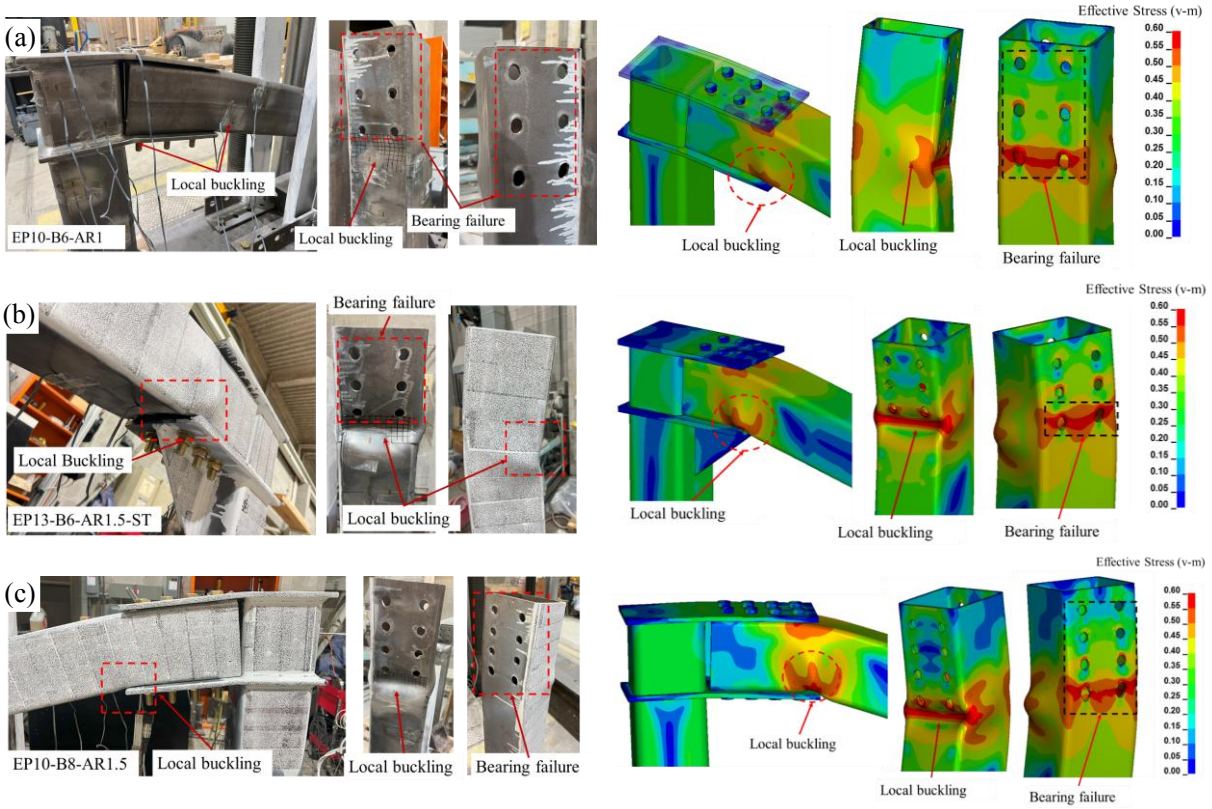

Fig. 4-5: Comparison between the proposed FEM and experimental results for three specimens: (a) EP10-B6-AR1.0, (b) EP13-B6-AR1.5-ST, and (c) EP10-B8-AR1.5.

4.2.2 Development of training database

Upon validating the FEM, a comprehensive parametric analysis was conducted involving 240 FEM covering a wide range of design parameters such as extended plate thickness, number of bolts, bolt arrangement, and bolt diameter. The interplay of these parameters is visually represented in Fig. 4-6. The specimens were coded as follows: the thickness of the extended plate (EP), the number of bolts (B), the bolt arrangement (AR) and the bolt diameter (D). For example, in EP13-B6-AR1.5-D19, where EP13 refers to an extended plate of 13 mm in thickness, B6 indicates the number of bolts to be 6, the symbol AR1.5 represents the ratio P_n/P_p to have a value of 1.5, and D19 refers to the bolt diameter of 19 mm. Utilizing the results extracted from the 240 models, the Pearson correlation coefficients (R) among all the input variables (i.e., extended plate

thickness, bolt arrangement, bolt diameter, and the number of bolts) and the target feature (i.e., ultimate capacity of the connection) were determined using Eq. 4-1. Where n is the number of data points, and (x) and (y) are the individual data points. The calculated correlation coefficients are organized in a correlation matrix, as shown in Fig. 4-7. The coefficient ranges from -1.0 to 1.0, where 1.0 and -1.0 indicate a perfect positive and negative linear relationship. It can be noticed from Fig. 4-7 that (i) none of the calculated correlation coefficients are equal to 1.0, indicating independence among the features, and (ii) the calculated correlation coefficients between the target feature (i.e. ultimate moment) and all the input variables are non-zero, indicating the importance of all input variables and, thus, the necessity of including input variables in the predictive models. Therefore, regression models would be developed based on the datasets, including merely input variables.

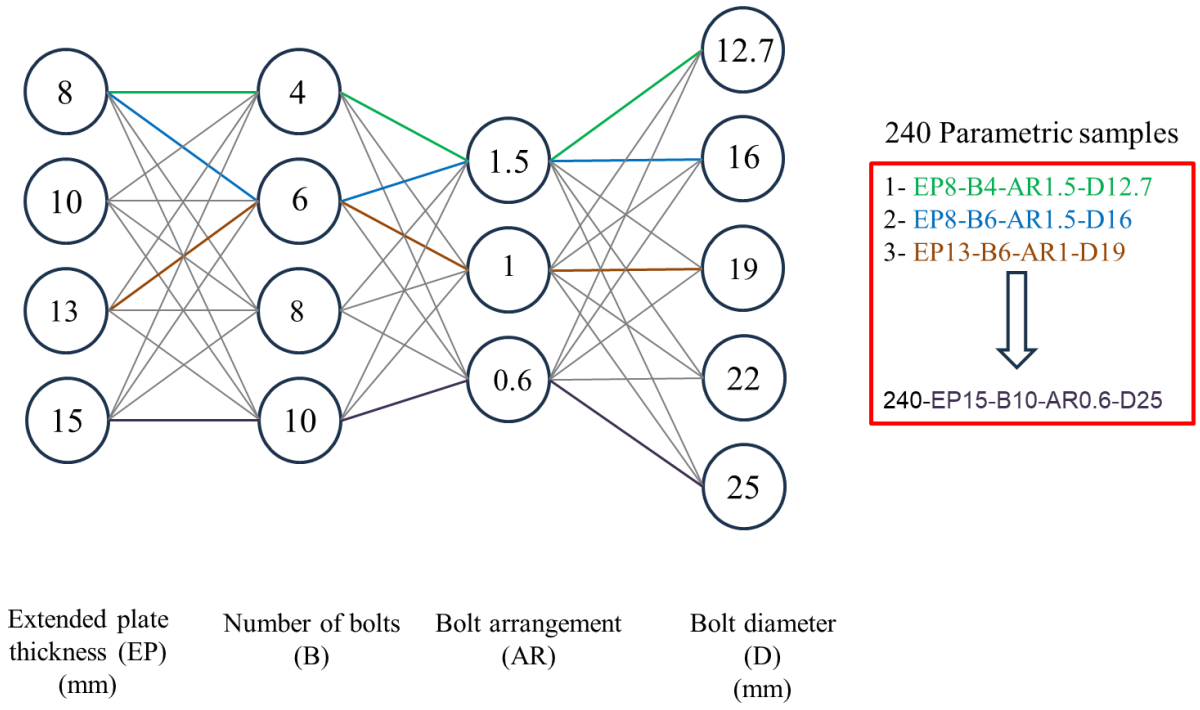

Fig. 4-6: A visual representation of the interplay between various parameters to generate 240 models

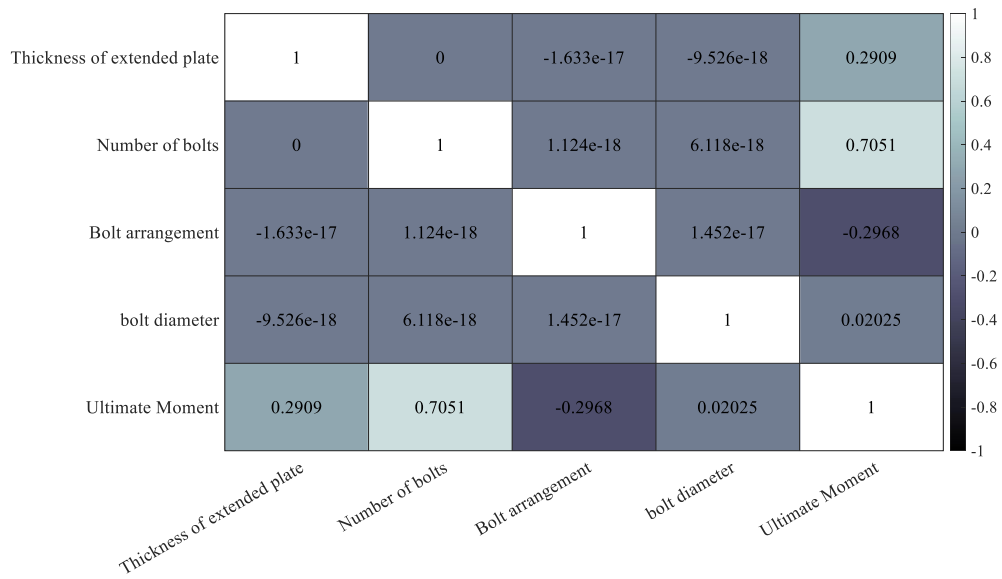

Fig. 4-7: Correlation matrix between inputs and output

$$R = \frac{n(\sum xy) - (\sum x)(\sum y)}{\sqrt{[n\sum x^2 - (\sum x)^2][n\sum y^2 - (\sum y)^2]}} \quad \text{Eq. 4-1}$$

4.3 Development of machine learning models

4.3.1 Decision tree and ensemble learning algorithms

Regression models and classification learning models were employed through machine learning to predict the ultimate moment and failure modes of the HSS connection. The proposed procedures for developing machine learning models are presented in a flow chart, as shown in Fig. 4-8. The database was split into training, validation and testing sets of 70%, 15%, and 15%, respectively. Three machine learning algorithms, including Decision tree (DT), Boosted trees, and Bagged trees, were used to develop the predictive machine learning models based on the train set data. Based on the test set data, the evaluation of machine learning model performance was conducted.

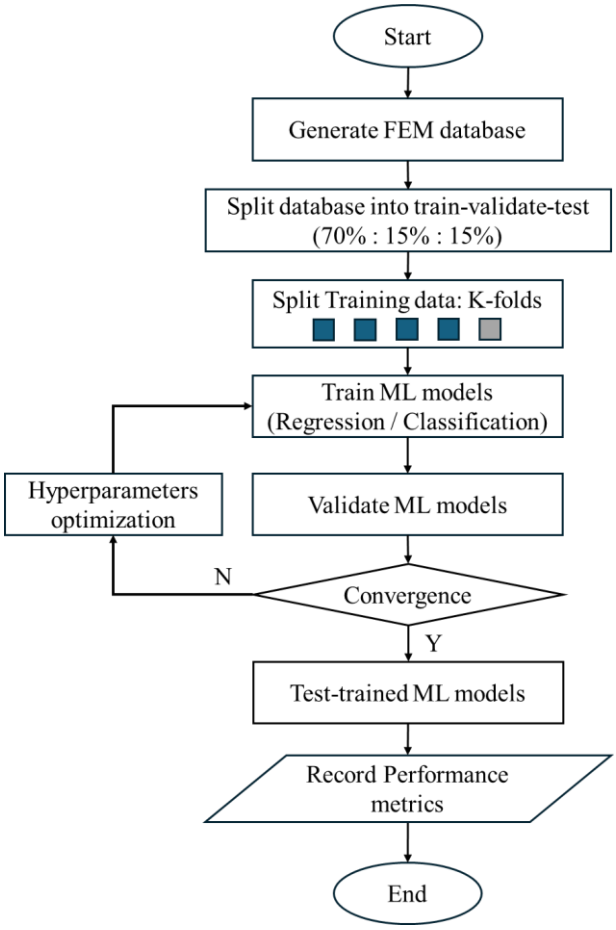

Fig. 4-8: Flow chart for machine learning development for regression and classification models

The Decision Tree (DT) algorithm is a widely used supervised machine learning technique that constructs a binary tree to model the training data. Each node in the tree represents a decision based on a specific feature, while the leaves represent the final outcomes or classifications. A key aspect of the DT algorithm is information entropy, which measures the samples' purity and helps create a well-structured tree. The algorithm operates through a transparent decision-making process, using conditional statements to make predictions. The complexity and computational requirements of a DT model are primarily influenced by the tree's depth, making the maximum depth a crucial hyperparameter to tune. This depth-wise generation ensures that the model can capture the necessary patterns in the data while balancing the risk of overfitting. The Bagged Tree algorithm, also known as Bootstrap Aggregating or Bagging, is a powerful ensemble learning technique used

in supervised machine learning. It involves training multiple decision trees in parallel on different subsets of the training data created through bootstrap sampling (sampling with replacement). Each tree is trained independently, and the final prediction is made by averaging the predictions of all the trees (for regression) or by taking a majority vote (for classification). This approach helps reduce variance and avoid overfitting, as the ensemble of trees provides a more robust and stable model than a single decision tree. Bagging leverages the diversity among the individual trees to improve the overall performance and generalization of the model. Finally, the Boosted Tree algorithm, commonly called Boosting, is an advanced ensemble learning technique used in supervised machine learning. Unlike Bagging, boosting builds models sequentially, where each new tree aims to correct the errors made by the previous ones. This iterative process focuses on the instances that were previously misclassified, giving them more weight in subsequent models. The final prediction is made by combining the predictions of all the trees, often through a weighted sum. Boosting helps to reduce bias and improve the model's accuracy by concentrating on the difficult-to-predict instances.

The model training for regression and classification learners was performed by MATLAB software ("MATLAB version: 9.13.0" 2022), where machine learning algorithms are based on a training set data of 70% and are validated and tested based on a dataset comprising 30% of the data. A five-fold cross-validation approach is a common technique used to avoid overfitting in model training, where the dataset is divided into five equal parts. The model is trained on four parts and tested on the remaining part. For classification modes, the output was six distinct failure modes extracted from the FEM analysis. Specifically, the modes are bolt shear failure, rupture failure of the extended plate, local buckling of the beam, local buckling of the column, bearing failure of the beam, and block shear failure of the beam. The relationships between each input parameter and

the output variable of all the data points are shown in Fig. 4-9. No simple and clear relationship between the input parameter and the output variable can be found, indicating the complexity of the prediction issue. Key hyperparameters for each machine learning algorithm were utilized to optimize the algorithm's model performance. The values of hyperparameters for each algorithm utilized in regression and classification models are listed in Table 4-4.

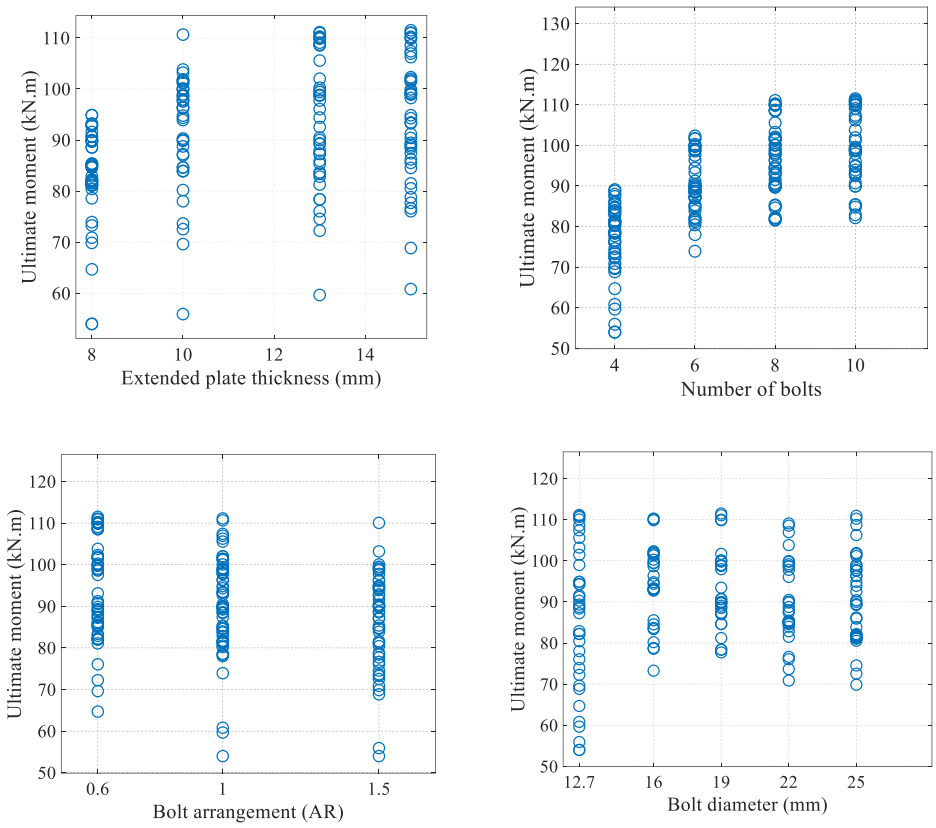

Fig. 4-9: Relationships between input parameters and the ultimate moment capacity in the database

Table 4-4: Summary of values of hyperparameters for each model

Algorithm	Hyperparameter	Value	
		Regression model	Classification model
Coarse decision tree	Minimum parent size	72	10
	Minimum leaf size	36	1
	Maximum splits	167	4
Medium decision tree	Minimum parent size	24	10
	Minimum leaf size	12	1
	Maximum splits	167	20
Fine decision tree	Minimum parent size	10	10
	Minimum leaf size	4	1
	Maximum splits	167	100
Optimized decision tree	Minimum parent size	10	10
	Minimum leaf size	2	1
	Maximum splits	167	41
Boosted tree ensemble	Minimum leaf size	8	------
	Number of learners	30	30
	Learning rate	0.1	0.1
	Maximum number of splits	------	20
Bagged tree ensemble	Minimum leaf size	8	------
	Number of learners	30	30
	Learning rate	1	1
	Maximum number of splits	------	167
Optimized ensemble method	Split criterion	------	Twoing rule
	Ensemble method	LSBoost	Bag
	Number of learners	26	464
	Learning rate	0.1794	0.0010
	Minimum leaf size	4	----
	Number of predictors	4	3
	Maximum number of splits	---	50

Based on the test set, statistical indices for six different regression models were calculated to evaluate the model performance, as shown in Fig. 4-10, the fitness indicator of the predictive model (i.e., Pearson correlation coefficient (R) and three prediction error indicators, which are the Mean absolute error (MAE), root mean square error (RMSE) and mean square error. The predicted true response for the ultimate moment capacity of the connection for different utilized machine learning models is shown in Fig. 4-.11. For capacity prediction, the optimizable Ensemble and then the Fine Tree model emerge as the best-performing models, achieving the highest R of 0.96 for both training and test datasets. This superior performance is due to several factors: optimizing the leaf

size to 4, similar to the Fine tree method, which allows for more precise splits; utilizing a learning rate of 0.17, which balances the speed and accuracy of learning; and employing 26 learners, which enhances the model's robustness and ability to generalize from the data.

On the other hand, accuracy was calculated to assess the performance of classification models as per Eq. 4-2, as shown in Fig. 4-12. The optimizable bagged tree model outperformed others with an accuracy of 95% for both validation and testing, utilizing a learning rate of 0.001 and a maximum of 50 splits. The low learning rate ensures that the model learns gradually, reducing the risk of overfitting, while the high number of splits allows for capturing complex patterns in the data. Following this, the boosted tree model also performs well with a learning rate of 0.1 and a maximum of 20 splits. The boosted tree's iterative learning approach helps correct errors from previous iterations, thereby improving accuracy. Also, two confusion matrix measures were used further to evaluate the developed classification models, precision and recall, as per Eq. 4-3, and Eq. 4-4, respectively. True positives are instances where the model correctly predicts the positive class; false positives are instances where the model incorrectly predicts the positive class; and false negatives refer to instances where the model incorrectly predicts a negative outcome where the actual outcome is positive. The decision tree models, including fine, medium, and coarse trees, struggled to accurately recognize the bearing failure of the beam and the block shear failure of the beam due to their limited ability to capture complex patterns and interactions within the data. These models are prone to overfitting, leading to poor generalization of unseen data. In contrast, ensemble methods enhance their ability to identify intricate patterns and interactions. This results in better performance, including higher accuracy, precision, and recall across all failure modes, as shown in Fig. 4-12. Ensemble methods are also more robust to variations in the data, making them

more effective at recognizing less frequent failure modes like bearing and block shear failure modes of the beam.

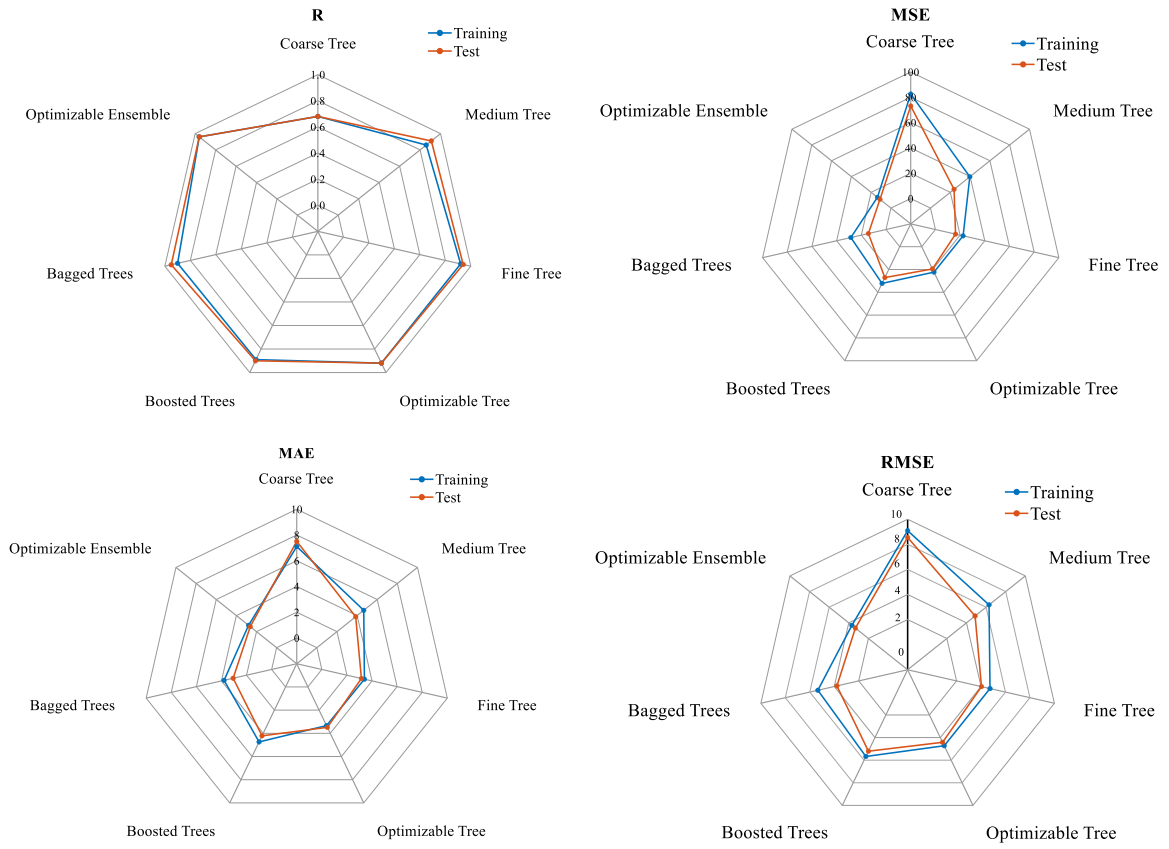

Fig. 4-10: Radar chart of performance metrics for regression models

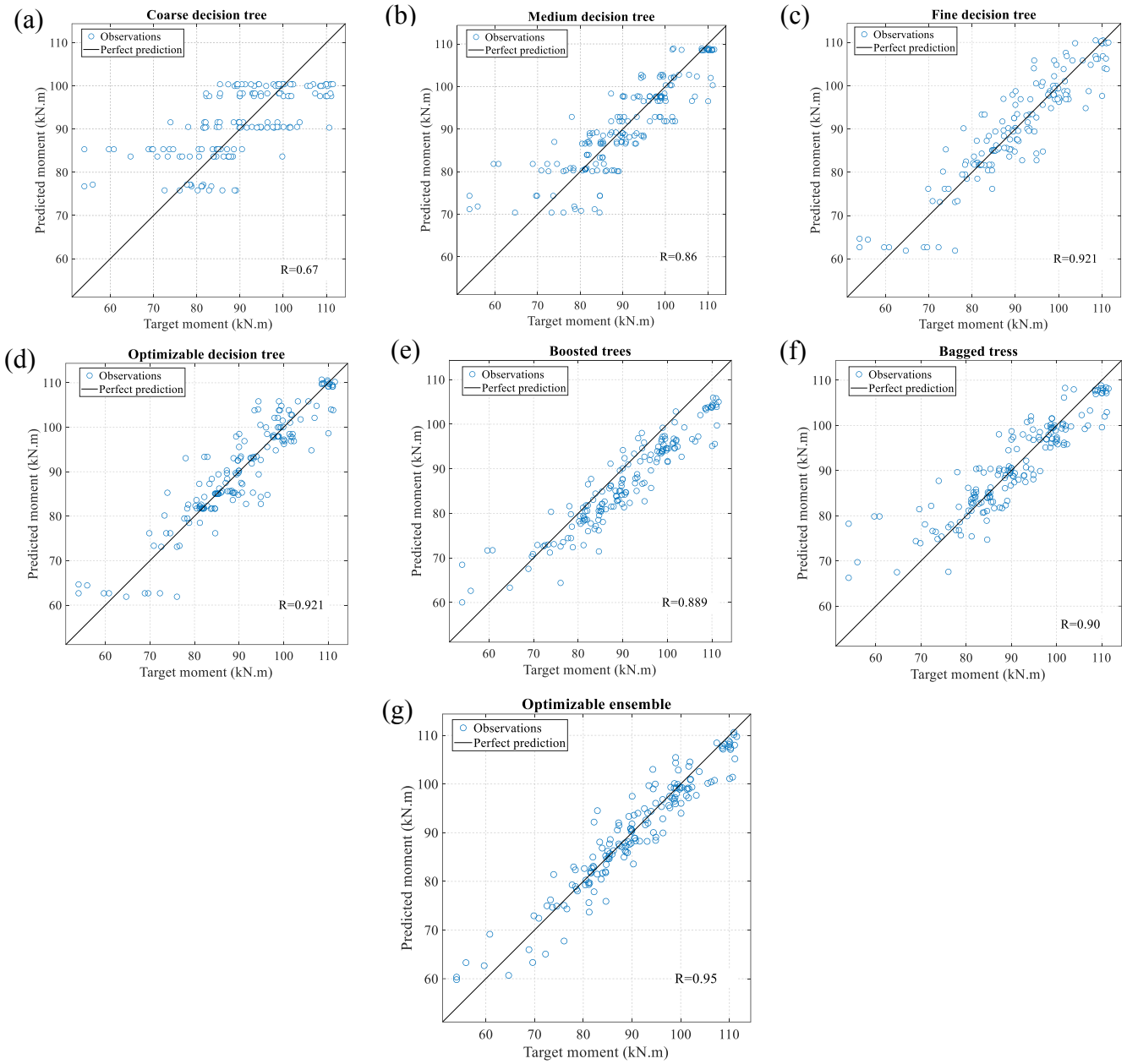

Fig. 4-11: Actual vs predicated capacity: (a) course tree, (b) medium tree, (c) fine tree, (d) optimizable tree, (e) boosted tree, (f) bagged tree, and (g) optimizable ensemble.

$$\text{Accuracy}=\frac{\sum \text{Correct Prediction}}{\sum \text{Total Number of Predictions}} \qquad \text{Eq. 4-2}$$

$$\text{Precision}=\frac{\text{True Postives}}{\text{True Postives+Flase Postives}} \qquad \text{Eq. 4-3}$$

$$\text{Recall}=\frac{\text{True Postives}}{\text{True Postives+Flase negatives}} \qquad \text{Eq. 4-4}$$

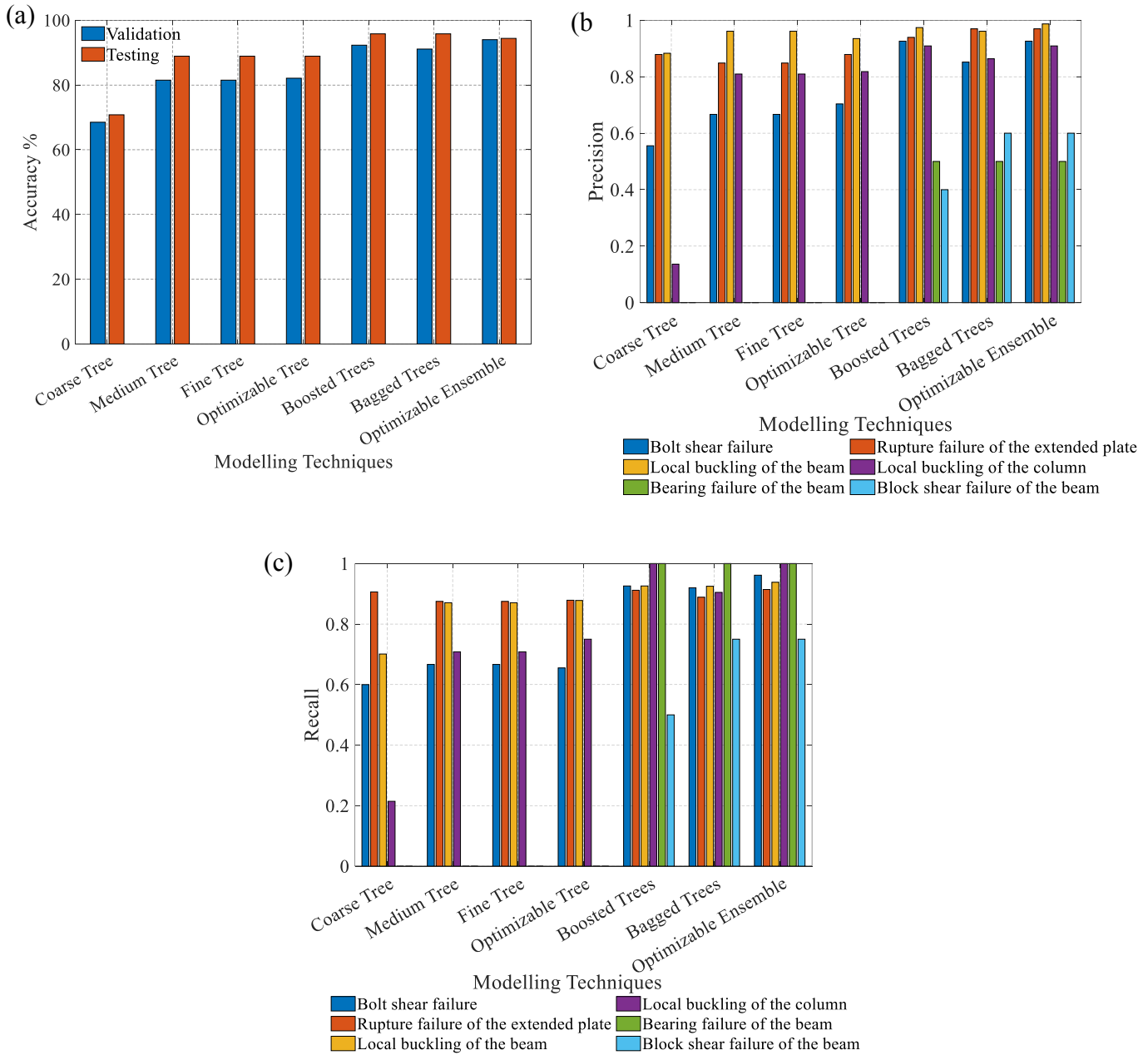

Fig. 4-12: Failure mode classification: (a) accuracy, (b) precision and (c) recall

4.3.2 Artificial neural network model

An Artificial Neural Network (ANN) typically consists of an input layer, a hidden layer with a specified number of neurons, and an output layer. Fig. 4-13 illustrates the architecture of the ANN used in this study. Each input parameter is connected to every node in the hidden layer, and each hidden layer node is subsequently connected to the output layer. The neural network assigns

weights, biases, and transfer functions to these connections to determine the output layer's values. This study utilized the Neural Network Toolbox in MATLAB, employing a Multi-Layer Perceptron Network (MLPN) to address the input-output fitting problem with a two-layer feed-forward network. The input parameters used to predict the ultimate capacity of the bolted connection included the extended plate thickness (EP), the number of bolts (N), the bolt arrangement (AR), and the bolt diameter (D). The Levenberg-Marquardt backpropagation training algorithm was chosen for its speed, consistent convergence, and suitability for small and medium-sized problems. To ensure accurate predictions without overfitting, the data in the MATLAB toolbox was divided into training, validation, and testing sets. 70% of the data was used to train the model. Meanwhile, 15% of the data was used for validation, measuring the network's generalization and stopping training when no further improvement was observed. The remaining 15% of the data was used for testing, providing an independent assessment of the model's performance during and after training. To assess the accuracy of the models, a comparison between the actual and predicted values was reviewed alongside an assessment of the impact of each input parameter. To review the accuracy of predicted values, the Pearson correlation coefficient (R), root Mean Square Error (RMSE), and mean Absolute error (MAE) were determined using Eq. 4-5, Eq. 4-6, and Eq. 4-7. Where x_i and y_i are the actual and predicted ultimate moment of the connection, and N is the total number of data points in each data set, $\bar{x}$ and $\bar{y}$ are the averages of the predicted and target ultimate moment of the connection.

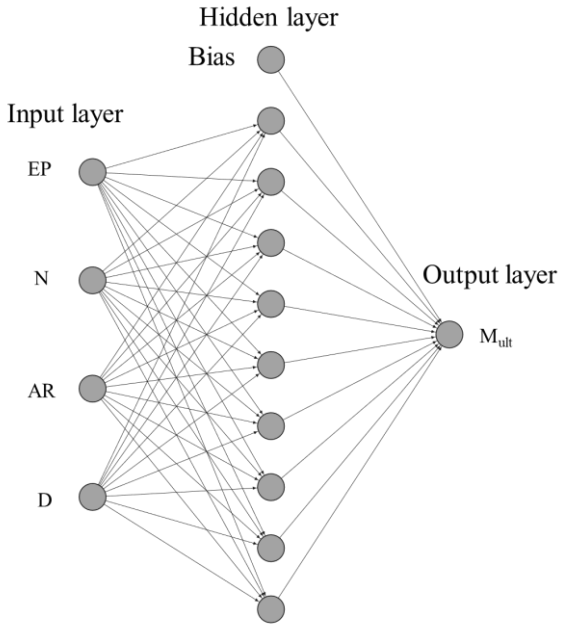

Fig. 4-13: Schematic diagram for Artificial neural network architecture

$$R=\frac{\sum_{i=1}^{N}(x_i-\bar{x}_i)(y_i-\bar{y}_i)}{\sqrt{\sum_{i=1}^{N}(x_i-\bar{x}_i)^2\ \sum_{i=1}^{N}(y_i-\bar{y}_i)^2}} \quad \text{Eq. 4-5}$$

$$RMSE=\sqrt{\frac{\sum_{i=1}^{N}(x_i-y_i)^2}{N}} \quad \text{Eq. 4-6}$$

$$MAE=\frac{1}{N}\sum_{i=1}^{N}|x_i-y_i| \quad \text{Eq. 4-7}$$

The accuracy of the ANN model with different numbers of neurons is illustrated in Table 4-5. The statistical parameters, including Pearson correlation coefficient (R) and root mean square error (RMSE), were obtained during training, validation and testing data sets. It can be noted that there is a clear correlation between the accuracy of the ANN prediction and the number of neurons in the hidden layer as the accuracy increases with the increase in the number of neurons. For instance, the R and RMSE values for the model with 3 neurons are 0.8430 and 6.5761, respectively, while

these same values for a model with ten neurons are 0.98026 and 2.3967, respectively. However, using more neurons than 10 in the ANN model potentially results in the same accuracy, and the model becomes complex and impractical for use in real-life engineering applications. Therefore, the 10-neuron model is selected to predict the ultimate moment of the connection as it shows a high level of accuracy and a stable level of convergence. Fig. 4-14 illustrates comparisons between the actual and predicted moments for training, validation, and testing. The constants $W_1(i,j)$ represent the connection weights between input (j) and the neurons in the hidden layer (i). Similarly, $W_2(i)$ denotes the connection weights between the neurons in the hidden layer (i) and the output. The bias for each neuron (i) in the hidden layer is denoted by $B_1(i)$, while B_2 is the output bias, which has a value of -1.41620. The values of $W_1(i,j)$), $W_2(i)$, and $B_1(i)$ for each neuron (i) are provided in Table 4-6. Analysis of the error percentage derived from the ANN revealed that the highest error percentage was -8.482, which accounts for 5% of the entire dataset. More than 80% of the datasets exhibited an error range from 2.903 to -2.798, as illustrated in Fig. 4-15. While for the testing datasets, comprising 36 models, over 40% had an error of -1.4%, the highest error recorded was -11.76%, representing 0.08 % of the testing datasets. These results indicate that the ANN model demonstrates robust performance and accuracy across most datasets.

Table 4-5: Assessment of the ANN models with different neurons.

Number of neurons	Training		Validation		Testing	
	RMSE	R	RMSE	R	RMSE	R
3	6.4795	0.8583	6.4496	0.7989	7.1263	0.8162
5	3.1103	0.9671	3.5612	0.9504	3.8570	0.9465
7	3.0639	0.9610	3.2950	0.9689	4.6290	0.9488
10	2.1412	0.9841	3.0379	0.9753	2.7699	0.9738
13	1.9314	0.9875	2.7497	0.9597	3.1218	0.9771
15	2.0254	0.9843	3.9693	0.9527	3.5641	0.9772

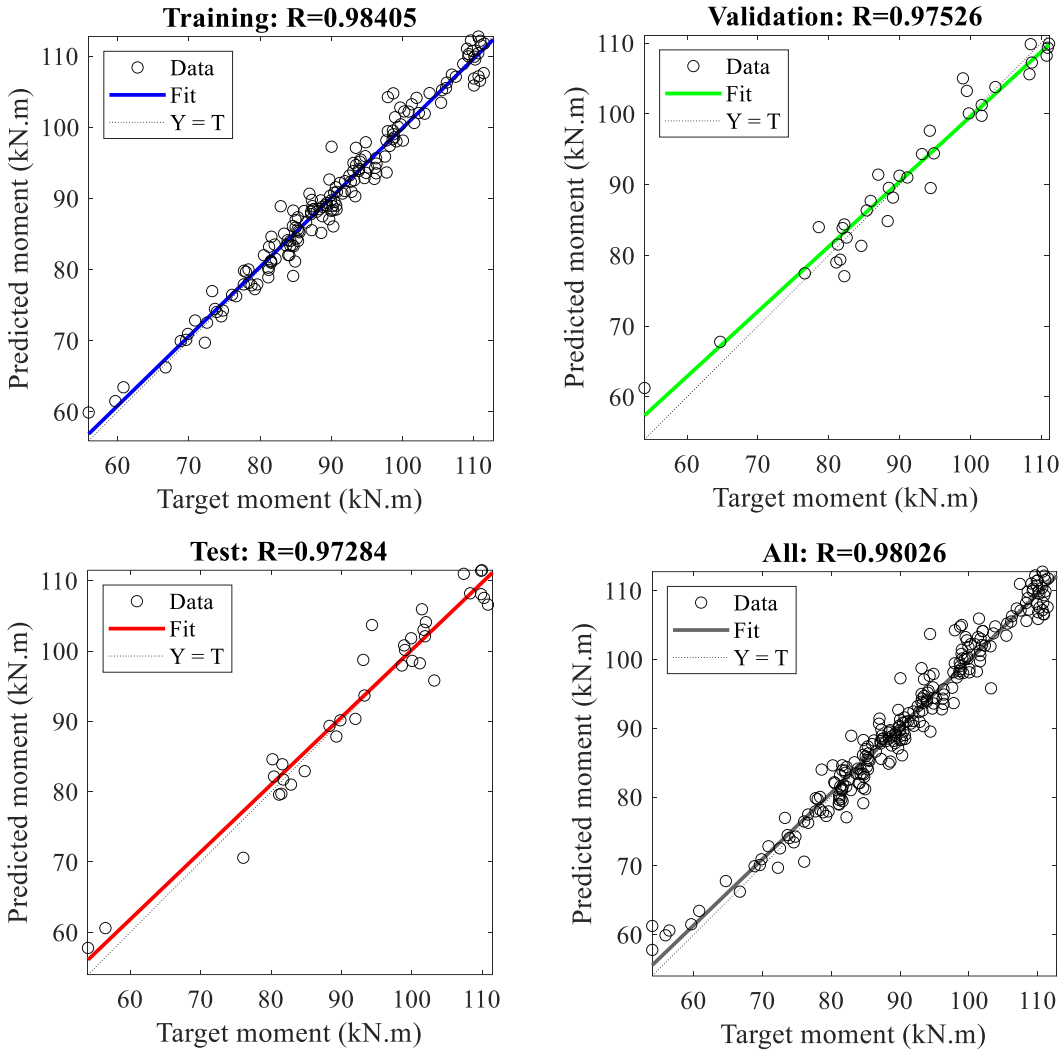

Fig. 4-14: Predicated moment vs actual moment from ANN model: (a) training; (b) validation; (c) test; and (d) All data

Table 4-6: The connection weight and the bias values.

Neuron	W_1 (i,j)				W_2 (i)	B_1(i)
	EP	N	AR	D	M_{ult}	
1	-2.47364	-2.28363	-0.8443	0.390558	0.071131	2.173453
2	-0.1372	-1.55145	-1.39357	0.324249	0.209536	-1.58817
3	0.49996	1.948104	1.049175	6.084407	0.404712	6.723949
4	0.024778	-1.60918	-0.0147	0.235838	-0.4885	-0.93488
5	0.703519	0.120842	1.000749	-2.21136	-0.17208	-0.57731
6	0.590466	-0.40258	2.915907	-4.72532	0.178989	-1.26707
7	-1.7667	0.41613	-0.17114	0.157138	0.351476	-0.67599
8	0.34207	1.645813	-1.00981	-0.73809	0.274675	-1.11549
9	0.71515	-0.21896	0.107892	-0.07766	2.019854	1.133684
10	-0.8923	0.843323	-1.18337	0.387192	0.125124	0.123547

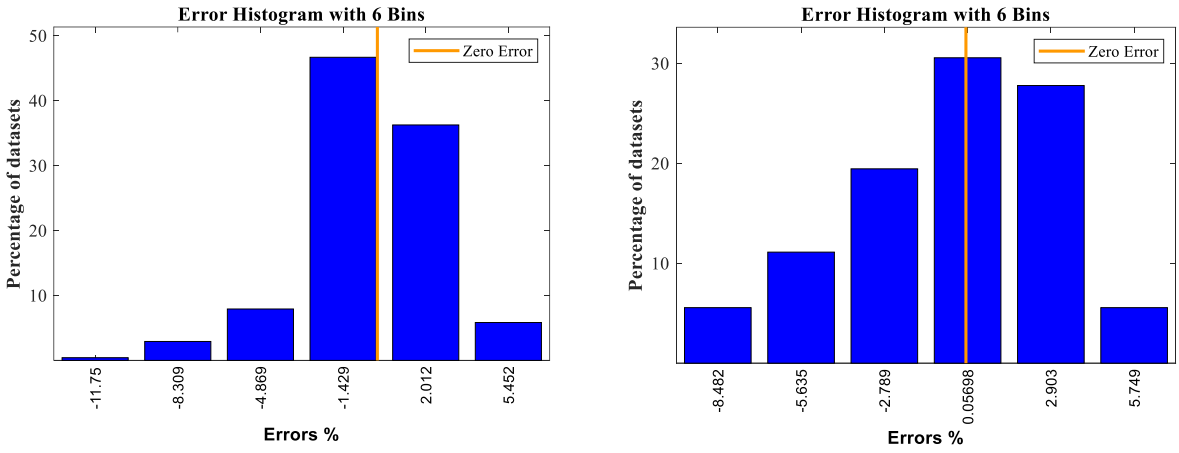

Fig. 4-15: Error histogram for predicting ultimate moment in ANN: (a) testing, and (b) all datasets

4.4 Mathematical formulas to predict ultimate capacity

A machine learning technique was used to develop a mathematical equation using symbolic regression that searched for the best-fitting model without using predefined models to reach a more accurate model. Symbolic regression employs genetic programming to evolve and optimize the structure of complex models and express them in mathematical form. A total of 240 results generated from the developed FEM were utilized using Heuristic Lab and Eureqa software (DataRobot 2024; "HeuristicLab" 2002). This dataset was divided into two subsets: a 70% training subset and a 30% testing and validation subset to predict the ultimate capacity of the connection. The input and output datasets were randomized before being handled. Four input features were used: extended plate thickness (i.e., EP), number of bolts (i.e., N), bolt arrangement (i.e., AR), and bolt diameter (i.e., D). In symbolic regression, a maximum of 10000 generations and a population size of 1000 were used. The many generations allowed the genetic programming algorithm to refine and optimize the candidate solutions iteratively, increasing the likelihood of discovering a well-fitting model. The large population size ensured a diverse pool of potential solutions, enhancing the algorithm's ability to explore a wide range of model structures equal to 9.9×10^{6}

solutions. Additionally, we set the mutation probability at 15%, introducing variability into the population, preventing premature convergence and promoting the discovery of novel and potentially more accurate models. The maximum symbolic expression tree depth and the maximum symbolic expression tree length were set to 15 and 30, respectively. The tree depth parameter controls the complexity of the equations by limiting the number of nested operations, ensuring that the resulting models remain interpretable and manageable. The tree length parameter restricts the total number of nodes in the expression tree, which helps prevent overfitting by avoiding excessively complex models. These parameters contributed to a robust and thorough search for the best-fitting mathematical expressions. Two symbolic equations were derived using arithmetic, exponential and logarithmic functions, as presented in. Eq. 4-8 and Eq. 4-9 . The Pearson correlation coefficient (R) was employed to examine the correlation between features for training and testing. Fig. 4-16 illustrates a scatter plot of actual versus predicted capacities for the two developed equations, both exhibiting a training R-value of 0.96 and a testing R-value of 0.91. The analysis revealed the influence of each input parameter on the ultimate capacity, with the number of bolts contributing the most at 52.08%, followed by extended plate thickness at 22.96%, bolt arrangement at 13.29%, and bolt diameter at 11.67%. The mathematical equations can predict the value of the ultimate moment capacity in a highly effective way, similar to machine learning models, within an acceptable error range.

$$M_{ult} = \left(\log\left(\frac{(c_0 * N + \log(c_1 * D))}{\left(c_2 * AR + \frac{c_3 * N}{(c_4 * AR + c_5 * D) * (c_6 * EP - (c_7 + c_8) * (c_9 * EP - (c_{10} * N) + \log(c_{11} * D)))} \right) * c_{12} * D} \right) * c_{13} + c_{14} \right) \quad \text{Eq. 4-8}$$

Where:

$c_0 = 0.42197$ $c_1 = 0.016149$ $c_2 = 1.7359$ $c_3 = 0.42197$ $c_4 = 1.4522$ $c_5 = 0.016149$ $c_6 = 0.7633$ $c_7 = 7.4196$
$c_8 = -1.5572$ $c_9 = 0.7516$ $c_{10} = 0.4729$ $c_{11} = 0.01614$ $c_{12} = 0.01578$ $c_{13} = 13.568$ $c_{14} = 80.735$

$$M_{ult} = a + \frac{b}{N} + \frac{c}{(d+N)^D} + e \times \frac{N}{(AR \times e^{EP})} - f \times AR \times D \quad \text{Eq. 4-9}$$

Where:

$a = 131.01$ $b = -136.39$ $c = -1.4818e19$ $d = 20.783$
$e = -4140.6$ $f = 0.64622$

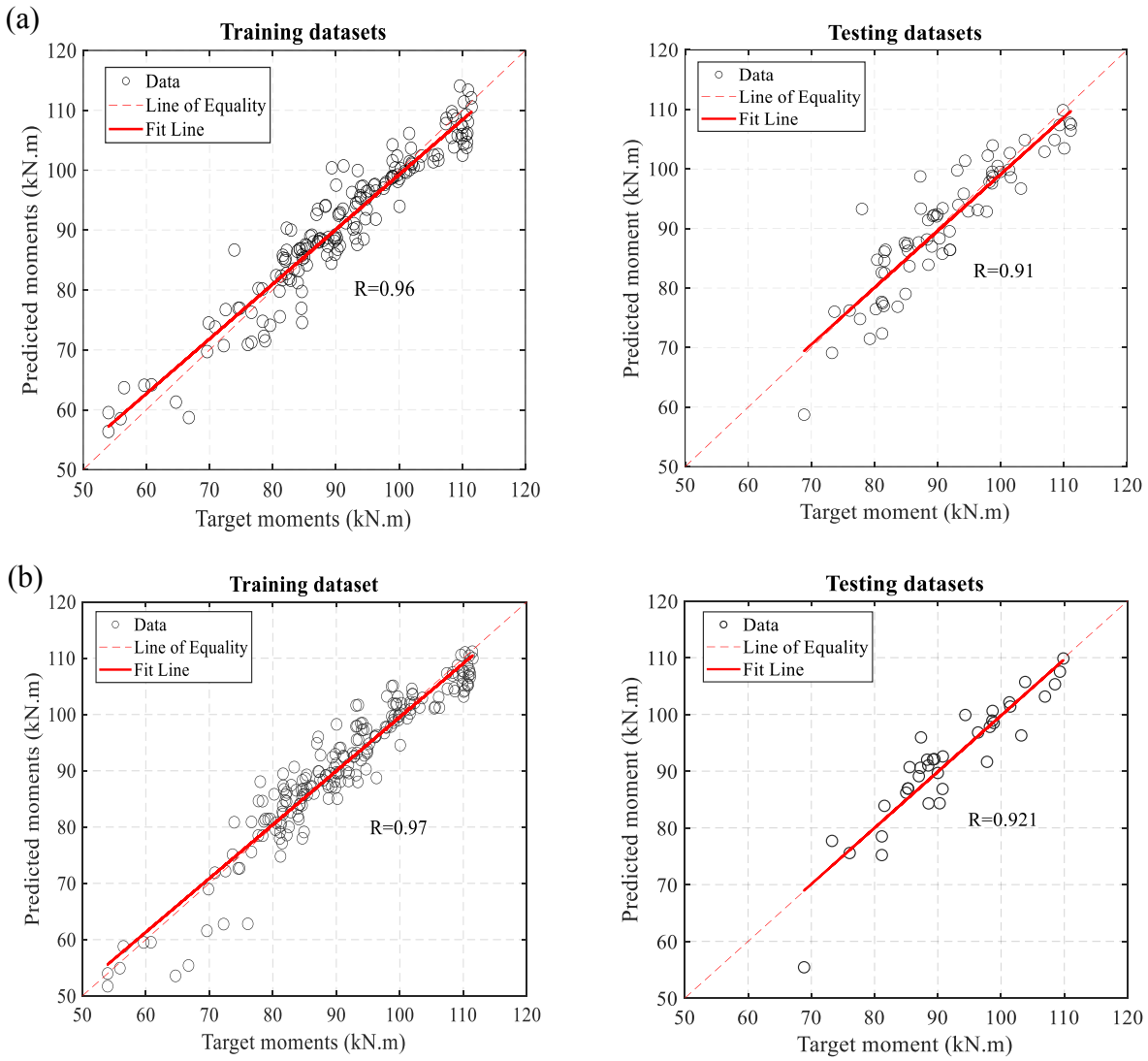

Fig. 4-16: Predicted versus target moment capacity for the connection using training and testing datasets across different software: (a) HeuristicLab, and (b) Eureqa

4.5 Conclusions

This study introduces interpretable prediction models that benefit engineers by predicting the ultimate capacity and failure modes of long-bolted HSS-to-HSS connections in panelized modular housing. An experimentally validated FEM was developed to generate a comprehensive dataset for training, validation, and testing of the proposed machine learning models. Several techniques were used to develop the prediction models, ranging from classical decision trees to ensemble methods, including bagging, boosted trees, and optimizable ensemble methods. Additionally, an artificial neural network was employed to predict the ultimate capacity, enhancing the regression models' Pearson correlation coefficient (R). Then, mathematical formulas were developed using genetic regression to predict the ultimate capacity with high accuracy further. The following conclusion could be drawn from the above analysis:

- Comparing the performance of the employed ensemble methods, it was observed that the best-performing model for capacity prediction was optimizable ensemble trees, which yielded the highest Pearson correlation coefficient (R) equal to 0.95 and utilized a learning rate of 0.1794, leaf size of 4 and number of learner equal to 26, resulting in a robust model with low computational effort. On the other hand, the artificial neural network model with ten neurons was observed to perform better than the decision tree and ensemble methods, with Pearson correlation coefficient (R) equal to 0.98 and a lower error percentage for all datasets of 8.4%.
- For the classification model, the optimizable bagged tree model yielded the highest accuracy for training and testing (i.e., 95%), utilizing a learning rate of 0.001 in classifying all failure modes compared to other decision tree methods that achieve no more than 80% accuracy and couldn’t identify the two failures of bearing and block shear failure mode.

- Genetic symbolic regression was employed to develop equations for predicting the ultimate moment capacity of the connection. The resulting equations demonstrated a Pearson correlation coefficient (R) of 0.97 for the training datasets and 0.92 for the testing datasets. Analysis revealed that the predicted capacity has the strongest relationship with the number of bolts, followed by the extended plate, bolt arrangement, and thickness diameter.

4.6 References

Abarkan, I., Rabi, M., Ferreira, F.P.V., Shamass, R., Limbachiya, V., Jweihan, Y.S., Pinho Santos, L.F., 2024. Machine learning for optimal design of circular hollow section stainless steel stub columns: A comparative analysis with Eurocode 3 predictions. Eng. Appl. Artif. Intell. 132, 107952. https://doi.org/10.1016/j.engappai.2024.107952

Akbari Hamed, A., Charkhtab Basim, M., 2020. Experimental-numerical study on weakened HSS-to-HSS connections using HBS and RBS approaches. Structures 28, 1449–1465. https://doi.org/10.1016/j.istruc.2020.09.076

Asgarkhani, N., Kazemi, F., Jakubczyk-Gałczyńska, A., Mohebi, B., Jankowski, R., 2024. Seismic response and performance prediction of steel buckling-restrained braced frames using machine-learning methods. Eng. Appl. Artif. Intell. 128. https://doi.org/10.1016/j.engappai.2023.107388

Asgarkhani, N., Kazemi, F., Jankowski, R., 2023. Machine learning-based prediction of residual drift and seismic risk assessment of steel moment-resisting frames considering soil-structure interaction. Comput. Struct. 289, 107181. https://doi.org/10.1016/j.compstruc.2023.107181

Chen, H., Liu, Y., Huang, Y., Huang, J., Caisong, L., Guo, Z., 2024. Maximum displacement prediction model for steel beams with hexagonal web openings under impact loading based on artificial neural networks. Eng. Appl. Artif. Intell. 136, 108932. https://doi.org/10.1016/j.engappai.2024.108932

Chen, Y., Huang, Y., Liu, H., Liu, Y., Zhang, T., 2023. Ultimate bearing capacity prediction method and sensitivity analysis of PBL. Eng. Appl. Artif. Intell. 123, 106510. https://doi.org/10.1016/j.engappai.2023.106510

Das, S., Teweldebrhan, B.T., Tesfamariam, S., 2024. High-dimensional multi-objective optimization of coupled cross-laminated timber walls building using deep learning. Eng. Appl. Artif. Intell. 136, 109055. https://doi.org/10.1016/j.engappai.2024.109055

DataRobot, 2024. Eureqa [WWW Document]. URL https://www.datarobot.com

Digital Research Alliance of Canada, 2019.

Du, W., Zhao, Y., Wang, Y., Wang, H., Yang, M., 2022. Novel machine learning approach for shape-finding design of tree-like structures. Comput. Struct. 261–262, 106731. https://doi.org/10.1016/j.compstruc.2021.106731

Elhadary, M., Bediwy, A., Elshaer, A., 2025. Structural performance of novel steel connection for indigenous modular houses, in: Lecture Notes in Civil Engineering. Springer Singapore, Moncton, New Brunswick, pp. 253–266. https://doi.org/10.1007/978-3-031-61535-1_21

Elhadary, M., Bediwy, A., Elshaer, A., 2024a. Novel steel connection for modular houses in indigenous communities: An experimental study. J. Constr. Steel Res. 220, 108850. https://doi.org/10.1016/J.JCSR.2024.108850

Elhadary, M., Bediwy, A., Elshaer, A., 2024b. Experimental investigation on a novel steel connection for modular indigenous houses, in: Canadian Society of Civil Engineering (CSCE) 2024 Annual Conference. Niagara Falls, Ontario.

Fadden, M., Asce, S.M., Mccormick, J., Asce, A.M., 2012. Cyclic quasi-static testing of hollow structural section beam members 138, 561–570. https://doi.org/10.1061/(ASCE)ST.1943-541X.0000506

Fadden, M., McCormick, J., 2013. Evaluation of HSS-to-HSS moment connections for seismic applications. Struct. Congr. 2013 Bridg. Your Passion with Your Prof. - Proc. 2013 Struct. Congr. 2334–2345. https://doi.org/10.1061/9780784412848.204

Fadden, M., Wei, D., McCormick, J., 2015. Cyclic testing of welded HSS-to-HSS moment connections for seismic applications. J. Struct. Eng. 141, 1–14. https://doi.org/10.1061/(asce)st.1943-541x.0001049

HeuristicLab [WWW Document], 2002. URL https://dev.heuristiclab.com/trac.fcgi/ (accessed 8.30.24).

Hu, J., Jiang, L., Hu, Y., He, J., Cheng, X., Yang, J., 2025. Machine learning-based axial compressive capacity estimation of cold-formed steel build-up sections. Thin-Walled Struct. 206. https://doi.org/10.1016/j.tws.2024.112669

Kazemi, F., Jankowski, R., 2023. Machine learning-based prediction of seismic limit-state capacity of steel moment-resisting frames considering soil-structure interaction. Comput. Struct. 274, 106886. https://doi.org/10.1016/j.compstruc.2022.106886

Kosteski, N., Packer, J.A., 2003. Longitudinal Plate and Through Plate-to-Hollow Structural Section Welded Connections. J. Struct. Eng. 129, 478–486. https://doi.org/10.1061/(asce)0733-9445(2003)129:4(478)

Kosteski, N, Packer, J.A., 2003. Welded Tee-to-HSS Connections 129, 151–159.

Lai, D., Demartino, C., Xiao, Y., 2024. Probabilistic machine leaning models for predicting the maximum displacements of concrete-filled steel tubular columns subjected to lateral impact loading. Eng. Appl. Artif. Intell. 135, 108704. https://doi.org/10.1016/j.engappai.2024.108704

Lawson, R.M., Prewer, J., Trebilcock, P.J., 1999. Modular construction using light steel framing. Steel Construction Institute.

Li, Y., Lou, J., Feng, Q., Wang, G., Xu, R., 2025. Prediction of the load–moment interaction curve for rectangular concrete-filled steel tube columns using composite multi-fidelity neural network. Eng. Appl. Artif. Intell. 142, 109904. https://doi.org/10.1016/j.engappai.2024.109904

Liu, X.C., Cui, F.Y., Zhan, X.X., Yu, C., Jiang, Z.Q., 2019. Seismic performance of bolted connection of H-beam to HSS-column with web end-plate. J. Constr. Steel Res. 156, 167–181. https://doi.org/10.1016/j.jcsr.2019.01.024

Liu, X.C., Wang, Y., Cui, X.X., Yu, C., Bai, Z.X., 2020. Seismic performance of bolted beam-to-column connection with rib-stiffened splicing plate. J. Constr. Steel Res. 174, 106300. https://doi.org/10.1016/j.jcsr.2020.106300

Liu, X.C., Yang, Z.W., Wang, H.X., Zhang, A.L., Pu, S.H., Chai, S.T., Wu, L., 2017. Seismic performance of H-section beam to HSS column connection in prefabricated structures. J. Constr. Steel Res. 138, 1–16. https://doi.org/10.1016/j.jcsr.2017.06.029

Liu, Y., Ji, W., Li, J., Liu, S.B., Yang, W., 2025. Shear performance prediction for corrugated steel web girders based on machine-learning algorithms. Thin-Walled Struct. 206, 112668. https://doi.org/10.1016/j.tws.2024.112668

Livermore software technology corporation (LSTC), 2007. Livermore software technology corporation (LSTC). (2007). LS-DYNA keyword user's manual, Vol. 1, Livemore, California, USA, R13.0.

Lu, Y., Wu, B., Li, W., Zhou, T., Li, Y., 2024. Regression-classification ensemble machine learning model for loading capacity and bucking mode prediction of cold-formed steel built-up I-section columns. Thin-Walled Struct. 205, 112427. https://doi.org/10.1016/j.tws.2024.112427

MATLAB version: 9.13.0, 2022.

Modular construction reports & industry analysis, 2023.

Nguyen, H.D., Lee, Y.J., LaFave, J.M., Shin, M., 2023. Seismic fragility analysis of steel moment frames using machine learning models. Eng. Appl. Artif. Intell. 126, 106976. https://doi.org/10.1016/j.engappai.2023.106976

Park, K., Jiansinlapadamrong, C., Chao, S.-H., 2021. Double-HSS Seismic Resistant Beam-to-Column Moment Connections. J. Struct. Eng. 147, 1–17. https://doi.org/10.1061/(asce)st.1943-541x.0003057

Rabi, M., Ferreira, F.P.V., Abarkan, I., Limbachiya, V., Shamass, R., 2023. Prediction of the cross-sectional capacity of cold-formed CHS using numerical modelling and machine learning. Results Eng. 17, 100902. https://doi.org/10.1016/j.rineng.2023.100902

Su, A., Cheng, J., Li, X., Zhong, Y., Li, S., Zhao, O., Jiang, K., 2024. Unified machine-learning-based design method for normal and high strength steel I-section beam–columns. Thin-Walled Struct. 199, 111835. https://doi.org/10.1016/j.tws.2024.111835

United Nations, 2019. "Adequate housing as a component of the right to an adequate standard of living, and the right to non-discrimination in this context."

Xu, Y., Zhang, M., Zheng, B., 2021a. Design of cold-formed stainless steel circular hollow section columns using machine learning methods. Structures 33, 2755–2770. https://doi.org/10.1016/j.istruc.2021.06.030

Xu, Y., Zheng, B., Zhang, M., 2021b. Capacity prediction of cold-formed stainless steel tubular columns using machine learning methods. J. Constr. Steel Res. 182, 106682. https://doi.org/10.1016/j.jcsr.2021.106682

Zhang, B., Xue, X., 2024. Ultimate axial strength prediction of concrete-filled double-skin steel tube columns using soft computing methods. Eng. Appl. Artif. Intell. 129, 107676. https://doi.org/10.1016/j.engappai.2023.107676

CHAPTER 5: NUMERICAL INVESTIGATION OF REINFORCEMENT TECHNIQUES FOR HSS-TO-HSS CONNECTION IN MODULAR HOUSES

5.1 Introduction

In Canada, modular construction technology is revolutionizing the construction industry and emerging as an innovative technology in many sectors, including commercial developments, residential buildings, schools and healthcare. This approach has proven its effectiveness in different healthcare facilities, such as the Montreal Heart Institute, which used modular construction to add an emergency cardiac care unit during a major expansion project (ATCO 2025a). In addition, modular constructions have played crucial roles during disasters. For example, Modular Aid Canada provided temporary shelter during the British Columbia wildfires (Canada 2025). Modular housing solutions have been increasingly recognized as an effective solution for addressing the housing shortage, especially in regions where transport and lifting constraints are significant. Modular structures are categorized into two primary categories: the 2D panelized system and the 3D volumetric system (i.e. box-like structures). The 2D panelized system consists of column and beam-floor modules, often referred to as a panelized steel modular structure. these systems involve off-site production of individual structural components, which are transported and assembled on-site. For example, a community project in northern Ontario reduced the construction time by assembling prefabricated wall panels on site (Gillies Lumber 2025). On the other hand, the 3D volumetric system involves designing and manufacturing the entire 3D modules in a factory and then transported and assembled on-site. A notable example is the modular classrooms in British Columbia built to meet urgent educational needs (ATCO 2025b).

The 2D panelized system offers several advantages over the volumetric 3D system, including reduced transportation costs, greater flexibility, and less resource wastage. It also faces fewer transport and lifting restrictions than the 3D system and typically requires less specialized labour. As a result, it is adaptable to various construction scenarios, providing greater flexibility (Lawson et al. 1999). However, the performance of modular structures in harsh climates, such as northern Canada, requires additional structural considerations to withstand extreme environmental loads, including wind and snow. High wind speeds generate uplift and lateral forces which can weaken connections over time, while accumulated snow increases vertical loads, causing potential damage to the structural connection. These challenges highlight the need for advanced reinforcement techniques. Stiffeners and concrete filling are two key reinforcement strategies. Stiffeners help distribute loads effectively and reduce stress concentrations, while concrete filling inside the column increases stiffness, prevents local buckling, and enhances overall stability. Combining both techniques improves the connection's resilience, particularly in extreme environmental conditions. In remote regions, where weather and logistical constraints add complexity, ensuring the structural integrity of modular housing is critical.

For 2D panelized steel modular structures, various studies have explored different joint configurations depending on the beam cross-section used, including HSS-to-HSS connections as well as HSS-to-W or H-shape beam connections. Liu et al. (2017) introduced a fully bolted connection that vertically connects upper and lower HSS columns through bolted flanges and horizontally connects H-shaped beams using extended cover plates and an endplate. Cyclic testing was performed to assess the influence of bolt configuration and slippage on joint stiffness, energy dissipation, and moment capacity (Liu et al. 2017, 2019). Further reinforcement improvements to the H-shaped beam connection were made by utilizing a trapezoidal stiffener, which enhanced

seismic performance by relocating web bolts onto the beam flange (Liu et al. 2020). In the HSS-to-HSS connection category, both bolted and welded configurations have been proposed to improve connection performance. Kosteski et al. (2003) proposed longitudinal plate and through plate-to-HSS welded connections, investigating the effects of different plate configurations on the strength and stability of the connection. They also explored the use of welded Tee-to-HSS connections, focusing on how the geometry of the Tee plate influenced load distribution and joint behavior (Kosteski and Packer 2003a; b). Hamed et al. (2020) conducted both experimental and numerical studies on HSS-to-HSS connections, using Hollow Beam Splice and Reduced Beam Section approaches to improve the seismic performance of the connections (Akbari Hamed and Charkhtab Basim 2020). Their research focused on optimizing the design to ensure better energy dissipation, identifying failure modes and enhancing resistance to cyclic loading. They demonstrated that incorporating these approaches, combined with strategic reinforcement, could improve connection behaviour under seismic forces. Park et al. (2021) examined the effectiveness of using HSS sections in both the beam and column to create more robust connections with reinforcing plates . They found that the use of double-HSS configurations, in conjunction with reinforcing plates and proper bolted connections, significantly increased the overall moment resistance of the joint, contributing to the overall seismic resilience of modular steel structures (Park et al. 2021). Fadden et al.(2012) conducted extensive investigations into both unreinforced and reinforced welded HSS-to-HSS connections. The unreinforced connections depend on the original shape of the HSS connection, while the reinforced connections incorporate additional elements, such as plates and stiffeners, to enhance strength, stiffness, and inelastic rotation under seismic loading. Their studies showed the positive impact of reinforcement on improving connection performance, particularly in terms of load distribution and resistance to seismic forces

(Fadden et al. 2012, 2015a; Fadden and McCormick 2013). Khan et al. (2020) improved the seismic behaviour of a novel joint in modular steel buildings by adding stiffeners as reinforcement. This enhancement increased the joint's capacity to resist seismic forces, effectively distribute loads, and maintain structural integrity during an earthquake (Khan and Yan 2020). Azimi et al. (2024) studied the impact of rib stiffeners and concrete filling on the stiffness of end-plate connections between CFST columns and I-section beams. Their finite element analysis, validated by experimental data, demonstrated that both reinforcement techniques improved the connection's stiffness and load-bearing capacity (Azimi and Ozakgul 2024). Elhadary et al. (2024) developed and validated modular HSS-to-HSS bolted connections specifically tailored to meet the unique structural requirements of northern and remote Indigenous communities. This novel connection design was carefully engineered to provide the necessary strength, stability, and resilience for modular structures in challenging environments (Elhadary et al. 2024b).

A significant research gap remains in understanding the effect of different reinforcement techniques, such as adding a stiffener below the extended plate, concrete infill within the column, and the use of both techniques on the structural performance of the HSS connection proposed by (Elhadary et al. 2024b), as shown in Fig. 5-1. While the existing studies have primarily focused on factors such as extended plate thickness, bolt number, and configuration. However, the impact of different reinforcement techniques has not been fully explored. To address this gap, a detailed parametric study using 162 finite element models (FEMs) was conducted to explore the impact of different reinforcement methods on the connection behavoir. The study provides valuable design guidelines and charts to predict failure modes, offering a streamlined design process for improving connection performance under monotonic loading. This research has potential implications for

transforming housing solutions in remote communities, contributing to more sustainable and resilient modular housing systems.

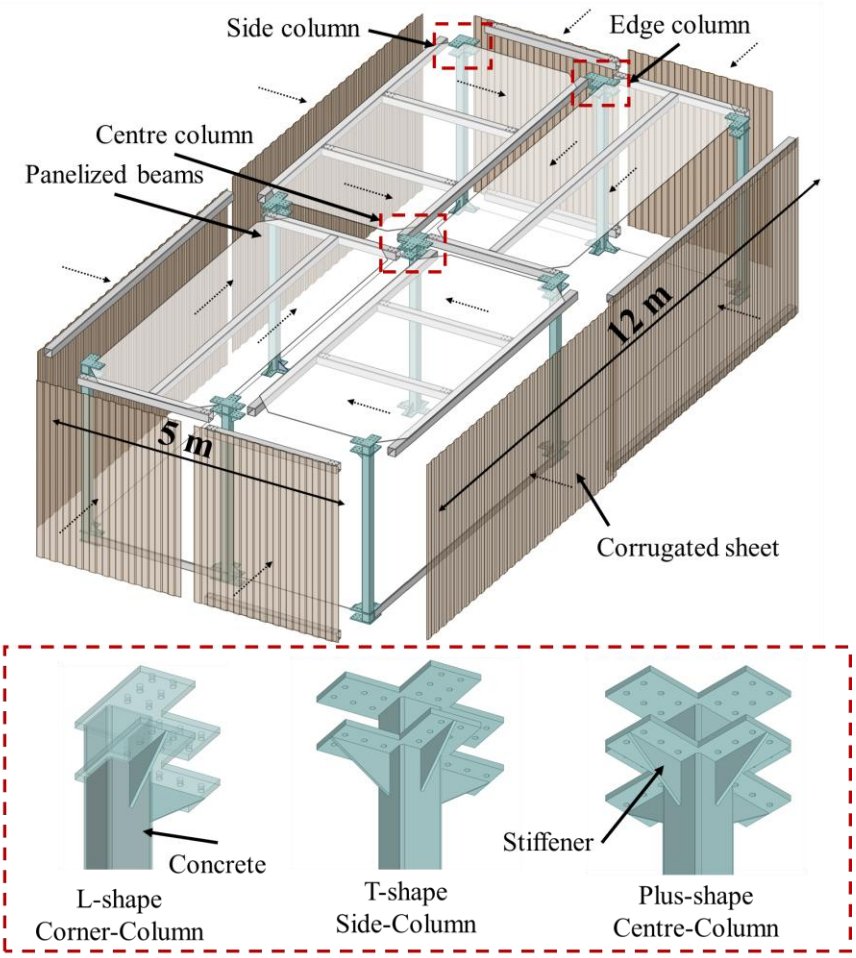

Fig. 5-1: Schematic diagram of the assembly technique of four box modules with different configurations of proposed column joints

5.2 Summary of the experimental program

Six specimens were tested under monotonic loading at Lakehead University's structural lab to evaluate the moment capacity, joint stiffness, and failure modes of the bolted steel connections (Elhadary et al. 2024b). The beam and column were fabricated from HSS 152×152×6.4 mm and HSS 152×152×9.5 mm, respectively. Both sections were fabricated from 350W steel. Long high-strength bolts of grade A325 were used for fastening. The specimens were subjected to a quasi-static loading protocol using a hydraulic actuator, applying a gradually increasing load until failure.

Boundary conditions were simulated by rigidly fixing the column base while allowing the beam to rotate, replicating real-world joint behaviour. Table 5-1 summarizes the geometric parameters of the tested steel connections, with each specimen coded based on key design variables: extended plate thickness (EP), number of bolts (B), bolt arrangement (AR), bolt diameter (D), and reinforcement technique if it exists. For example, in EP8-B10-AR1.0-D22-ST & Conc., where "EP8" denotes an extended plate with a thickness of 8 mm, "B10" indicates 10 bolts, "AR1.0" represents a ratio of "P_n/P_p" equal to 1.0, and "D22" refers to a bolt diameter of 22 mm. "ST & Conc." signifies a specimen strengthened with stiffeners beneath the lower extended plate and reinforced with concrete inside the column. The experimental specimens showed different failure modes, including bolt bearing failure, extended plate yielding, and local buckling of the beam, depending on the connection configuration.

Table 5-1: Main design parameters of the test specimens (Elhadary et al. 2024b)

Specimen ID	Number of Bolts	Extended Plate Thickness (mm)	Bolt Arrangement (P_n/P_p)	Stiffener
EP13-B6-AR1.5	6	13	1.5	no
EP10-B6-AR1.5	6	10	1.5	no
EP10-B6-AR1.0	6	10	1	no
EP13-B8-AR1.5	8	13	1.5	no
EP13-B6-AR1.5-ST	6	13	1.5	yes
EP10-B8-AR1.5	8	10	1.5	no

5.3 Numerical study

5.3.1 Finite element model details

A 3D FEM of a modular beam-to-column connection was developed using LS-DYNA software (Livermore software technology corporation (LSTC) 2007) and validated with the experimental results conducted by (Elhadary et al. 2024b). The FEMs were executed by the Digital Research Alliance of Canada (Digital Research Alliance of Canada 2021) (i.e., SHARCNET). Each simulation required an average duration of 48 hours to achieve the designated termination point,

encompassing 760 computational time steps. All specimen components were fabricated from steel 350W and grade A325 high-strength long bolts of diameter 5/8" (15.875 mm) were used to assemble the joint. The steel profiles' elastic-plastic and kinematic hardening behaviours were modelled using a material model named “Mat_Piecewise_Linear_Plasticity”. The nonlinear behaviour of concrete material, considering strain rate effects, was modelled using “Mat_CSCM_Concrete”. Table 5-2 lists the values of the material properties of the normal concrete and steel coupons obtained from the experimental tests conducted by (Elhadary et al. 2024b). The true stress-equivalent strain of steel 350W and grade A325 used to model the plastic behavior of materials, including strain hardening, yielding, and failure, is shown in Fig. 5-2. Fig. 5-3 describes the boundary conditions applied on the FEM aligned with the experimental test conditions, where the column was restrained by fixed support, the beam was laterally restrained in the X-direction, and the prescribed motion in the Y-direction was applied on the bracket plate of dimension 340×170 mm with a moment lever arm of 1080 mm. All model components were modelled using eight-node 3D solid elements with reduced integration, which contains hourglass model control to avoid shear self-locking. Several mesh densities were used in the FEM for different sections within the connection regions with a total number of 390,000 solid elements, as shown in Fig. 5-4. Inflation layers were used around the bolt holes to better capture the gradient of stresses. A cold-formed steel (CFS) beam was discretized using a fine mesh of 4 mm, and seven layers of smaller mesh were used to model profile thickness. This approach was adopted by a mesh sensitivity conducted by (Elhadary et al. 2025; Elhadary and Elshaer 2021). The contacts between connection components (i.e., Frictional components) were modelled using surface-to-surface-Mortar contact. The penalty formulation with a friction coefficient of 0.3 (i.e., representing the surface hardening by sandblasting) is defined by all the tangential responses for all contact

surfaces. The contacts between two extended plates with columns (i.e., welded components) were modelled using surface-to-surface-mortar-tied contact. The bolt clearance of 2 mm was modelled to capture the actual bolt behaviour mechanism releasing bolt pretension load result of snug tightening. All models were incorporated with non-linear material properties, non-linear time step analysis (i.e., implicit analysis), large deformation, and full Newton-Raphson with a modified arch length method.

Table 5-2: Material properties used for the concrete and steel profiles of the connection

Material	Model	Parameter	Value
Concrete	Mat_CSCM_Concrete	Mass density (g/mm^3)	2.3*10^{-3}
		Unconfined compression strength (MPa)	30
		Maximum aggregate size (mm)	19
Steel 350W	Mat_Piecewise_Linear_Plasticity	Mass density (kg/mm^3)	7.83e^{-6}
		Young's modulus (GPa)	200
		Poisson's ratio	0.3
A325 high-strength bolts	Mat_Piecewise_Linear_Plasticity	Mass density (kg/mm^3)	7.83e^{-6}
		Young's modulus (GPa)	210
		Poisson's ratio	0.3

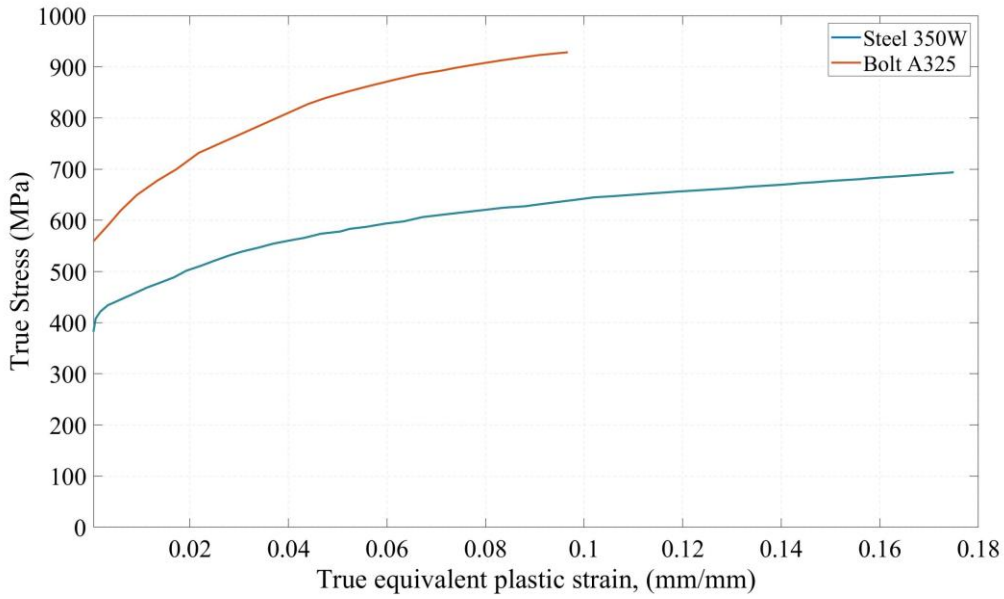

Fig. 5-2: The true stress-equivalent strain curves for tested steel coupons according to ASTM 2014 (ASTM 2014)

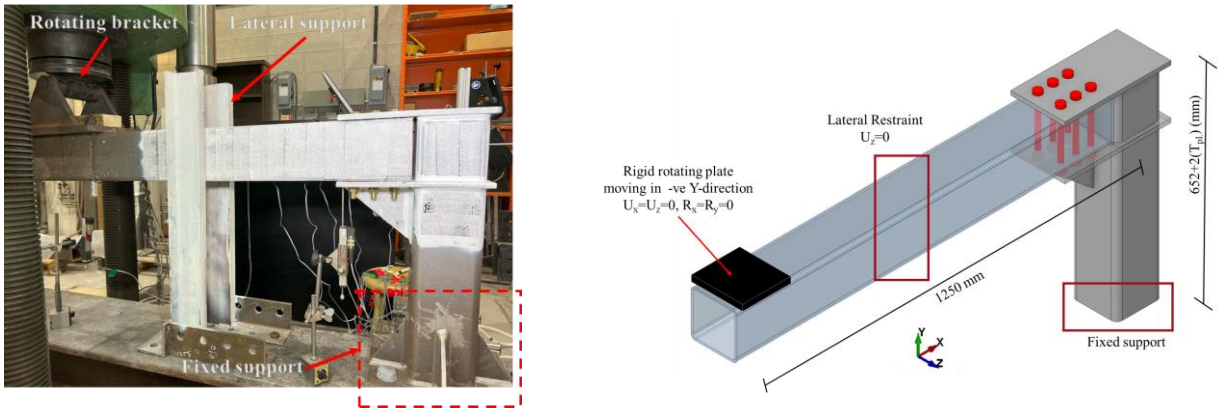

Fig. 5-3: Boundary conditions of the proposed FEM and tested specimens

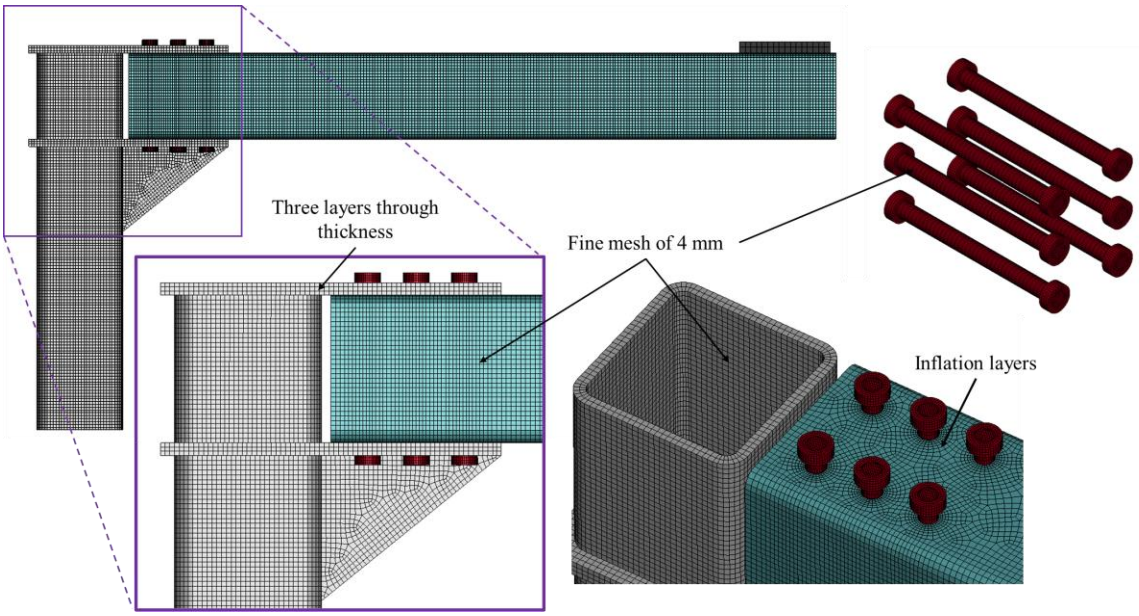

Fig. 5-4: Mesh configuration of the FEM model

5.3.2 Model validation

Fig. 5-5 shows the comparison between the moment-rotation curves obtained from the experiment test and the proposed FEM for six specimens, where the moment was determined by multiplying the force extracted from the load cell by the distance of the load point to the column face (1080 mm), whereas the connection rotation was calculated by subtracting the column rotation from the beam rotation. The FEM agreed well with its corresponding specimens from the experimental program, with an average error of 3%, as shown in Table 5-3. The FEM successfully captured the

impact of bolt clearance during the loading process, which was identified as a rotational horizontal displacement without a substantial increase in connection capacity. Fig. 5-6 shows the failure mode derived from the proposed FEM and the corresponding specimens incorporated within the experimental program. The FEM effectively captured various failure modes that occurred during the loading of specimens. Some models, such as EP10-B6-AR1.0, EP13-B8-AR1.5, EP10-B8-AR1.5, and EP13-B6-AR1.5-ST, experienced bolt bearing failure, which subsequently triggered local buckling at the beam's compression flange. On the other hand, models like EP10-B6-AR1.5 and EP13-B6-AR1.5 underwent block shear failure following the immediate occurrence of the beam's local buckling.

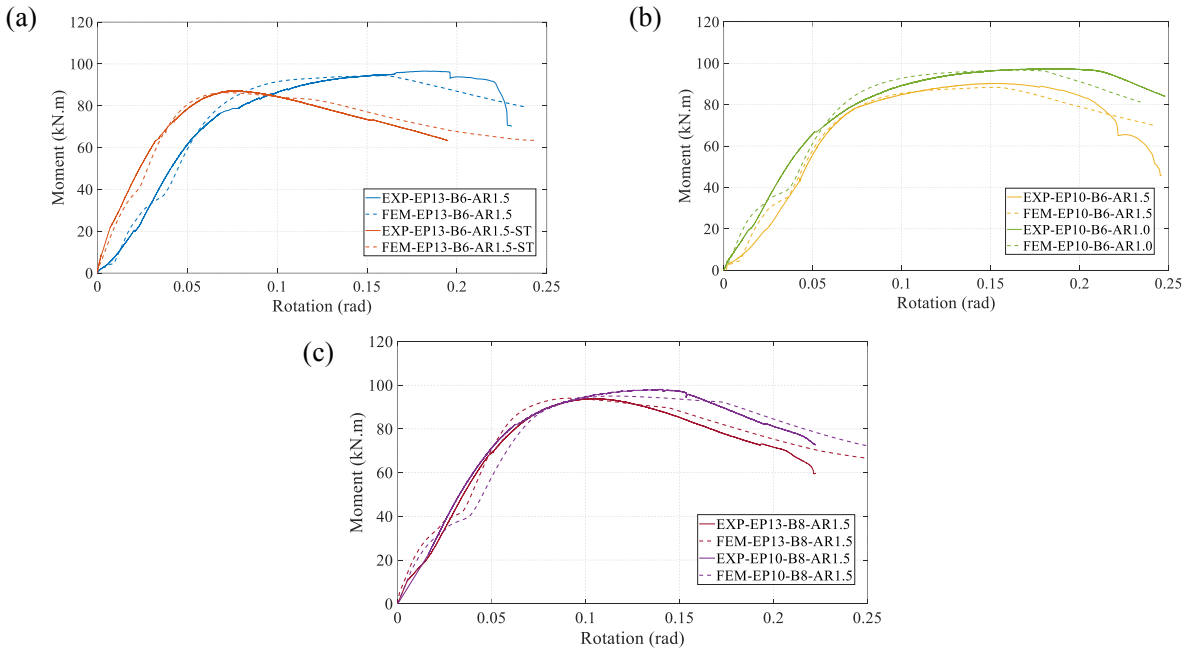

Fig. 5-5: Comparison between the moment-rotation curve of the test specimens and the FEM: (a) EP13-B6-AR1.5, EP13-B6-AR1.5-ST, (b) EP10-B6-AR1.5, EP10-B6-AR1.0, and (c) EP13-B8-AR1.5, and EP10-B8-AR1.5.

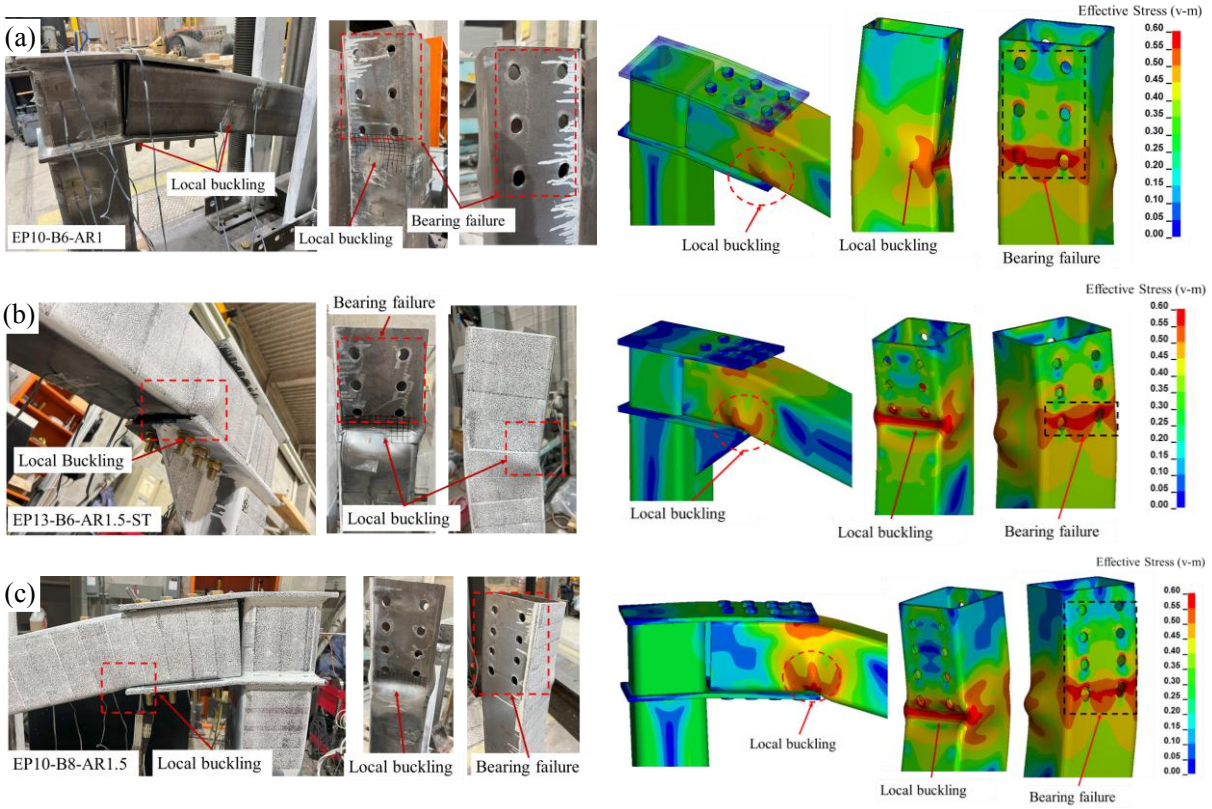

Fig. 5-6: A comparison between the proposed FEM and experimental results for three specimens: (a) EP10-B6-AR1.0, (b) EP13-B6-AR1.5-ST, and (c) EP10-B8-AR1.5.

Table 5-3: Comparison between experimental test and FEM results

Specimen ID	Mode of Failure	Experimental Ultimate moment (kN.m)	FEM Ultimate moment (kN.m)	FEM/EXP
EP13-B6-AR1.5	Local buckling and block shear failure at the beam.	96.3	94.4	0.98
EP10-B6-AR1.5	Local buckling and block shear failure at the beam.	90.2	88.3	0.98
EP10-B6-AR1.0	Local buckling and bolt bearing failure at the beam	97.1	96.6	0.99
EP13-B8-AR1.5	Local buckling and bolt bearing failure at the beam	93.8	94.03	1.01
EP13-B6-AR1.5-ST	Local buckling and bolt bearing failure at the beam	87.1	86.2	0.99
EP10-B8-AR1.5	Local buckling and bolt bearing failure at the beam	97.8	95.03	0.97

5.4 Study Parameters

A comprehensive parametric analysis involving 162 FEM was conducted to investigate the impact of different geometric parameters along with different reinforced techniques for the column on the mechanical performance of the L-shape modular connection. These models incorporate a combination of several parameters, including the thickness of the extended plate (T_{pl} = 8, 13, 15 mm), the number of bolts (B = 6, 8, 10), the bolt diameter (D = 16, 22 mm), and the bolt arrangement ratio (AR = 1.5, 1, 0.6), all of which are based on the CSA S16 (CSA 2019) guidelines for bolt pitch limitations. The ratio between perpendicular and parallel pitch between bolts P_n/P_p was implemented using the AR abbreviation (i.e., AR1.5=P_n/P_p=1 .5, AR1= P_n/P_p=1, and AR0.6= P_n/P_p=0 .6). Additionally, three reinforcement techniques are applied to strengthen the column and lower extended plate: stiffeners, concrete, and a combination of both stiffeners and concrete. A concrete mix of 30 MPa was poured inside the HSS column to enhance rigidity and buckling resistance. The interplay of these parameters is visually represented in Fig. 5-7 and Fig. 5-8. The extended plate dimensions depended on the bolt arrangement in HSS sections and the number of bolts. However, other parameters were kept constant throughout the parametric study, such as the length of the specimen, cross sections of the beam and column, and the pitch distance between bolts perpendicular to the member axis (Pn), which was considered as a factor of section depth (H) as follows: P_n=0.5H. The parallel edge distance was set equal to the normal edge distance to prevent premature rupture failure of the lower extended plate by tearing failure. Utilizing the results extracted from the 162 FEM, design charts have been developed to predict failure modes and guide the selection of various parameters, aiding decision-making during the design stage. Six models were analyzed for the L-shaped long bolt HSS connection under monotonic load, with each beam subjected to a different displacement rate to assess its impact on the general performance of

the proposed connection. The L-shape connection had a fixed bolt configuration of EP15-B6-AR1.5-ST for both sides. For the L-shape prototype connection, the displacement load for both beam 1 and beam 2 was applied simultaneously. The displacement percentages applied to beam 2 were 20%, 30%, 40%, 50%, 60%, and 70% of the failure displacement of beam 1, as shown in Table 5-4. The value of 210 mm displacement was determined when the load dropped to 80% of the ultimate load based on the studied one-dimensional connection. The boundary conditions and the mesh configuration for the L-shape are illustrated in Fig. 5-9.

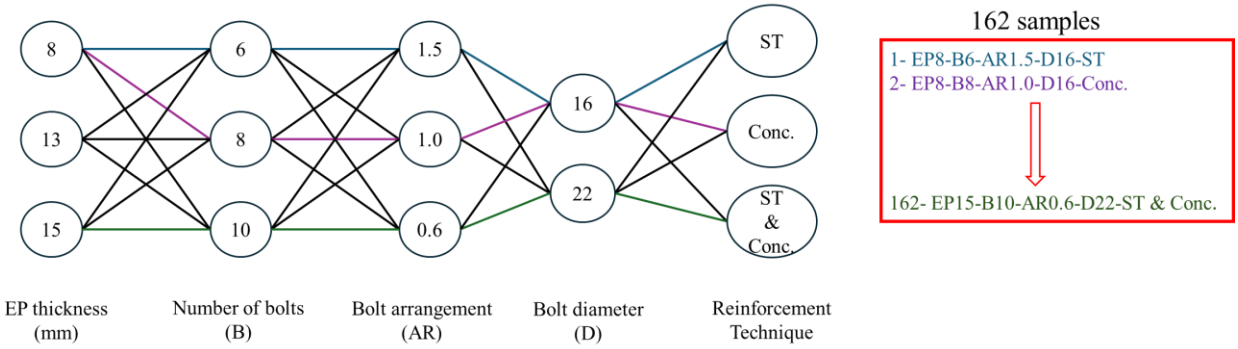

Fig. 5-7: A visual representation of the interplay between various parameters to generate 162 models

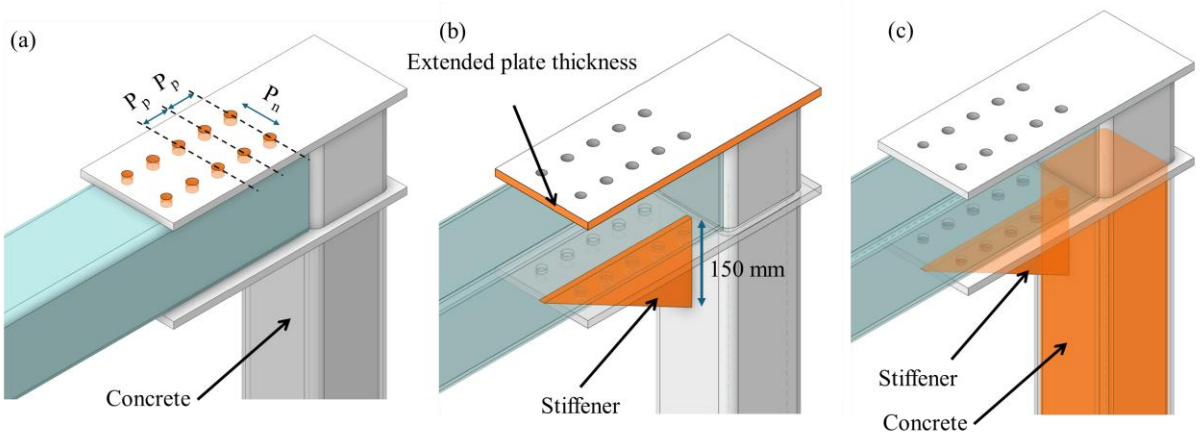

Fig. 5-8: Different reinforcement techniques incorporated in the study: (a) concrete, (b) stiffener, and (c) stiffener and concrete

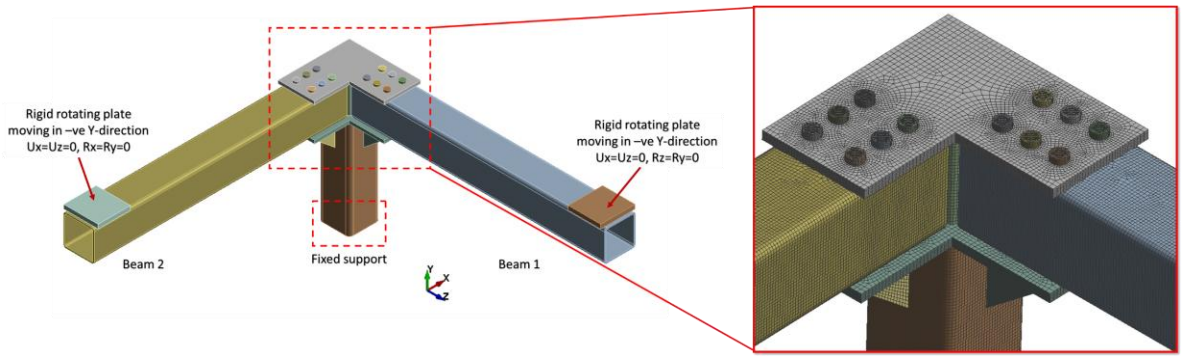

Fig. 5-9: Boundary conditions for the L-shape of the HSS connection

Table 5-4: Studied parameters of two-dimensional L-shape prototype connection

Specimen number	Connection ID		Applied displacement	
	beam 1	beam 2	beam 1	beam 2
1	EP15-B6-AR1.5-ST	EP15-B6-AR1.5-ST	210 mm	42 mm
2	EP15-B6-AR1.5-ST	EP15-B6-AR1.5-ST	210 mm	63 mm
3	EP15-B6-AR1.5-ST	EP15-B6-AR1.5-ST	210 mm	84 mm
4	EP15-B6-AR1.5-ST	EP15-B6-AR1.5-ST	210 mm	105 mm
5	EP15-B6-AR1.5-ST	EP15-B6-AR1.5-ST	210 mm	126 mm
6	EP15-B6-AR1.5-ST	EP15-B6-AR1.5-ST	210 mm	147 mm

5.5 Results and Discussion

The moment rotation curves of 162 FEMs with different reinforced techniques are shown in Fig. 5-10 to 5-12. Different failure modes were found within the 162 FEMs based on the different studied geometric parameters, such as bolt bearing failure, local buckling of the beam, tensile rupture failure of the upper extended plate, local buckling of the column cape, local buckling of the stiffener and local buckling of the column, as shown in Fig. 5-13. The following sections will explain how the studied parameters trigger the specific failure modes. Each parameter's influence on the failure modes will be thoroughly analyzed and discussed for a comprehensive understanding.

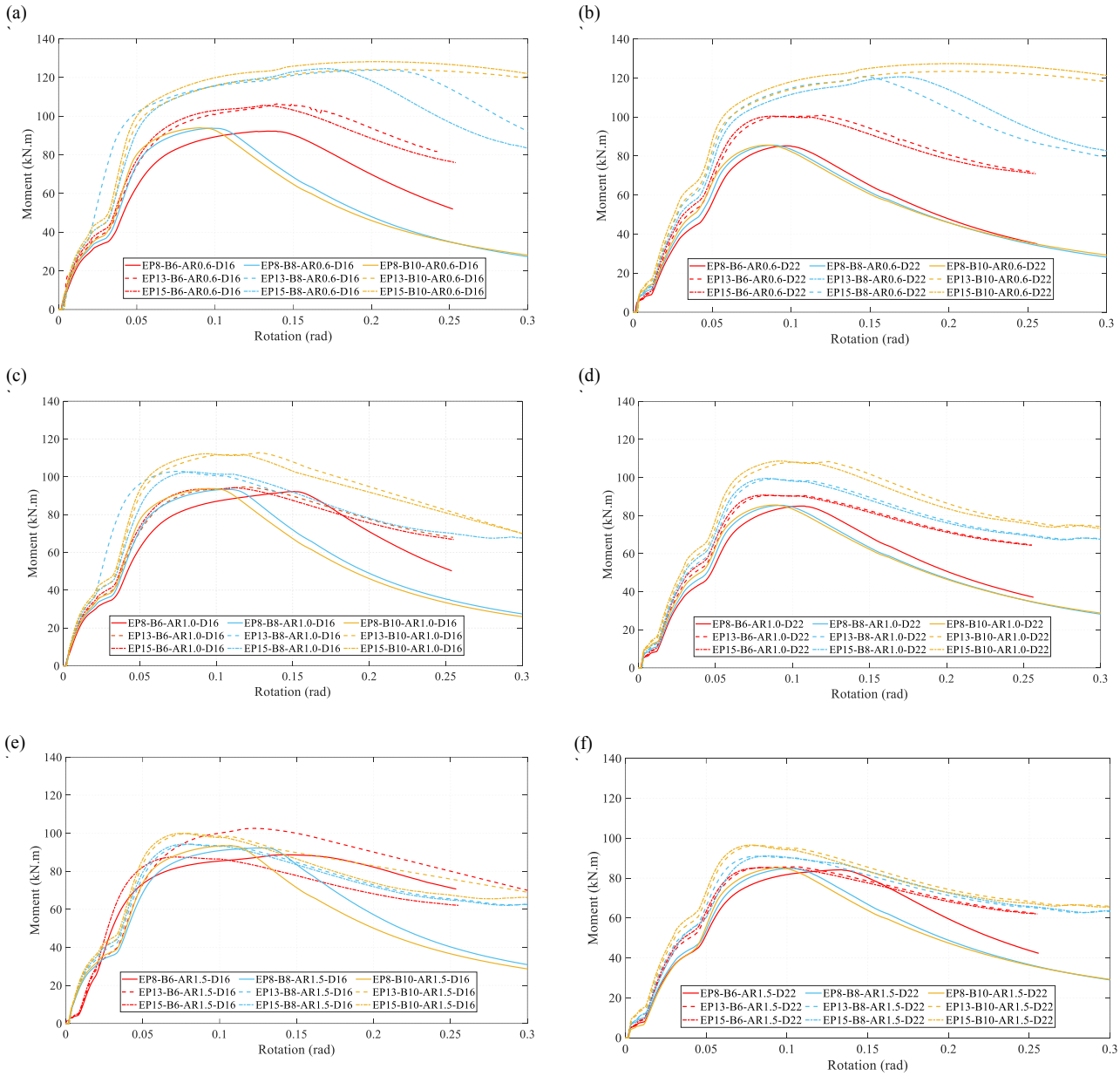

Fig. 5-10: Moment-rotation curves for FEMs reinforced by concrete with different extended plate thicknesses and bolt numbers (a) AR0.6-D16, (b) AR0.6-D22, (c) AR1.0-D16, (d) AR1.0-D22, (e) AR1.5-D16, and (f) AR1.5-D22

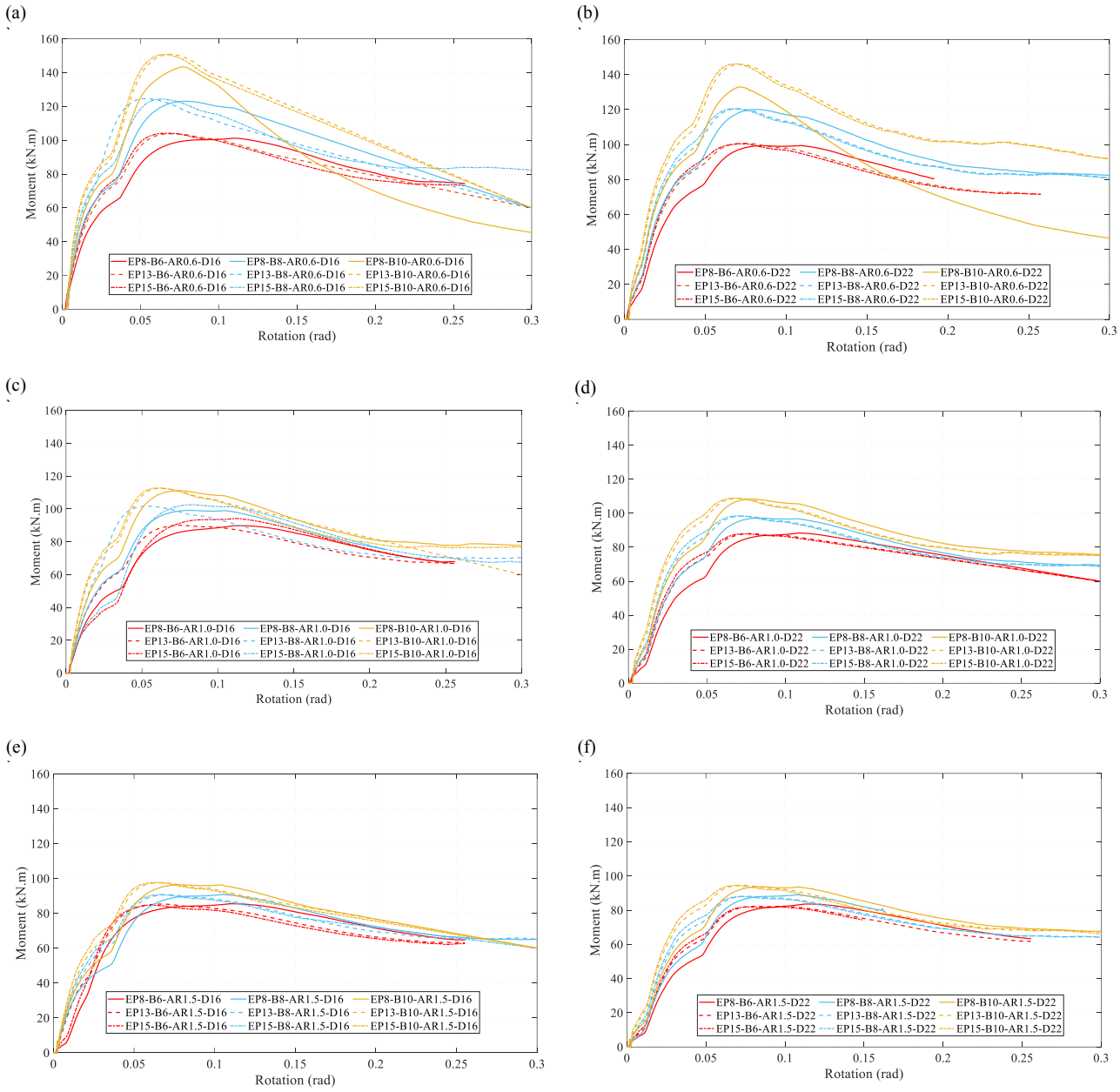

Fig. 5-11: Moment-rotation curves for FEMs reinforced by concrete and stiffener with different extended plate thicknesses and bolt numbers (a) AR0.6-D16, (b) AR0.6-D22, (c) AR1.0-D16, (d) AR1.0-D22, (e) AR1.5-D16, and (f) AR1.5-D22

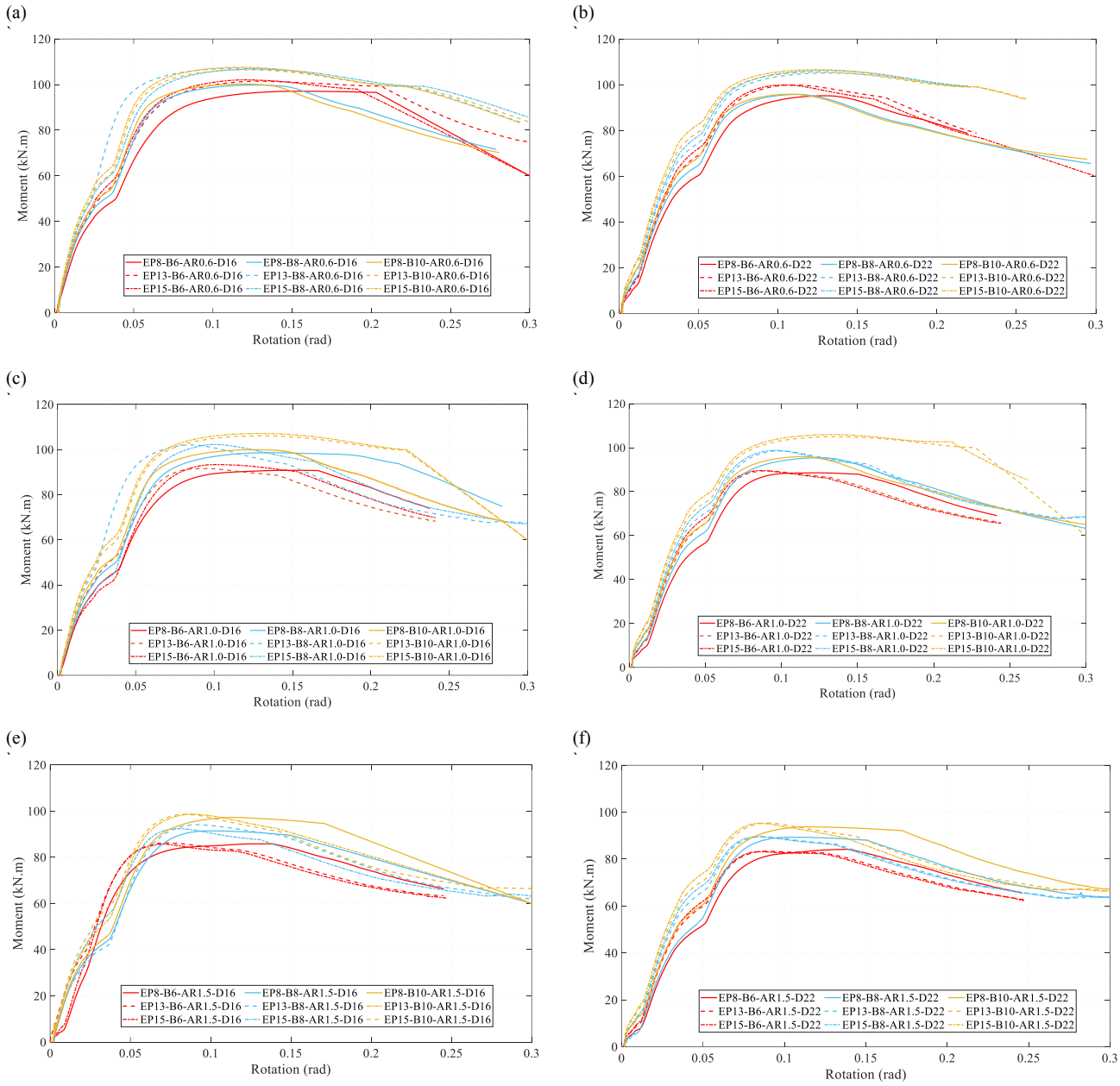

Fig. 5-12: Moment-rotation curves for FEMs reinforced by stiffener with different extended plate thicknesses and bolt numbers (a) AR0.6-D16, (b) AR0.6-D22, (c) AR1.0-D16, (d) AR1.0-D22, (e) AR1.5-D16, and (f) AR1.5-D22

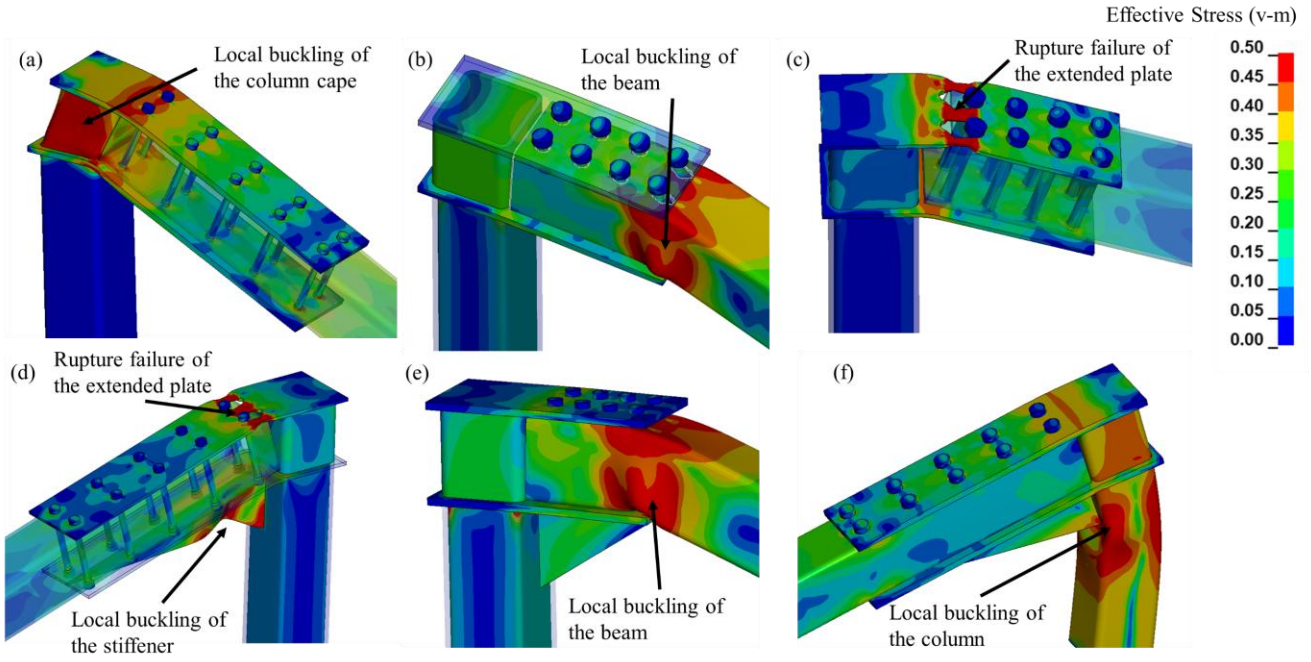

Fig. 5-13: The failure mode of different specimens (a) EP13-B10-AR0.6-D16-Conc.; (b) EP13-B8-AR1-D22-Conc.; (c) EP8-B8-AR1.0-D22-Conc.; (d) EP8-B10-AR0.6-D16-ST & Conc.; (e) EP13-B8-AR1.5-D16-ST & Conc.; and (f) EP15-B10-AR0.6-D16-ST

5.5.1 Influence of Bolt Arrangement

Three distinct bolt arrangements (AR1.5, AR1.0, and AR0.6), which considered the minimum and maximum limits of the bolt pitches according to CSA S16-19 (CSA 2019), were studied using three different reinforcement techniques for columns and connections. Each technique affected the load-bearing mechanics of the respective bolt arrangement. The bolt arrangement influenced the connection failure mechanism, localizing the failure mode at various locations such as the beam, column, column cap, stiffener, or extended plate. The applied force on the beam is distributed through the bolt bearing and the beam bearing on the extended plate. The AR1.5 bolt arrangement triggered bolt-bearing failure at an earlier loading stage, leading to stress concentration in the outer bolt row, and causing local buckling of the beam across the three reinforcement techniques. These reinforcement techniques had varying impacts on the ultimate moment capacity and ultimate rotation. Concrete reinforcement proved to be the most effective, increasing the ultimate capacity

by 1.45 times the plastic moment capacity with a bolt configuration of eight bolts. This configuration allowed the extended plate to rotate, which did not restrict the bolt bearing on the beam flange. On the other hand, reinforcement of the connection with a stiffener was the least effective, achieving an ultimate capacity of only 1.3 times the plastic moment of the beam, as the stiffener caused the yielding of the column flange. Concrete reinforcement resulted in higher capacity, reaching 1.4 times the plastic moment of the beam, compared to reinforcement by stiffener. Reinforcement by concrete and stiffener decreased the ultimate rotation of the connection (0.05 rad) by 58% and 29% compared to reinforced concrete and stiffener reinforcement (0.12 and 0.07 rad, respectively). Reinforcement of the column to increase its rigidity by concrete, particularly with bolt arrangement AR1.5, only led to a decreased ultimate rotation of 0.02 rad. This is not significant, as the bolt arrangement AR1.5 triggered the failure of the beam by local buckling.

The three reinforcement techniques significantly impacted the mechanical performance and failure mode of the AR0.6 bolt arrangement, featuring an eight-bolt configuration. Stiffener reinforcement induced local buckling in the column due to the bearing force exerted by the stiffener, resulting in yielding at a lower capacity compared to other methods. In contrast, concrete reinforcement prevented local buckling by increasing the column's rigidity. However, the connection's ultimate rotation increased to 0.25 radians as the extended plate experienced extensive rotation and yielding, delaying bolt-bearing failure. This occurred due to increased bolt pitches and significant force transfer through the extended plates until the beam buckled locally under stress concentration from the bolt bearing. Reinforcement using both stiffener and concrete is highly recommended, particularly with maximum pitch bolt arrangements (AR0.6), as it prevents unfavourable failures like local buckling of the column, adhering to the "strong column, weak beam" principle observed

in AR1.5 arrangements as the connection failed by local buckling of the beam. Additionally, this combined reinforcement technique reduces the connection's ultimate rotation by 76% and 60% compared to using either concrete or stiffener reinforcement alone, as it limits the extensive rotation of the column and extended plate. Furthermore, it achieves the highest ultimate moment capacity among the reinforcement techniques, reaching 1.8 times the plastic moment of the beam.

The AR1.0 bolt arrangement demonstrated a combined behaviour similar to the AR1.5 and AR0.6 arrangements, with the reinforcement technique and a number of bolts determining the failure mode and ultimate capacity of the connection. For configurations with eight and six bolts and extended plates of 13mm and 15mm thickness, all reinforcement techniques resulted in local buckling of the beam, with minimal differences in ultimate capacity. The stiffener technique proved to be the most effective, achieving 1.53 times the plastic moment of the beam by preventing the extended plate from yielding and allowing the bolts to bear the load. To reduce the ultimate rotation of the connection to 0.04 radians, it is recommended to use stiffener and concrete techniques, as they help mitigate the extensive rotation and yielding of the extended plate due to its length and bolt arrangement. To uphold the principle of "strong column, weak beam" and prevent undesirable failures in the column or extended plate, it is recommended to use concrete and stiffener reinforcement techniques for all bolt arrangements (AR1.5, AR1.0, and AR0.6). This approach ensures that the connection achieves its capacity through bolt-bearing failure, leading to local buckling of the beam. Unlike other reinforcement methods, this technique prevents the undesirable failure modes observed in bolt arrangements AR1.0 and AR0.6, regardless of other studied parameters.

5.5.2 Influence of Extended Plate Thickness

The thickness of the extended plate (8 mm, 13 mm, and 15 mm) significantly influences the failure mode and capacity of the proposed connection, as shown in Fig. 5-10, Fig. 5-11, and Fig. 5-12. When an 8 mm thick extended plate was used, regardless of the number of bolts and bolt diameter, the connection experienced premature failure due to tensile rupture within the smaller/net cross-section of the plate at the level of the bolts Fig. 5-13.c. However, using a stiffener and concrete reinforcement technique eliminated this premature failure. This approach led to increased stress concentration as more loads were transferred through the stiffener than the extended plate, especially with bolt arrangements AR1.5 and AR1.0. For the bolt arrangement AR0.6 with ten bolts, the stiffener yielded and buckled locally, as shown in Fig. 5-13.d. Reinforcement by stiffener alone could eliminate rupture failure of the extended plate with bolt arrangement AR1.5, as this arrangement triggers bolt bearing at an earlier stage, transferring almost all forces through the outer bolt row. The stiffener reinforcement could also eliminate rupture failure of the extended plate with bolt arrangement AR1.0 with six bolts. However, when the extended length of the plates exceeded 276 mm, the stiffener began to bear more on the column, yielding and allowing more rotation for the extended plate, leading to its rupture.

Increasing the thickness of the extended plates from 8 mm to 13 mm and from 8 mm to 15 mm resulted in an average ultimate capacity enhancement of 20% and 25%, respectively, particularly for concrete reinforcement techniques. However, for other reinforcement methods, the increase in thickness does not significantly affect the ultimate capacity due to the presence of a stiffener, which prevents the extended plate from rotating under the applied moment on the connection. It is important to note that the reinforcement technique involving stiffeners and bolt arrangements (i.e., the length of the extended plate) plays a crucial role in preventing premature connection failure

due to rupture of the extended plate, even when its thickness is 8 mm. This approach ensures that the desired failure occurs through local buckling of the beam.

5.5.3 Effect of bolt numbers and diameter

The study investigated the impact of the connection mechanism by utilizing three different numbers of bolts (six, eight, and ten) with two different bolt diameters and various reinforcement techniques. Fig. 5-14, Fig. 5-15, and Fig. 5-16 illustrate the failure modes experienced by the specimens based on the number of bolts and bolt arrangements (AR1.0, AR1.5, and AR0.6) with different reinforcement techniques. These techniques played a crucial role in enhancing moment capacity and altering failure modes. For bolt arrangement AR0.6, using six bolts with concrete or stiffener techniques resulted in a favourable failure mode through local buckling of the beam. However, increasing the number of bolts from 6 to 8 or 6 to 10 with stiffener reinforcement led to local buckling of the column. For concrete reinforcement, increasing the number of bolts from 8 to 10 caused local buckling of the column cap, as shown in Fig. 5-13.a. The combination of stiffener and concrete techniques, especially with the highest number of bolts, was found to be the most effective, achieving a higher capacity of 2.2 times the plastic moment of the beam, as shown in Fig. 5-16. For bolt arrangement AR1.5, increasing the number of bolts from 6 to 8 or from 6 to 10 did not influence the failure mode for any of the reinforcement techniques. The connection consistently failed by local buckling of the beam, as the AR1.5 arrangement triggered bolt bearing mechanics at an earlier stage, resulting in the same ultimate moment capacity for all three reinforcement techniques. However, increasing the number of bolts from 6 to 8 or from 6 to 10 did increase the ultimate capacity by an average of 9% and 16%, respectively, as shown in Fig. 5-14.

For all reinforcement techniques with bolt arrangement AR1.0, using different numbers of bolts resulted in a favourable failure mode, with the beam failing by local buckling. However, with

stiffener reinforcement, increasing the number of bolts to ten caused more bearing on the column flange, leading to local buckling of the column. Increasing the number of bolts from 6 to 8 and 6 to 10 improved the connection capacity for 16 mm and 22 mm bolt diameters by an average of 11% and 18%, respectively, as shown in Fig. 5-15. This increase in bolts distributed the bearing forces more effectively and delayed the local buckling of the beam. For the 22 mm bolt diameter, the average ultimate moment capacity decreased by 10% for different bolt numbers and arrangements compared to the 16 mm bolt diameter. This reduction is attributed to the larger bolt-hole area at the beam flange, which caused higher stress concentration earlier at the beam's compression flange due to bolt-bearing force, leading to local buckling of the beam at a lower capacity value. It is worth noting that the bolt diameter does not influence the failure mode of the connection, as the smallest bolt diameter of 16 mm was designed to resist ultimate bolt bearing and bolt shear failure. Therefore, it is recommended not to increase the bolt diameter, as it triggers local buckling failure of the beam

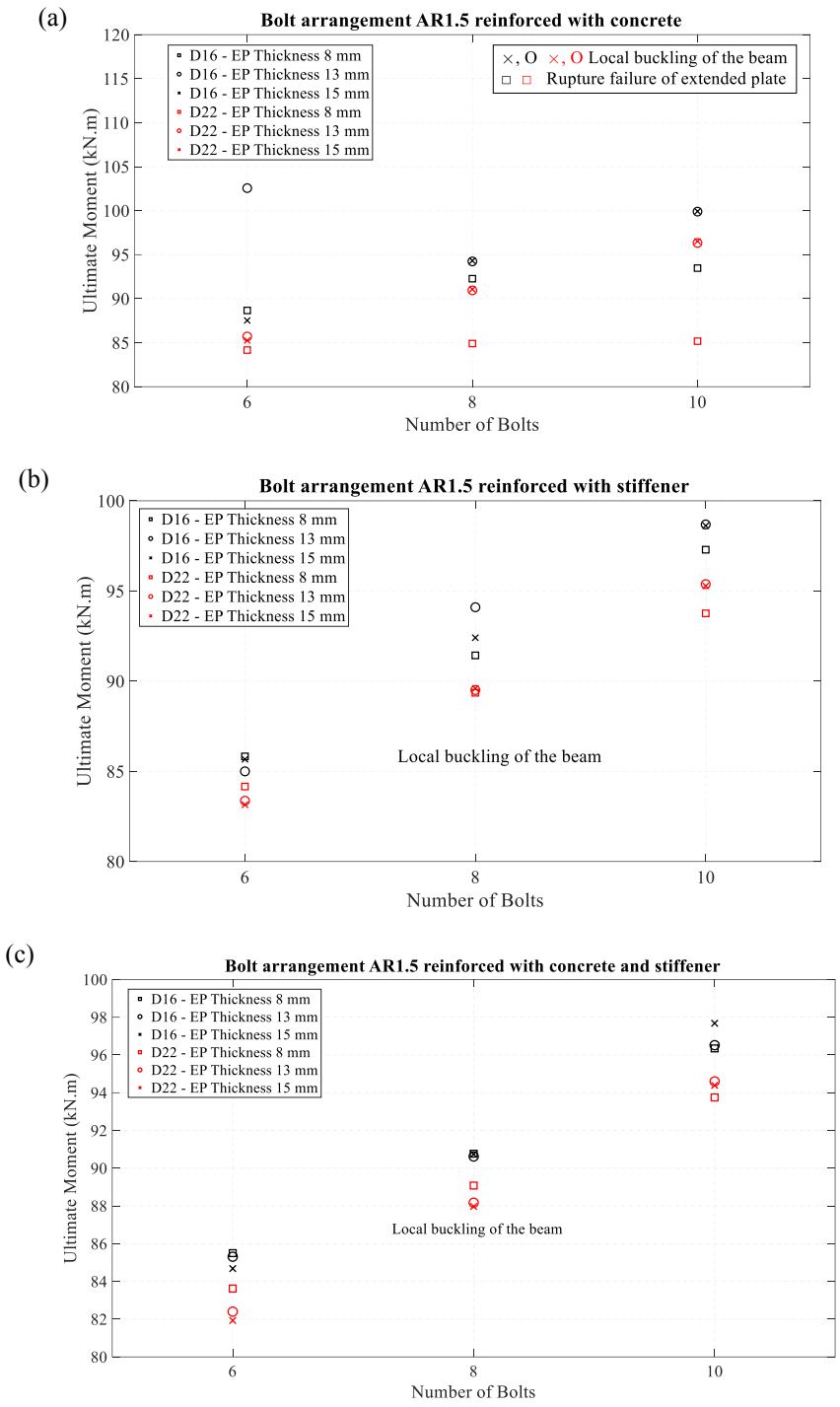

Fig. 5-14: Relation between the number of bolts vs extended plate thickness vs bolt diameter vs ultimate moment of bolt arrangement AR1.5 for different reinforcement techniques: (a) concrete, (b) stiffener, and (c) concrete with stiffener

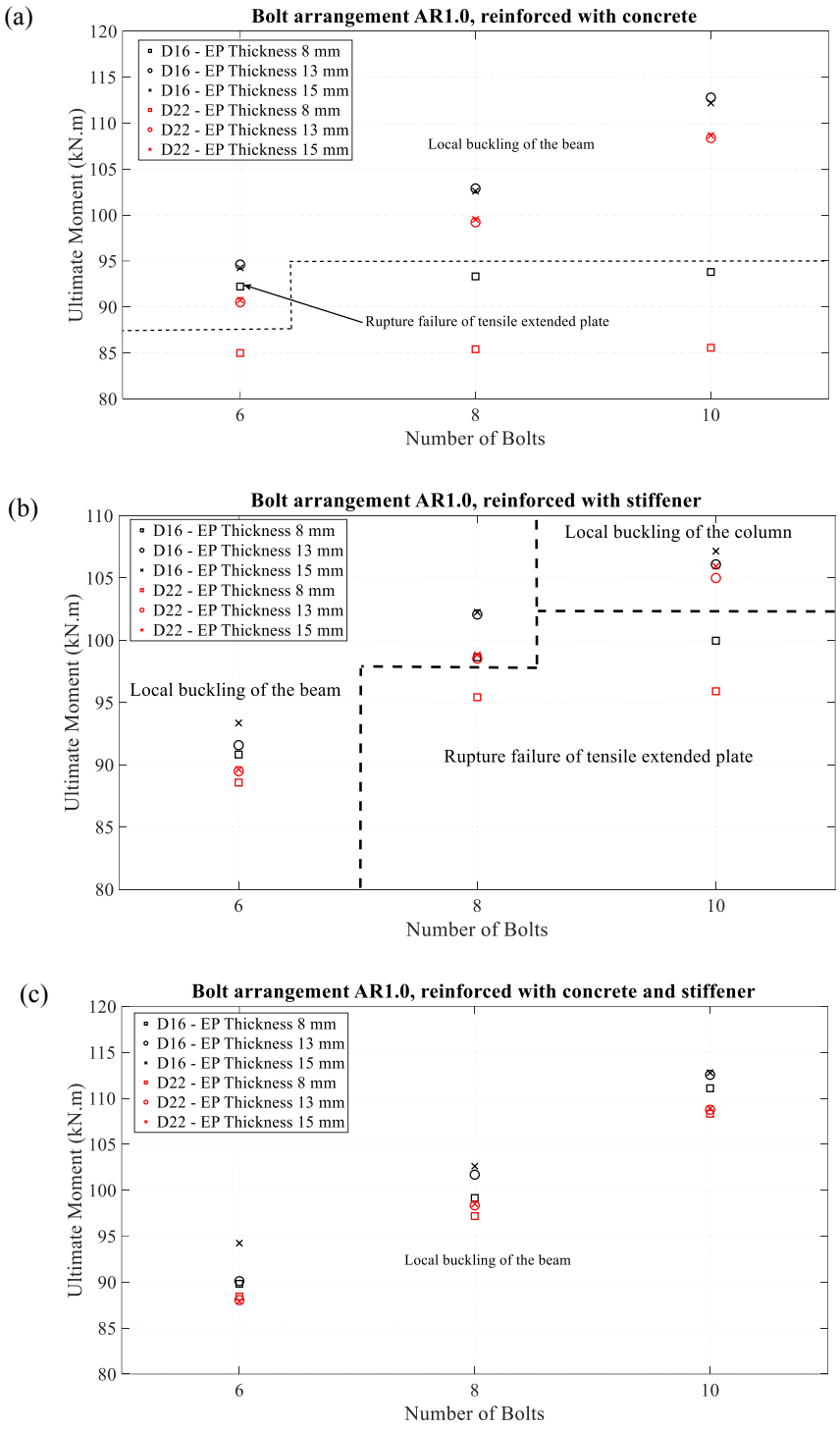

Fig. 5-15: Relation between the number of bolts vs extended plate thickness vs bolt diameter vs ultimate moment of bolt arrangement AR1.0 for different reinforcement techniques: (a) concrete, (b) stiffener, and (c) concrete with stiffener

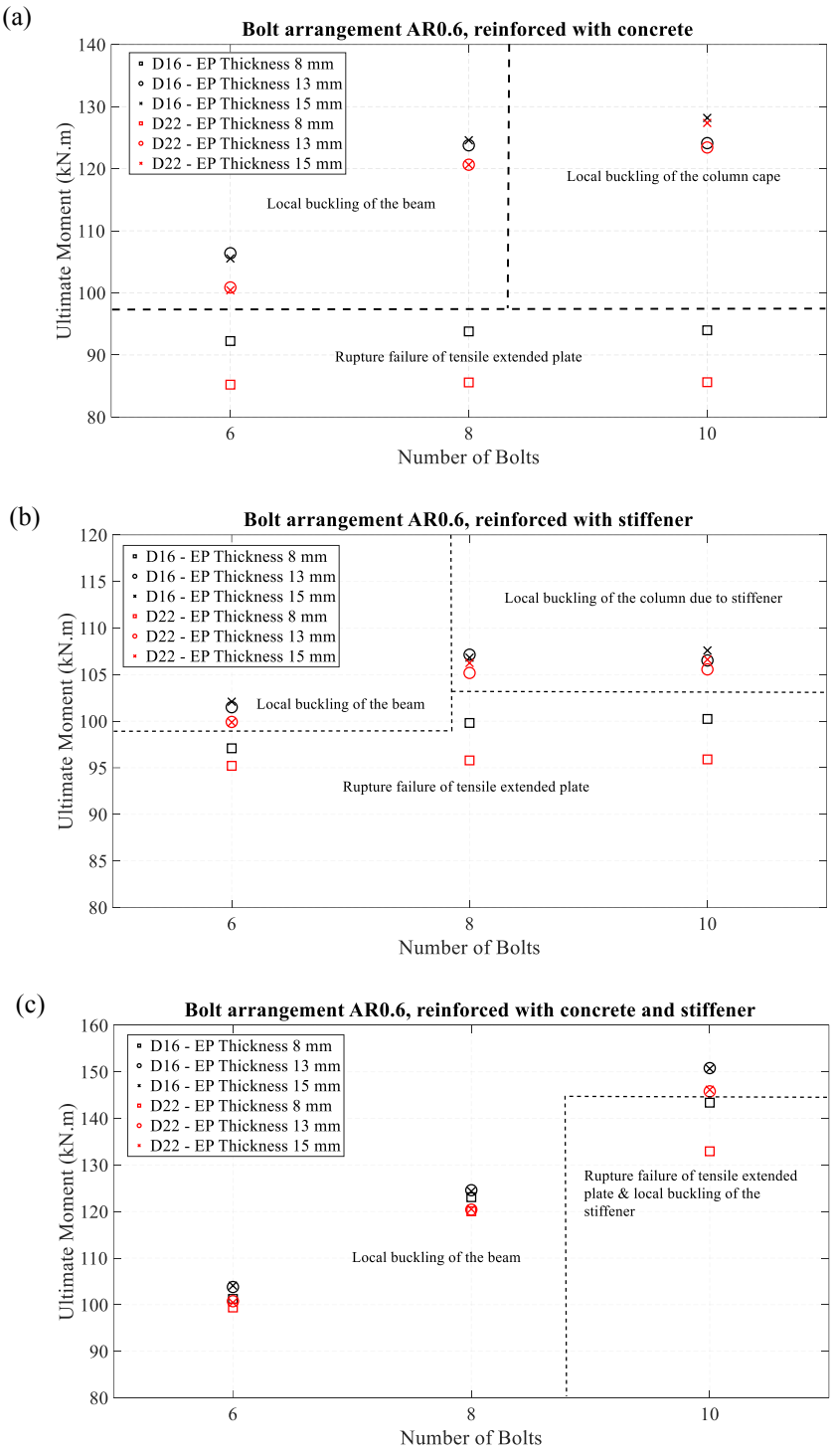

Fig. 5-16: Relation between the number of bolts vs extended plate thickness vs bolt diameter vs ultimate moment of bolt arrangement AR0.6 for different reinforcement techniques: (a) concrete, (b) stiffener, and (c) concrete with stiffener

5.6 Comparison between different reinforcement techniques

Fig. 5-17 and Fig. 5-18 present a comparison of different reinforcement techniques in terms of their impact on the ultimate moment and rotation of the connection. Each reinforcement technique is compared to unreinforced models across different bolt configurations. It was found that bolt arrangements, particularly AR1.5 and AR1.0, had a dominant role in enhancing ultimate capacity, regardless of the reinforcement techniques used and the number of bolts. However, for bolt arrangement AR0.6, the combined use of concrete and stiffeners increased the ultimate capacity of the ten-bolt configuration by 35% compared to the unreinforced model because it delayed stress concentration, which caused local buckling of the beam flange. On the other hand, when the number of bolts was reduced to six, this delay in stress concentration diminished, causing the connection to exhibit a similar ultimate moment to that of the unreinforced configuration. For the AR0.6 arrangement, using concrete reinforcement proved especially beneficial in the eight- and ten-bolt configurations. It helped mitigate local buckling in the column, enabling the beam to carry a higher load as the outer bolts remained less affected by stress concentration. As a result, the ultimate capacity increased by 1.5 times compared to their unreinforced models. Reinforcement techniques had a significant effect on the ultimate rotation, as shown in Fig. 5-18. For the AR1.5 bolt configuration, utilizing either the stiffener or concrete reinforcement technique individually led to a 60% reduction in the ultimate rotation compared to the unreinforced models. However, when both were combined, ultimate rotation decreased by 70% across all bolt configurations (i.e., six, eight, and ten bolts) compared to the unreinforced models. In the AR0.6 bolt arrangement, concrete reinforcement reduced ultimate rotation by an average of 35% across different bolt configurations. Meanwhile, the stiffener technique proved more effective in improving column rigidity, reducing ultimate rotation by approximately 50% for all bolt configurations while also preventing excessive deformation of the extended plates. However, while stiffeners improved

rotational behaviour, they did not significantly increase the overall capacity, as the column yielded due to bearing effects. The use of concrete and stiffeners had a greater impact on reducing the ultimate rotation, achieving an 84% reduction for eight and ten-bolt configurations and a 60% reduction for six-bolt configurations compared to their unreinforced configurations. This was mainly because the concrete reinforcement prevented column yielding, which otherwise resulted from the stiffener bearing. Using either the stiffener or concrete technique with bolt arrangement AR1.0 had the same impact as bolt arrangement AR1.5, as increased capacity through bearing without causing more deflection in the extended plate. Both configurations decreased the ultimate rotation by an average of 52% compared to unreinforced configurations. However, when utilizing both stiffener and concrete techniques, the rotation response changes. For the six-bolt configuration, the behaviour is similar to the bolt arrangement AR1.5. When the number of bolts is increased to eight and ten, the behaviour aligns with bolt arrangement AR0.6, resulting in a decrease in ultimate rotation by an average of 76% compared to unreinforced configurations.

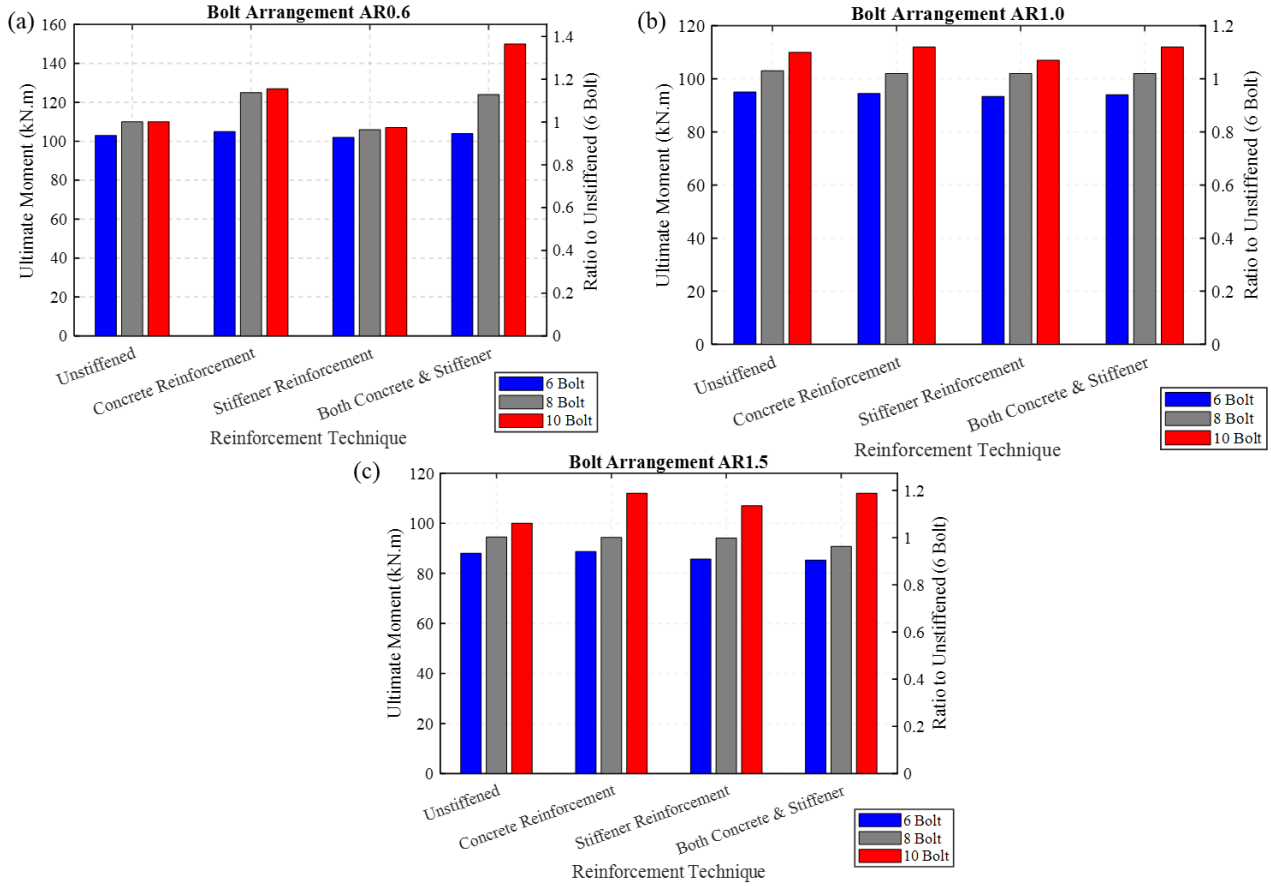

Fig. 5-17: Comparison of ultimate connection capacity for different bolt arrangements using different reinforcement techniques: (a) AR0.6, (b) AR1.0, and (c) AR1.5

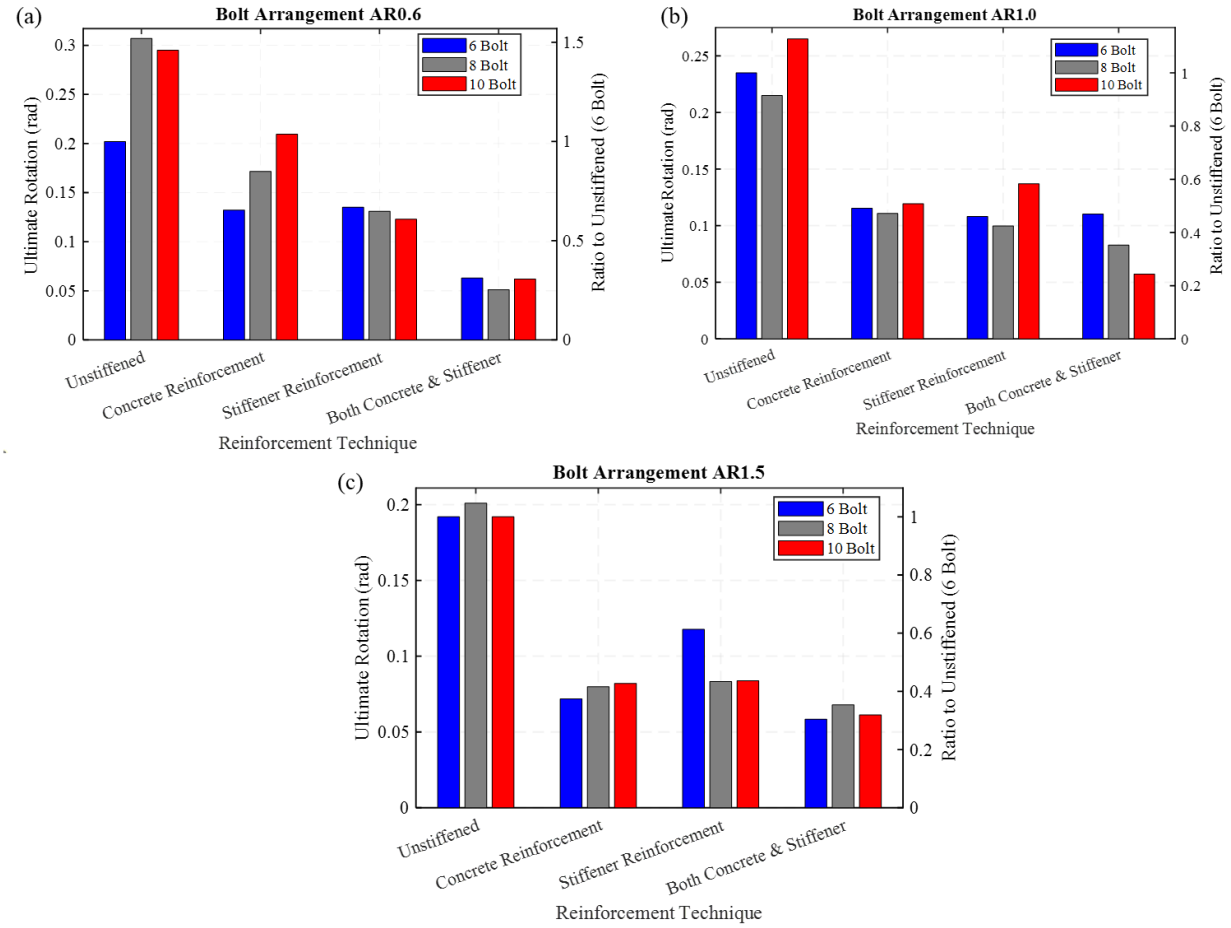

Fig. 5-18: Comparison of ultimate connection rotation for different bolt arrangements using different reinforcement techniques: (a) AR0.6, (b) AR1.0, and (c) AR1.5

5.7 Performance of L-shape connection under different applied displacements

Six L-shaped specimens were tested, utilizing the bolt configuration EP15-B6-AR1.5-ST for two beams. This configuration aimed to induce bolt bearing on the beam at an early stage, achieving a favourable failure mode by forming a hinged support at the beam. The moment-rotation curves for both beams under different displacement ratios are presented in Fig. 5-19. It was observed that the column experienced varying rotations for the two beams. After reaching the target load for beam 2, the load path was primarily transferred by the stiffener from beam 2 to the column, leading to plastic deformation of the column beneath the stiffener, as shown in Fig. 5-20.c. Beam 2 exhibited a 50% higher rotation rate than beam 1, especially with applied displacements from 40% to 70%,

due to the bi-bending moment applied to the column. The L-shaped connection demonstrated similar behaviour to the one-dimensional prototype, particularly for beam 1, where the connection failed due to local buckling of the beam at various displacement ratios without any failure signs in the extended plates.

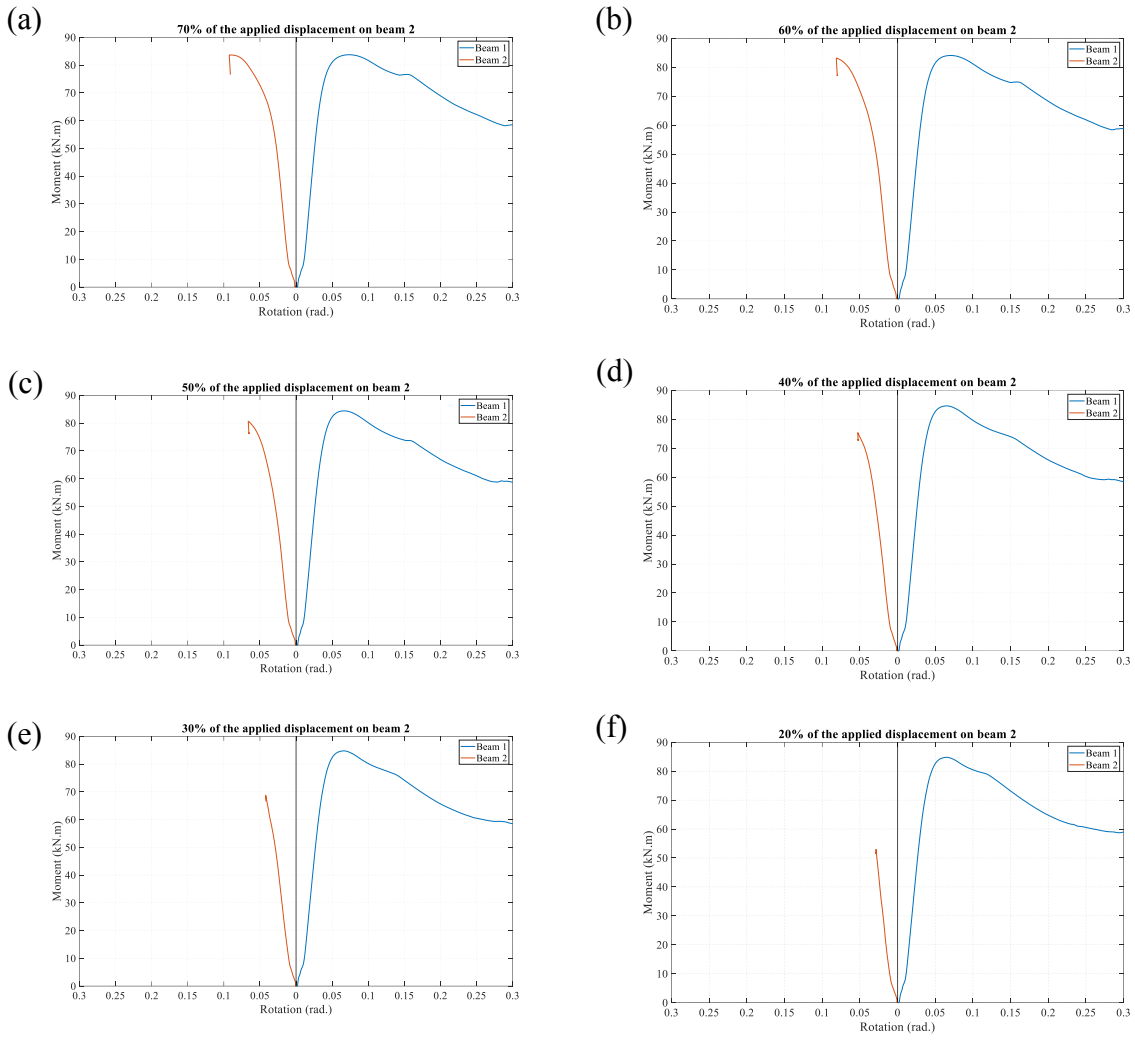

Fig. 5-19: Moment rotation curves for the two beams in the L-shape prototype connection under different applied displacements (a) 70%; (b) 60%; (c) 50%; (d) 40%; (e) 30%; and (f) 20%

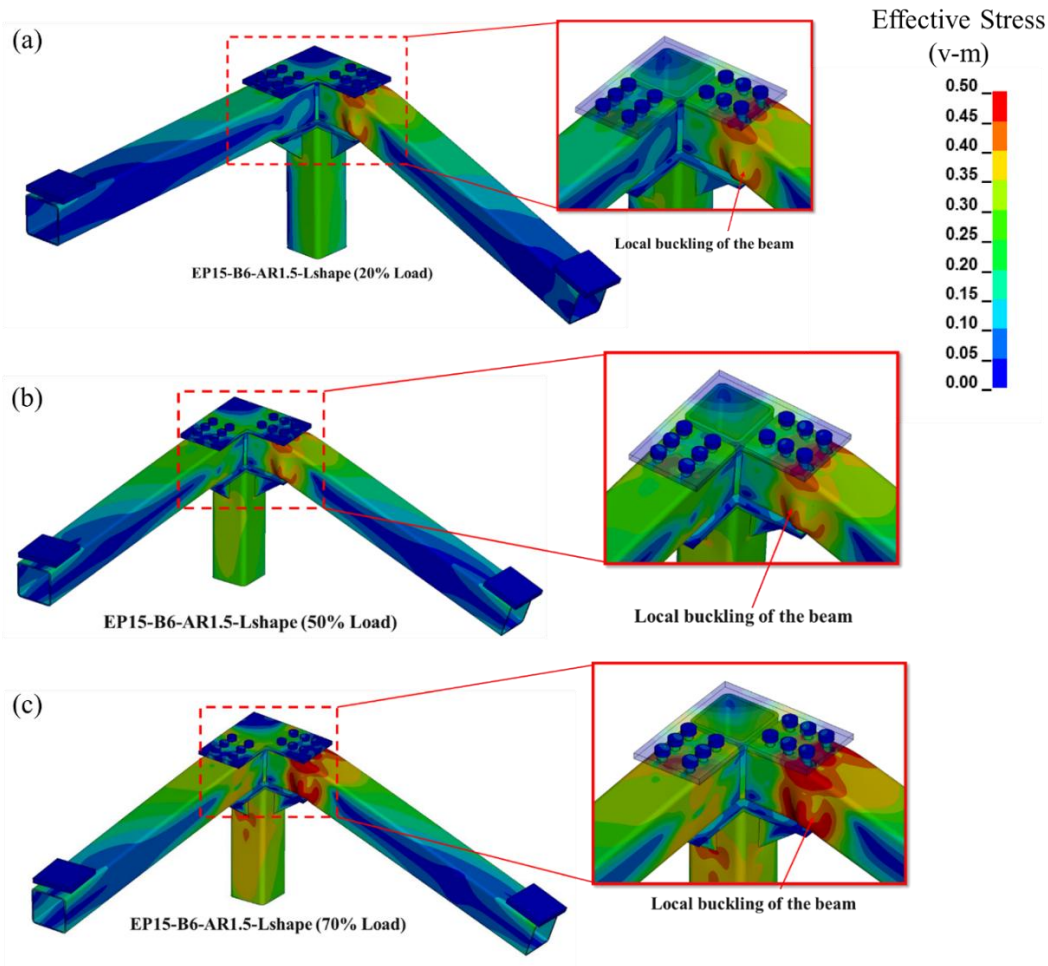

Fig. 5-20: Failure modes of the L-shape prototype connection under different applied displacement ratios between beam 2 to beam 1: (a) 20%, (b) 50%, and (c) 70%.

5.8 Failure mode prediction charts

A total of 162 FEM and six test specimens were conducted to cover the main design parameters, making it essential to summarize the failure modes for developing design charts. These charts help predict the failure mode of a connection by adjusting various design parameters. The failure modes are categorized into five types: (1) Rupture of the tensile extended plate, (2) Local buckling of the stiffener, (3) Local buckling of the column cape, (4) Local buckling of the column, (5) Local buckling of the beam. The first two failures are considered premature, occurring suddenly at lower values before reacshing the connection's maximum capacity, which is less than the plastic moment of the beam. Additionally, the latter failure often leads to local buckling of the stiffener, especially

when concrete is used within the column. Conversely, local buckling of the column and column cape is considered an unfavourable failure mode, affecting the connection's integrity. Ideally, the failure mode should occur in the beam to adhere to the "strong column, weak beam" principle. These charts provide a streamlined method to achieve the desired connection strength and failure modes by selecting the optimal Reinforcement techniques, bolt diameter, number of bolts, and extended plate thickness without performing multiple iterations of full design analysis each time. Fig. 5-21 presents three failure mode charts for different bolt arrangements (AR1.5, AR1.0, AR0.6). Each chart contains subplots, where the first subplot illustrates the relationship between the connection's nominal moment and the beam's plastic moment, with the number of bolts ranging from 6 to 10 for different reinforcement techniques and bolt diameters. The subsequent subplots, categorized by three extended plate thicknesses (8, 13, 15 mm), show the relationship between the number of bolts and failure modes for different extended plate thicknesses. The design charts had certain constraints, such as maintaining constant column and beam cross-sections throughout the study. Specifically, the beam cross-section was HSS 152x152x6.4, and the column cross-section was HSS 152x152x9.54, based on the experimental specimens (Elhadary et al. 2024b). The charts can be utilized for two main purposes: (i) To select the desired failure mode for the connection by determining the required combination of reinforcement technique, extended plate thickness, number of bolts, and bolt diameter, (ii) To determine the required nominal connection moment by utilizing the secondary subplots of the chosen extended plate thickness and preferred failure mode associated with the used number of bolts, bolt diameter, and reinforcement technique. Fig. 5-21.c demonstrates the first method on the failure mode charts, allowing the selection of the preferred failure mode for the joint, such as the local buckling of the beam. This selection can be made from the lower subplots (highlighted in gray), considering an extended plate thickness of 8 mm.

Subsequently, the number of bolts and their diameter associated with the reinforcement technique (indicated by the dashed line) can be determined. In this case, it would be 8 bolts with a diameter of 16 mm, reinforced by concrete and a stiffener, necessary to achieve the desired failure mode. Finally, the upper graph can be used to accurately predict the ultimate moment of the joint based on that geometric combination, which will equal 1.8 times the plastic moment of the beam.

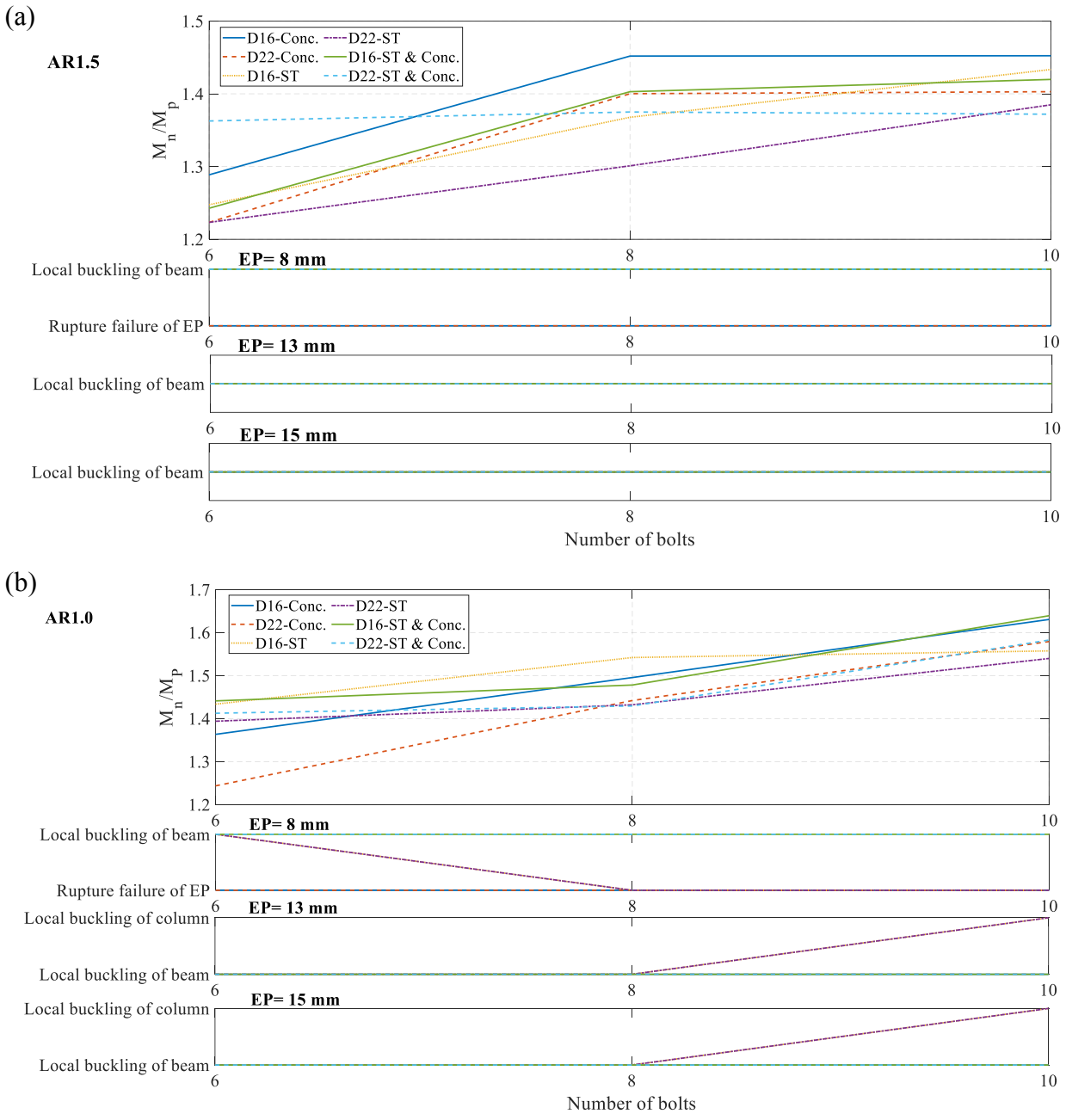

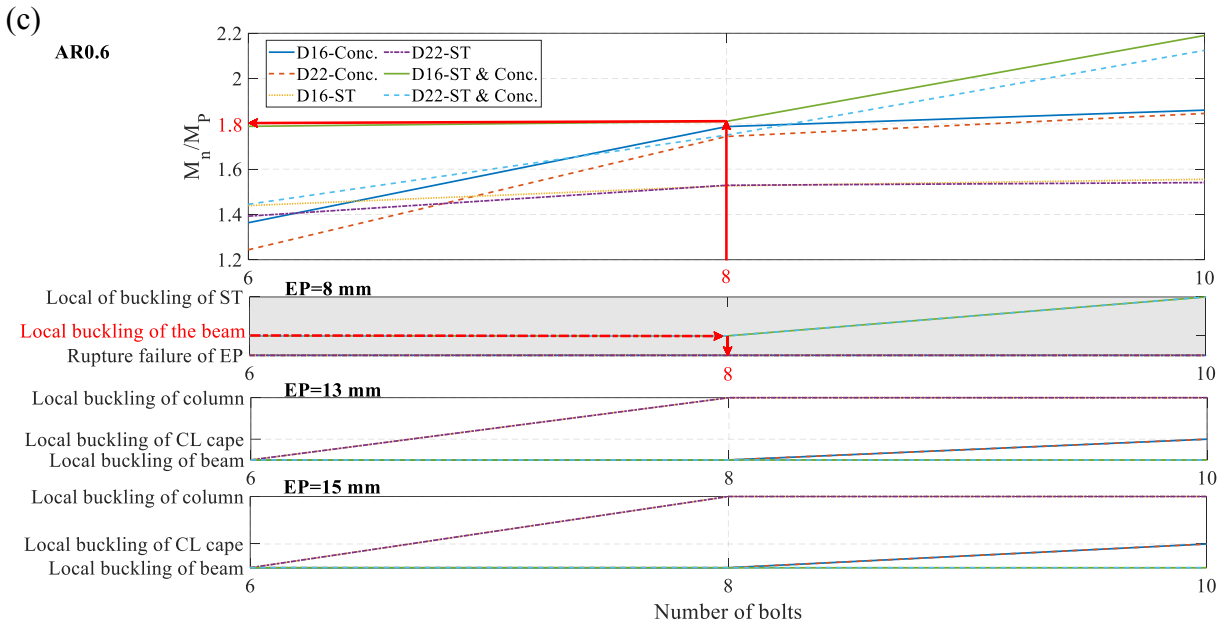

Fig. 5-21: Failure modes prediction charts for different reinforcement techniques and geometric parameters; (a) AR1.5; (b)AR1.0; and (c) AR0.6

5.9 Conclusions

This study investigates the mechanical performance of various reinforcement techniques for HSS-to-HSS connections in panelized modular houses designed for remote Indigenous regions. A total of 162 finite element models were developed using LS-Dyna software, validated against experimental results, and demonstrated good agreement with an average error of less than 3%. The analysis focused on the influence of these techniques on ultimate moment capacity, ultimate rotation, and failure modes across different geometric parameters. The findings reveal that these reinforcement techniques significantly impact mechanical performance, connection capacity gain, and failure modes. The following conclusions can be drawn from this analysis:

- It was found that the thickness of the extended plate (i.e., 8 mm, 13 mm, and 15 mm) plays a crucial role in determining the failure mode and capacity of the connection. Plates with a thickness of 8 mm are susceptible to premature tensile rupture. However, this failure mode can be effectively addressed through the application of stiffeners and concrete

reinforcement techniques. Increasing the plate thickness enhances the ultimate capacity, with a 20% and 25% increase observed for 13 mm and 15 mm plates, respectively. The reinforcement technique, especially involving stiffeners and specific bolt arrangements AR1.5, is crucial in preventing premature failure and ensuring desired failure through local buckling of the beam.

- For the AR1.5 bolt arrangement, concrete reinforcement was the most effective, increasing the ultimate capacity by 1.45 times the plastic moment capacity and allowing the extended plate to rotate without restricting the bolt bearing on the beam flange. Stiffener reinforcement was the least effective, achieving only 1.3 times the plastic moment due to column flange yielding. Combined concrete and stiffener reinforcement decreased ultimate rotation by 58% compared to individual reinforcement, achieving higher capacity and preventing premature failures.
- For the AR0.6 bolt arrangement, stiffener reinforcement induced local buckling in the column, resulting in lower capacity due to the bearing force exerted by the stiffener. In contrast, concrete reinforcement prevented local buckling by increasing the column's rigidity, but it also increased the ultimate rotation to 0.25 radians due to extensive rotation and yielding of the extended plate. The combined use of concrete and stiffener reinforcement is highly recommended, as it prevents local buckling, reduces ultimate rotation by 76%, and achieves the highest ultimate moment capacity, reaching 1.8 times the plastic moment.
- For the AR1.0 bolt arrangement, stiffener reinforcement was the most effective, achieving 1.53 times the plastic moment by preventing extended plate yielding and allowing the bolts to bear the load. Concrete reinforcement was effective but less so than stiffener

reinforcement, with minimal differences in ultimate capacity. The combined use of concrete and stiffener reinforcement is recommended to reduce ultimate rotation to 0.04 radians, upholding the "strong column, weak beam" principle and preventing undesirable failures in the column or extended plate

- The number of bolts (i.e., six, eight, and ten) significantly impacts the connection mechanism and failure modes across different bolt arrangements (AR1.0, AR1.5, and AR0.6) and reinforcement techniques. For AR0.6, using six bolts with concrete or stiffener techniques resulted in favourable local buckling of the beam, but increasing the number of bolts led to local buckling of the column or column cap. The combination of stiffener and concrete techniques with the highest number of bolts achieved the highest capacity (i.e., 2.2 times the plastic moment).
- For AR1.5, increasing the number of bolts did not change the failure mode but increased the ultimate capacity by 9% to 16%. For AR1.0, different numbers of bolts resulted in favourable local buckling of the beam, but increasing to ten bolts with stiffener reinforcement caused local buckling of the column. Increasing the number of bolts improved connection capacity by 11% to 18%, but larger bolt diameters (22 mm) decreased capacity due to higher stress concentration. Therefore, it is recommended to use the smallest bolt diameter (16 mm) to avoid premature local buckling of the beam.
- Design charts are proposed for different bolt arrangements that can predict failure modes by altering design parameters. The accuracy of the failure mode chart is validated with the tested specimens for the proposed connection.

5.10 References

Akbari Hamed, A., Charkhtab Basim, M., 2020. Experimental-numerical study on weakened HSS-to-HSS connections using HBS and RBS approaches. Structures 28, 1449–1465. https://doi.org/10.1016/j.istruc.2020.09.076

ASTM, 2014. A370: Standard test methods and definitions for mechanical testing of steel products. ASTM Int. 1–50.

ATCO, 2025a. Montreal Heart Institute modular hospital [WWW Document]. URL https://structures.atco.com/en-ca/modular-buildings/health-clinics.html (accessed 1.11.25).

ATCO, 2025b. Modular classrooms [WWW Document]. URL https://structures.atco.com/en-ca/modular-buildings/health-clinics.html?form=MG0AV3 (accessed 1.11.25).

Azimi, A., Ozakgul, K., 2024. Effect of rib stiffeners on end-plate connections of concrete-filled steel tubular (CFST) columns and I-section beams. Arab. J. Sci. Eng. https://doi.org/10.1007/s13369-024-09719-7

Canada, M.A., 2025. Emergency housing solutions [WWW Document]. URL https://modularaidcanada.ca/?form=MG0AV3 (accessed 1.11.25).

CSA, 2019. CSA-S16-19: Design of steel structures. Toronto, ON.

Digital Research Alliance of Canada, 2019.

Elhadary, M., Bediwy, A., Elshaer, A., 2025. Structural performance of novel steel connection for indigenous modular houses, in: Lecture Notes in Civil Engineering. Springer Singapore, Moncton, New Brunswick, pp. 253–266. https://doi.org/10.1007/978-3-031-61535-1_21

Elhadary, M., Bediwy, A., Elshaer, A., 2024. Novel steel connection for modular houses in indigenous communities: An experimental study. J. Constr. Steel Res. 220, 108850. https://doi.org/10.1016/J.JCSR.2024.108850

Elhadary, M., Elshaer, A., 2021. Behaviour of beam-column connection of modular steel buildings Keywords :, in: CSCE 2021 Annual Conference. Springer Singapore, Whistler, British Columbia.

Fadden, M., Asce, A.M., Wei, D., Asce, S.M., Mccormick, J., Asce, A.M., 2015. Cyclic Testing of Welded HSS-to-HSS Moment Connections for Seismic Applications 141, 1–14. https://doi.org/10.1061/(ASCE)ST.1943-541X.0001049

Fadden, M., Asce, S.M., Mccormick, J., Asce, A.M., 2012. Cyclic quasi-static testing of hollow structural section beam members 138, 561–570. https://doi.org/10.1061/(ASCE)ST.1943-541X.0000506

Fadden, M., McCormick, J., 2013. Evaluation of HSS-to-HSS moment connections for seismic applications. Struct. Congr. 2013 Bridg. Your Passion with Your Prof. - Proc. 2013 Struct. Congr. 2334–2345. https://doi.org/10.1061/9780784412848.204

Gillies Lumber, 2025. Pre-fabricated wall panels [WWW Document]. URL https://gillieslumber.ca/products/pre-fabricated-wall-panels/?form=MG0AV3 (accessed 1.11.25).

Khan, K., Yan, J.B., 2020. Finite element analysis on seismic behaviour of novel joint in prefabricated modular steel building. Int. J. Steel Struct. 20, 752–765. https://doi.org/10.1007/s13296-020-00320-w

Kosteski, N., Packer, J.A., 2003. Longitudinal Plate and Through Plate-to-Hollow Structural Section Welded Connections. J. Struct. Eng. 129, 478–486. https://doi.org/10.1061/(asce)0733-9445(2003)129:4(478)

Kosteski, N, Packer, J.A., 2003. Welded Tee-to-HSS Connections 129, 151–159.

Lawson, R.M., Prewer, J., Trebilcock, P.J., 1999. Modular construction using light steel framing. Steel Construction Institute.

Liu, X.C., Cui, F.Y., Zhan, X.X., Yu, C., Jiang, Z.Q., 2019. Seismic performance of bolted connection of H-beam to HSS-column with web end-plate. J. Constr. Steel Res. 156, 167–181. https://doi.org/10.1016/j.jcsr.2019.01.024

Liu, X.C., Wang, Y., Cui, X.X., Yu, C., Bai, Z.X., 2020. Seismic performance of bolted beam-to-column connection with rib-stiffened splicing plate. J. Constr. Steel Res. 174, 106300. https://doi.org/10.1016/j.jcsr.2020.106300

Liu, X.C., Yang, Z.W., Wang, H.X., Zhang, A.L., Pu, S.H., Chai, S.T., Wu, L., 2017. Seismic performance of H-section beam to HSS column connection in prefabricated structures. J. Constr. Steel Res. 138, 1–16. https://doi.org/10.1016/j.jcsr.2017.06.029

Livermore software technology corporation (LSTC), 2007. Livermore software technology corporation (LSTC). (2007). LS-DYNA keyword user's manual, Vol. 1, Livemore, California, USA, R13.0.

Park, K., Jiansinlapadamrong, C., Chao, S.-H., 2021. Double-HSS Seismic Resistant Beam-to-Column Moment Connections. J. Struct. Eng. 147, 1–17. https://doi.org/10.1061/(asce)st.1943-541x.0003057

CHAPTER 6: CONCLUSIONS AND RECOMMENDATIONS

6.1 Summary

This thesis introduces a novel steel connection designed for modular houses in remote Indigenous communities, focusing on the mechanical behavior of bolted HSS-to-HSS moment connections. The research employs both experimental analysis and finite element models (FEM) to evaluate moment-rotation curves, stiffness, ductility, and failure modes. The research program included testing the proposed steel bolted connection under monotonic load, where a Digital Image Correlation (DIC) technique is utilized to enhance the understanding of strain distribution and load transfer mechanisms. The thesis also explored the mechanical performance of various geometric parameters and reinforcement techniques for HSS-to-HSS connections through finite element models validated against experimental results. In addition, machine learning prediction and classification models were introduced to predict the ultimate capacity and failure modes of long bolted HSS-to-HSS connections.

6.2 Main Contributions

The main conclusions pertaining to the newly developed steel connection for modular houses are as follows:

- An experimental study was conducted in which specimens were tested under monotonic loading to evaluate the structural performance of the proposed connection. The study focused on joint strength, stiffness, failure modes, and ductility. The examined parameters, including the presence of stiffeners, bolt configurations, extended plate thickness and the number of bolts, were found to significantly affect the mechanical behavior of the connection.

- An extensive parametric study was carried out to investigate the influence of lower and upper limits of different geometric parameters on the structural performance of the unstiffened connection. A 3D finite element model was used for this analysis, which was validated with experimental results that showed an average error of less than 3%. Based on this study, failure mode charts were developed for various bolt arrangements in unreinforced models. These charts can predict failure modes by adjusting key design parameters. The accuracy of the charts was confirmed by comparing the predicted failure modes with the performance of the tested specimens for the proposed connection.
- Machine learning was applied in both regression and classification models to predict the ultimate capacity of the connection and the failure mode based on various geometric parameters. The regression models, including decision trees, ensemble trees, and neural networks, were used to predict the ultimate capacity, significantly reducing the time required by finite element models while demonstrating good accuracy. Meanwhile, the classification models were employed to predict the failure mode of the connection, offering valuable insights based on the different geometric configurations. Overall, this machine learning approach showed promising results in improving prediction accuracy and efficiency.
- A detailed parametric study was conducted to assess the impact of different reinforcement techniques on the performance of long bolt connections. The study revealed that bolt arrangements played a significant role in enhancing ultimate capacity, independent of the reinforcement technique or bolt count. However, combining concrete and stiffeners notably increased the ultimate capacity where concrete reinforcement helped prevent column

buckling and increased capacity by 1.5 times compared to the unreinforced model. Overall, the combination of concrete and stiffeners proved to be the most effective reinforcement strategy, particularly for larger bolt configurations, improving both capacity and rotation reduction. These results highlight the importance of selecting the right reinforcement method based on bolt arrangement and performance objectives. Additionally, failure mode charts were created for different reinforced bolt arrangements to predict failure modes by modifying key design parameters.

6.3 Future work and recommendations

- The proposed steel bolted HSS-to-HSS connection can be evaluated as a lateral force-resisting system in panelized modular structural frames through full-scale tests and finite element analyses.
- The dimensions of the proposed connection can be adjusted to serve as a seismic moment-resisting connection. Finite element analyses can be conducted on the beam-column connection with these modified connectors to determine the optimal geometry.
- The connection can be extended for use as a column cap and connected to columns and beams made of different materials, such as wood, to reduce the structure's overall weight.
- A full-scale panel with four connections, each featuring different corrugated sheet profiles, can be tested to assess its contribution to resistance against lateral loads.